PHASE CURRENT RECONSTRUCTION AND PEAK PREDICTION FOR SWITCHED RELUCTANCE GENERATORS

by

Prashant Carl Buck

APPROVED BY SUPERVISORY COMMITTEE:

Dr. Poras T. Balsara, Chair

Dr. Babak Fahimi, Co-Chair

Dr. Dinesh K. Bhatia

Dr. Bilal Akin

This dissertation is dedicated

to my mother Dipti, my father Amarjit,

and my wife Priyanka.

PHASE CURRENT RECONSTRUCTION AND PEAK PREDICTION FOR SWITCHED RELUCTANCE GENERATORS

by

PRASHANT CARL BUCK, B.TECH, MS

DISSERTATION

Presented to the Faculty of

The University of Texas at Dallas

in Partial Fulfillment

of the Requirements

for the Degree of

DOCTOR OF PHILOSOPHY IN

ELECTRICAL ENGINEERING

THE UNIVERSITY OF TEXAS AT DALLAS

August 2019

ACKNOWLEDGMENTS

This dissertation is a culmination of many years of hard work and perseverance and the realization of achieving a childhood dream of becoming an engineer. During the pursuit of my doctoral degree, I faced many emotional, spiritual, and intellectual challenges. Had it not been for the support of those around me, this childhood dream would have never come true.

I am extremely grateful and fortunate to have had the opportunity of working closely with my advisor, Professor Poras Balsara. He gave me the encouragement I always needed and as the challenges grew, at times he had more confidence in me than I had in myself. The relationship I developed was not only limited by the scope of academics but also included an overall personal growth in becoming a better person, something I will always cherish. I would like to thank him for all his time, his invaluable feedback, and the promise he saw in me to fund me through the years of my doctoral studies.

I would also like to thank Professor Babak Fahimi for all the guidance and feedback he provided me during my research on the switched reluctance machine. He provided me with vital insight, novel ideas, and motivation which helped me complete my doctoral studies. He also gave me the opportunity to be part of the Renewable Energy and Vehicular Technology (REVT) laboratory, something I will always be grateful for. I would also like to thank the other members of my dissertation committee, Professor Dinesh Bhatia, for his support, helpful feedback, and invigorating discussions during our meetings, and Professor Bilal Akin, who provided me with the necessary guidance.

None of this would have transpired if it wasn't for my parents, they instilled in me a passion for hard work, dedication, sincerity, and perseverance. I am so grateful for their support and love and for always being there for me. They have journeyed with me through the highs and the lows, I am so grateful and fortunate to be blessed by their presence. I would like to especially thank my wife, Priyanka, for her love, care, support and patience, without which I would not have been able to reach this milestone in life.

I would like to sincerely thank the rest of my family and friends, who have supported and prayed for me throughout my doctoral studies. Above all, I would like to thank God, for choosing me and giving me the strength and the capability to be able to contribute to the noble field of science and most importantly, for a chance to glorify Him.

July 2019

PHASE CURRENT RECONSTRUCTION AND PEAK PREDICTION FOR SWITCHED RELUCTANCE GENERATORS

Prashant Carl Buck, PhD
The University of Texas at Dallas, 2019

Supervising Professors: Dr. Poras T. Balsara, Chair
Dr. Babak Fahimi, Co-Chair

The threat of rising temperatures and increasing sea levels due to the high carbon emissions and greenhouse gases, has prompted a worldwide push towards the production of clean energy through renewable sources. Renewable technologies gained significant traction, especially after the 2015 United Nation's Paris Agreement, which united countries to preserve the planet for a better future.

Electric machines play an important role in the renewable energy sector, as they are widely used in wind turbines and electric and hybrid electric vehicles. However, the commonly used machines use a large amount of permanent magnets, whose prices have been increasing due to the limited supplies of rare earth elements used in their production and also because of their increasing demand.

A switched reluctance machine (SRM) is a suitable candidate in the renewable energy sector as it does not use permanent magnets and is extremely versatile and robust. Due to the lack of permanent magnets in a switched reluctance generator (SRG), the machine suffers from low power densities compared to its competition. The research presented in this dissertation pushes the envelope of an SRG's produced charge, making it more competitive in the renewable energy sector.

Maximizing the output charge of an SRG involves its operation at high speed in single pulse mode, wherein the motional back EMF is allowed to build up and reach a substantial value. This results in an SRG's phase currents entering into a state of positive feedback, wherein even switching off the phase does not bring down their value. Operating the machine in this scenario results in higher output charge; however, it makes the phase currents uncontrollable. The phase currents peak and begin to fall only after the motional back EMF reduces, which occurs as the rotor approaches its unaligned position. Protection of the drive circuit is imperative; however, if the unknown peak values of the phase current exceed the current ratings of the diodes, the drive circuit will be damaged. As a result, either an SRG is not operated in the positive feedback mode (thereby losing out on the additional charge produced) or the drive's power converter is over engineered for a high current rating, in order to sustain the unknown current levels.

Since the system is extremely nonlinear, it poses significant modeling and control challenges in order to safely operate an SRG in single pulse positive feedback. Due to the time delay associated with numerical methods of integration, an iterative approach to predict the phase current is impractical. The presented research reconstructs the phase current of an SRG and predicts its current peak by detecting an optimal turn-off angle, which leads to a more controllable machine with reduced drive constraints and higher output charge, all while maintaining the same size. The research also analyzes the effect of a freewheeling phase in the high speed mode of operation of an SRG.

TABLE OF CONTENTS

LIST OF FIGURES

LIST OF TABLES

LIST OF SYMBOLS

a_j	j^{th} element of sequence a	230
N	Number of elements in a sequence	230
s_j	j^{th} element of filtered sequence s	230
n	Moving average window size	230
$V_{L(avg)}$	Averaged value of the voltage across the phase inductance	232
i_{avg}	Averaged value of phase current	232
$L(\theta_x, i_x)$	Instantaneous phase inductance at $theta_x$ and i_x	233
$L_{avg}(0, i)$	Averaged value of the aligned position phase inductance	234
$L_{avg}(\pm 15, i)$	Averaged value of the mean midpoint position phase inductance	236
$L_{avg}(\pm 30, i)$	Averaged value of the mean unaligned position phase inductance	237
D_S	Source diode	252
V_S	Source voltage	252
C	DC link capacitor	252
R_{pcb}	Drive's circuit board resistance	252
R_w	Phase winding resistance	252
V_{srm}	Voltage across the terminals of a switched reluctance machine	252
$R_{DS(on)}$	MOSFET on resistance	253
t_{on}	Phase turn on time	259
t_{offx}	Phase turn-off time instance ($x = a, b, c$)	259
t_{endx}	Time instance at which the generating phase current returns to zero ($x = a, b, c$)	259
Q_{inv}	Invested charge	260
Q_{har}	Harvested charge	260
Q_{net}	Net charge	261
E_{out}	Output electrical energy	261
P_{out}	Output electrical power	261
T_c	Time period of a generating cycle	261

CHAPTER 1

INTRODUCTION

Chapter 1 provides an overview of global energy requirements, the importance of adopting renewable sources into the energy mix, the demand for rare earth elements used for the production of permanent magnets, and the importance of end of life recycling of renewable technologies. In addition, the importance of switched reluctance machines (SRMs) and their role in the renewable energy sector are presented, along with their origin, architecture, and various topologies. Furthermore, the advantages and limitations of switched reluctance machines are listed. Lastly, the organization of subsequent chapters of this dissertation is presented.

1.1 Overview of Global Energy Requirements

This section provides an overview of global energy requirements and the path various regions of the world are on, in achieving their energy goals in a sustainable manner. Useful energy is produced[1] through various sources, which are classified into two categories, namely nonrenewable sources and renewable sources. The decision to use either source of energy depends on several factors prevalent in the region; however, the threat of increasing temperatures and consequently increasing sea levels around the world has urged nations to unite and take preventive measures rather than exacerbate the planet's rising temperatures [13]. A worldwide effort to reduce greenhouse gases (GHGs), which would eventually keep the global temperatures in check, has caused a shift in the production of energy from nonrenewable fossil fuels to cleaner renewable sources of energy.

[1] According to the law of conservation of energy, energy can neither be created nor destroyed, it can only be transformed from one form to another. Human ingenuity and skill can only convert energy from one form to another, it cannot create it. Therefore, it is technically more appropriate to state that, energy is *converted* from a source rather than stating that energy is *produced* by a source. However, it is not uncommon to encounter the latter and should be overlooked, the implication of both statements remains the same.

Developing regions around the world, where energy consumption is expected to rise significantly are identified and their decision to use renewable sources of energy is explored. For developing regions, the shift to energy production through renewable sources can be a daunting task as it involves building extensive renewable power plants, which in turn require a significant amount of investments. For such regions, the investments could be put towards addressing more immediate needs rather than moving to a cleaner source of energy production, resulting in an overall sluggish effort.

On the other hand, developed regions around the world already produce a significant portion of their energy through renewable sources; however, there is still room for improvement in order to reduce the carbon emissions and GHGs. Developed regions (and a few developing regions) have also targeted the next biggest source of carbon emissions, i.e., the transportation sector. The push for the inclusion of clean energy sources in the transportation sector is also presented in this section.

1.1.1 Identifying Upcoming Energy Demanding Regions of the World

There is an ever increasing demand for electrical energy at a global level, regions around the world have distinct energy requirements, giving rise to specific energy consumption profiles. The energy requirements of growing populations, development of infrastructure and manufacturing industries, along with the growth of the economy are key factors which dictate a region's energy demand. Consequently, there is an increase in focus and investments towards the production and distribution of electrical energy.

The United States Energy Information Administration (EIA), an agency of the United States Department of Energy (DOE), in its most recently published energy outlook, i.e., the International Energy Outlook 2018 (IEO2018), focused on the impact of three developing regions, i.e., China, India, and Africa and their impact on the global energy markets [14]. The considered regions are highly populated and have high economic growth, leading to an increase in the demand for energy, which is likely to affect the global energy markets.

The IEO2018 predicts the growth of the three regions from 2015 to 2040. For China, it is expected that its economy will grow at an average rate of 5.7% per year, making it the world's largest producer of energy intensive goods, also indicating China's manufacturing authority at the global level. The next region, India, is expected to achieve an economic growth of 7.1% per year, the fastest among the three regions considered. India is also projected to have the world's largest population by 2040, thereby putting a significant demand on its energy production, albeit still maintaining a lower total and per capita energy consumption level compared to China and the United States. Lastly, Africa's economy is expected to grow at an average rate of 5.0% per year with most of its energy demand made by the region's developing infrastructure. By 2040, Africa's per capita energy consumption is expected to be even lesser than that of India's.

1.1.2 International Treaties Promoting Production of Clean Energy

The choice of using a particular source of energy is determined by various factors, the usage of fossil fuels and nonrenewable sources of energy are globally discouraged, while the usage of renewable sources of energy is urged and highly encouraged. The United Nations Framework Convention on Climate Change (UNFCCC), an international environmental treaty, plays a major role in determining the source of energy used by the identified regions. While the UNFCCC does not directly dictate the usage of a particular source of energy, it does encourage its Parties to reduce their GHG emissions. According to Article 2 of the UNFCCC, the objective of the convention states the following: *"stabilization of greenhouse gas concentrations in the atmosphere at a level that would prevent dangerous anthropogenic interference with the climate system"* [15].

The Paris Agreement, an agreement within the UNFCCC, placed specific goals on its participating Parties towards the reduction of GHG emissions. Under Article 2 of the Paris Agreement, one of its objectives states the following: *"Holding the increase in the global* *average temperature to well below 2.0 °C above pre-industrial levels and pursuing efforts to limit the temperature increase to 1.5 °C above pre-industrial levels, recognizing that this would significantly reduce the risks and impacts of climate change"* [16]. China, India, and most countries of Africa ratified to the Paris Agreement and began striving to achieve and exceed the goals laid out by the agreement. In 2015, according to the UNFCCC, China and India were responsible for 20.09% and 4.10% of the total global emissions, respectively [17], a significant amount, which needed to be controlled. Next, plans for clean energy production in China, India, and Africa are presented.

1.1.3 Clean Energy Production in China

To address the issue of increasing carbon emissions, in 2015, the National Development and Reform Commission (NDRC) of the People's Republic of China submitted its Nationally Determined Contributions (NDC) to the UNFCCC, essentially laying out its plans to reduce GHG emissions [18]. In the 2015 NDC, China pledged to achieve a set of goals by 2030, which would put the nation on a greener path, thereby, aligning itself with the objective of the Paris Agreement. The main goals laid out by China in their 2015 NDC were:

- To reduce the carbon dioxide emissions per unit of gross domestic product (GDP) by 60% to 65% from the 2005 levels.
- To increase the energy produced through non fossil fuels to 20%, i.e., through renewable and nuclear sources combined, specifically setting a target of 200 GW for installed wind capacity and 100 GW for installed solar capacity by the end of 2020 itself.
- To increase the volume of forests by 4.5 billion cubic meters compared to 2005 level.

In 2017, the NDRC published its climate report, laying out China's progress towards reaching the goals laid out in its earlier 2015 NDC. The report stated that by the end of 2016, China had installed non fossil fuel based power plants capable of generating upto

587 GW of power, accounting for 36.6% of the total national installed capacity [19]. Out of the total non fossil fuel installed capacity, wind alone accounted for around 147 GW or 9.1% of the total installed capacity. Also, the total energy generated through non fossil fuels was close to 1695 TW h, which accounted for 29.1% of the total energy generated. Figure 1.1 shows China's total installed capacity and its installed wind capacity upto 2017 [20], along with its total projected capacity and its projected wind capacity by 2040 [21].

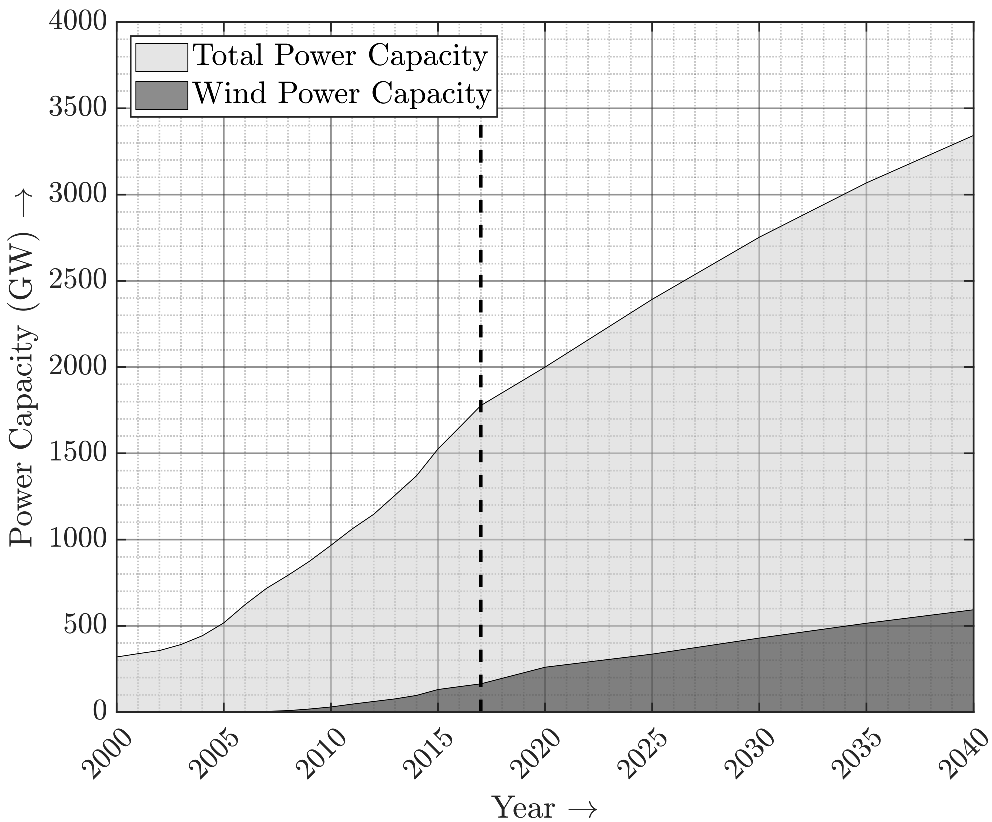

Figure 1.1: China's installed capacity upto 2017 along with its projected capacity by 2040

In 2017, China's wind and solar energy markets were the largest in the world [22]. The 13th Renewable Energy Development Five-Year Plan (2016 to 2020) adopted by the Chinese National Energy Administration (NEA) targeted to increase the installed wind capacity to 210 GW by 2020. However, seeing that the goal could be surpassed, China revised its installed wind capacity target to an ambitious 260 GW by the end of 2020 [23, 24].

1.1.4 Clean Energy Production in India

India's pledge to the Paris Agreement included reducing its GHG emissions by 35% below its 2005 levels by 2030 [25]. To meet the targeted emission levels, India's shift in the usage from nonrenewable to renewable sources of energy has been aggressive. India canceled plans to build 13.7 GW worth of coal based power plants in 2017 and has also reduced the amount of coal imported into the country. The Government of India Ministry of Power Central Electricity Authority (GoI CEA) reported a reduction in the GHG emissions from its existing coal plants by placing higher standards and newer and advanced filtration techniques within their coal plants [26].

In order to meet and exceed the goals set by the Paris Agreement, India aimed at achieving an installed capacity of 175 GW through renewable sources by 2022. In their 2016 annual report, the Government of India Ministry of New and Renewable Energy (GoI MNRE) reported an increase in energy production through renewable sources. The GoI MNRE in their annual report also stated that, in 2016, India's installed capacity through renewable sources was close to 50 GW, putting it fifth in the list of countries with the highest installed capacity through renewable sources behind China, the United States, Germany, and Japan [27]. Of the targeted installed capacity of 175 GW through renewable sources, the GoI MNRE projects a total of 60 GW of installed wind capacity alone. Some sources also report that India may surpass its targeted installed capacity and be able to achieve an installed capacity of close to 225 GW through renewable sources by 2022 [28].

1.1.5 Clean Energy Production in Africa

The IEO2018 identifies the African continent as a region of high growth in terms of the manufacturing sector, as a result, an increase in Africa's industrial energy usage is expected. To keep up with the projected energy demand, Africa is expected to establish several new power plants by 2040. In terms of clean energy sources, the African continent has an enormous potential for generating electricity through wind energy. If the entire wind potential were harvested, it is estimated that the African continent would be capable of generating several times its electricity consumption levels [29]. However, the wind potential is not evenly distributed across the entire continent. Countries of the African continent which have particularly excellent wind resources include Cape Verde, Morocco, Tunisia, and Egypt in northern Africa, Niger in west Africa, Chad in central Africa, Ethiopia, Kenya, Sudan, Somalia, and Uganda in east Africa, and Tanzania, South Africa, and Zambia in the southern portion of the African continent [30].

Africa's installed wind capacity has been on the rise, it was reported to be 2.46 GW in 2014, increasing to 4.52 GW in 2017. Future projections estimate Africa's installed wind capacity to reach 14 GW by 2022 and close to 85 GW by 2030 [30, 31].

1.1.6 Future of the Transportation Sector

Due to the significant consumption of fossil fuels by the transportation sector, many countries have introduced legislation and set goals to increase electric alternatives in order to combat and reduce carbon emissions. In July of 2017, the French Environment Minister announced intentions to ban the sale of all new petrol and diesel vehicles by 2040 as part of France's renewed commitment to the UNFCCC Paris Agreement. The Netherlands also plans to ban the sale of all new petrol and diesel vehicles by 2030. Since 2017, the Dutch passenger railway operator, Nederlandse Spoorwegen, has already been operating all its electric trains using renewable energy, mainly through harvested wind energy [32]. China, one of the largest auto makers in the world [33] has also set a goal to ban the sale of new petrol and diesel vehicles by 2040. The ban on petrol and diesel vehicles is an attractive option for several countries, as they would be more likely to meet the goals of the UNFCCC Paris Agreement. Some of the countries which have announced bans over their transportation sector are listed in Table 1.1.

Table 1.1: Countries intending to ban the sale of all new petrol and diesel vehicles

Country	**Start of Ban**
Taiwan	2040 [34]
France	2040 [35]
India	2030 [36]
Netherlands	2030 [36]
Norway	2025 [36]
United Kingdom †	2040 [36]
Austria	2025 [36]
Ireland	2030 [34]
Israel ††	2030 [34]
Sweden	2030 [37]

† Scotland (part of the United Kingdom) announced the start of the ban by 2032 [36].
†† Israel announced the application of the ban to imported vehicles only [34].

1.2 Supply and Demand for Rare Earth Elements and Permanent Magnets

In 2015, the UNFCCC Paris Agreement urged its Parties to adopt clean energy sources in order to combat the planet's increasing GHG levels and rising temperatures. In response, developing regions around the world pledged to reduce their reliance on coal fired power plants and focus more on the expansion of their wind and solar power plants. Developed regions (and a few developing regions) have also taken the initiative in reducing the consumption of petroleum in their transportation sector by setting goals to switch to electric vehicles (EVs) and hybrid electric vehicles (HEVs), eventually banning the use of gasoline vehicles altogether. However, the proposed clean energy solutions are accompanied by their own sets of concerns and secondary environmental effects. Harvesting wind energy requires the use of wind turbines and generators, while electric vehicles require motors and generators to achieve the desired results, both applications rely heavily on the use of electric machines, i.e., motors and generators. As a result, there is a high demand for electric machines, consequently the materials required in their construction are in high demand as well, one such material is the permanent magnet (PM).

Some examples of commercially available permanent magnets include aluminium nickel cobalt (AlNiCo) or Alnico, samarium cobalt (SmCo), neodymium iron boron (NdFeB) or Neo, samarium iron nitride (SmFeN), and ferrite. Elements used in the production of permanent magnets such as samarium (Sm), dysprosium (Dy), and neodymium (Nd) belong to the lanthanide series of the periodic table, also known as rare earth elements (REEs), while their oxides are known as rare earth oxides (REOs). The REEs are not as rare as the name suggests, the etymology has more to do with the unsustainable mining practices and extraction processes of the elements from their ores. For reference, the static depletion index of REOs (i.e., ratio of the reserves to the present consumption) is approximately 870 years, to put that in context, copper (an essential element in the construction of electric machines) has a static depletion index of 34 years, something which should be equally concerning [38]. The mining and extraction process is not only a major economic challenge, but has an adverse environmental impact as well. Contamination of potential sources of drinking water and ingestion of fine particulate mine waste are the typical issues related with mining, which in turn have the potential to affect human health and well being. Also, during the extraction process, carbonates present in the ores are liberated to yield useful REEs, leaving behind a carbon footprint and GHG emissions.

Though the REEs are not extremely rare, their increasing demand and limited supplies are a growing concern. For instance, the availability of neodymium for the production of neo magnets is expected to eventually limit the production of electric vehicles. The geographical availability of REEs is also a concerning factor. In 2016, China held a monopoly over the supply of REEs, 85% of the global REE supply originated from China, while Australia was the second largest contributor of REEs, producing around 10% [39]. In the past, China has not only been the largest producer of REEs, but also the largest consumer of REEs as well.

As a result, world markets are highly dependent on China's REE exports and are extremely susceptible to their changing export policies. For example, in July of 2010, China's Ministry of Commerce announced a reduction in their export of REEs by 40%, creating a large supply instability and price volatility in the global REE market [40].

Close to 70 weight percent of ferrite and REE based permanent magnets are used in electric machines [41]. In wind and automotive applications, the use of dysprosium (Dy) and neodymium (Nd) for the production of rare earth magnets is significantly high. In the fourth generation wind turbines, the direct drive permanent magnet generators are a popular machine of choice due to their improved efficiencies over their predecessors.[2] However, they use somewhere between 250 kg to 600 kg of neo magnets per MW of output power or around 400 metric tons of neo magnets per GW of output power [42]. The projected annual use of rare earth magnets for the purpose of wind turbines is estimated to be around 16 kt from 2018 through 2025, similarly, the use of rare earth magnets in the transportation sector is expected to be around 17 kt in 2020 [41], while the total use of REOs for clean technologies is expected to be close to 52 kt by 2030 [39]. Based on the aggressive adoption of clean energy solutions, dysprosium (Dy) and neodymium (Nd) demand may increase by 700% and 2600%, respectively by 2035 [38].

The concern regarding the production and usage of rare earth magnets does not lie with the geophysical availability of REEs, but rather lies with whether the supply of REEs can keep up at the same pace as the projected demand. The projected demand for REEs and rare earth magnets depend on multiple factors, such as the level of deployed clean technologies, the market share of rare earth magnets within the clean technologies, and the chemical composition of REEs used in the production of rare earth magnets. However, even

[2] Earlier generation wind turbines use an induction generator which operate at around 1800 rpm. However, the wind energy is only capable of operating the machine at 10 to 12 rpm. To increase the shaft speed from 10 to 12 rpm upto 1800 rpm, a gear box with an approximate gear ratio of 1:170 is used. Since the use of a gearbox requires regular maintenance and repairs, a direct drive approach is preferred [42].

after considering a medium demand growth scenario for REEs, studies still have a common theme, i.e., the supply is expected to lag the demand for REEs [43], making the evolution of new designs and alternate solutions to permanent magnet technologies imperative.

1.3 Recycling of Electric Machines

In a world of expanding clean technologies, the aspect of end of life recycling for electric machines is becoming increasingly apparent due to their high market proliferation. The recycling of electric machines in the wind and transportation industries, once thought of as a secondary concern due to their limited usage, is no longer the case. Electric machines using permanent magnets have the benefit of increased power densities over their non magnetic alternatives, making them a preferred choice in the wind and transportation industries. However, due to their enormous projected demands and inadequate REE supplies, their rapid growth could be hampered.

Electric machines consist of materials like cast iron, steel, aluminum, copper, and neo magnets. During the recycling of electric machines, due to the valuable nature of copper and neo magnets, they are extracted by first dismantling the machines rather than using heat during the smelting process which would damage the permanent magnets, making them unsalvageable. Based on the design and structure of different electric machines, the placement of permanent magnets and copper windings vary, as a result, different dismantling techniques are required. Efficient dismantling of electric machines needs to be performed effectively and systematically. Current challenges arise due to the lack of a comprehensive recycling infrastructure, for instance, the recycling of neo magnets is primarily carried out only in China [44]. However, due to the limited supply of REEs and China's erratic export policy, other countries are also forced into exploring efficient recycling options [45] in order to meet the rising demand of permanent magnets.

1.4 Future Concerns in a World Dominated by Renewable Technologies

Renewable technology is undoubtedly the path to a cleaner and greener future for the planet; however, its secondary and tertiary affects should be identified and addressed as well, especially due to its extremely aggressive incorporation by numerous countries worldwide. Identification and prioritization of the concerns surrounding renewable technology will eventually prompt the solutions, which in the long run results in a more mature and sustainable technology.

When it comes to the wind energy sector, the most heavily contested issue is its capability of producing continuous output power, owing to wind being an intermittent source of energy. The price per unit of electricity produced from the wind energy sector is still higher than coal power plants albeit not as consistent and reliable in terms of continuity. Other considerations while expanding the wind energy sector include the energy consumed in the production of the windmills and all of its components, the on-site transportation and installation difficulties, maintenance costs, end of life recycling, and waste disposal. Environmentally, the wind energy sector may cause changes in wind intensities and cause harm to different avian species [46, 47], long term affects of which are currently unclear, though worth investigating further. The aesthetics of windmills is also viewed in a negative light by some.

Solar energy is also a great alternative to coal fired power plants; however, concerns revolving solar energy include the vast amount of real estate required for the installation of the solar panels, the reliance on a bright and sunny day, the use of highly hazardous materials in the manufacturing process, and most importantly, the end of life recycling of solar panels.

While considering the transportation sector, there is a massive global movement aiming to eventually ban petroleum vehicles and adopt electric and hybrid electric vehicles (Table 1.1). Electric and hybrid electric vehicles are undisputedly the solution towards creating a cleaner and greener future; however, there are a few considerations which need to be worked out side by side. The most important consideration is the capability of the grid being able to handle the vast number of vehicles plugged into it while replenishing their batteries. Proper infrastructure must be setup to prevent over burdening the grid. Another concern is the cost of electric and hybrid electric vehicles, they need to enter the markets at a more affordable price point. Lastly, issues like vehicle safety, battery manufacturing and recycling are all areas to continue working and improving on.

Undoubtedly, renewable technologies are the solution to the problem of rising carbon emissions and GHGs; however, they are susceptible to the questions of reliability in terms of continuous output power and sustainability due to ever increasing energy demands of the world. Scaling renewable technologies poses challenges on the resources and the economy of nations. The most important change must come at the microscopic level, i.e., it falls down to the consumer to be more mindful and conservative in their consumption of energy, a provision taken for granted in this day and age.

1.5 The Switched Reluctance Machine

This section presents the applications, origin, architecture, various topologies, and finally lists the advantages and limitations of switched reluctance machines. The advantages of a switched reluctance machine make it a suitable candidate for the use in renewable technologies, such as the wind energy sector and in electric and hybrid electric vehicles, especially due to the limited supplies of permanent magnets.

1.5.1 Applications of Switched Reluctance Machines

The Wind Energy Sector

As discussed in the previous sections, the generation of electricity through renewable sources of energy is one of the main areas of innovation when it comes to combating climate change and reducing carbon emissions. With the possibility of onshore and offshore installation options, the generation of electricity through wind energy is at the forefront of renewable technologies. A few machines commonly used for wind turbine applications are the induction machine, the permanent magnet machine, and the synchronous generator.

The limitations of induction machines include the requirement of a gearbox and the use of copper windings on the rotor. The copper windings on the rotor suffer from undesired copper losses and also add to the weight of the rotor, resulting in a slow response time.

Permanent magnet machines use large amounts of permanent magnets which drastically increase the weight and cost of the machine. Due to the use of permanent magnets, the machine is also affected by an undesired cogging torque. The recovery of permanent magnets also poses a significant challenge during the end of life recycling of the machine.

Synchronous generators have windings on the rotor as well as the stator, as a result, they are expensive and more challenging to manufacture. In synchronous generators, the rotor windings are excited by a DC voltage source using slip rings and brushes, as a result, the machine requires regular maintenance and servicing.

An ideal wind generator should have a compact size, have minimum losses, be reliable and fault tolerant, be able to operate at low wind speeds, and be able to respond quickly to varying wind speeds. A switched reluctance generator (SRG) has many favorable characteristics which make it a suitable candidate for wind generators, especially for the small to medium power plants [48–50]. Since a switched reluctance generator has a high efficiency over a wide speed range, even the use of a gearbox can be eliminated and it can be operated in a direct drive configuration [51]. By eliminating the gearbox, maintenance of the machine is significantly reduced, a feature especially attractive for offshore wind turbines.

The Transportation Sector

Electric and hybrid electric vehicles rely heavily on the use of the induction machine and the permanent magnet machine, similar to the wind energy sector. As mentioned above, both the induction and the permanent magnet machines have their respective limitations, creating an opportunity for a more robust, low cost alternative. Electric machines without permanents magnets are especially drawing significant attention due to the limited supply and high prices of REEs. Claw pole machines are also used in automobiles; however, in addition to using permanent magnets, they are sensitive to changes in temperature, something which is expected in automobiles.

Extended range requirements and large amounts of on board electronics in electric and hybrid electric vehicles ideally need an efficient and small sized electric machine for starter, alternator, traction drive, and regenerative braking purposes. Due to its high efficiency, high reliability, and high starting torque, along with the capability of operating at low and high DC voltages, over a wide temperature and speed range, and as a motor or a generator, a switched reluctance machine can be used in electric and hybrid electric vehicles as a starter and alternator [52–57], as part of the propulsion system [58, 59], or as part of the regenerative braking system [60, 61].

Apart from road vehicles, switched reluctance machines have also shown promise in the aerospace sector as aircraft starters and generators [62–65], while the linear topology of switched reluctance machines is suitable for locomotive drive applications [66–68].

1.5.2 Origin of the Switched Reluctance Machine

The modern day switched reluctance machine is based on the electric machine proposed by W.H. Taylor in the nineteenth century [69]. The name *switched reluctance* was first used by S.A.Nasar in 1969 for a very primitive version of the machine [70]. In the United States, the term *variable reluctance* is preferred, but it may be misconstrued for the stepper motor. A switched reluctance machine differs from the stepper motor, as they have larger *steps* and fewer *poles*. A second difference between the two is that, switched reluctance machines are operated in a closed loop configuration, while stepper motors are operated in an open loop configuration.

It was Professor Lawrenson at the University of Leeds, who is considered as the father of the switched reluctance drive technology [7, 71]. Along with researchers from the University of Nottingham, Professor Lawrenson founded SR Drives Limited. At SR Drives Limited in 1980, Professor Lawrenson and some of his colleagues, associated the name switched reluctance machine to its present day architecture. In 1989 and 1990, Hancock and Hendershot [72] also referred to the motor as the *brushless reluctance motor* and the *electronically commutated reluctance motor* to emphasize the absence of slip rings and brushes, which till date is one of the machine's attractions. SR Drives Limited was then acquired by Emerson Electric Company of St. Louis, Missouri in 1994 and is presently part of the Nidec Corporation since 2017 [73]. In 1990 and 2005, Professor Lawrenson was awarded the prestigious and coveted Institution of Engineering and Technology (IET) Faraday Medal and the Institute of Electrical and Electronics Engineers (IEEE) Edison Medal, respectively [71]. The medals were awarded for his contributions to the field of electric machines, especially in the development and commercialization of switched reluctance drives.

1.5.3 Architecture of a Switched Reluctance Machine

Before the architecture of a switched reluctance machine is presented, it is worth briefly reviewing the goals of electric machines and some of its terminologies. Electric machines are unique in a way that, they can either convert mechanical energy into electrical energy (i.e., generation) or convert electrical energy into mechanical energy (i.e., motoring). The main goal of generators is to efficiently convert mechanical energy into electrical energy. Conversely, the main goal of motors is to efficiently convert electrical energy into mechanical energy. Motors are capable of producing two types of output motion, i.e., they can produce either rotary or linear motion. Since the research contained in this dissertation is limited to the rotary style machine, no analysis on the linear machine is presented.

During motoring, the parameter of most interest is the torque produced by the machine, i.e., T. Switched reluctance motors produce reluctance torque, which is torque produced as the reluctance of the flux path between the stationary and the movable components of the machine reduces (hence its name). Since the reluctance and the corresponding inductance for a given flux path are inversely proportional to each other, the reluctance torque can also be thought of as the torque produced as the inductance of the excited phase changes.

A rotary style machine typically comprises of a rotating part referred to as a *rotor* and a stationary part referred to as a *stator*. The rotor and stator of a switched reluctance machine are typically made up of stacked laminated soft iron sheets which are designed to facilitate the largest change in the phase inductance when the rotor changes its position. The rotor and stator of electric machines may either be slotted or salient. Slotted rotors and stators can be filled with either permanent magnets or windings. From the standpoint of electric machines, the word *salient* implies that the machine's rotor or stator contain *protruding teeth*. In the case of a switched reluctance machine, both the rotor and stator are salient in nature, due to which the machine is referred to as a doubly salient machine. Figure 1.2 shows the two dimensional cross sectional view of a switched reluctance machine with its salient rotor and stator design. The protruding teeth are called *poles* and Figure 1.2 shows a pair of rotor poles and a pair of stator poles. The stator pole pair is also referred to as a *phase*. Diametrically opposite stator poles (i.e., a phase) have a common winding wrapped around them called a *stator phase winding*. When a particular stator phase winding is excited, i.e., a voltage is applied across its terminals and a current begins to flow through the winding, it is also called an *excited stator phase* and leads to the magnetization of that particular phase.

Due to the placement of the phase windings on the stator pole of the machine, the electrical energy is supplied to, or harvested from stationary windings and does not interact with the rotor of the machine, which in turn eliminates the need for brushes or slip rings. Contrary to what the name suggests, the reluctance of the machine is actually not switched, the *switching* refers to the switching of phase currents (more accurately known as *commutation*), while the *reluctance* in the machine's name refers to the changing reluctance as the

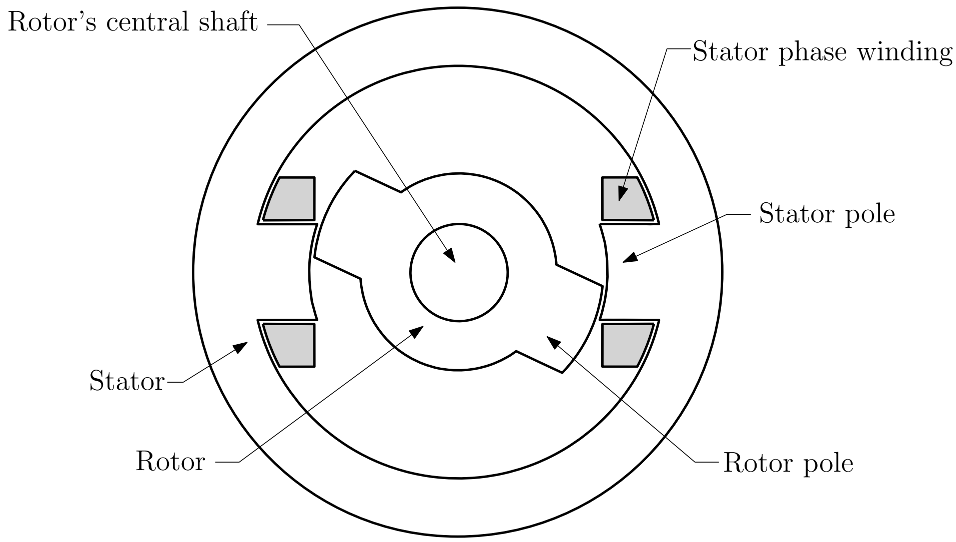

Figure 1.2: A two dimensional cross sectional view of a single phase SRM

rotor rotates. Because switched reluctance machines can have several combinations of rotor and stator poles, there is a specific convention used to represent them, which is: N_s/N_r, where N_s denotes the number of stator poles and N_r denotes the number of rotor poles. The machine shown in Figure 1.2 has two rotor poles and two stator poles, as a result, it is represented as a 2/2 machine. Some of the different switched reluctance machine topologies are presented in the next section.

1.5.4 Tolopologies of Switched Reluctance Machines

Over the years, a plethora of different switched reluctance machine topologies have been presented, of which, a few of the popular and common topologies are presented in this section. Switched reluctance machines belong to the doubly salient class of machines and based on their various topologies, are classified into separate categories as shown in Figure 1.3. By definition, a switched reluctance machine's rotor doesn't use any permanent magnets; however, there is no definition restricting the use of permanent magnets on the machine's stator. Typically, a switched reluctance machine is visualized as a machine completely free of permanent magnets. Thus, a separate category is assigned to classify doubly salient machines

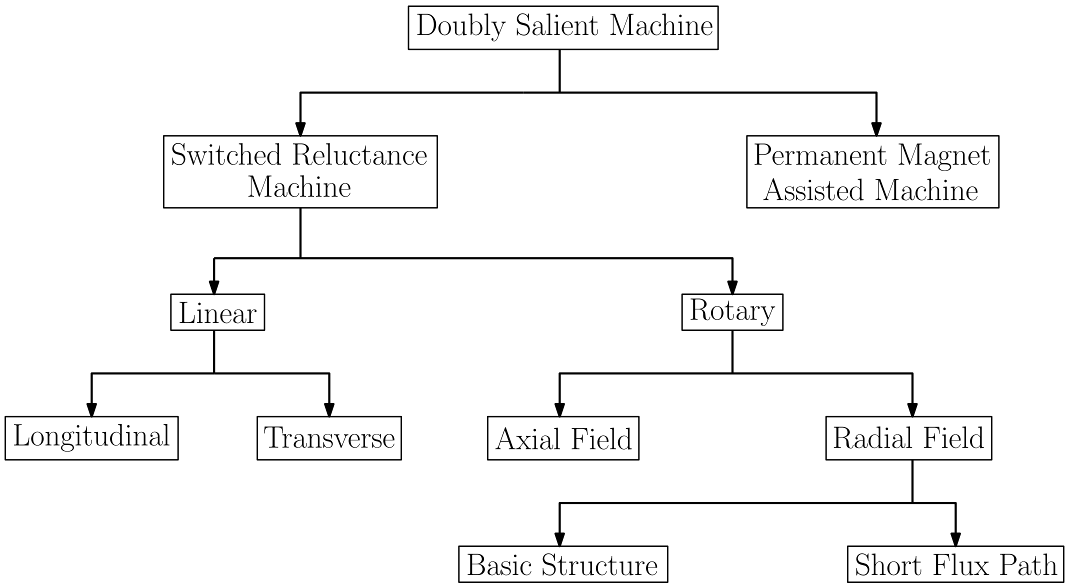

Figure 1.3: Classification of different SRM topologies [1]

using permanent magnets, i.e., the permanent magnet assisted machines, though some could argue that the classification should fall under the broader category of the switched reluctance machine itself. The work presented in this dissertation addresses only the basic structure, though it is applicable to the other topologies as well.

At the highest level of the hierarchy, a switched reluctance machine is divided into linear and rotary type machines. Linear switched reluctance machines (LSRMs) are further divided into two broad categories, i.e., longitudinal and transverse type machines. A longitudinal LSRM is shown in Figure 1.4 and is given its name due to its longitudinal flux path through the stator and translator, i.e., the magnetic circuit is parallel to the direction of motion of the translator [66].

A transverse LSRM on the other hand, is shown in Figure 1.5 and is given its name due to its transverse flux path through the stator and translator, i.e., the magnetic circuit is perpendicular to the direction of motion of the translator [74]. Modified versions of LSRMs have also been presented in previous studies. Modifications include the addition of a second stator, i.e., a double stator LSRM [75] or the use of an asymmetric structure for

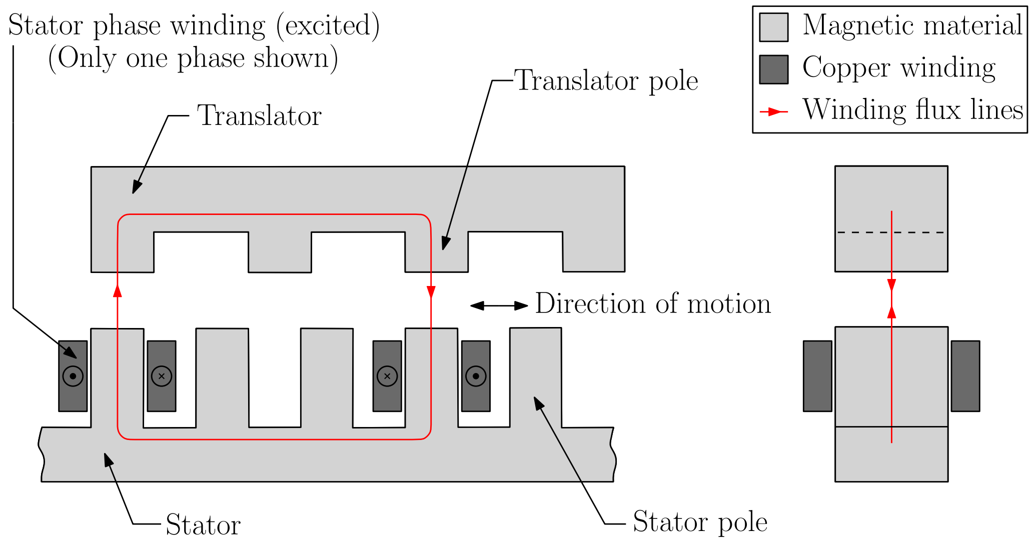

(a) Side view (b) Front view

Figure 1.4: A two dimensional cross sectional view of a longitudinal LSRM

the translator [76], which boasts of reduced magnetic saturation. LSRMs are used in a wide range of applications, some of them include precise motion control [77], propulsion system of railway vehicles [78], low-speed and high-speed mass transit applications, and elevators [79].

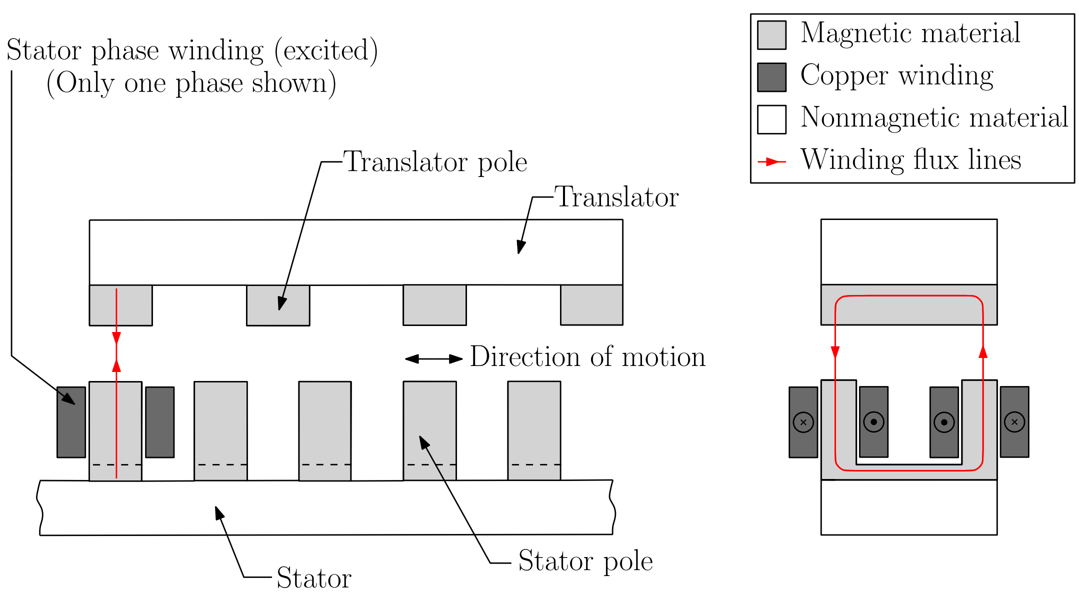

(a) Side view (b) Front view

Figure 1.5: A two dimensional cross sectional view of a transverse LSRM

As shown in Figure 1.3, rotary type switched reluctance machines are further divided into axial field and radial field type machines. In axial field switched reluctance machines (AFSRMs), the flux takes a path along the axis of rotation of the machine, i.e., the flux flows along the length of the machine as shown in Figure 1.6. An AFSRM can also be viewed as circular versions of a longitudinal LSRM, as the magnetic circuit and the axis of rotation are parallel to each other. An AFSRM has much lower torque ripple and higher power densities and is suitable for hybrid electric vehicle applications [80]. Modified versions of an AFSRM include the multiple stacked machine, in which there is more than one rotor [81].

Radial field switched reluctance machines are further divided into the basic structure, the short flux path, and the permanent magnet assisted type machines. The basic switched reluctance machine structure has been presented in Section 1.5.3 and is the machine topology considered in the subsequent chapters of this dissertation. A modified version of the basic structure includes the addition of a second stator, i.e., the double stator switched reluctance machine (DSSRM) [2, 82], which is shown in Figure 1.7.

A DSSRM has two stators (an inner and outer stator) and a single hollow cylindrical rotor which lies between them, as a result, the weight of the rotor is reduced, giving it a lower moment of inertia and consequently, a faster response time. The stator windings are placed diametrically on the inner and outer stator forming a single phase of the machine, as shown in Figure 1.7. Due to the diametrically placed windings, the radial forces on the rotor are minimized while maximizing the tangential forces, thereby reducing the vibrations and acoustic noise levels of the machine [83].

The next subcategory of radial field switched reluctance machines are short flux path machines. As the name suggests, the flux path of these machines is shorter when compared to the basic structure, in which the flux lines pass through the rotor and the stator back iron. There are multiple techniques of achieving shorter flux paths in the machine. Figure 1.8 shows the first technique, which involves placing the phase windings on adjacent stator poles.

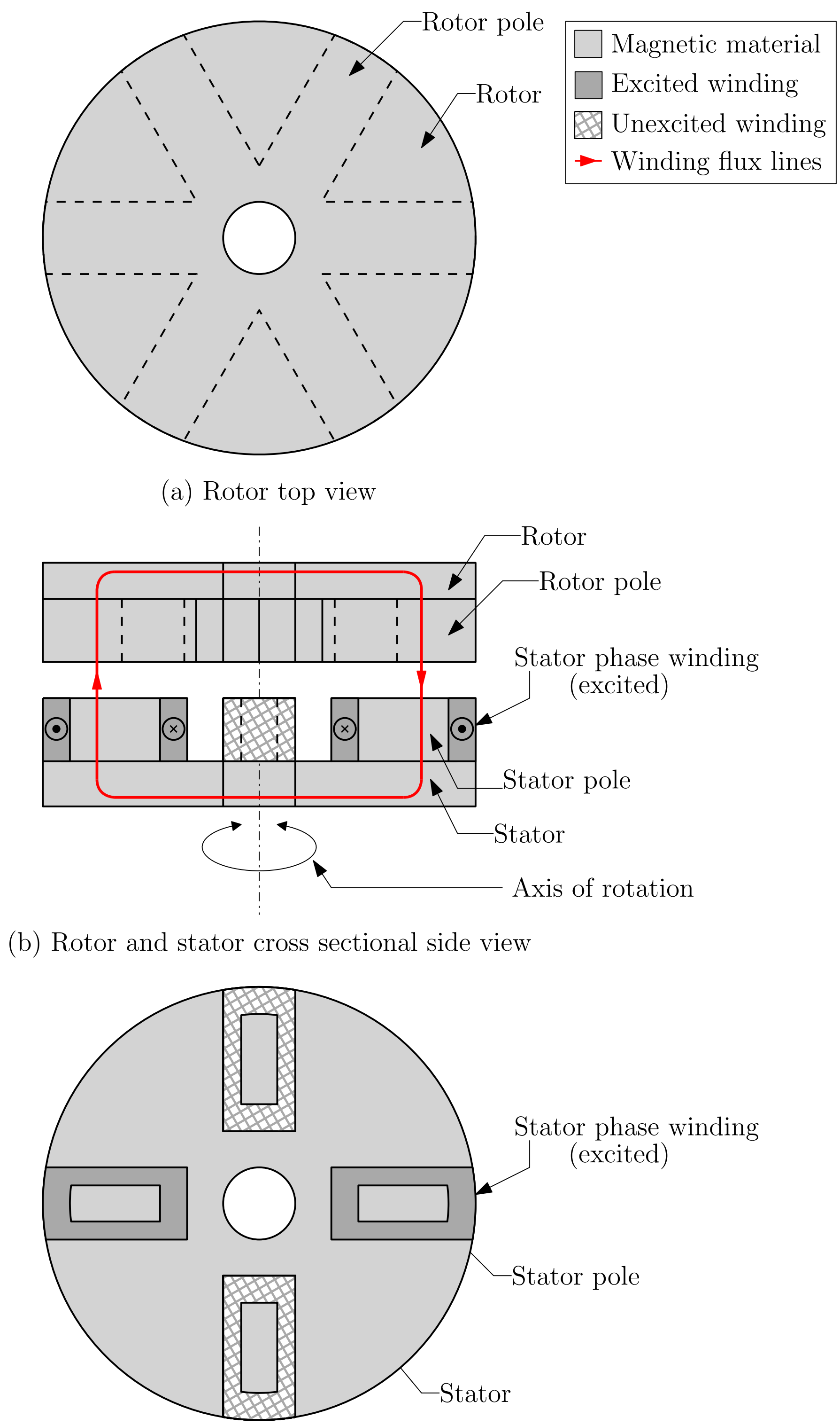

(a) Rotor top view

(b) Rotor and stator cross sectional side view

(c) Stator top view

Figure 1.6: A two dimensional view of a single stacked AFSRM

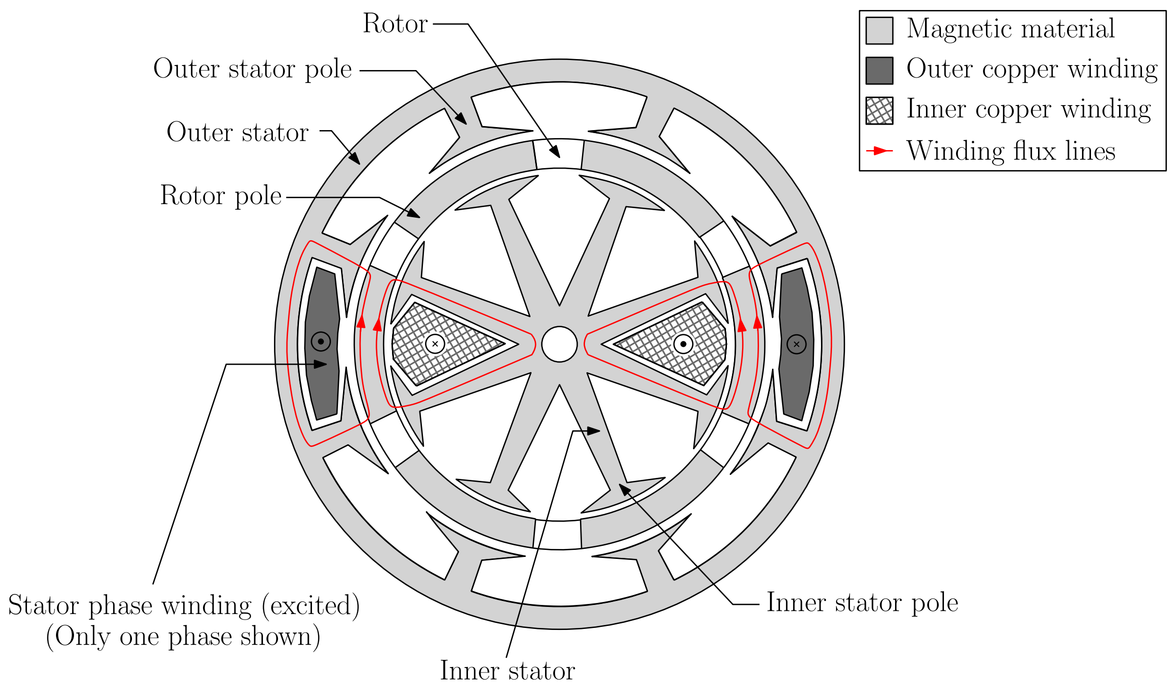

Figure 1.7: A two dimensional cross sectional view of a DSSRM. Adapted from [2], © 2010 IEEE

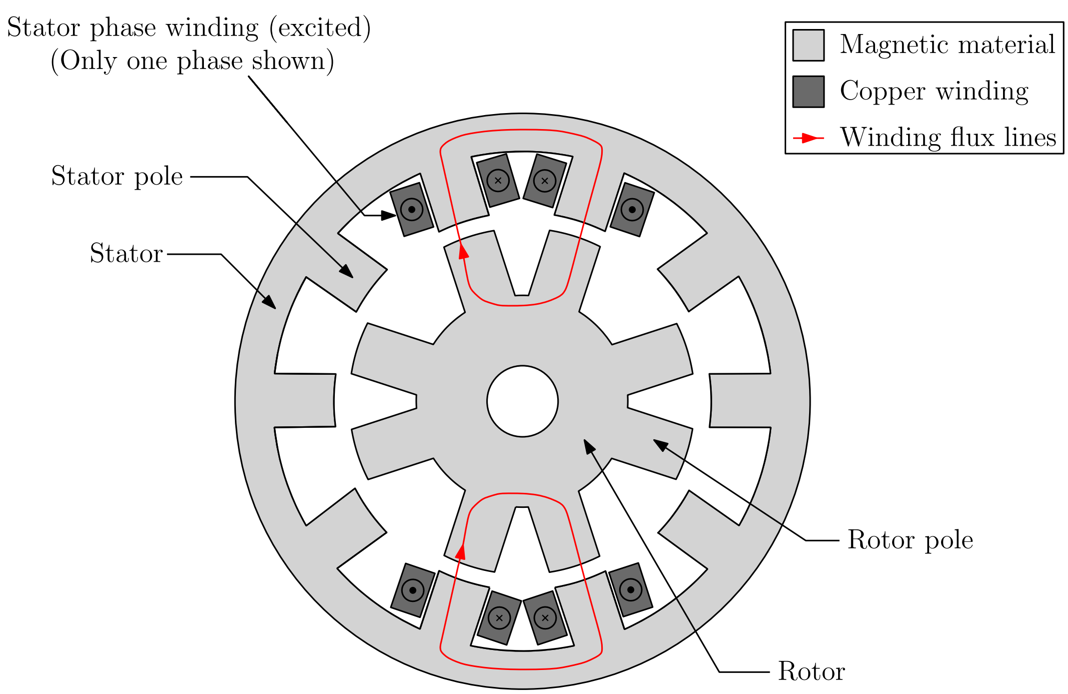

Figure 1.8: A two dimensional cross sectional view of a short flux path SRM

The shape of the rotor is also modified accordingly, such that the adjacent poles of the rotor and stator form the completed magnetic circuit. The advantages of a short flux path machine include reduced eccentric forces between the rotor and stator poles and reduced core losses due to shorter flux paths [84].

Another technique to achieve a short flux path in the machine is by physically altering the design of the stator by adding poles which are shared during commutation cycles, i.e., a shared pole or common pole short flux path machine shown in Figure 1.9, also known as the single body E-core switched reluctance machine [85]. The shared poles do not have any windings around them and only assist in creating a shorter path for the flux lines to flow through.

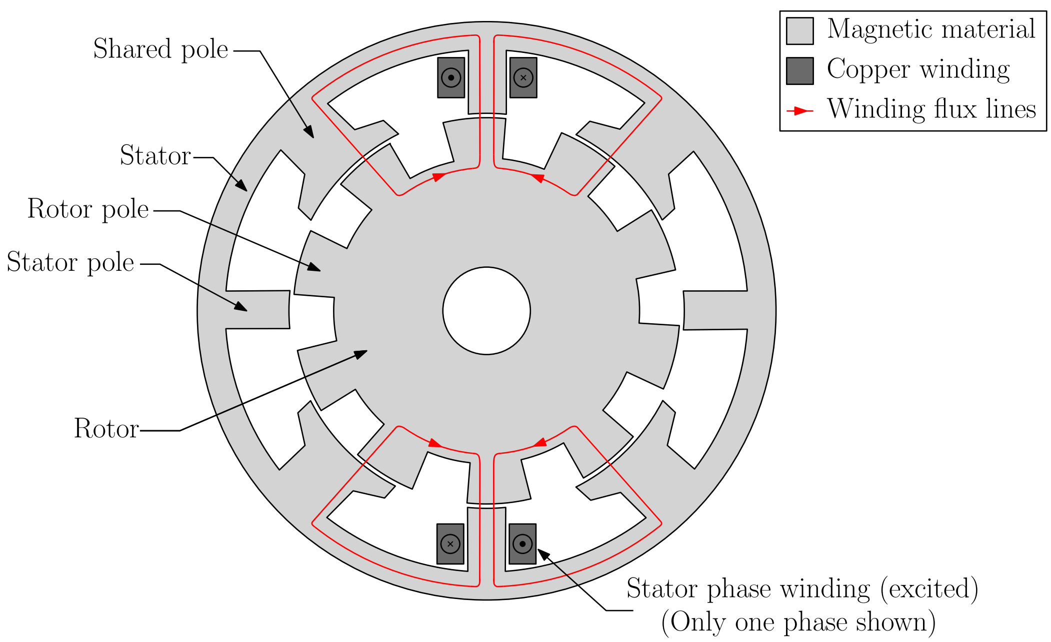

Figure 1.9: A two dimensional cross sectional view of a shared pole short flux path SRM. Adapted from [3], © 2013 IEEE

Some topologies of shared pole (or common pole) machines are also equipped with permanent magnets to increase the power density and electromechanical efficiency of the machines. These machines are classified as permanent magnet assisted doubly salient machines. Within this classification, there are several options available for the placement of the permanent magnets. Figure 1.10 shows the placement of the permanent magnets inside the shared pole of the machine. The polarity of the permanent magnets produces a magnetic field which points into the shared pole [3].

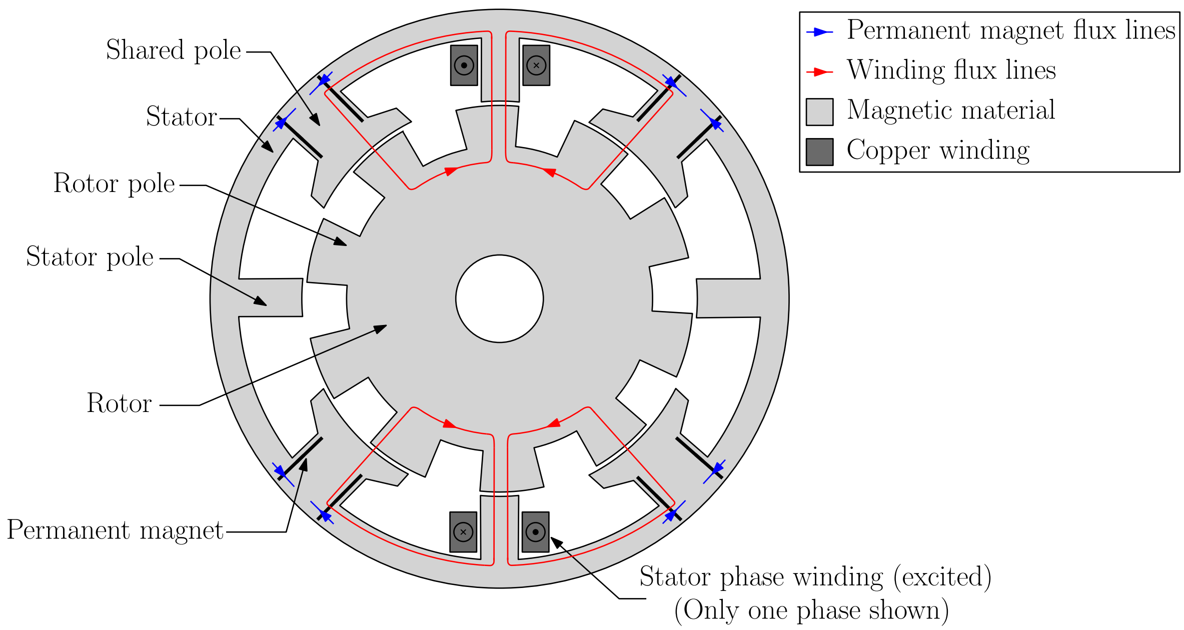

Figure 1.10: A two dimensional cross sectional view of an inset permanent magnet shared pole short flux path machine. Adapted from [4], © 2013 IEEE

Similarly, the permanent magnets can be placed inside the stator pole wound by the phase windings as well, in that case, the polarity of the permanent magnets is opposite to the polarity shown in Figure 1.10 [4]. However, by placing the permanent magnets within the stator of the machine, the structural integrity of the stator is compromised. Figure 1.11 shows the placement of the permanent magnet on the surface of the shared pole, by doing so, the machine still benefits from the advantages of the added permanent magnets without compromising the structural integrity of the stator [86].

Another example of a machine assisted by permanent magnets is the doubly salient permanent magnet (DSPM) machine, shown in Figure 1.12. The DSPM machine has permanent

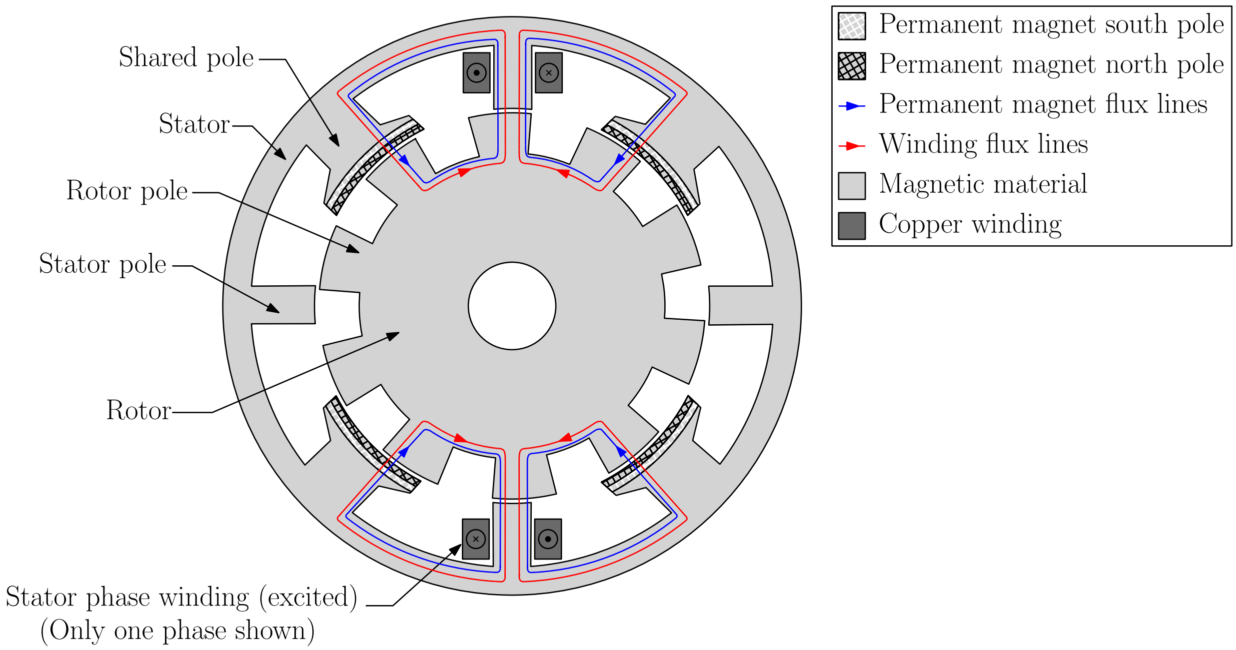

Figure 1.11: A two dimensional cross sectional view of a surface mounted permanent magnet shared pole short flux path machine. Adapted from [4], © 2013 IEEE

magnets inserted on opposite ends of the stator back iron, giving the machine a square or *football* like shape, also adding extra weight to the machine. The advantages of the DSPM machine include higher efficiencies and improved power densities [5].

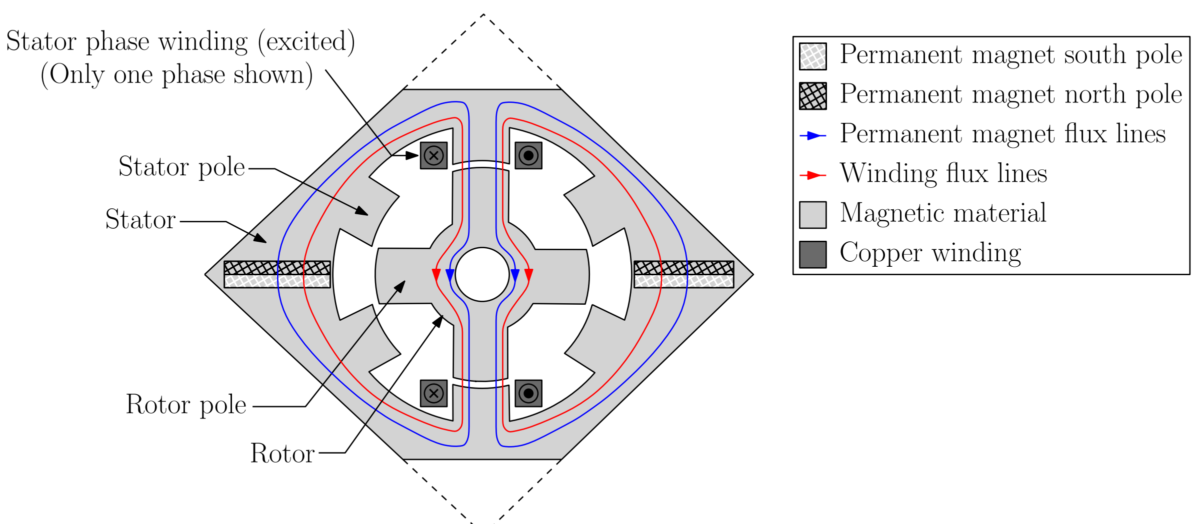

Figure 1.12: A two dimensional cross sectional view of a DSPM. Adapted from [5], © 1995 IEEE

Figure 1.13 shows a two dimensional cross sectional view of a flux reversal machine (FRM) [87, 88]. An FRM combines the benefits of a switched reluctance and permanent magnet machine. The winding flux linkage in the flux reversal generator switches its direction as the rotor rotates. The flux reversal takes place because of the staggered placement of the permanent magnets, i.e., the orientation of the north and south poles of the permanent magnets alternate in adjacent stator poles. While generating, since the flux linkage alternates, an alternating current is produced in the phase windings. Because of an FRM's simple and robust rotor design and fault tolerant capabilities, it is suitable for aerospace and industrial applications and also for automotive generators. Due to the placement of permanent magnets in the FRM shown in Figure 1.13, there is noticeable permanent magnet flux leakage, which is overcome by placing the permanent magnets in the inset of the stator poles, parallel to the winding flux lines (i.e., similar to the inset placement of permanent magnets in the shared pole shown in Figure 1.10). Such a configuration also protects the permanent magnets from getting demagnetized [6].

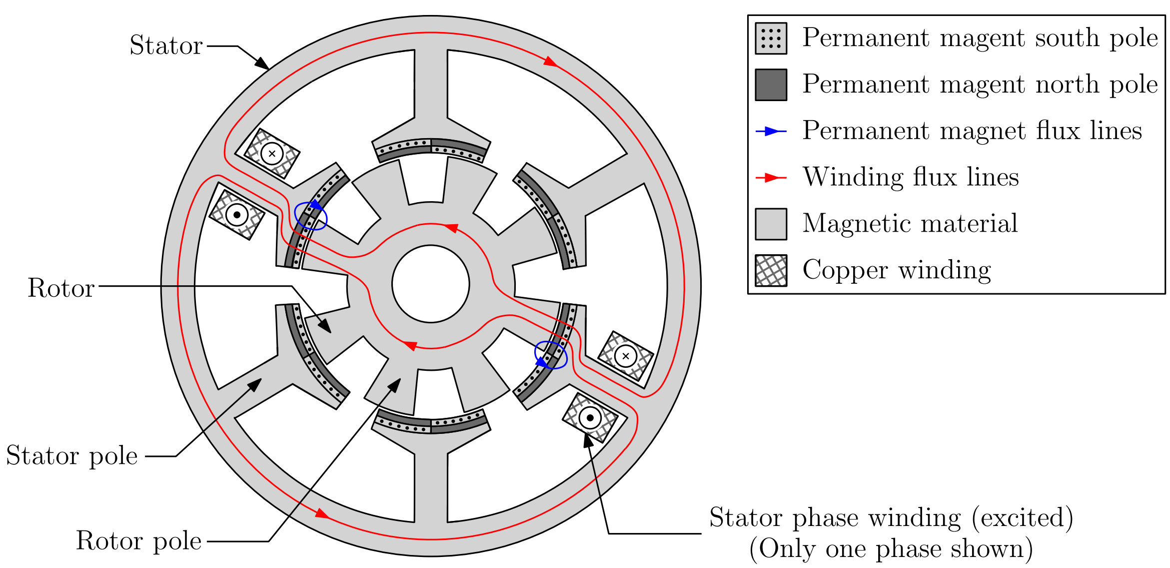

Figure 1.13: A two dimensional cross sectional view of an FRM with surface permanent magnets. Adapted from [6], © 2009 IEEE

1.5.5 Advantages of Switched Reluctance Machines

Major advantages of switched reluctance machines are listed below. Simplistic design and lack of permanent magnets make it a strong contender in the renewable energy sector, resulting in a significant amount of resources going into its research.

- The machine's rotor does not have any windings or permanent magnets, as a result, it is easy to manufacture, lightweight, and economically advantageous. Due to its low weight, the rotor has a low moment of inertia, which results in a high acceleration and a quick response time. The lack of windings and permanent magnets on the rotor makes it mechanically more robust, allowing for high-speed operation. Simplistic design of the rotor also ensures that losses associated with it are extremely low when compared to induction and DC machines.

- The phase windings are placed concentrically around the stator poles only, thus making the stator easy to manufacture and economically advantageous (unlike for instance, a machine with the more complicated distributed winding architecture). Since the phase windings are placed only on the stator, the losses and heat are also associated mainly with the stator, as a result, cooling is easier as the stator lies on the exterior and is easy to access.

- Since phase windings are placed only on the stator, electrical energy is not transferred to or from the rotor, as a result, no brushes or slip rings are used. Therefore, the robustness of the machine increases and its required maintenance is reduced. The phase windings are separate from each other, as a result, an electrical fault in one of the phase windings cannot propagate to the remaining phase windings, thereby adding another layer of robustness and fault tolerance. For higher reliability, the switched reluctance machine is designed with a large number of phases; however, that does not necessarily map in a one to one manner to the number of phases on the drive's power converter. Based on the machine's configuration, multiple phases can be operated simultaneously, thereby reducing the number of phases of the drive's power converter. Also, the machine's back emf is a function of the current in the phase winding (explained more in detail in subsequent chapters). Therefore, if a particular phase (i.e., winding) were to experience an electrical fault, and the current is cutoff (i.e., zero current), the resulting back emf induced in that phase would also be zero.

- Unlike the induction machine, the permanent magnet synchronous machine, and the brushless DC machine, a switched reluctance machine does not produce any undesired cogging or crawling torque, as a result, no additional control is required to mitigate their effects.

1.5.6 Limitations of Switched Reluctance Machines

This section lists a few of limitations of switched reluctance machines, the significant one being the machine's low power density.

- The salient rotor and stator structures have a tendency of producing higher levels of acoustic noise, vibrations, and torque ripple. However, acoustic noise and vibration effects are mitigated by filling the interpolar spaces of the rotor with non magnetic materials. Depending on the materials used, the weight of the rotor would also increase. Changes made to the machine's topology also help in reducing acoustic noise and vibrations, for instance a double stator switched reluctance machine [83] has lower acoustic noise and vibrations compared to the basic switched reluctance machine structure. On the other hand, torque ripple can be reduced by increasing the number of stator phases or by controlling the overlapping phase currents, among other techniques [89–91].

- While lack of permanent magnets and REEs reduce the price of a switched reluctance machine, in terms of power density, the machine is put at a disadvantage when compared to its competitors, i.e., the permanent magnet synchronous machine and the brushless DC machine. However, while operating at high speeds, a switched reluctance machine not only closes in on the power density gap but may sometimes even exceed the power densities of its competitors. On the other hand, the power density of a switched reluctance machine is comparable to an induction machine, i.e., a machine without permanent magnets.

- A switched reluctance machine always requires a driving power converter and does not have line start capability unlike an induction machine. Also, most simple switched reluctance drive circuits require the rotor position to complete the feedback loop. As a result, a position encoder is required on the rotor shaft. The use of a position encoder is a limitation as they are not extremely robust and require maintenance. A faulty position encoder can render a switched reluctance machine inoperable, thereby acting as the Achilles heel of the drive system. Sensorless drives systems for switched reluctance machines have also been extensively explored [92–94]; however, they are accompanied by increased control complexities.

- The effects of fringing fields and magnetic saturation make a switched reluctance machine highly nonlinear, posing extremely complex modeling and control challenges. Modeling of a switched reluctance machine involves obtaining curve fitting expressions through regression analysis, based on the data obtained through system identification. The curve fitting expressions comprehensively capturing the essence of the machine with its magnetic saturation are generally extremely complex mathematical expressions. The effects of the complex model are also felt while designing the controller for a switched reluctance drive system.

1.6 Organization of the Subsequent Chapters

This dissertation contains six chapters. The five remaining chapters have been organized in the following manner:

Chapter 2

In this chapter, the operating principles of a switched reluctance machine and drive system are presented. This includes the machine's rotational dynamics along with its magnetic and electrical parameters. Also presented are the equivalent circuit models, the effects of saturation, and the motoring and generating modes of operation of a switched reluctance machine. Lastly, the operation of the drive's power converter, i.e., the asymmetric bridge converter is presented.

Chapter 3

This chapter presents the mathematical models of a switched reluctance machine. Prior flux and inductance based modeling schemes along with their limitations are analyzed. An approach to reconstruct the phase current using numerical methods of integration is explored and lastly, the proposed modeling scheme with and without the phase resistance is derived.

Chapter 4

A technique to predict the peak value of the phase current for switched reluctance generators is derived and presented in this chapter. The mathematical model is then validated by comparing its results to the experimentally gathered data. The effect of the machine's winding resistance on the model is also analyzed and documented.

Chapter 5

This chapter examines the effect of a free wheeling stage in the high-speed operating mode of switched reluctance generators. The effect of free wheeling on the amount of charge generated by the machine is analyzed.

Chapter 6

In this chapter, concluding remarks and future research work is presented.

CHAPTER 2

OPERATING PRINCIPLES OF A SWITCHED RELUCTANCE MACHINE AND ITS DRIVE SYSTEM

This chapter presents the operating principles of a switched reluctance machine and the drive system, such as the rotational dynamics of the machine, evolution of magnetic and electrical parameters, equivalent circuit models, effects of saturation on the machine, motoring and generating modes of operation, and the functioning of the drive power converter.

2.1 Rotational Dynamics and the Magnetic and Electric Parameters

In this section, the rotational dynamics along with the magnetic and electrical parameters of the machine are presented. The magnetic parameters considered are the phase inductance and phase flux linkage, while the electrical parameters considered are the applied phase voltage and phase current. Evolution of the magnetic and electrical parameters are examined as the rotor rotates, changing its angular position.

2.1.1 Rotational Dynamics

For the purpose of analysis, the 2/2 machine depicted in Figure 1.2 is considered. Practically, a machine with two rotor and two stator poles will not produce significant output power. This machine is selected only to make the understanding and analysis process easier. In practice, switched reluctance machines have a higher number of rotor and stator poles. During generation, the machine's output power is proportional to the number of stator phases, as a result, a single phase machine will generate less electricity. On the other hand, during motoring, the machine shown in Figure 1.2 is limited by the number of rotor poles and will not be able to produce continuous output motion as the rotor poles will get locked with the excited stator phase and remain in that position even after the excitation of the stator phase is removed, unless externally disturbed. For machines with multiple stator phases, the phases are excited in a specific order to achieve useful output power from the machine.

Figure 2.1(a) shows a two dimensional cross sectional view of a single phase switched reluctance machine with its rotor at the *aligned position*, while Figure 2.1(b) shows the rotor at the *unaligned position*. The position of the rotor is measured in terms of the angle made by the reference rotor pole (R or R'), the center O, and the reference stator pole (S or S'). The center O acts as the vertex of the rotor and stator axes. Conventionally, angles measured in the counterclockwise direction are assigned a positive value, while those measured in the clockwise direction are assigned a negative value. However, while assigning a sign to the rotor's angle, a different convention is followed. A negative sign is assigned when the reference rotor approaches the reference stator pole, while a positive sign is assigned when the reference rotor pole leaves the reference stator pole, i.e., the sign of the rotor's angle depends on the rotor's direction of rotation.

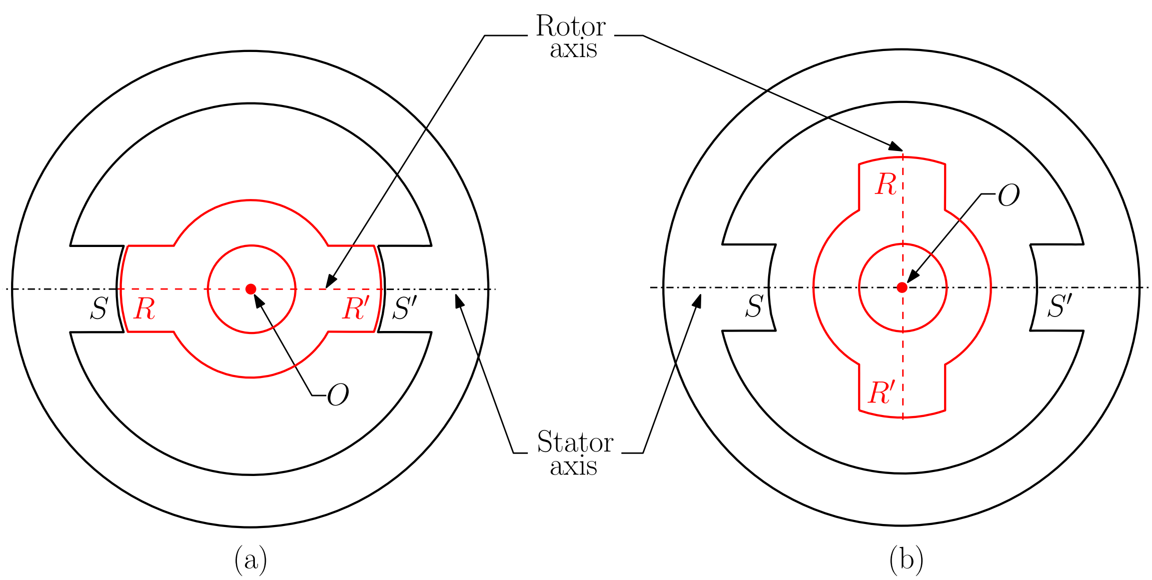

Figure 2.1: A two dimensional cross sectional view of a single phase SRM with its rotor at the (a) aligned position and (b) unaligned position

For example, at the unaligned position shown in Figure 2.1(b), if R' and S' are considered as the reference rotor and stator poles, respectively, and if the rotor's rotation is in the counterclockwise direction, the rotor position is represented as $-90°$; however, if the rotor's rotation is in the clockwise direction, the rotor position is represented as $+90°$. If the rotor is made to rotate by 180° in either the clockwise or the counterclockwise direction, the rotor still appears to be in exactly the same position as shown in Figure 2.1(b) and physically there would be no difference between the two positions (i.e., the other unaligned position); however, the rotor position would be represented as $+90°$ for counterclockwise rotor rotation and $-90°$ for clockwise rotor rotation. Since both the positions are the same from a physical standpoint, a repetitive pattern is observed, known as a complete cycle. The unaligned position is an unstable equilibrium position for the rotor and from a magnetic standpoint, does not experience any flux saturation between the rotor and stator poles.

On the other hand, Figure 2.1(a) represents the aligned position at which, the reference rotor pole R' is perfectly aligned with the reference stator pole S' and the rotor's position is represented as 0°. At the aligned position, the rotor pole R and the stator pole S are also perfectly aligned with each other. Similar to the unaligned position, if the rotor is made to rotate by 180° in either the clockwise or the counterclockwise direction, the rotor still appears to be in exactly the same position as shown in Figure 2.1(a) and physically there would be no difference between the two positions. Therefore, the rotor is at its aligned position even when its position is $\pm180°$, i.e., rotor pole R' aligns itself with stator pole S and rotor pole R aligns itself with stator pole S'. The aligned position is a stable equilibrium position for the rotor and from a magnetic standpoint, is prone to severe flux saturation between the rotor and stator poles.

A complete cycle is defined as the angle traveled by the rotor beginning at any one position and ending at a second position at which, physically the rotor appears to be at same as the first position (i.e., the rotor's appearance repeats itself, though the reference rotor poles changes its position). As a result, a complete cycle is a function of the number of rotor poles. Conventionally, a complete cycle begins at the unaligned position while the reference rotor pole approaches the reference stator pole and ends at the other unaligned position while the reference rotor pole leaves the reference stator pole. Consider a switched reluctance machine with three stator phases (i.e., six stator poles) and four rotor poles as shown in Figure 2.2. Assume, R_1' and S' as the reference rotor and stator poles, respectively and clockwise direction of rotation of the rotor, then Figure 2.2(a) represents the unaligned rotor position at $-45°$, while Figure 2.2(b) represents the other unaligned rotor position at $+45°$. Physically, the rotor position appears to be the same in Figure 2.2(a) and Figure 2.2(b); however, the reference pole R_1' has changed its position by $90°$. The angle traveled by the rotor from $-45°$ to $+45°$ represents a complete cycle and the periodic behavior of the rotor for the 6/4 machine shown in Figure 2.2, occurs every $90°$.

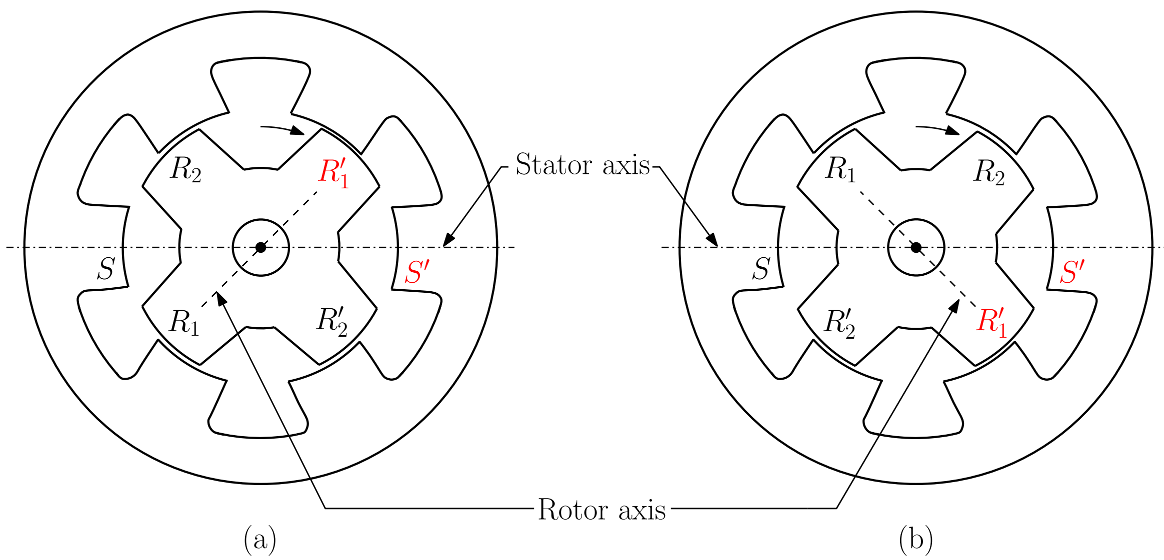

Figure 2.2: A two dimensional cross sectional view of a 6/4 SRM with the rotor at its unaligned positions at (a) $-45°$ and (b) $+45°$

The analysis of the 2/2 and 6/4 machine reveal that the periodic behavior of the machine is a function of the total number of rotor poles (N_r). Assuming that all the rotor poles are spaced equally, the periodic behavior of the machine is observed every $(360/N_r)°$ or every $(2\pi/N_r)$ rad. The angles considered so far are all the mechanical angles that the rotor rotates; however, the electrical angles for one complete cycle (i.e., where the rotor repeats its appearance) is 360° or 2π rad and does not depend on the number of rotor poles.

Figure 2.3 graphically represents and maps the relationship between the electrical angle θ_e and the mechanical angle θ_m. The extreme left and right positions represent the two unaligned positions whereas the center position represents the aligned position while considering R_2 as the reference rotor pole and S as the reference stator pole.

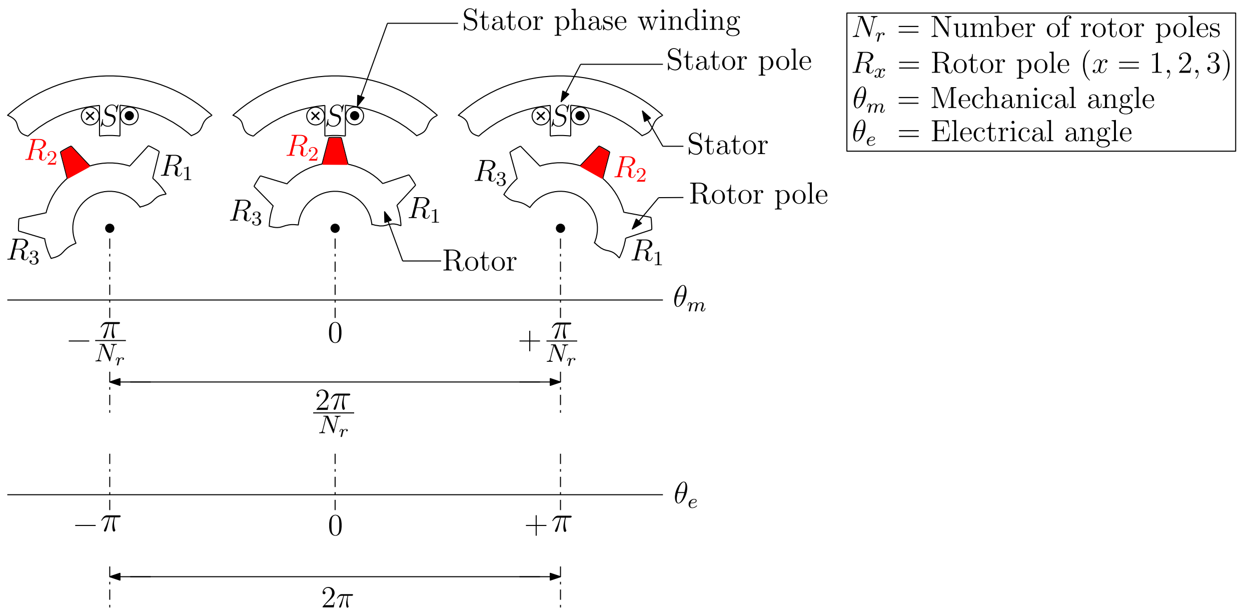

Figure 2.3: Reference rotor pole R_2's position in terms of the mechanical angle (θ_m) and the electrical angle (θ_e)

2.1.2 Magnetic and Electric Parameters

Referring to Figure 2.1, when the rotor is at the aligned position, and the stator windings are excited, the reluctance of the flux path is at its minimum value while the inductance of the phase is at its maximum value (since the phase inductance and the flux linkage are inversely proportional to each other). The reluctance of the flux path is minimum because the size of the air gap between the rotor and stator poles is at its smallest possible value. Conversely, when the rotor is at the unaligned position, and the stator windings are excited, the reluctance of the flux path is at its maximum value while the inductance of the phase is at its minimum value. The reluctance of the flux path is maximum because the size of the air gap between the rotor and stator poles is at its largest possible value. Intermediate rotor positions (between aligned and unaligned positions) experience corresponding values of reluctance and inductance based on the size of the air gap between the rotor and stator poles.

Another important parameter is the torque produced by the machine's rotor shaft. Consider Figure 1.2 and assume that the rotor is rotating in the counterclockwise direction (perhaps with the help of an external mechanical source). When the rotor is at the position shown in Figure 1.2 and the phase windings are excited, it experiences a force which aids in its counterclockwise rotation. The force experienced by the rotor due to the excitation of the phase windings is the produced torque (T) and because it aids the rotor in the direction of rotation, it is a positive value. Once the rotor reaches its aligned position, if the stator phase windings are kept excited, the rotor will want to remain at the aligned position (as the aligned position is a stable equilibrium position, at which the reluctance of the flux path is minimum) and no longer produce a positive torque which aids in the rotor's counterclockwise rotation, in fact it produces no torque, i.e., zero torque. However, because of the rotational moment of inertia of the rotor, it will continue rotating past the aligned position heading towards the other unaligned position; however, due to the continued excitation of the phase windings, the rotor experiences a force opposing its counterclockwise rotation, i.e., the rotor experiences a negative torque which prevents it from leaving its aligned position (i.e., the stable equilibrium position, where the reluctance of the flux path is minimum). The evolution of the machine's phase inductance and output torque for a rotating rotor are shown in Figure 2.4. In later sections of this dissertation, it is derived that the torque is a function of the slope of the phase inductance. As a result, during constant values of phase inductance, the torque produced is zero.

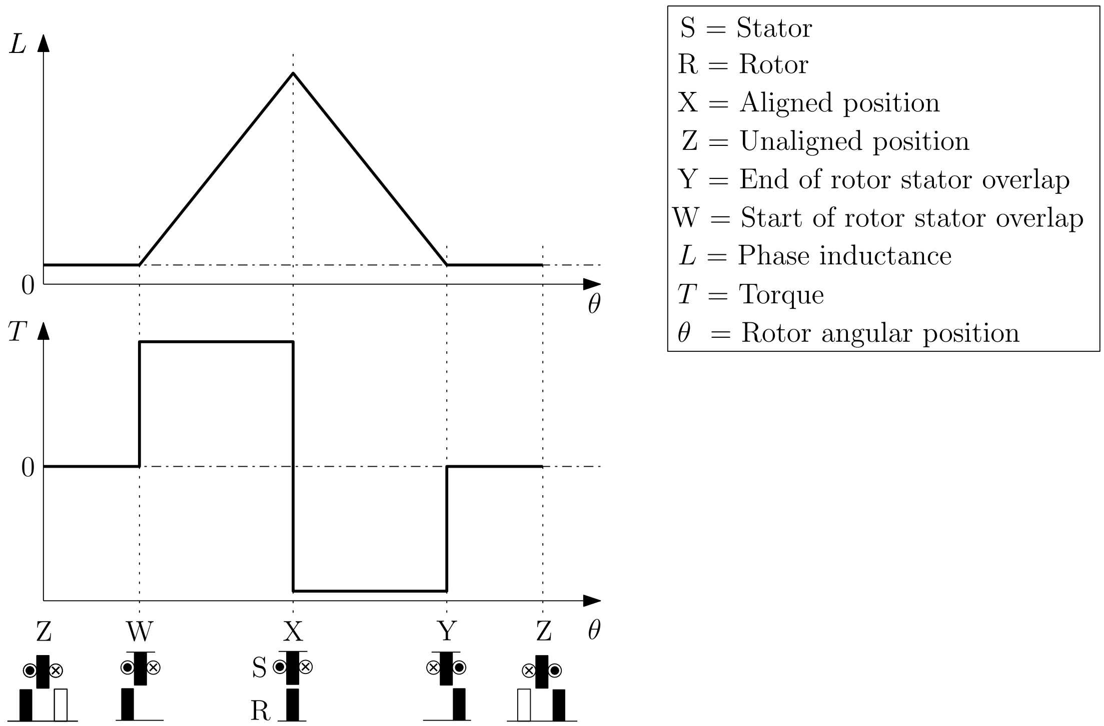

Figure 2.4: Phase inductance and torque profiles for a continuously excited stator phase winding [7]

Based on the intuitive analysis for the generation of torque, a rule of thumb is established suggesting that, a positive torque is produced in the region where the inductance of the phase increases (i.e., as the rotor rotates from its unaligned position towards its aligned position) and a negative torque is produced in the region where the inductance of the phase decreases (i.e., as the rotor rotates from its aligned position towards its other unaligned position). In Figure 2.4, at the aligned position, the inductance changes its slope from a positive value to a negative value. The abrupt change in slope takes place only when the length of the rotor pole arc β_r is equal to the length of the stator pole arc β_s. If the arc lengths are unequal, the inductance profile would have a zero slope region around both sides of the aligned position. Figure 2.5 shows the rotor and stator pole arcs.

In Figure 2.4, position X represents the aligned position of the rotor pole with respect to the stator pole, position Y represents the end of the overlap of the rotor pole arc with

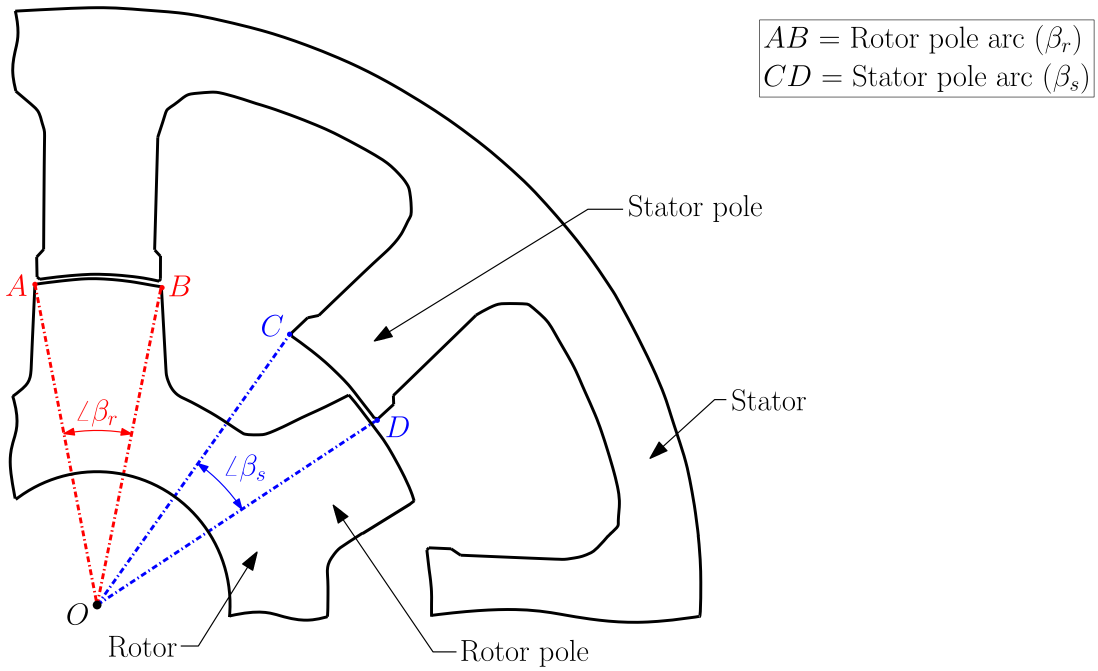

Figure 2.5: A two dimensional cross sectional view of an SRM highlighting the rotor and stator pole arcs β_r and β_s, respectively and their corresponding angles subtended at the center O of the machine $\angle\beta_r$ and $\angle\beta_s$, respectively. Adapted from [8], © 2002 IEEE

respect to the stator pole arc as the rotor leaves its aligned position heading towards its unaligned position, position Z represents the position, where the rotor pole is completely unaligned with the stator pole (i.e., the rotor axis is at an angle of $\pm\pi/N_r$ rad with respect to the stator axis), and position W represents the rotor position, where the rotor pole arc begins to overlap with the stator pole arc as the rotor rotates from its unaligned position heading towards its aligned position.

So far, in the analysis of a switched reluctance machine shown in Figure 1.2, positive and negative torques are produced in one cycle, because the stator phase is excited throughout the cycle. Averaging the torque over one complete cycle, results in an overall zero torque, which is not useful as it implies that the rotor endlessly oscillates (in an ideal frictionless environment) back and forth around the active stator pole. In order to only generate positive torque and get rid of the negative torque, the stator phase winding must not be excited after the rotor crosses the aligned position. Therefore, a control scheme which switches off the stator phase when the reference rotor pole reaches its aligned position must be used. The stator phase is switched off when a zero or negative voltage is applied across the terminals of the stator phase windings. In summary, for the production of only positive torque, a positive phase voltage must be applied as the rotor rotates from position W towards position X, and a zero or negative phase voltage must be applied as the rotor rotates from position X towards position Y.

The switching on and off of the phase voltage is referred to as commutation and a cycle wherein torque is produced due to one current or voltage pulse is known as a *stroke*. Also, the application of a positive voltage across the terminals of the stator phase windings results in the *magnetization* of the phase, whereas the application of a zero or a negative voltage across the terminals of the stator phase windings results in the *demagnetization* of the phase. The commutation results in a set of voltage and current pulses, which are continuously switched, and as mentioned earlier, is what gives a switched reluctance machine its name. Figure 2.6 maps out the torque produced, the phase voltage across the stator phase windings, and the phase current flowing through the stator phase windings. The flat top of the phase voltage and phase current waveforms represent an average value, which is achieved using hysteresis control wherein the phase is switched on and off (i.e., a positive and zero phase voltage) multiple times between position W and position X. At position X, when the phase is finally switched off, its voltage is negative. In summary, for the production of positive torque only, the phase voltage is a set of controlled pulses during the region in which the phase inductance has a positive slope. For the production of continuous positive torque rather than the pulses shown in Figure 2.6, additional stator phases are required, which when switched, fill up the blank spaces between the torque pulses shown in the figure.

An additional magnetic parameter, i.e., the phase flux linkage is also mapped in Figure 2.6. The flux linkage ψ between the rotor and stator is related to inductance of the

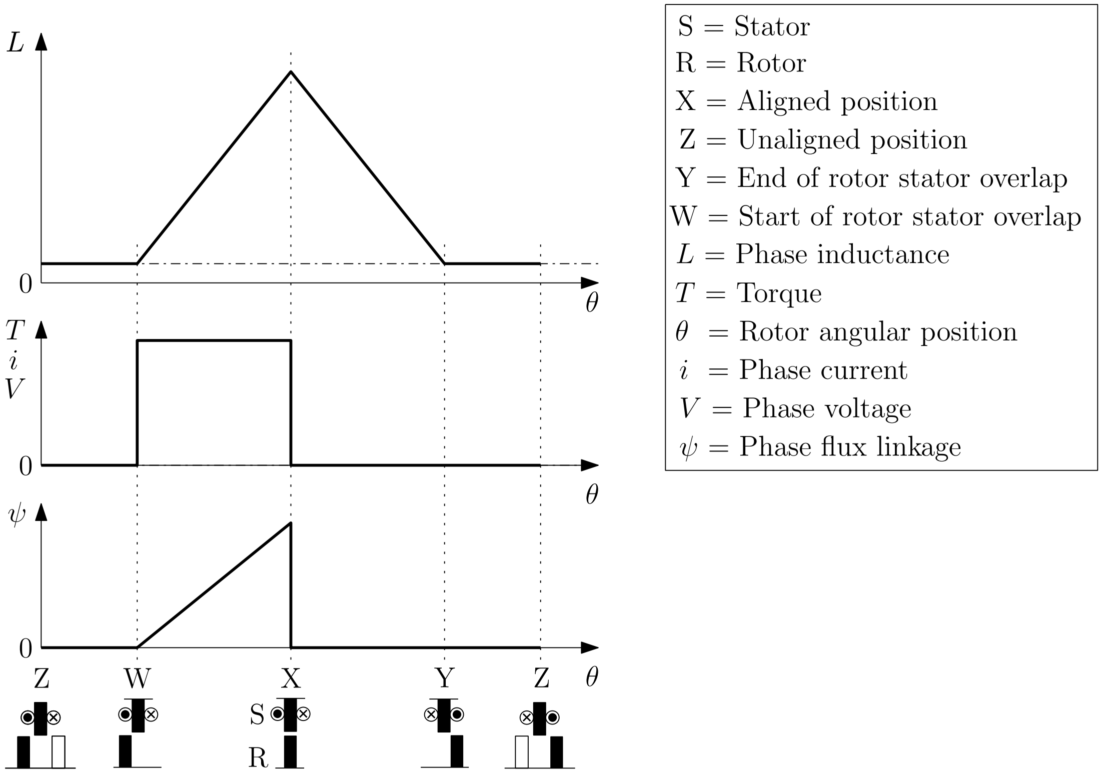

Figure 2.6: Phase inductance, current, voltage, flux linkage, and torque profiles for a controlled excitation of the stator phase winding [7]

phase L, and the phase current through the stator phase windings i, by the following expression:

$$\psi = Li \tag{2.1}$$

Using the expression for the flux linkage from Equation 2.1, the waveform of the flux linkage shown in Figure 2.6 is similar to the inductance profile during the region of increasing inductance, and zero at other instances. As the rotor rotates from its unaligned position Z to its aligned position X, the air gap between the rotor and stator pole decreases and the reluctance of the flux path reduces, as a result, the flux linkage also increases.

However, the waveforms of phase current and flux linkage shown in Figure 2.6 are unrealistic and impractical, the phase current waveform does not resemble a perfect pulse as shown in the figure and *reconstruction of the phase current* is much more challenging. To better understand the magnetic and electric profiles, consider the following equations defining the relationship among the voltage across the phase inductance V_L, time t, the phase inductance (L), and the phase current (i):

$$V_L = L\frac{di}{dt} \tag{2.2}$$

Rearranging Equation 2.2, the following expression for the slope of the phase current is obtained:

$$\frac{di}{dt} = \frac{V_L}{L} \tag{2.3}$$

The leading edge of the phase current shown in Figure 2.6 has an infinite positive slope. Such a slope would only be possible if the value of the phase inductance in Equation 2.3 were zero. In reality, the value of the phase inductance is small, but not in fact zero. Consequently, the non zero phase inductance results in a finite positive slope (a fairly steep one at that) for the leading edge of the phase current and is shown in Figure 2.7. On the other hand, the trailing edge of the phase current shown in Figure 2.6 has an infinite negative slope. The trailing edge of the phase current occurs at the aligned position, at which the phase inductance is at its maximum value and the stator phase is switched off, implying that the phase voltage is negative, as a result, V_L becomes negative. According to Equation 2.3, the trailing edge of the phase current will have a relatively smaller finite negative slope (when compared to the leading edge) and the phase current will take longer to go back down to zero, i.e., resulting in an undesired current *tail*. The trailing edge tail current at the aligned position is also shown in Figure 2.7. Since the flux linkage is a product of phase inductance and phase current, a non zero phase inductance and the tail current profile results in a tail for the flux linkage as well. The tail current is responsible for the production of negative torque while motoring, an undesired phenomenon.

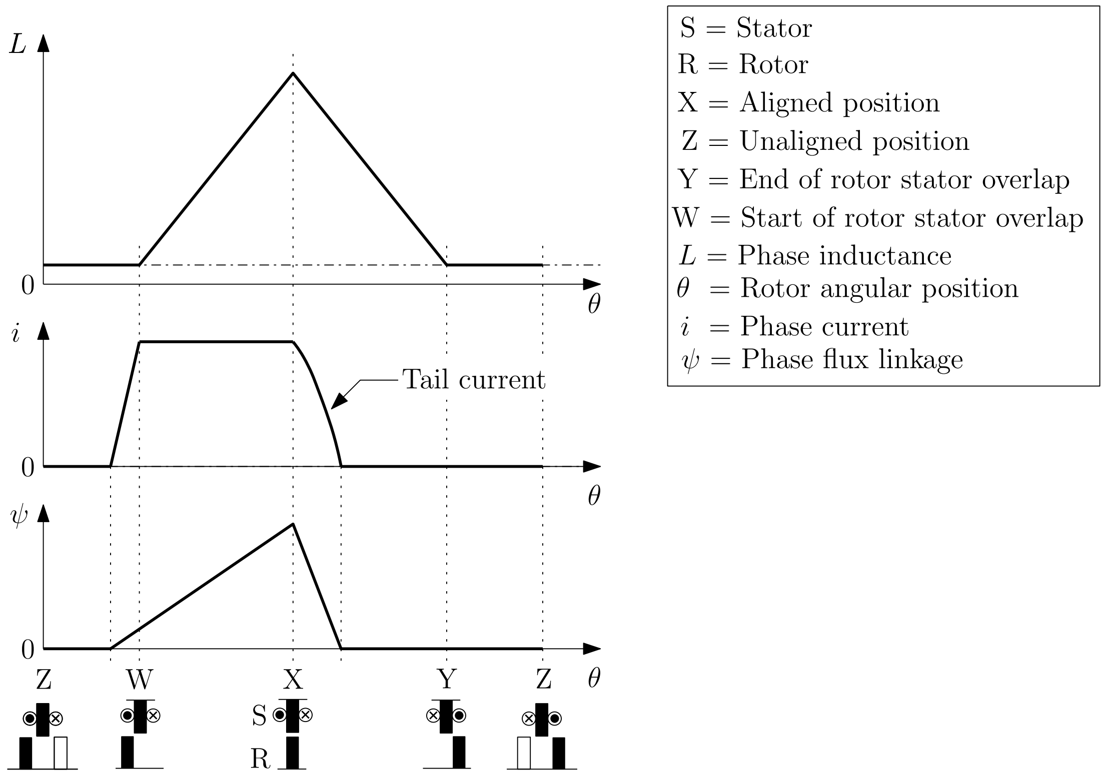

Figure 2.7: Phase inductance profile along with phase current and flux linkage profiles with finite slopes [7]

2.2 Equivalent Circuit of a Switched Reluctance Machine

This section presents the equivalent circuit of a switched reluctance machine. In order to develop the equivalent circuit, it is best to begin with the equation describing the machine's phase voltage. Using Faraday's law of electromagnetism, the phase voltage of a switched reluctance machine is given by the general expression:

$$V = \frac{d\psi}{dt} \tag{2.4}$$

It should be noted that the phase voltage (V) defined so far represented the voltage across ideal stator phase windings with zero resistance, as a result, no resistive voltage drops were considered (due to winding and parasitic resistances). However, in the presence of winding and parasitic resistances, the phase voltage is not the same as the voltage across the stator phase windings. The voltage across the stator phase windings is referred to as the *DC link voltage* or the *bus voltage*, i.e., V_{bus}. The phase voltage differs from the bus voltage by accounting for an additional voltage drop due to the resistance of the stator phase windings R (all other parasitic resistances, such as the drive circuit board resistances are also included in R). The two voltages are related to each other by the following expression:

$$V = V_{bus} - iR \tag{2.5}$$

For the sake of simplicity, the following analysis considers the phase voltage rather than the bus voltage. By using the expression for the flux linkage from Equation 2.1 in Faraday's law, i.e., Equation 2.4, the following set of equations are obtained:

$$\begin{aligned} V &= \frac{d(Li)}{dt} \\ &= L\frac{di}{dt} + i\frac{dL}{dt} \end{aligned} \tag{2.6}$$

Since, mutual inductance between phases is less than the self inductance of a phase, it is neglected in the analysis [95]. The first term on the right hand side of Equation 2.6 represents the voltage across the phase inductance and is denoted by V_L, the second term is attributed towards the machine's back EMF and is denoted by e. As a result, Equation 2.6 is expressed as:

$$V = V_L + e \tag{2.7}$$

where, the voltage across the phase inductance (V_L) is the same as that described by Equation 2.2 and the back EMF (e) is described by the following expression:

$$e = i\frac{dL}{dt} \tag{2.8}$$

Analysis of a switched reluctance machine is generally performed as the rotor rotates from its unaligned position to its aligned position during motoring, and from its aligned position to its unaligned position during generation. Therefore, it is more insightful to switch from the time domain (t) to the rotor's position domain (θ). This can easily be achieved by introducing an expression for angular velocity ω in Equation 2.6. The expression for the angular velocity (ω) is given by:

$$\omega = \frac{d\theta}{dt} \tag{2.9}$$

Rearranging Equation 2.9, the following expression is obtained:

$$\frac{1}{dt} = \frac{\omega}{d\theta} \tag{2.10}$$

Replacing time (t) by introducing the angular velocity (ω) from Equation 2.10 in Equation 2.6, results in the following expression for the phase voltage (V):

$$V = \omega L \frac{di}{d\theta} + \omega i \frac{dL}{d\theta} \tag{2.11}$$

The voltage across the phase inductance (V_L) and the back EMF (e) of the machine, expressed in terms of angular velocity (ω) are obtained by using Equation 2.10 in Equations 2.2 and 2.8, respectively:

$$V_L = \omega L \frac{di}{d\theta} \tag{2.12}$$

$$e = \omega i \frac{dL}{d\theta} \tag{2.13}$$

Using the expressions for voltage across the machine's phase (i.e., Equation 2.11), an equivalent circuit model is constructed and shown in Figure 2.8.

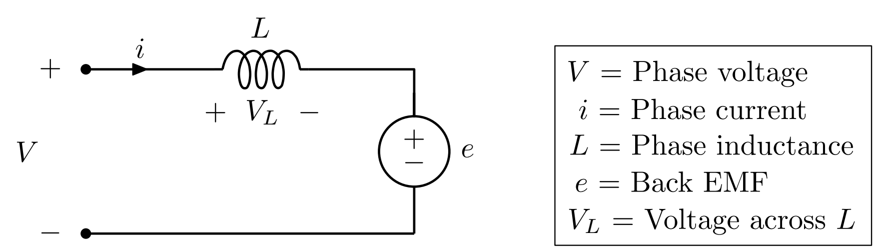

$$V_L = L\frac{di}{dt} = \omega L \frac{di}{d\theta} \qquad e = i\frac{dL}{dt} = \omega i \frac{dL}{d\theta}$$

Figure 2.8: Equivalent circuit of a switched reluctance machine

Adding the winding resistance (R) and the bus voltage (V_{bus}) from Equation 2.5 in Equation 2.11, a more comprehensive voltage equation is obtained:

$$V_{bus} - iR = \omega L \frac{di}{d\theta} + \omega i \frac{dL}{d\theta} \tag{2.14}$$

The equation above is rearranged to obtain the bus voltage expression for a switched reluctance machine and is expressed as:

$$V_{bus} = iR + \omega L \frac{di}{d\theta} + \omega i \frac{dL}{d\theta} \tag{2.15}$$

Similarly, an equivalent circuit model of the machine including the winding resistance (R) and its bus voltage (V_{bus}) is constructed and shown in Figure 2.9, where the voltage drop across the winding resistance is denoted by V_R.

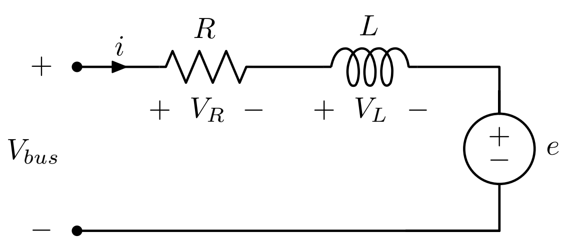

R = Winding resistance
i = Phase current
L = Phase inductance
e = Back EMF
V_R = Voltage across R
V_L = Voltage across L
V_{bus} = Bus voltage

$$V_R = iR \qquad V_L = L\frac{di}{dt} = \omega L \frac{di}{d\theta} \qquad e = i\frac{dL}{dt} = \omega i \frac{dL}{d\theta}$$

Figure 2.9: Equivalent circuit of a switched reluctance machine (including winding resistance)

2.3 Saturation in Switched Reluctance Machines

This section briefly and intuitively presents the effects of saturation in switched reluctance machines. It has already been established that the phase inductance (L) varies with rotor position (θ). However, the rotor position is not the only parameter the phase inductance depends on, it also depends on the phase current. For high values of phase current, the flux linkage through the machine core no longer scales according to Equation 2.1 and begins to saturate, especially as the reference rotor pole aligns itself with the reference stator pole.

Figure 2.10 shows the two dimensional cross sectional view of an 8/6 switched reluctance machine. The machine is modeled using ANSYS Maxwell [9], a finite element analysis tool. Figure 2.10(a) shows the rotor pole at its aligned position (i.e., position X shown in Figure 2.4), where the rotor poles are perfectly aligned with a pair of excited stator poles. The simulation is performed by exciting the phase windings with a constant current of 10 A. The figure clearly shows an excessive amount of flux lines at the rotor and stator pole boundaries. At the aligned position, since the path for the flux lines has the lowest reluctance, the flux lines tend to be extremely dense and are *limited* by the surface areas of the rotor and stator poles, creating a bottleneck for the flux lines and causing them to saturate. The *limitation* is most noticeable when the phase current is high and the reluctance for the flux path is low, i.e., when the phase inductance is high, and begins to ease off as the reluctance increases. Such a combination occurs when the rotor pole is close to or at the aligned position as shown in Figure 2.10(a). At the aligned position, once the flux linkage reaches a certain value, increasing the phase current does not cause a proportional increase in the flux linkage. Intuitively, this is because higher phase currents are no longer capable of squeezing in additional lines of flux through the rotor and stator pole boundaries. As a result, while considering saturation, Equation 2.1 holds true only in an instantaneous manner.

Figure 2.10(b) shows the rotor at a position without any overlap with the pair of excited stator poles (i.e., positions W or Y shown in Figure 2.4), as a result the reluctance of the flux path is significantly higher (because the flux lines must leave the stator's iron core, travel through the air gap, enter the rotor's iron core, leave the rotor's iron core and travel through the air gap on the other side, and finally reenter the opposite stator pole). At the unaligned position, the factor *limiting* the flux lines is no longer the surfaces of the rotor and stator poles, but in fact the reluctance of the flux path. Typically, the flux linkage at the unaligned position does not experience saturation (unless extremely high values of currents develop, which would cause other parts of the drive to fail before saturation poses a concern).

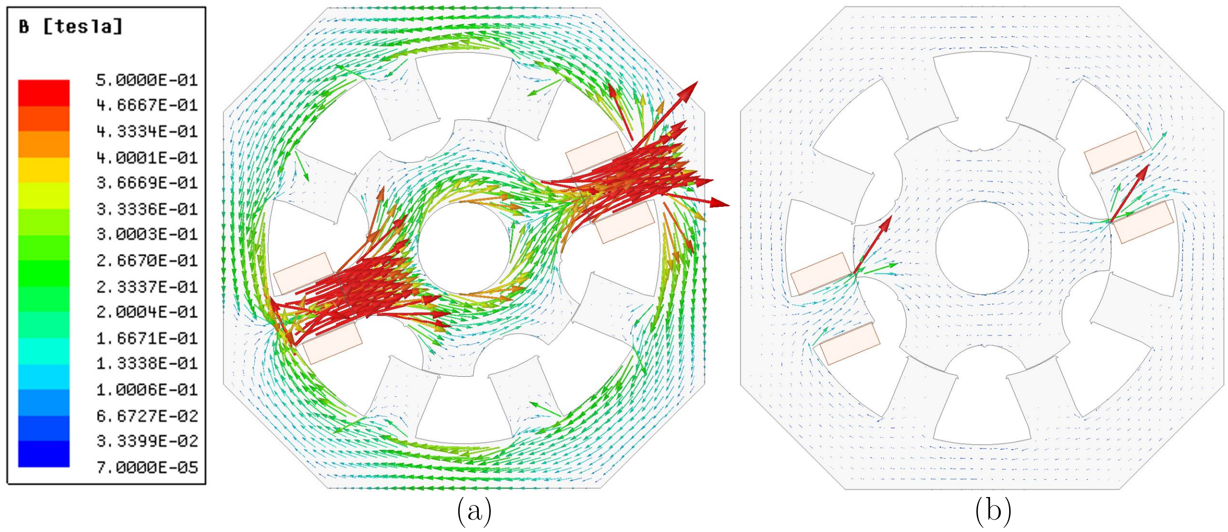

Figure 2.10: Flux linkage in an 8/6 SRM when the rotor is at (a) the aligned position and (b) a position without any overlap with the excited stator poles. Simulation results are obtained using ANSYS Maxwell [9]

In summary, there are two factors which limit the flux linkage from increasing linearly as the current increases, i.e., the reluctance of the flux path (which is directly proportional to the size of the air gap between the rotor and stator poles) and the physical geometry of the rotor and stator pole surfaces. At the aligned position, the reluctance of the flux path is minimum; however, the geometry or size of the rotor and stator pole surfaces act as the limiting factor for the flux lines. On the other hand, at the unaligned position, the reluctance of the flux path is much larger and acts as the limiting factor for the flux lines (the size of the rotor and stator surfaces is unimportant at the unaligned position).

From the intuitive explanation of flux saturation, a rudimentary plot of the flux linkage versus phase current is shown in Figure 2.11. The two curves plotted in the figure represent the flux linkages at the aligned and unaligned positions. The aligned position flux curve is represented by ACD, where the AC portion of the curve (during which the phase current is still low) has a more or less constant slope representing the aligned position phase inductance L_a, i.e., the inductance value at lower current levels. On the other hand, the CD portion of the curve represents saturation (as the phase current becomes larger) and has a smaller

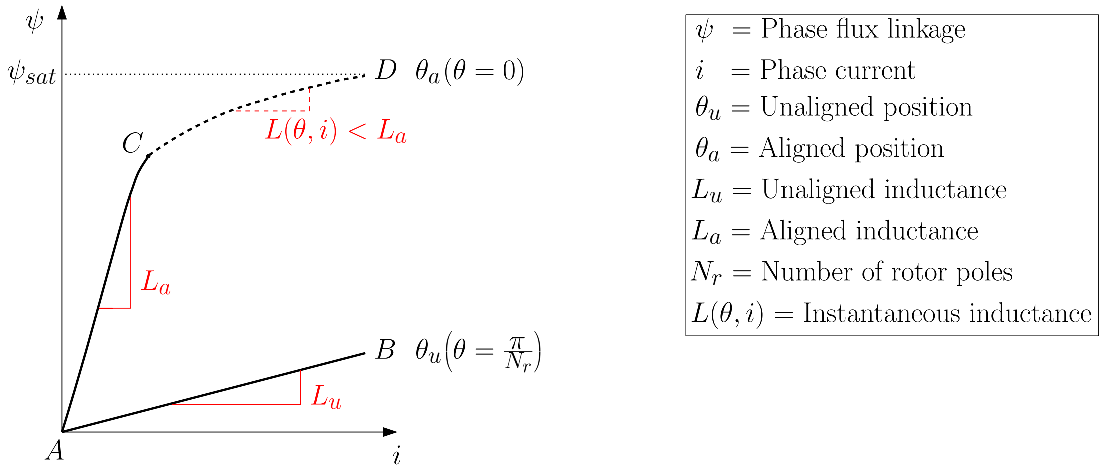

Figure 2.11: Flux linkage versus phase current plot when the rotor is at the aligned position (ACD) and the unaligned position (AB)

slope when compared to the AC portion of the curve. The smaller slope of the CD portion of the curve implies that the instantaneous phase inductance at higher current levels begins to drop and is smaller than aligned position inductance (L_a).

At the unaligned position, the flux curve represented by AB has more or less a constant slope for the entire range of current values. The slope of the unaligned flux curve represents the unaligned position phase inductance L_u. The constant slope of AB implies that the unaligned phase inductance is a constant and is independent of the value of the phase current. This further implies that saturation does not factor in at the unaligned position. Under extremely high values of current, where AB (after its extrapolation) intersects the line: $\psi = \psi_{sat}$, the core could then experience saturation even at the unaligned position. However, this would happen at an extremely high value of current and to keep matters simple, such a scenario is usually not considered as it does not occur in practice. In summary, for positions closer to the aligned position, as phase current increases, the flux linkage begins to saturate and the instantaneous inductance begins to drop. On the other hand, at the unaligned position, the machine is predominantly immune to saturation.

Since phase inductance (L) varies with rotor position (θ) as well as phase current (i) (i.e., phase inductance is a function of rotor position and phase current), it should be more accurately represented as $L(\theta, i)$. Also, the phase current is a function of the phase inductance $L(\theta, i)$ and rotor position (θ), as a result, it should also be more accurately represented as $i(L(\theta, i), \theta)$. Rearranging Equation 2.11, and making the slope of the phase current with respect to the angular position (θ) the subject of the formula, the following expression is obtained:

$$\frac{di(L(\theta, i), \theta)}{d\theta} = \frac{V - \omega i(L(\theta, i), \theta)\dfrac{dL(\theta, i)}{d\theta}}{\omega L(\theta, i)} \tag{2.16}$$

The phase current and the instantaneous phase inductance have a strong interdependence on each other and give rise to the classic *causality dilemma* or, the *"chicken and the egg"* problem. For the sake of simplicity, $L(\theta, i)$ is replaced by L and $i(L(\theta, i), \theta)$ is replaced by i, which leads to a simpler expression (however, the interdependencies are not lost):

$$\frac{di}{d\theta} = \frac{V - \omega i\dfrac{dL}{d\theta}}{\omega L} \tag{2.17}$$

Equation 2.17 can also be represented in terms of the machine's back EMF (e) from Equation 2.13 and is expressed as:

$$\frac{di}{d\theta} = \frac{V - e}{\omega L} \tag{2.18}$$

Equation 2.17 is the *current differential equation* of a switched reluctance machine and is a very important equation. A lot of insight about the machine's behavior is obtained by analyzing the current differential equation which is presented in later sections and chapters of this dissertation.

Next, the operating modes of a switched reluctance machine are presented. Since the machine is capable of operating both, as a motor as well as a generator, there are essentially two operating modes. The excitation of the phase depending on the rotor position (θ) defines whether the machine operates as a motor or as a generator.

2.4 Motoring Mode of Operation

While operating as a motor, a switched reluctance machine produces net positive torque. The production of positive torque involves exciting the stator phases in a specific order such that, the rotor rotates in the desired direction. Different switched reluctance machine configurations (i.e., different combinations of the number of rotor and stator poles) have different excitation patterns in order for the rotor to rotate in the clockwise or counterclockwise directions. Based on the configuration of a switched reluctance machine, the rotor either rotates in the same or in the opposite direction as the stator's rotating magnetic field. Figure 2.12 shows the two dimensional cross sectional view of two different switched reluctance machine configurations.

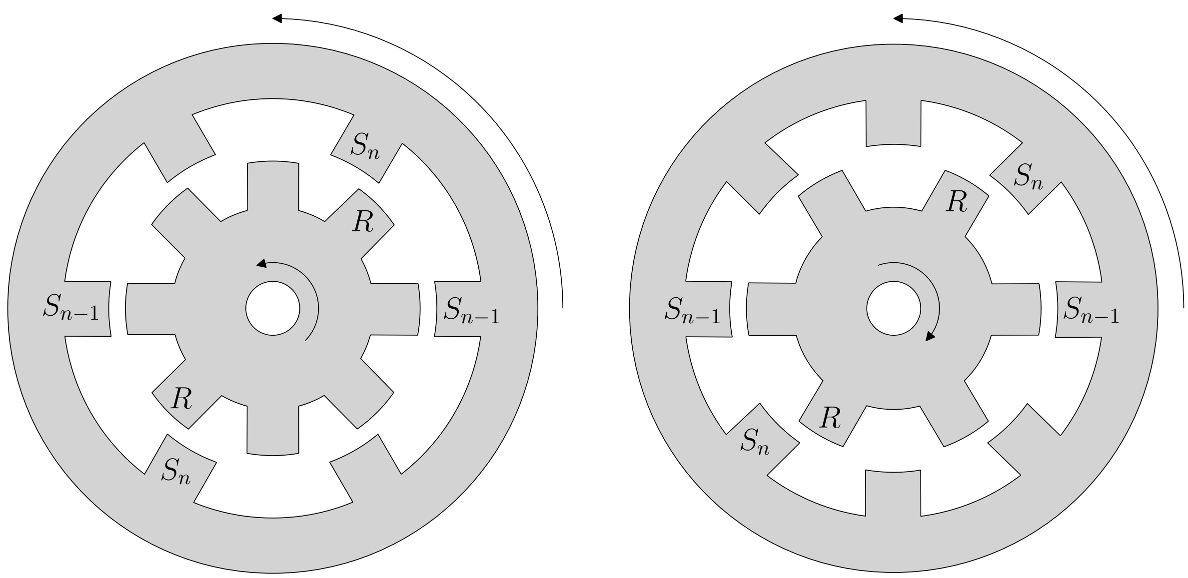

(a) (b)

S_{n-1} = Previously excited stator phase
S_n = Currently excited stator phase
R = Reference rotor pole

Figure 2.12: Stator's counterclockwise rotating magnetic field produces (a) counterclockwise rotor rotation in a 6/8 SRM and (b) clockwise rotor rotation in an 8/6 SRM

Figure 2.12(a) shows a two dimensional cross sectional view of a 6/8 switched reluctance machine in which the stator's counterclockwise rotating magnetic field causes the reference rotor pole R to rotate in the counterclockwise direction as well. On the other hand, Figure 2.12(b) shows a two dimensional cross sectional view of an 8/6 switched reluctance machine in which the stator's counterclockwise rotating magnetic field causes the reference rotor pole R to rotate in the clockwise direction.

As stated earlier, in machines with a higher number of stator phases, multiple phases can be excited at the same time, Figure 2.13 shows a two dimensional cross sectional view of a 12/8 switched reluctance machine, where stator phases A and B, are both excited simultaneously. This way the drive power converter need not have the same number of phases as the number of stator phases of the machine, resulting in a smaller and more economic motor drive.

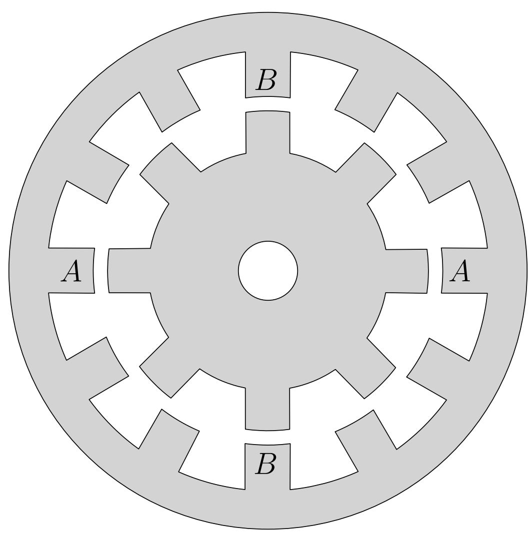

Figure 2.13: A 12/8 SRM in which phases A and B are both excited simultaneously

For the production of positive torque, the stator's rotating magnetic field must always lead the reference rotor pole. As already stated, the region where positive torque is produced is the region between the unaligned and aligned positions, during which the machine's phase inductance increases and has a positive slope (i.e., from position W to position X shown in Figure 2.4). While considering Equation 2.18 for the identified region, the denominator on the right hand side of the equation is always positive, as angular velocity (ω) and phase inductance (L) are both positive quantities. As a result, the sign of the slope of phase current with respect to rotor position ($di/d\theta$) is determined by the numerator on the right hand side of Equation 2.18, the numerator has the phase voltage (V) and the back EMF (e) working in contention with each other, giving rise to two scenarios. When the phase voltage is greater than the back EMF of the motor, the slope of phase current with respect to rotor position is positive and indicates an increasing phase current. On the other hand, when the phase voltage is lesser than the back EMF of the motor, the slope of phase current with respect to rotor position is negative and indicates a decreasing phase current.

On analyzing the current differential equation, the following inference is made: a high positive phase voltage (i.e., greater than the back EMF) results in an increase in the machine's phase current, whereas a zero or negative phase voltage results in a decrease in the machine's phase current. From a controls perspective, the machine is completely controllable as the machine's phase current is increased or decreased by switching the phase on or off, respectively. Due to complete control over the machine's phase current, a simple control technique, such as *hysteresis control* [7] can be employed with considerable ease.

2.4.1 Nonlinear Torque Expression

Intuitively, torque produced by a machine is proportional to its phase current (i.e., a higher phase current produces more flux linkage between the rotor and stator, resulting in a higher torque); however, for an exact expression for the torque produced, it needs to be mathematically derived. To derive an expression for the torque produced by a switched reluctance machine, the bus voltage (V_{bus}) from Equation 2.5 is used in Equation 2.4 to get the following expression:

$$V_{bus} = iR + \frac{d\psi}{dt} \tag{2.19}$$

The total instantaneous input electrical power P_{e_tot} is expressed as a product of phase current (i) and input voltage (i.e., bus voltage) which is obtained by multiplying Equation 2.19 by phase current and is expressed as:

$$\begin{aligned} P_{e\_tot} &= iV_{bus} \\ &= i^2R + i\frac{d\psi}{dt} \end{aligned} \tag{2.20}$$

The first term on the right hand side of Equation 2.20 represents the ohmic losses or the resistive power, P_r dissipated across the winding resistance (and any other parasitic resistances), while the second term on the right hand side of Equation 2.20 represents the input electrical power to a switched reluctance machine P_e. Expressing the total instantaneous input electrical power in terms of its two components, the following expression is obtained:

$$P_{e\_tot} = P_r + P_e \tag{2.21}$$

where,

$$P_r = i^2R \tag{2.22}$$

$$P_e = i\frac{d\psi}{dt} \tag{2.23}$$

The input electrical energy E_e is obtained by integrating the input electrical power (P_e) with respect to time (t), resulting in the following expression:

$$\begin{aligned} E_e &= \int i\frac{d\psi}{dt}\ dt \\ &= \int i\ d\psi \end{aligned} \tag{2.24}$$

The input electrical energy is responsible for the flux linkage in the machine, as a result, is equal to the stored magnetic energy in the machine E_{mag} (excluding losses during the conversion of energy from the electrical to the magnetic domain). Therefore, the stored magnetic energy is expressed as:

$$E_{mag} = \int i \, d\psi \tag{2.25}$$

Based on Equation 2.25, the stored magnetic energy is graphically highlighted and shown in Figure 2.14.

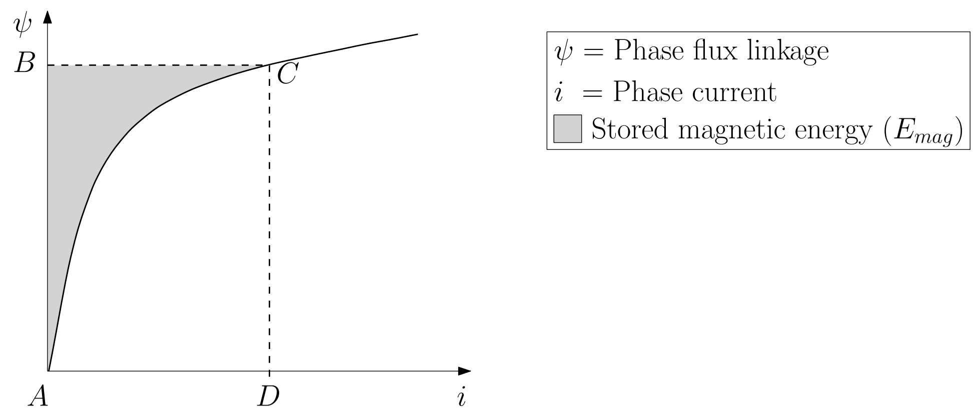

Figure 2.14: Stored magnetic energy at a particular rotor position considering a nonlinear magnetization curve

To obtain an expression for the torque produced by a switched reluctance machine, a scenario where the rotor rotates from position θ_1 (closer to the unaligned position) to position θ_2 (closer to the aligned position) is considered and shown in Figure 2.15. The evolution of flux linkage and phase current is marked by arrows as the rotor rotates from position θ_1 to position θ_2. The AE portion of the curve represents an increasing phase current at a particular rotor position θ_1 (similar to position W in Figure 2.6), similarly the ED portion of the curve represents a constant phase current as the rotor rotates from position θ_1 to position θ_2 (i.e., the flat topped phase current waveform between positions W and X in Figure 2.6), and lastly, the DA portion of the curve represents a decreasing phase current at a particular rotor position θ_2 (similar to position X in Figure 2.6).

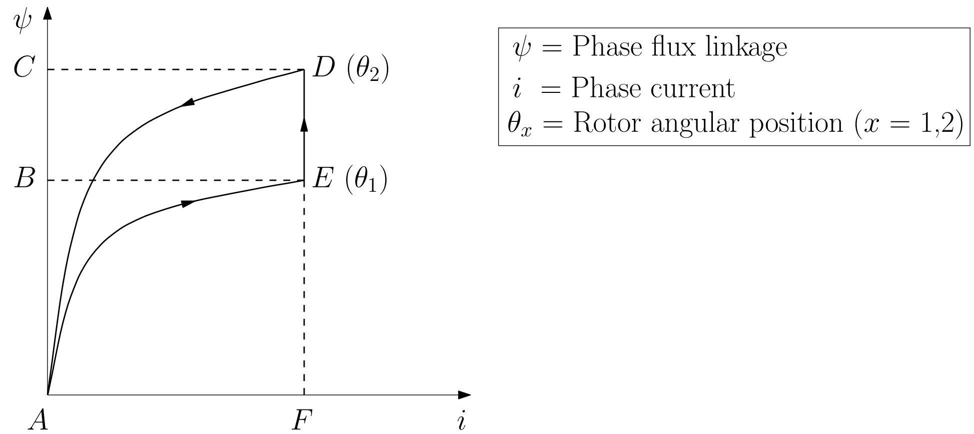

Figure 2.15: Evolution of flux linkage and phase current as the rotor rotates from position θ_1 to position θ_2

At position θ_1, the energy extracted from the supply is E_{mag1} and is shown in Figure 2.16, represented by area $AEBA$. The energy extracted from the supply helps build up the flux linkage and phase current as shown by curve AE in Figure 2.16 (The assumption is that the phase current builds up to its peak value instantaneously, i.e., at rotor position θ_1).

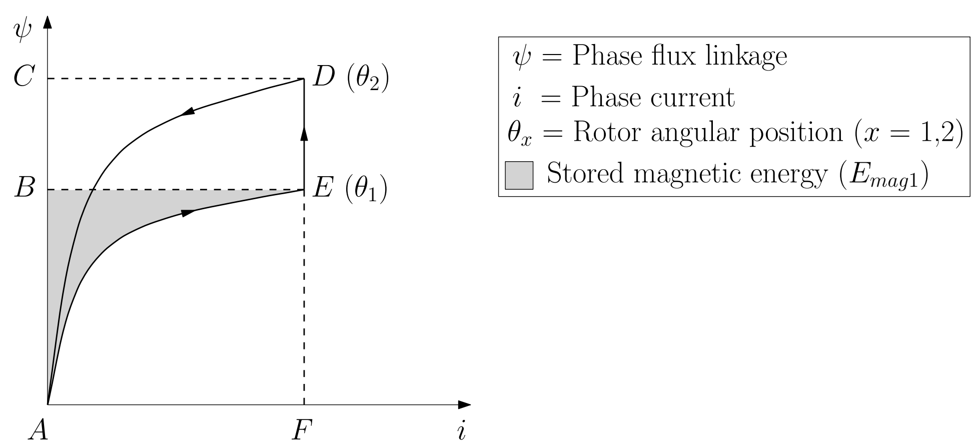

Figure 2.16: Stored magnetic energy (E_{mag1}) at rotor position θ_1 (energy taken from the supply)

As the rotor rotates from position θ_1 to position θ_2, more energy is extracted from the supply to overcome the effects of back EMF and maintain a constant phase current (assuming the phase current is a constant, represented by ED). The additional energy extracted from the supply E_{EMF} is represented by area $BEDCB$ and is shown in Figure 2.17

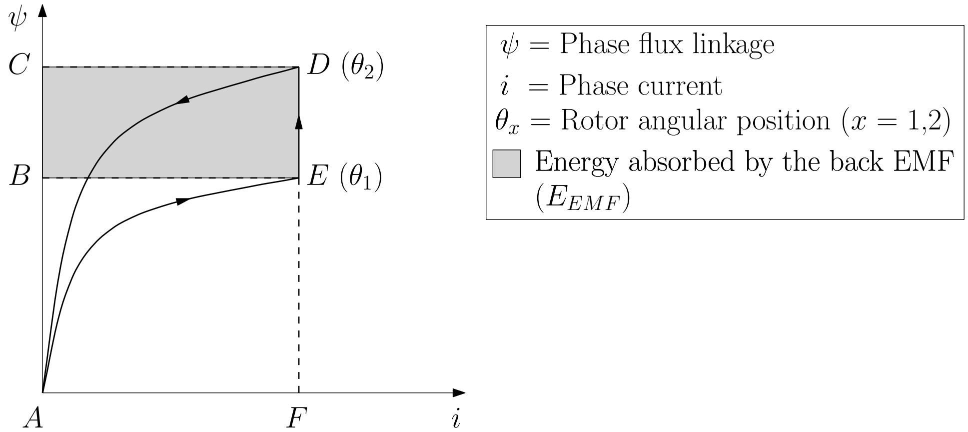

Figure 2.17: Energy absorbed by the back EMF (E_{EMF}) as the rotor rotates from position θ_1 to position θ_2 (energy taken from the supply)

At rotor position θ_2, the phase current is made to go back to zero and flows back into the supply, as a result, the stored magnetic energy at that position E_{mag2} is also returned to the supply. The stored magnetic energy is shown in Figure 2.18, represented by area $ADCA$, while the evolution of the flux linkage and the phase current is represented by curve DA (The assumption is that the phase current goes back down to zero instantaneously, i.e., at rotor position θ_2).

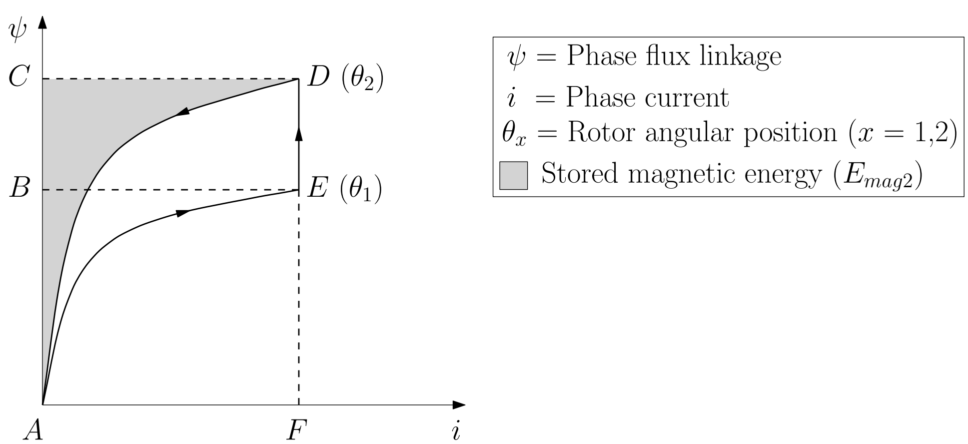

Figure 2.18: Stored magnetic energy (E_{mag2}) at rotor position θ_2 (energy returned to the supply)

As the rotor rotates from position θ_1 to position θ_2, the energy extracted from the supply is the sum of the stored magnetic energy at position θ_1 (E_{mag1}) and the energy absorbed by the back EMF (E_{EMF}). At position θ_2, the stored magnetic energy is returned back to the supply (E_{mag2}). The difference between the energies accounts for the energy spent to produce torque in the machine and is represented as the mechanical energy E_m. The expression for the mechanical energy is as follows:

$$E_m = E_{mag1} + E_{EMF} - E_{mag2} \tag{2.26}$$

Graphically, the mechanical energy spent to produce torque in a switched reluctance machine is highlighted in Figure 2.19, represented by area $AEDA$. As stated earlier, the assumption is that the phase current remains constant (as shown by ED in Figure 2.19) as the rotor rotates from position θ_1 to position θ_2.

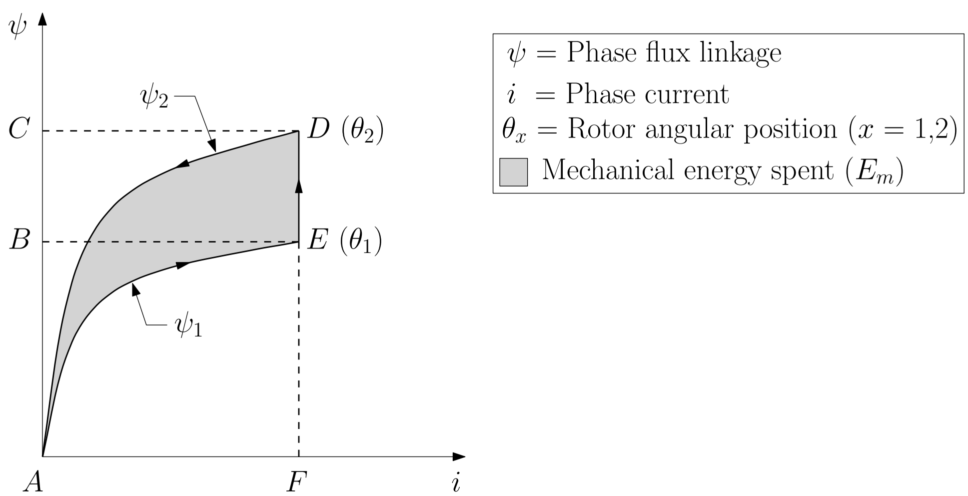

Figure 2.19: Mechanical energy spent (E_m) to produce torque in an SRM

The area highlighted in Figure 2.19 can be represented in terms of Equation 2.25; however, it is customary to represent the area integrated with respect to phase current rather than flux linkage. The change of variable (i.e., from flux linkage in Equation 2.25 to phase current) is achieved using the expression for *co-energy* E_c which is the compliment of the stored magnetic energy (shown earlier in Figure 2.14) and is highlighted and shown in Figure 2.20.

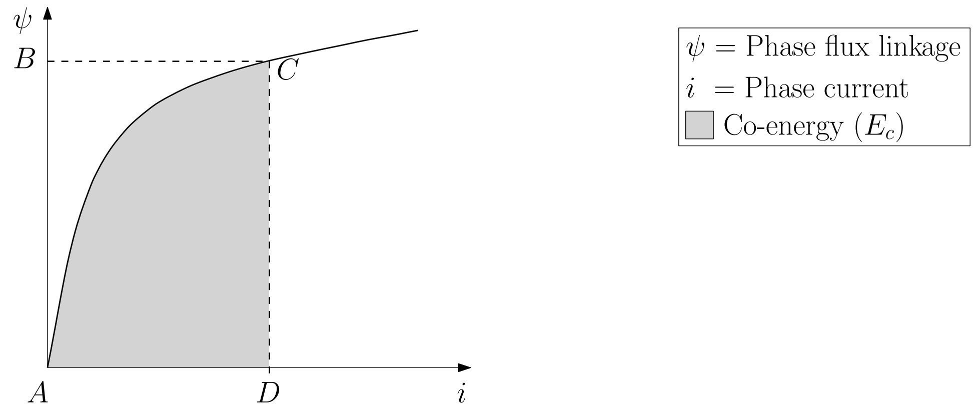

Figure 2.20: Co-energy (compliment of the stored magnetic energy) at a particular rotor position

The expression for the co-energy is similar to the one for the stored magnetic energy, except for the change of variable. The co-energy is expressed as:

$$E_c = \int \psi \; di \tag{2.27}$$

The mechanical energy (E_m) represented by area $AEDA$ in Figure 2.19 is expressed in terms of the co-energy as:

$$E_m = \int \psi_2 \; di - \int \psi_1 \; di \tag{2.28}$$

where, ψ_1 and ψ_2 represent the flux linkage expressions at positions θ_1 and θ_2, respectively. The rate of change of mechanical energy results in mechanical power P_m and is expressed as:

$$P_m = \frac{dE_m}{dt} \tag{2.29}$$

The mechanical power is also expressed as the product of speed and torque. In the case of a motor, mechanical power is the product of angular velocity (ω) and torque (T) and is expressed as:

$$P_m = \omega T \tag{2.30}$$

Using the expression for angular velocity (ω) from Equation 2.9, Equation 2.30 is also expressed as:

$$P_m = \frac{d\theta}{dt}T \tag{2.31}$$

Equating the mechanical power from Equations 2.29 and 2.31, the following expression is obtained:

$$T = \frac{dE_m}{d\theta} \tag{2.32}$$

For a very small incremental change in rotor position (θ), the mechanical energy (E_m) is the same as co-energy (E_c), and under the assumption that phase current remains constant (represented by curve ED in Figure 2.19), the expression for the produced torque is:

$$T = \frac{\partial E_c}{\partial \theta} \tag{2.33}$$

Since it is assumed that phase current is a constant, the use of partial derivatives in Equation 2.33 is justified.

2.4.2 Linear Torque Expression

To obtain an expression for torque produced by a switched reluctance machine during its linear region of operation, the linear magnetization curve shown in Figure 2.21 is considered. The area highlighted in Figure 2.21 represents the stored magnetic energy (E_{mag}) at a particular rotor position. While considering the linear magnetization curve shown in Figure 2.21, the stored magnetic energy is represented by the area of triangle ΔACB. The base of the triangle, i.e., AD represents phase current (i), while the height of the triangle, i.e., AB represents flux linkage (ψ), which according to Equation 2.1 is equal to the product of phase inductance (L) and phase current (i). Therefore, the more familiar expression for

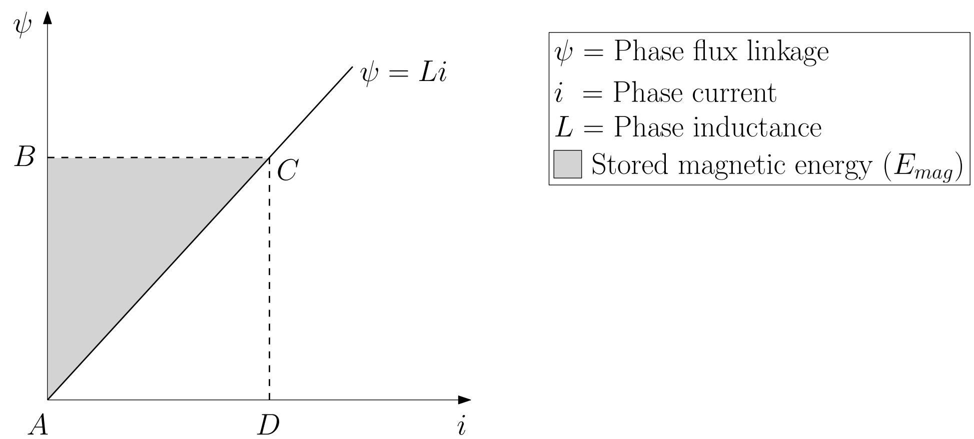

Figure 2.21: Stored magnetic energy at a particular rotor position for a linear magnetization curve

stored magnetic energy is obtained:

$$
\begin{aligned}
E_{mag} &= \frac{1}{2} \cdot AD \cdot AB \\
&= \frac{1}{2} L i^2 \qquad (2.34)
\end{aligned}
$$

Magnetic power P_{mag} is obtained by considering the rate of change of the stored magnetic energy at any instance of time, and using Equation 2.34 is expressed as:

$$
\begin{aligned}
P_{mag} &= \frac{d}{dt}\left(\frac{1}{2} L i^2\right) \\
&= \frac{1}{2} i^2 \frac{dL}{dt} + L i \frac{di}{dt} \qquad (2.35)
\end{aligned}
$$

Using Equations 2.1 and 2.23, input electrical power (P_e) for linear magnetization curves is expressed as:

$$P_e = L i \frac{di}{dt} + i^2 \frac{dL}{dt} \qquad (2.36)$$

Using the law of conservation of energy (and power), the mechanical power (P_m) is expressed by the following set of equations:

$$\begin{aligned}
P_m &= P_{e_tot} - P_r - P_{mag} \\
&= (P_r + P_e) - P_r - P_{mag} \\
&= P_e - P_{mag} \\
&= Li\frac{di}{dt} + i^2\frac{dL}{dt} - \left(\frac{1}{2}i^2\frac{dL}{dt} + Li\frac{di}{dt}\right) \\
&= \frac{1}{2}i^2\frac{dL}{dt}
\end{aligned} \tag{2.37}$$

Using the expression for mechanical power from Equation 2.31 and equating it to Equation 2.37, an expression for the torque produced by a switched reluctance machine in its linear region of operation is expressed as:

$$T = \frac{1}{2}i^2\frac{dL}{d\theta} \tag{2.38}$$

An interesting inference is that the produced torque does not depend on the direction of phase current, this is because the phase current is raised to the second power in Equation 2.38. However, the produced torque does depend on the slope of phase inductance with respect to rotor position ($dL/d\theta$) as indicated by the equation, implying that positive torque is produced when the phase is excited while the rotor travels from position W to position X, whereas negative torque is produced when the phase is excited while the rotor travels from position X to position Y as shown in Figure 2.4.

During the motoring mode of a switched reluctance machine, the production of negative torque is undesirable. If the phase current is not returned to zero after the aligned position, negative torque is produced by the machine (as shown in Figure 2.4); however, if the rotor and stator pole arc lengths (shown in Figure 2.5) are unequal, then a flat inductance profile (also known as a *dead zone*) is observed around the aligned position, during which the slope of phase inductance with respect to rotor position is zero, as a result, no torque is produced, not even the undesired negative torque. This phenomenon is shown in Figure 2.22, even though the tail current persists from the aligned position X to the rotor position θ_2, no negative torque is produced (since $dL/d\theta = 0$). Therefore, based on the derived torque expression of Equation 2.38, improvements can be made to the machine's design which mitigate the effects of the tail current phenomenon. It is also worth nothing that the rise and fall of the phase current in Figure 2.22 is linear because the phase inductance is constant for those regions and the phase current follows Equation 2.3.

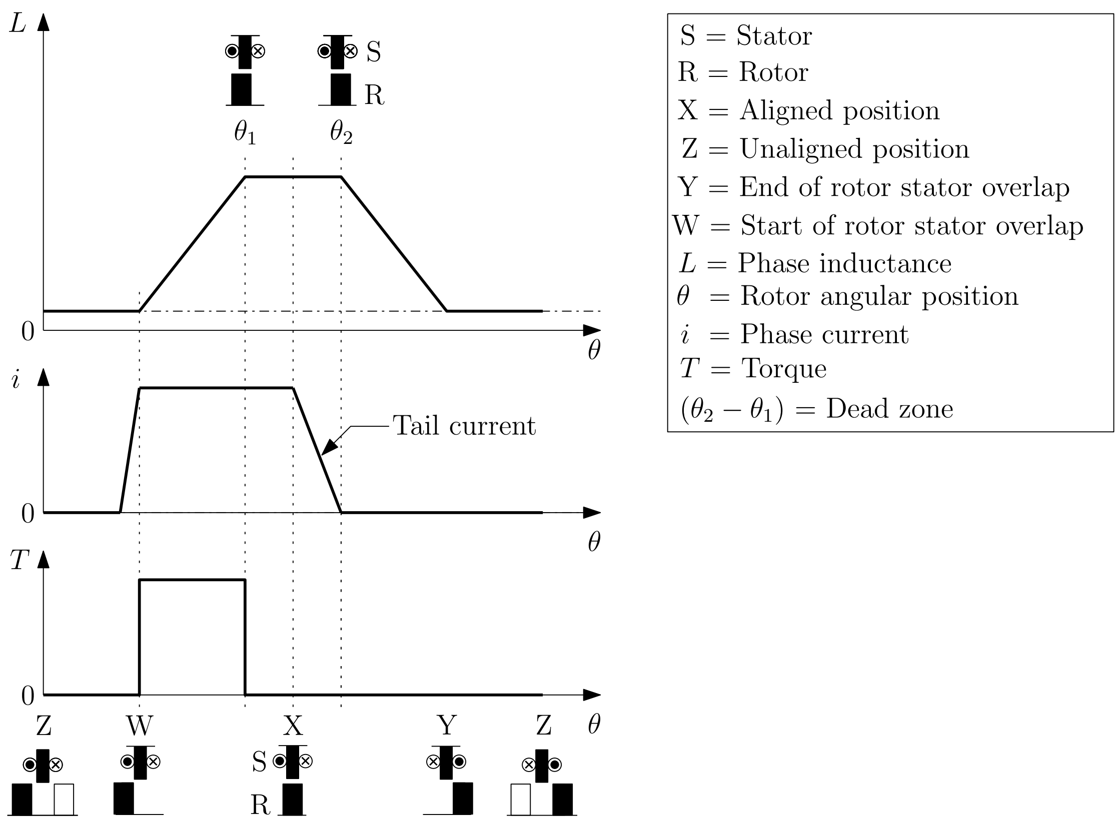

Figure 2.22: Phase inductance, current, and torque profiles for an SRM with unequal rotor and stator pole arc lengths

2.4.3 Power, Torque, and Speed Characteristics

This section presents the characteristics of a switched reluctance machine's mechanical power (P_m), its torque (T) and their dependency on speed or angular velocity (ω). A switched reluctance machine is capable of operating over a wide speed range which is one of its major attractions. The torque produced by a switched reluctance machine is directly proportional to the phase current (indicated by Equation 2.38), while the angular velocity of the machine is directly proportional to the bus voltage. However, as angular velocity increases, the machine's back EMF also increases, limiting the phase current, which results in a drop in the produced torque.

Power and torque variations with angular velocity are best understood by examining their waveforms shown in Figure 2.23. For lower values of angular velocity, depicted by region 1 in Figure 2.23, the back EMF of the machine is low, as a result, the machine is operated at its rated current value, where maximum torque is produced and is a constant, i.e., T_c. Using Equation 2.30, the mechanical power linearly increases in region 1 with a slope of T_c. Region 1 is also called the *constant torque* region.

The constant torque is observed until the angular velocity reaches its *base* speed ω_B, beyond which the torque produced by a switched reluctance machine begins to drop. This region is depicted by region 2 in Figure 2.23 and is characterized by constant mechanical power, i.e., P_{mc}. At angular velocities beyond the base speed, the back EMF of the machine reaches a value high enough to prevent any further increase in the phase current value due to the applied bus voltage, as a result, the torque begins to drop. In accordance with Equation 2.30, the produced torque is proportional to the inverse of the angular velocity. Region 2 is also known as the *constant power* region and is the region where maximum power is produced.

For speeds beyond the constant power region, depicted by region 3 in Figure 2.23, the back EMF of the machine is extremely high and causes the phase current to drop significantly, as a

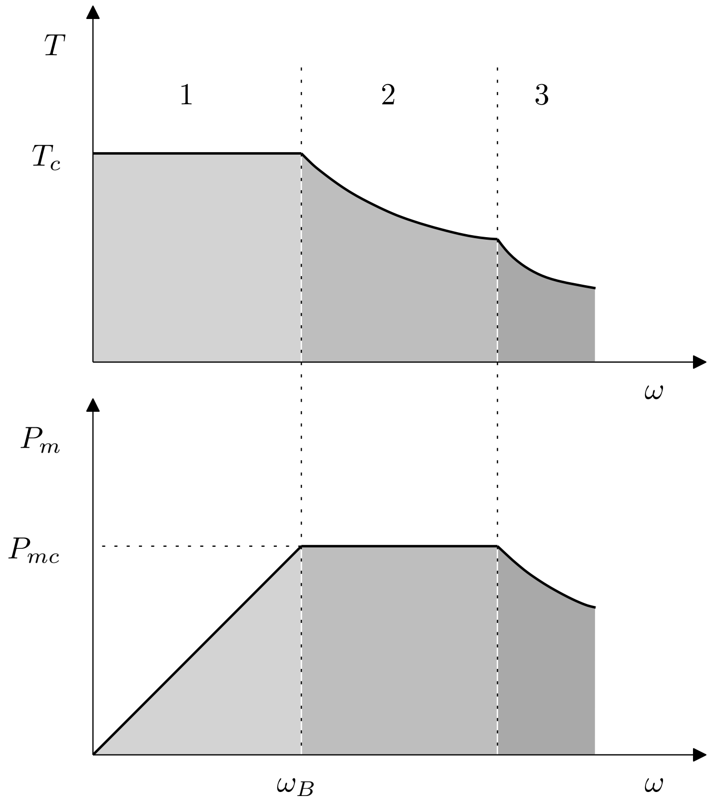

ω = Angular velocity
T = Torque
P_m = Mechanical power
ω_B = Base speed
T_c = Constant torque in region 1
P_{mc} = Constant power in region 2

$P_m = \omega T$	$P_m(\omega)$	$T(\omega)$
Region 1	ωT_c	T_c
Region 2	P_{mc}	$\frac{P_{mc}}{\omega}$
Region 3	$\propto \frac{1}{\omega}$	$\propto \frac{1}{\omega^2}$

Figure 2.23: Power, torque, and speed characteristics of a switched reluctance machine [10]

result, the mechanical power is proportional to the inverse of angular velocity and according to Equation 2.30, the produced torque is proportional to the inverse of the square of angular velocity [10].

2.5 Generating Mode of Operation

A switched reluctance machine is also capable of operating as a generator. It is harder to intuitively understand the operation of the machine as a generator. For the machine to operate as a generator, the machine's active phase must produce current (or charge). During generation, the machine's shaft is connected to an external mechanical source, i.e., a *prime mover*. Under this mode of operation, a switched reluctance machine converts the prime mover's mechanical energy into electrical energy. Generation takes place as the rotor pole travels away from the active stator pole (i.e., from position X to position Y in Figure 2.4). In that region, the phase inductance of the machine decreases and has a negative slope, i.e., $dL/d\theta < 0$. Factoring out the negative sign from $dL/d\theta$ and introducing it in Equation 2.17, the following expression is obtained:

$$\begin{aligned} \frac{di}{d\theta} &= \frac{V - \omega i\left(-\left|\frac{dL}{d\theta}\right|\right)}{\omega L} \\ &= \frac{V + \omega i\left|\frac{dL}{d\theta}\right|}{\omega L} \end{aligned} \tag{2.39}$$

The above equation can also be represented in terms of the machine's back EMF (e) from Equation 2.13 and is expressed as:

$$\frac{di}{d\theta} = \frac{V + |e|}{\omega L} \tag{2.40}$$

In Equation 2.39, the following parameters are all positive: angular velocity (ω), phase current (i), phase inductance (L), and the modulus of the slope of phase inductance $|dL/d\theta|$. The only parameter that can have a bipolar (i.e., positive or negative) value is the phase voltage (V) of the machine, which depends on the switching configuration of the drive's power converter and determines the trajectory of the phase current. For the left hand side of Equation 2.39 (i.e., $di/d\theta$) to be a positive quantity, the numerator on the right hand side must be a positive quantity. Initially, when the phase current is zero, then it is entirely upto the phase voltage to ensure that the numerator is a positive quantity, which occurs when the phase voltage is positive. When the phase voltage is positive, the phase current starts to increase, which in turn causes the back EMF (e) to increase as well. However, for the machine to operate as a generator, it must build the phase current without the continued application of a positive phase voltage. Therefore, to achieve that, one possibility is to switch off the phase after establishing a sufficient amount of back EMF. It is worth nothing that, when the phase is switched off, the phase voltage changes polarity and becomes negative, i.e., the switching configuration of the drive's power converter changes, which results in a negative phase voltage. The detailed functionality of the drive's power converter circuit is presented in subsequent section.

Thus, the generating action consists of two steps, the first step involves the magnetization of the phase (also referred to as the *investing* phase or the *charge build up* phase), while the second step involves the demagnetization of the phase (also referred to as the *harvesting* phase). The phase voltage in Equation 2.40 changes its polarity when the phase is switched off, after which the machine returns the phase current to the supply. Therefore, during the generating mode, it is of interest to analyze the current differential equation (i.e., Equation 2.40) after the phase is switched off and the phase voltage is negative. When the phase is switched off, Equation 2.40 is then modified and expressed as:

$$\frac{di}{d\theta} = \frac{-V + |e|}{\omega L} \tag{2.41}$$

Equation 2.41 implies that the phase (V) is a positive quantity (since the negative sign is factored out) and is more accurately expressed as:

$$\frac{di}{d\theta} = \frac{-|V| + |e|}{\omega L} \tag{2.42}$$

Upon further inspection, it is observed that once the phase is switched off, the numerator on the right hand side of Equation 2.42 has two terms of opposite polarity which create contention. The contention gives rise to three possible scenarios, wherein the negative term (i.e., the phase voltage) is greater than, equal to, or less than the positive term (i.e., the established back EMF) at the instance the phase is switched off. Each scenario produces a different phase current trajectory and is presented next.

2.5.1 Negative Feedback Scenario (V > e)

The first of three possible scenarios occurs when the phase voltage is greater than the established back EMF when the phase is switched off. This scenario is shown in Figure 2.24.

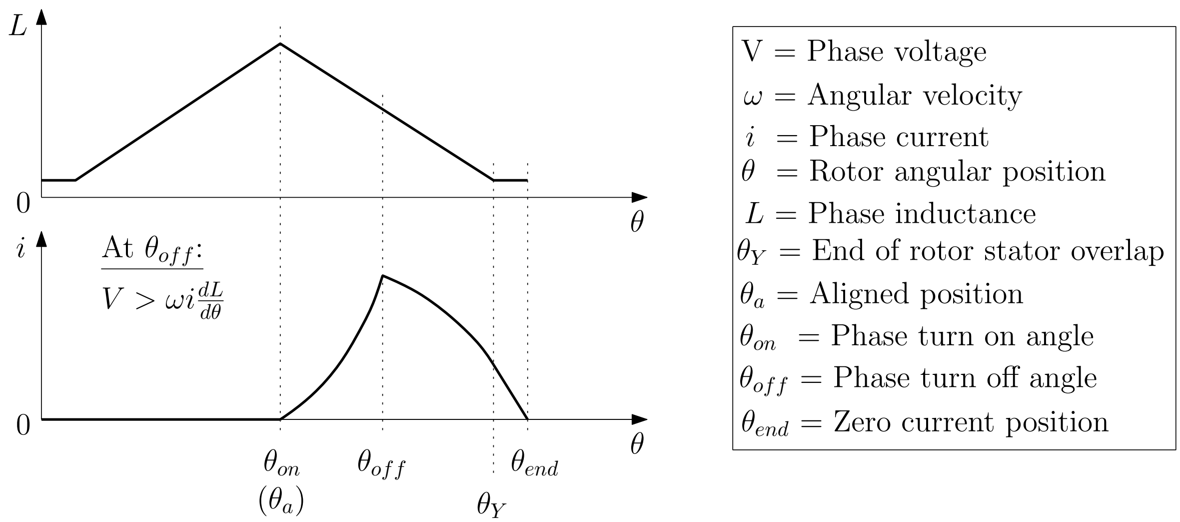

Figure 2.24: Generating phase current when the phase voltage (V) is greater than the back EMF (e) at the turn-off angle (θ_{off})

Since the phase voltage is greater than the established back EMF when the phase is switched off, the numerator on the right hand side of Equation 2.42 is negative, implying that the left hand side of the equation is also negative, i.e., $di/d\theta < 0$. A negative left hand side of Equation 2.42 causes an instant change in the slope of the phase current trajectory (i.e., from a positive value to a negative value) and it begins to fall as shown in Figure 2.24 after the turn-off angle θ_{off}. In this scenario, the current is always controllable at every instance (i.e., it can be increased or decreased based on the polarity of phase voltage). The area under the phase current curve from the turn-on angle θ_{on} to θ_{off} is proportional[1] to the charge invested into the machine, while the area under the phase current curve from θ_{off}

[1]Electrical charge is defined as the product of current and time. The area under the phase current curve with respect to rotor position is proportional to charge, as rotor position is proportional to time (through angular velocity as expressed in Equation 2.9). The area under the phase current (in A) curve with respect to rotor position needs to be divided by the angular velocity (in $^\circ\,s^{-1}$) in order to represent charge (in C).

to θ_{end} (i.e., the rotor position, where the phase current returns to zero) is proportional to the charge harvested by the machine. The charge harvested by the machine in this scenario is not very high; however, the fact that the phase current is controllable (i.e., the system remains in negative feedback) is a benefit to consider.

2.5.2 Zero Feedback Scenario (V = e)

The second scenario occurs when the phase voltage is equal to the established back EMF when the phase is switched off. This scenario causes the numerator on the right hand side of Equation 2.42 to become equal to zero, implying that the left hand side of the equation is also zero, i.e., $di/d\theta = 0$. Since $di/d\theta = 0$, the current remains at a constant value even after the phase is switched off and is shown in Figure 2.25.

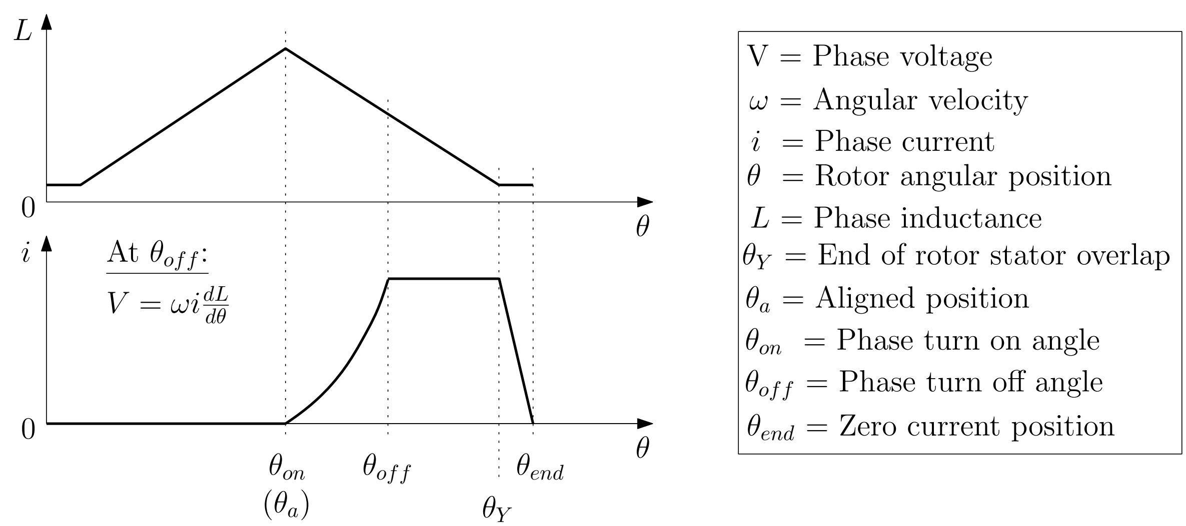

Figure 2.25: Generating phase current when the phase voltage (V) is equal to the back EMF (e) at the turn-off angle (θ_{off})

In this scenario, compared to the first one, there is clearly an increase in the amount of charge harvested by the machine (i.e., proportional to the area under the phase current curve from θ_{off} to θ_{end}). However, it comes at a cost, which is the loss of control over the phase current. The phase current can no longer be reduced as desired even after the phase voltage is negative when the phase is switched off. Once the phase inductance reaches its minimum constant unaligned value (i.e., L_u at θ_Y), the back EMF becomes zero (in accordance with Equation 2.13).Because of a zero back EMF, the sign of the numerator on the right hand side of Equation 2.42 is dictated only by the phase voltage, which is negative when the phase is switched off, as a result, at θ_Y, the left hand side of the equation is a negative quantity, causing the phase current to decrease linearly (as the inductance is constant after θ_{end}).

In this scenario, the machine is still stable in some sense as the phase current is not in positive feedback; however, control over the machine's phase current is severely compromised.

2.5.3 Positive Feedback Scenario (V < e)

The last scenario occurs when the phase voltage is less than the established back EMF when the phase is switched off. In this scenario, the numerator on the right hand side of Equation 2.42 is a positive quantity, implying that the left hand side of the equation is also a positive quantity, i.e., $di/d\theta > 0$. Since $di/d\theta > 0$, the phase current continues to increases even after the phase is switched off and is shown in Figure 2.26.

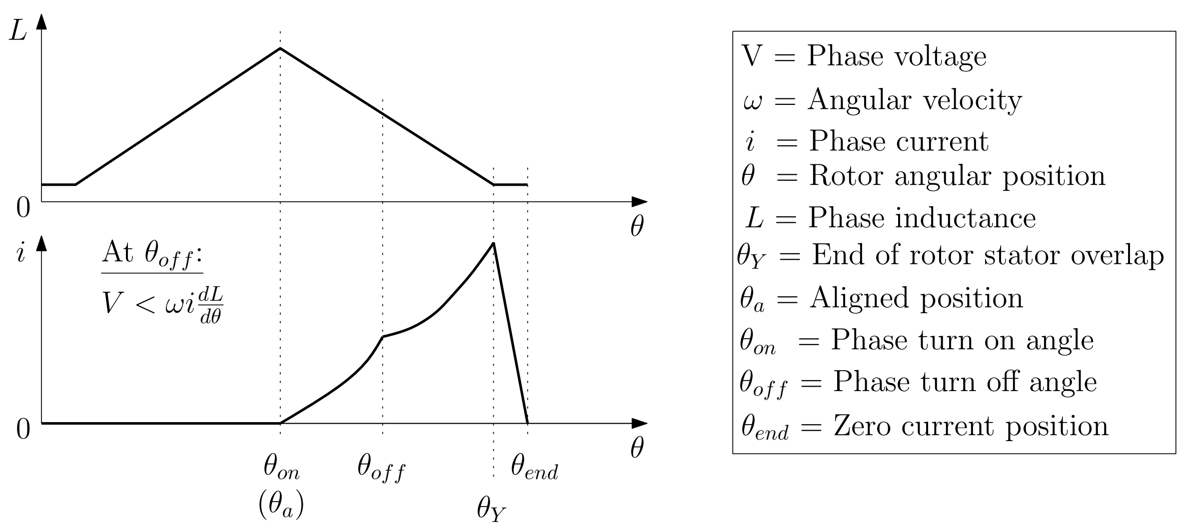

Figure 2.26: Generating phase current when the phase voltage (V) is less than the back EMF (e) at the turn-off angle (θ_{off})

Of the three scenarios discussed, this scenario results in the maximum charge harvested from the machine and is the most advantageous from the standpoint of *maximizing output power*. However, this scenario is accompanied by a complete loss of control over the phase current. When the phase is switched off, the phase current enters into a state of positive feedback and begins to snowball to uncontrollable levels. The phase current begins to fall only when the phase inductance reaches its constant minimum unaligned inductance value (i.e., L_u at θ_Y) which results in a zero back EMF and is similar to the reason the phase current falls in the second scenario. Clearly, this scenario is the one with the highest risk but also the one with the highest reward, as the charge harvested is the maximum of the three scenarios (i.e., proportional to the area under the phase current curve from θ_{off} to θ_{end}). Being able to reconstruct the phase current would be extremely beneficial from a control standpoint and would allow a designer to exploit this scenario.

In summary, the generation of charge from a switched reluctance machine is a two step process, it involves an initial investment phase followed by a secondary harvesting phase. Both the phases occur when the slope of phase inductance with respect to rotor position is negative (i.e., when phase inductance decreases). During the investment phase, the machine is magnetized by a positive phase voltage, allowing the phase current to build up to a certain level. Once a sufficient amount of charge has been invested into the machine, and the phase current crosses a certain threshold value, where the back EMF is greater than the negative phase voltage, the harvesting phase begins. During the harvesting phase, the phase current flows back into the supply (i.e., a storage element like a battery for instance) and the machine gets demagnetized. The key factor is determining the amount of charge *sufficient* during the investment phase. There is a minimum amount of charge needed to be invested, or else the returns from the machine during the harvesting phase will be minimal. On the other hand, a large investment may be good to magnetize the machine, but may cause the machine to produce unsafe levels of currents which can damage the power electronics circuitry connected to the machine.

It is not always necessary to have a continuous DC bus voltage to magnetize the phases during every cycle (as that would imply that switched reluctance generators are not self-sufficient), an initial DC bus voltage (for instance, from a battery) can start the generating process and then be disconnected. In such a scenario, once the phase current in a particular stator phase is established, some of it is rerouted into the other phases, causing charge to be invested in the other phases (i.e., magnetizing the other phases) and making the generation process self-sufficient [96]. In such a scenario, the machine is referred to as a *self excited* switched reluctance generator.

In some cases, the phase is switched on before the rotor's aligned position, this allows for a non zero positive value of phase current $i_{initial}$ at the aligned position (θ_a). Switching on the phase before the aligned position is referred to as *phase advancing*, which causes the required back EMF to be established earlier compared to the case without phase advancing, resulting in higher amount of charge harvested from the machine (as the phase is switched on earlier and the phase current is allowed to increase for a longer period). Figure 2.27 shows the phenomenon of phase advancing.

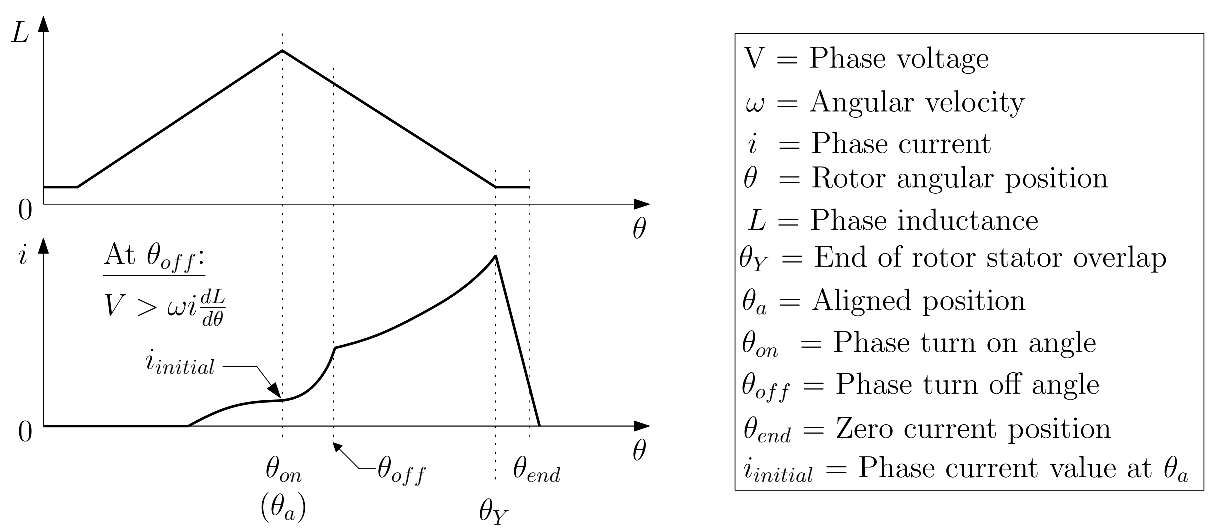

Figure 2.27: Generating phase current with phase advancing when the phase voltage (V) is less than the back EMF (e) at the turn-off angle (θ_{off})

2.5.4 Comparison of Negative, Zero, and Positive Feedback Scenarios

During a switched reluctance machine's generating mode of operation, the behavior of its phase current after the phase is switched off depends on the established back EMF at the turn-off angle (θ_{off}). If the magnitude of back EMF is lesser than the magnitude of phase voltage at the turn-off angle, the phase current enters a state of negative feedback and starts decreasing after the phase is switched off. On the other hand, if the magnitude of back EMF is equal to the magnitude of phase voltage at the turn-off angle, the phase current enters a state of zero feedback and remains the same until the phase inductance reaches its minimum constant unaligned value (L_u), after which it starts decreasing. Lastly, if the magnitude of back EMF is greater than the magnitude of phase voltage at the turn-off angle, the phase current enters a state of positive feedback and starts increasing after the turn-off angle (even though the phase is switched off). Eventually, the phase current begins to decrease only after the phase inductance reaches its minimum constant unaligned value. Therefore, the established back EMF at the turn-off angle dictates whether the phase current decreases, remains the same or increases after the phase is switched off. The expression for back EMF is defined by Equation 2.13 and is rewritten as:

$$e = \omega i \frac{dL}{d\theta} \tag{2.43}$$

From Equation 2.43, it is observed that back EMF is a function of the machine's phase current (i) and angular velocity (ω). The evolution of the generating phase current is first examined for varying turn-off angles and a constant angular velocity. If the turn-off angle is varied, while the angular velocity is constant, since the back EMF is a function of phase current, it is higher at a larger turn-off angle (as a longer magnetization period results in a higher phase current at the turn-off angle). As a result, for a larger turn-off angle, the phase current tends to enter a state of positive feedback (the exact behavior of the phase current depends on the exact operating point of the machine defined by the value of phase voltage, instantaneous phase inductance, rotor position, slope of phase inductance with respect to rotor position, among others). Similarly, the back EMF is lower at a smaller turn-off angle (as a shorter magnetization period results in a lower phase current at the turn-off angle). As a result, for a smaller turn-off angle, the phase current tends to enter a state of negative feedback. Also, for a particular turn-off angle, when the magnitude of back EMF is equal to the magnitude of phase voltage, the phase current enters a state of zero feedback. The evolution of generating phase currents for three different turn-off angles (i.e., θ_{offa}, θ_{offb}, and θ_{offc}, where $\theta_{offa} < \theta_{offb} < \theta_{offc}$) at a constant angular velocity is shown in Figure 2.28.

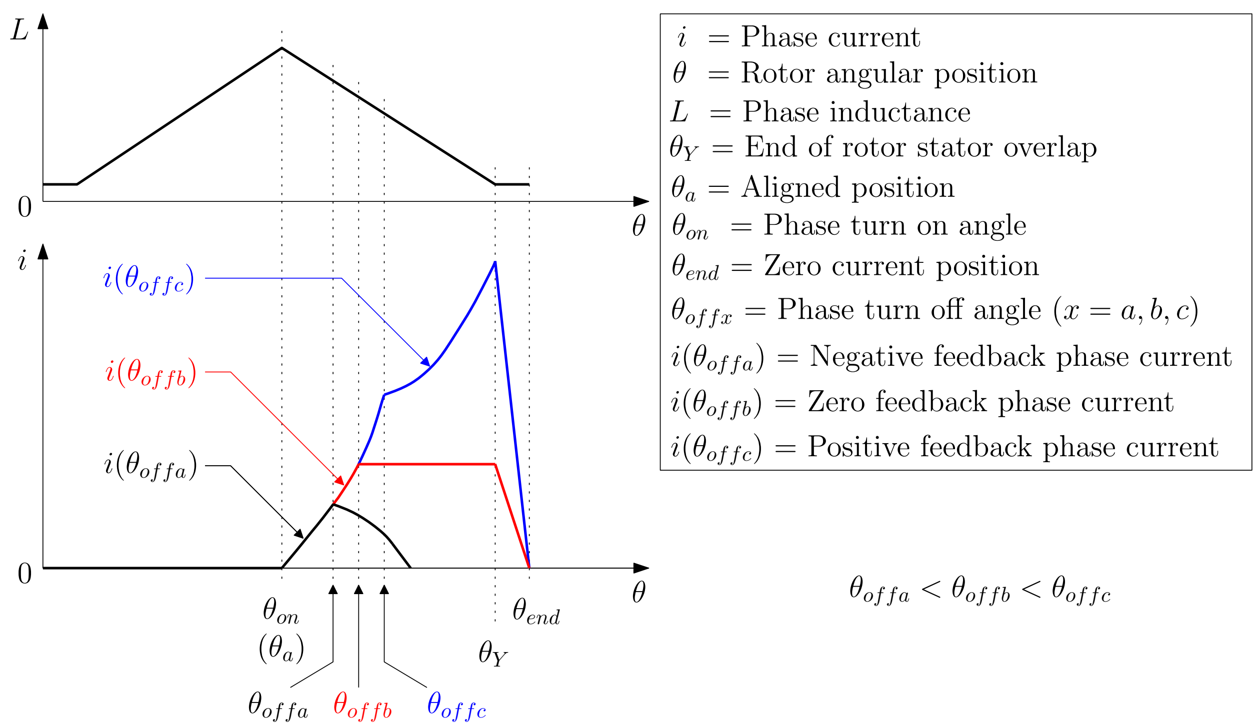

Figure 2.28: Comparison of generating phase currents in negative, zero, and positive feedback for turn-off angles θ_{offa}, θ_{offb}, and θ_{offc}, respectively

From Figure 2.28, the phase current in positive feedback yields the maximum harvested charge (i.e., proportional to the area under the phase current curve from θ_{offx} to θ_{end}, where $x = a, b, c$ represents the negative, zero, and positive feedback scenarios, respectively). The positive feedback scenario also yields the maximum *net charge*, defined as the difference between the harvested and invested charge (i.e., proportional to the area under the phase current curve from θ_{on} to θ_{offx}), also resulting in maximum output power from the machine. The generating phase currents shown in Figure 2.28 differ from each other due to varying turn-off angles (i.e., θ_{offa}, θ_{offb}, and θ_{offc}); however, they all have the same angular velocity.

Next, the evolution of the generating phase current is examined for varying angular velocities. Since back EMF is directly proportional to a machine's angular velocity, a lower angular velocity (i.e., lower mechanical energy) establishes a lower back EMF in the machine, while a higher angular velocity (i.e., higher mechanical energy) establishes a higher back EMF in the machine. This also holds true through intuition, as a higher amount of mechanical energy (i.e., angular velocity) yields a higher amount of converted electrical energy (i.e., back EMF). As a result, for lower angular velocities, the phase current tends to enter a state of negative feedback, while for higher angular velocities, it tends to enter a state of positive feedback. So far, the behavior of phase current (i.e., negative, zero, or positive feedback) after the turn-off angle is examined; however, depending on the angular velocity, the slope of phase current before the turn-off angle also varies and is examined next. Equation 2.40 describes the generating current differential equation and is rewritten as:

$$\frac{di}{d\theta} = \frac{V + |e|}{\omega L} \tag{2.44}$$

From Equation 2.44, the slope of phase current with respect to rotor position ($di/d\theta$) is inversely proportional to angular velocity (ω). Based on the analysis presented, the evolution of generating phase currents for three different angular velocities (i.e., ω_a, ω_b, and ω_c, where $\omega_a < \omega_b < \omega_c$) at a constant turn-off angle is shown in Figure 2.29.

From Figure 2.29, it is observed that when the angular velocity is lowest (ω_a), the slope of phase current with respect to rotor position during the magnetization phase is the highest; however, due to a low angular velocity, the phase current enters a state of negative feedback after the turn-off angle. Similarly, when the angular velocity is highest (ω_c), the slope of

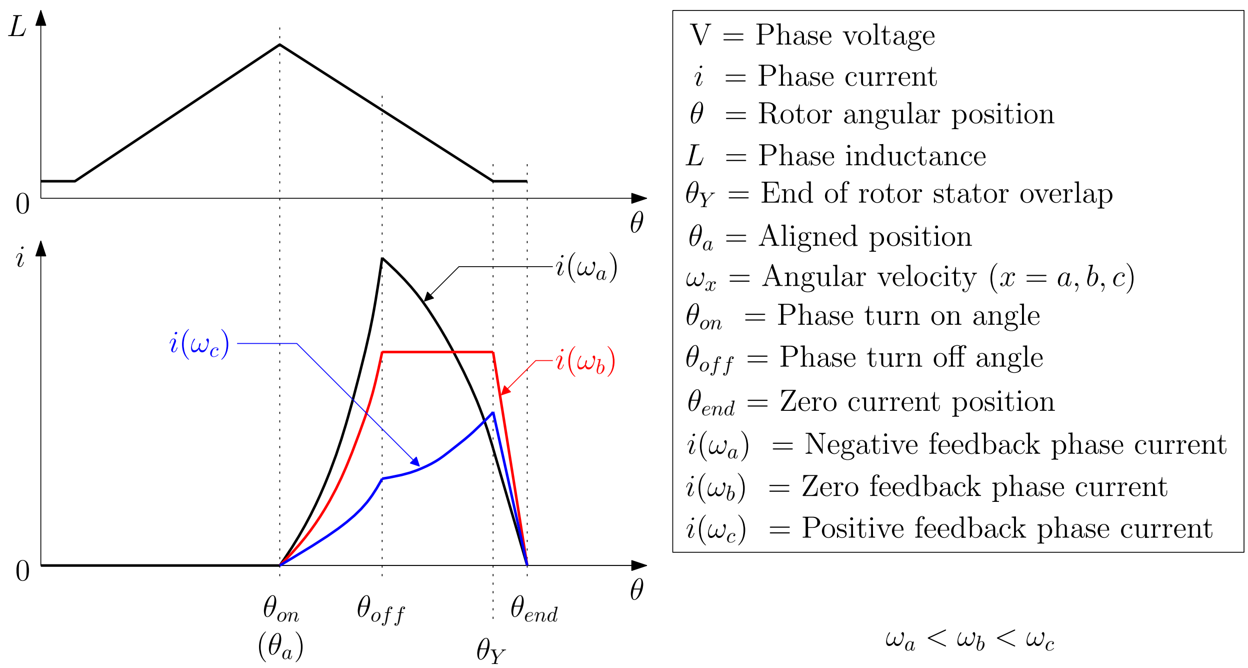

Magnetization phase relations

$$\frac{di(\omega_a)}{d\theta} = \frac{V + |e|}{w_a L} \quad ; \quad \frac{di(\omega_b)}{d\theta} = \frac{V + |e|}{w_b L} \quad ; \quad \frac{di(\omega_c)}{d\theta} = \frac{V + |e|}{w_c L} \quad ; \quad \frac{di(\omega_a)}{d\theta} > \frac{di(\omega_b)}{d\theta} > \frac{di(\omega_c)}{d\theta}$$

Figure 2.29: Comparison of generating phase currents in negative, zero, and positive feedback for angular velocities ω_a, ω_b, and ω_c, respectively

phase current with respect to rotor position during the magnetization phase is the lowest; however, due to a high angular velocity, the phase current enters a state of positive feedback after the turn-off angle. From Figure 2.29, it is worth noting that charge harvested from the phase current in negative feedback, i.e., $i(\omega_a)$ is the highest, whereas it is lowest from the phase current in positive feedback, i.e., $i(\omega_c)$. However, the output power of a switched reluctance generator is determined based on the net charge and not the harvested charge. Therefore, while examining the net charge of the three scenarios shown in Figure 2.29, it is maximum when the phase current is in a state of positive feedback when the phase is switched off. Experimental results for the two sets of operating points presented in this section are provided and analyzed in detail in Appendix H. The analysis includes a method to calculate invested, harvested, and net charge along with output electrical energy and power.

2.6 The Asymmetric Bridge Converter

This section presents an asymmetric bridge converter which is used as part of a switched reluctance machine's drive. There are plenty of converters which are used to drive a switched reluctance machines [97–100]; however, the most common drive circuit used to control the machine is an asymmetric bridge converter. A single phase of an asymmetric bridge converter in shown in Figure 2.30, in which metal oxide semiconductor field effect transistors (MOSFETs) and diodes are used as the switches; however, other transistors may also be used. For a higher degree of accuracy, the circuit must also include additional parasitic components, such as the on resistances of the transistors, the diode's forward voltage drops and so forth. For simplicity, the circuit shown in Figure 2.30 is considered and include only the major components which play the most significant role. A switched reluctance machine's phase is denoted by M, which represents the machine's phase inductance and back EMF (the winding resistance and other parasitic resistances are lumped into R as shown Figure 2.30).

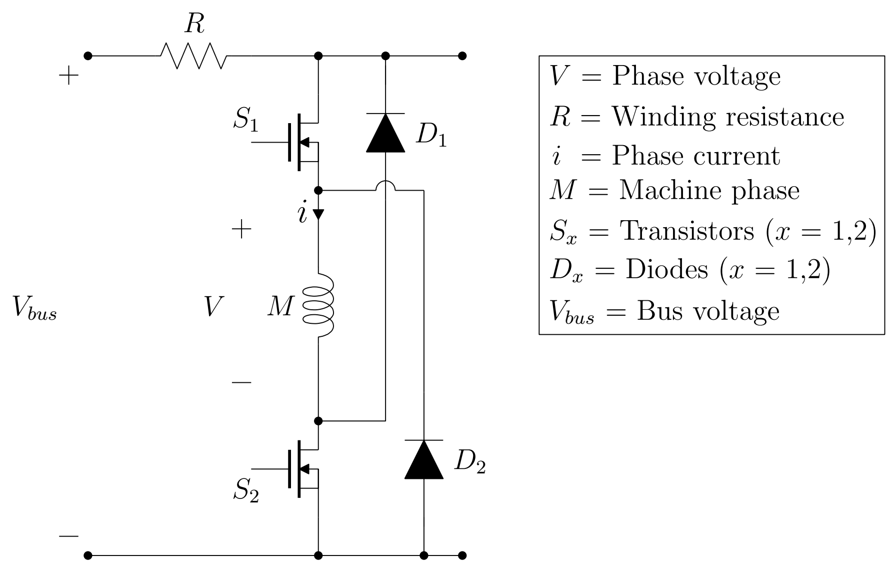

Figure 2.30: Single phase of an asymmetric bridge converter

The control signals to an asymmetric bridge converter (for a single phase converter) are the gate signals to the two transistor switches S_1 and S_2. Since there are two switches, there are four possible switching combinations for the converter. The first possible switching combination occurs when both the transistors S_1 and S_2 are switched on. Under such a switching combination, the converter is depicted by Figure 2.31. When S_1 and S_2 are both switched on, the diodes do not conduct and the phase voltage (V) of the machine is expressed in accordance with Equation 2.5 as: $V_{bus} - iR$. During this switching combination, the phase voltage is positive and the state is referred to as the *on state*. During this switching combination, the phase current through the phase inductance (L) increases.

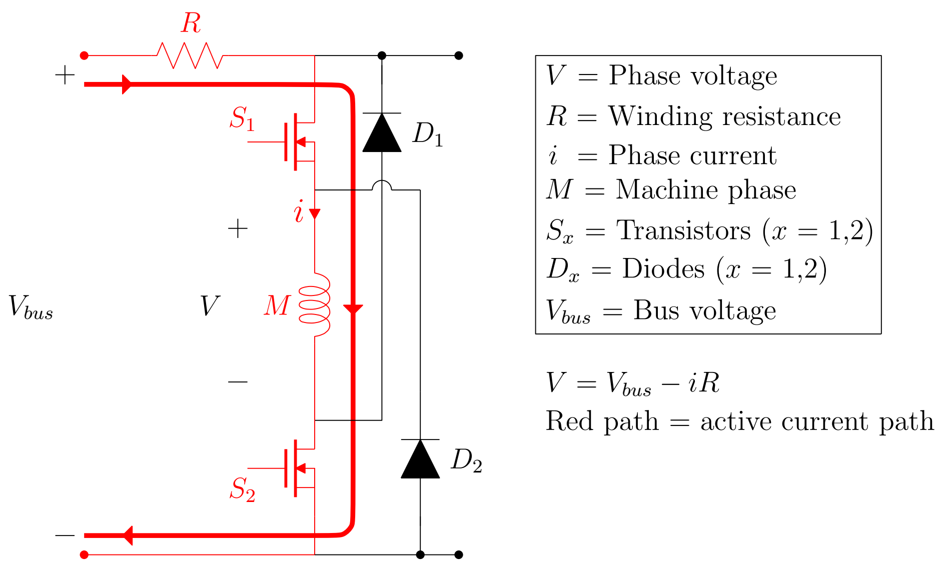

Figure 2.31: Single phase of an asymmetric bridge converter in its on state, i.e., switches S_1 and S_2 are on and diodes D_1 and D_2 are off

The second possible switching combination occurs when both the transistors S_1 and S_2 are switched off. Under such a switching combination, the converter is depicted by Figure 2.32. When S_1 and S_2 are both switched off, the diodes begin to conduct and using Equation 2.5, the phase voltage (V) of the machine is expresses as: $-V_{bus} - iR$. During this switching combination, the phase voltage is negative and the state is referred to as the *off state*. During this switching combination, the phase current is likely to decrease (unless it is in a state of zero or positive feedback).

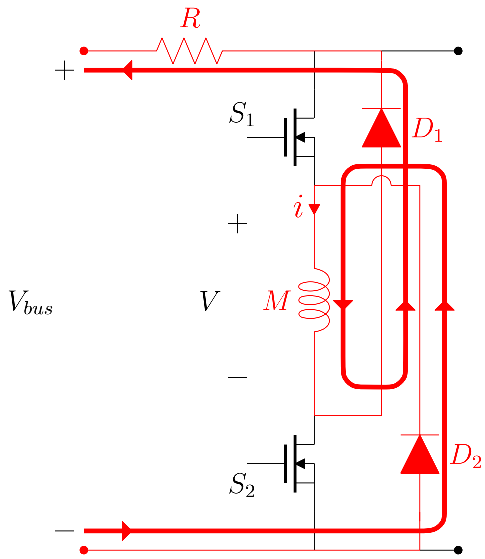

V = Phase voltage
R = Winding resistance
i = Phase current
M = Machine phase
S_x = Transistors (x = 1,2)
D_x = Diodes (x = 1,2)
V_{bus} = Bus voltage

$V = -V_{bus} - iR$
Red path = active current path

Figure 2.32: Single phase of an asymmetric bridge converter in its off state, i.e., switches S_1 and S_2 are off and diodes D_1 and D_2 are on

The last two switching combinations occur when either S_1 is switched on and S_2 is switched off or when S_1 is switched off and S_2 is switched on (i.e., only one of the two transistors are switched on at any instance). The two such switching combinations are shown in Figure 2.33. When only one of the transistors is switched on, the phase current freewheels through one of the diodes and flows through the transistor which is switched on. Figure 2.33(a) shows a switching combination, where transistor S_1 is switched off and transistor S_2 is switched on. For the phase current to complete its loop, diode D_2 turns on and begins to conduct (diode D_1 does not conduct). Figure 2.33(b) shows a switching combination, where transistor S_1 is switched on and transistor S_2 is switched off. For the phase current to complete its loop, diode D_1 turns on and begins to conduct (diode D_2 does not conduct). During both these switching combinations, the phase voltage is zero and ideally the phase current freewheels indefinitely until the switching combination is changed (in reality, power is lost due to the parasitic resistive elements in the current path), this state is referred to as the *freewheeling state*.

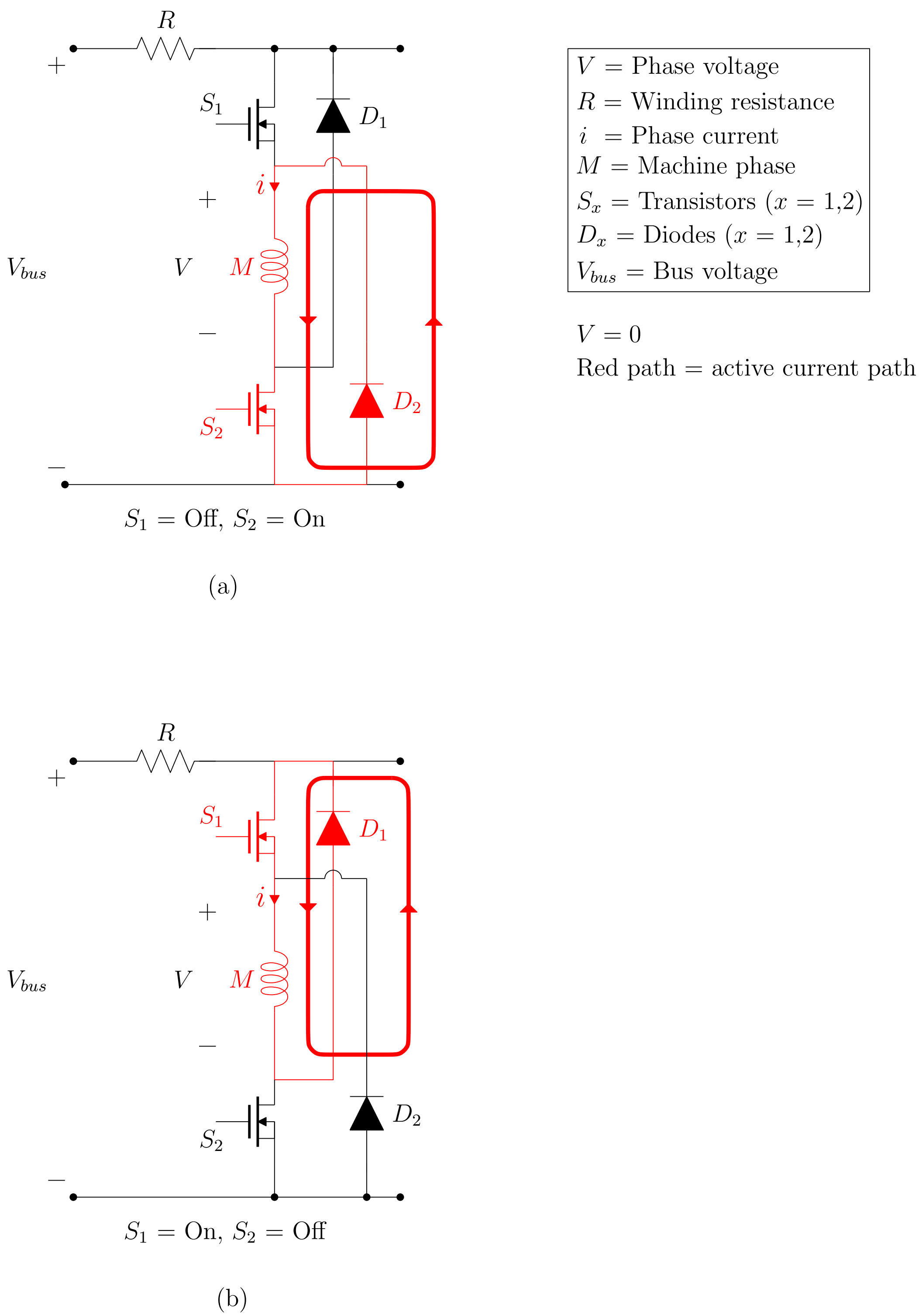

Figure 2.33: Single phase of an asymmetric bridge converter in its freewheeling states, i.e., when (a) S_2 and D_2 are on and S_1 and D_1 are off and (b) S_1 and D_1 are on and S_2 and D_2 are off

When the switching combination is changed from the on state to the off state (or vice versa), the switching is known as *hard switching*. On the other hand when the switch combination is changed from the on state to the freewheeling state, the switching is known as *soft switching*.

In summary, based on the switching combination, three voltage levels are achieved, i.e., a positive voltage level, a zero voltage level, and a negative voltage level. Depending on the maximum operating value of the phase current, the diodes and the transistors with the correct current ratings must be selected. The switches can be easily selected for appropriate current levels while the machine operates as a motor because throughout motoring, there is complete control over the phase current (i.e., as the phase current approaches the rated current of the switches, it can be decreased by turning off the phase). However, when the machine operates as a generator, its phase current is not always controllable and can reach undesirable levels when in positive feedback and cannot be decreased even after the phase is switched off. To design for such unforeseeable circumstances, diodes with higher current ratings are selected for the drive's power converter, i.e., the drive power converter is overdesigned. Therefore, the design constraints on the diodes during the generating mode are significantly higher than during the motoring mode.

As stated earlier, the motoring tail current is an undesired phenomenon and produces negative torque, a technique of reducing its effect is by using a higher demagnetization negative phase voltage compared to the magnetization positive phase voltage, thereby causing the phase current to fall to zero quickly without its lingering tail. In this case, the asymmetric bridge converter is modified in order to provide a positive phase voltage V_1 during the magnetization phase and a separate negative phase voltage V_2 during the demagnetizing phase, where $V_2 > V_1$. However, such a drive is accompanied with an overhead of generating a separate voltage level as well (for instance, through a switching DC to DC converter). A single phase of such a converter is shown in Figure 2.34.

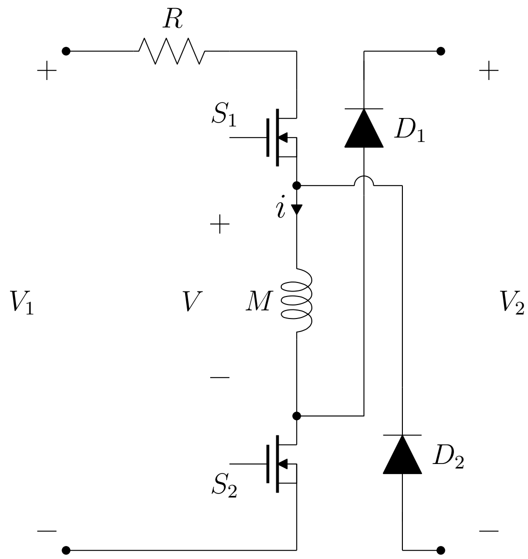

V = Phase voltage
V_1 = Magnetization voltage
V_2 = Demagnetization voltage
R = Winding resistance
i = Phase current
M = Machine phase
S_x = Transistors (x = 1,2)
D_x = Diodes (x = 1,2)

Figure 2.34: Single phase of an asymmetric bridge converter with dual voltage supplies

CHAPTER 3

MODELING OF A SWITCHED RELUCTANCE MACHINE

This chapter presents mathematical models of a switched reluctance machine. First, prior flux and inductance based modeling schemes which are widely accepted are analyzed and their limitations are presented. Next, an approach to reconstruct the machine's phase current using numerical methods of integration is explored. Lastly, the proposed modeling scheme with and without the phase resistance[1] is derived and simulation results based on the model are compared with experimental results.

While modeling complex systems, it is not always practical to include all the system dynamics and characteristics into the model, doing so could take a large amount of computation time and effort and not provide much useful information in return. As a result, models are always accompanied with inaccuracies and limitations, and it is upto the designer to create a model which strikes a balance between accuracy and mathematical simplicity. It was best put by British mathematician George Box, who stated that *"all models are wrong"* [101]; however, he did emphasize that some models are more useful than others.

Unlike simple plants and electrical networks, modeling of a switched reluctance machine poses a few challenges. Due to its highly nonlinear magnetization curves and inter variable dependencies, it is extremely tedious and impractical to apply Maxwell's equations (among others) to obtain the closed form expressions for its electrical and magnetic parameters, such as phase inductance (L) and flux linkage (ψ). Instead, three dimensional models of the machine are created in finite element analysis (FEA) tools, which return large amounts of data based on specific inputs, thereby encapsulating the machine's dynamics and characteristics. The FEA tool breaks up the machine into multiple small surfaces or a mesh (i.e., tessellation) and applies the laws of electromagnetism at each surface. Running such a simulation

[1]Accepted for publication under the title: A Phase Current Peak Prediction Technique to Increase the Output Power of Switched Reluctance Generators for Wind Turbines, in the: 2019 IEEE Energy Conversion Congress and Exposition (ECCE), © 2019 IEEE.

may take several hours or even days depending on available computing resources, accuracy of the constructed three dimensional model, accuracy of the data desired (i.e., the number of small surfaces the machine is broken into), among others. Of course data can always be recorded experimentally rather than from an FEA tool which utilizes the user constructed three dimensional model of the machine. The modeling technique wherein the mathematical model of a machine is constructed based on its measured dynamic response to given inputs is called system identification [102, 103], and is the basis of modeling a switched reluctance machine.

However, the entire dynamics of the machine are not modeled using a black box approach but rather a grey box approach wherein one of the parameters is modeled based on the obtained data (either from an FEA tool or experimentally gathered from the machine) and the remaining parameters are constructed through the electrical and magnetic laws governing them. Therefore, the modeling process typically involves assigning a curve fitting expression (using regression techniques) to the obtained data. Usually, the parameters that are modeled using the data are either the machine's phase inductance (L) or flux linkage (ψ). Examples of such modeling schemes are presented next.

3.1 Prior Modeling Schemes

Two of the most widely accepted modeling schemes for switched reluctance machines are presented in this section. In this dissertation, they are referred to as the *Flux based modeling scheme* and the *Inductance based modeling scheme*. Both modeling schemes use system identification followed by regression analysis to develop expressions for the magnetic parameters. While using system identification, two design flows can be followed, either the data is obtained through FEA tools (based on the user constructed three dimensional model of the machine) or the data is gathered experimentally from the machine itself. The two options are depicted in Figure 3.1.

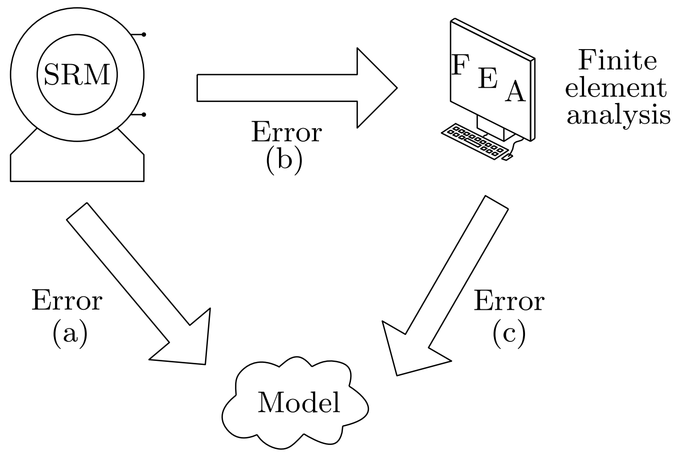

Figure 3.1: Possible design flow while modeling an SRM

The first approach involves taking the measurements directly from the machine (i.e., experimentally gathered data); however, in the case of a switched reluctance machine such a task is tedious and requires very precise measurements. Also, to acquire the entire data set, a lot of readings must be taken in an iterative manner, i.e., measuring magnetic parameters like phase inductance and flux linkage for various values of phase current at several rotor positions. The model of the machine is then constructed using curve fitting expressions through regression techniques. The design flow is prone to errors introduced by curve fitting and is represented along path (a) in Figure 3.1.

The second approach involves creating the three dimensional model of the machine as accurately as possible using computer aided design (CAD) tools. Next, the created three dimensional model is then imported into an FEA tool and the model is subject to electromagnetic analysis. Finally, the model of the machine is then constructed using curve fitting expressions through regression techniques. This design flow is represented along paths (b) and (c) in Figure 3.1. Generally, as a rule of thumb, upto a 10% error is expected along path (b) (depending on the accuracy of the three dimensional model). The error along path (c) is introduced due to curve fitting and is equivalent to the error along path (a) of the first design flow.

3.1.1 The Flux Based Model

The first modeling scheme, i.e., the flux based model was initially presented in 1990 by D. A. Torrey and J. H. Lang [104] and then revisited again in 1995 [11]. According to Figure 2.11, the magnetization curves (i.e., the plot of flux linkage versus phase current) of the machine exhibit nonlinearities due to saturation. The machine's flux linkage (ψ) depends on two variables, i.e., phase current (i) and rotor position (θ), as a result, it is more accurately represented as $\psi(\theta, i)$. A suitable expression to fit the curves shown in Figure 2.11 has been presented in [104], and the expression has the following exponential form:

$$\psi(\theta, i) = a_1(\theta)(1 - e^{a_2(\theta)i}) + a_3(\theta)i \tag{3.1}$$

The three magnetizing coefficients $a_1(\theta)$, $a_2(\theta)$, and $a_3(\theta)$ of Equation 3.1 are all functions of rotor position. Their correlation with the machine's magnetization curve is shown in Figure 3.2.

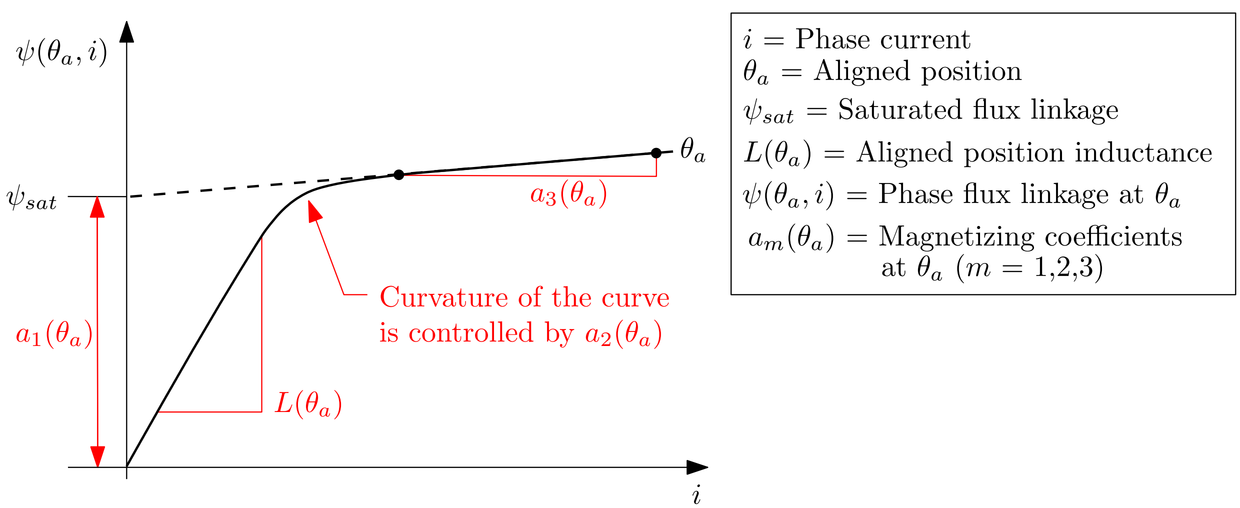

Figure 3.2: Magnetization curve and magnetizing coefficients at the aligned position [11]

The magnetization curve shown in Figure 3.2 is analyzed at two different values of phase current, i.e., at lower values, where saturation does not occur, and at higher values, where saturation occurs. For the flux linkage function described by Equation 3.1 to fit the magnetization curve shown in Figure 3.2, the value of magnetizing coefficient $a_2(\theta)$ is always negative. To obtain the other magnetic parameter, i.e., phase inductance, the derivative of flux linkage with respect to phase current is considered (using Equation 3.1), which represents the slope of the magnetization curves. The derivative of flux linkage with respect to phase current represents the instantaneous phase inductance which is expressed as:

$$L(\theta, i) = \frac{d\psi(\theta, i)}{di} = -a_1(\theta)a_2(\theta)e^{a_2(\theta)i} + a_3(\theta) \tag{3.2}$$

The expression for instantaneous phase inductance varies depending on the effect of saturation. The expressions for instantaneous phase inductance at lower and higher values of phase current are presented next.

Instantaneous Phase Inductance for Lower Values of Phase Current

While considering lower values of phase current (i.e., $i \to 0$), where flux linkage does not saturate, using Equation 3.2, the instantaneous phase inductance is expressed as:

$$\lim_{i \to 0} L(\theta, i) = -a_1(\theta)a_2(\theta) + a_3(\theta) \tag{3.3}$$

From Equation 3.3, it is inferred that at lower values of phase current, the instantaneous phase inductance is completely independent of phase current. Intuitively, this holds true because at lower values of phase current, the machine does not experience saturation and the instantaneous phase inductance at a particular rotor position is constant. Therefore, in the linear region (i.e., in the absence of saturation), the instantaneous phase inductance is expressed as a function of only rotor position as follows:

$$L(\theta) = -a_1(\theta)a_2(\theta) + a_3(\theta) \tag{3.4}$$

Instantaneous Phase Inductance for Higher Values of Phase Current

While considering higher values of phase current (i.e., $i \rightarrow \infty$), where flux linkage saturates, using Equation 3.2, the instantaneous phase inductance is expressed as:

$$\lim_{i \rightarrow \infty} L(\theta, i) = a_3(\theta) \tag{3.5}$$

The result in Equation 3.5 is obtained because magnetizing coefficient $a_2(\theta)$ is always negative, if the negative sign of $a_2(\theta)$ is factored out, the first term on the right hand side of Equation 3.2 becomes: $a_1(\theta)|a_2(\theta)|e^{-|a_2(\theta)|i}$, which tends to zero as phase current tends to infinity.

The magnetizing coefficients $a_1(\theta)$, $a_2(\theta)$, and $a_3(\theta)$ are calculated based on the magnetization curve shown in Figure 3.2. The data for the magnetization curve can either be obtained through an FEA simulation at a particular rotor position or it can be experimentally gathered by locking the rotor at a particular position. Once the data is obtained, the slope of the curve at lower values of phase current represents the unsaturated phase inductance $L(\theta)$, while the slope of the curve at higher values of phase current represents the saturated phase inductance and is equal to the magnetizing coefficient $a_3(\theta)$. The magnetizing coefficient $a_1(\theta)$ is calculated from the magnetization curve where the flux linkage begins to saturate, i.e., ψ_{sat}, which is obtained by visually inspecting the magnetization curve. Using Equation 3.4 and substituting the expressions for the unsaturated phase inductance $L(\theta)$ and magnetizing coefficients $a_1(\theta)$ and $a_3(\theta)$, the expression for magnetizing coefficient $a_2(\theta)$ is given as:

$$a_2(\theta) = \frac{a_3(\theta) - L(\theta)}{a_1(\theta)} \tag{3.6}$$

Now that the method to determine the magnetizing coefficients at a particular rotor position is established, the data for the next rotor position is obtained and the magnetizing coefficients for the new rotor position are calculated once again (since the magnetizing coefficients are a function of rotor position). The method is executed in an iterative manner until all rotor positions are considered. Doing so, will result in multiple values of the magnetizing coefficients (as shown in Figure 3.3), which can then be curve fit using regression analysis. The authors in [104] suggest using a cosine Fourier series with an appropriate number of Fourier terms to accurately capture the variation of the magnetizing coefficients with respect to rotor position. The Fourier cosine series of the following type is suggested:

$$a_m(\theta) = \sum_{k=0}^{\infty} A_{mk} \cos(kN_r\theta) \tag{3.7}$$

where, a_m represents the m^{th} magnetizing coefficient (and $m = 1, 2, 3$), A_{mk} represents the k^{th} Fourier coefficient of the m^{th} magnetizing coefficient, N_r represents the number of rotor poles of the machine (specifying the periodicity of the Fourier series), and θ represents the rotor position. The units of the magnetizing coefficients are as follows: $a_1(\theta)$ represents the saturated flux value and therefore has a unit of Wb, $a_3(\theta)$ represents the saturated inductance and has a unit of H, lastly $a_2(\theta)$ is obtained from Equation 3.6 and has a unit of $\mathrm{H\,Wb^{-1}}$ or $\mathrm{A^{-1}}$.

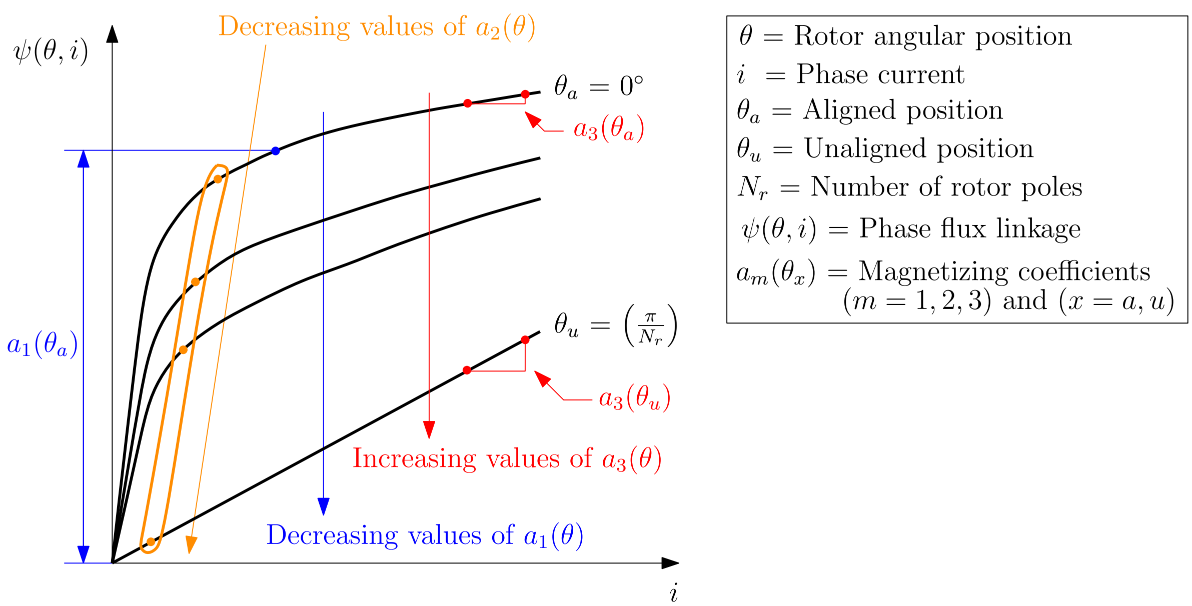

Figure 3.3: Magnetization curves of an SRM at various rotor positions

Flux Based Model Curve Fitting

This section presents the construction of the flux based model based on data gathered from an FEA tool (ANSYS Maxwell [9]) for a switched reluctance machine, specifications of which are listed in Table A.1 in Appendix A. From the multiple magnetization curves (for different rotor positions) shown in Figure 3.3, the variation of magnetizing coefficients $a_1(\theta)$, $a_2(\theta)$, and $a_3(\theta)$ can be examined, as a result, their effect on Equation 3.1 can be better understood. As the rotor rotates from its aligned position (θ_a) to its unaligned position (θ_u), the magnetizing coefficient $a_1(\theta)$ (representing ψ_{sat}) decreases, since the effect of saturation reduces closer to the unaligned position. The magnetizing coefficient $a_2(\theta)$, as stated earlier, is a negative quantity, which also decreases in magnitude as the rotor rotates from its aligned position to its unaligned position. The value of the magnetizing coefficient $a_2(\theta)$ (in accordance with Equation 3.1), defines the shape of the magnetization curve, especially the prominence of the *knee* in the curve. The magnetizing coefficient $a_2(\theta)$ is analogous to the time constant τ_{RC} of an *RC* circuit and the effect it has on the charging voltage curve. Lastly, as the rotor rotates from its aligned position to its unaligned position, magnetizing coefficient $a_3(\theta)$, which represents the slope of the magnetization curves at larger values of phase current, increases. Again, this is because the effects of saturation reduce closer to the unaligned position and the flux linkage between the rotor and stator poles is not restricted by the machine's geometry.

After organizing the data from the FEA tool, the next step involves the application of regression techniques to obtain expressions for the magnetizing coefficients as functions of rotor position. Figure 3.4 shows the variation of magnetizing coefficient $a_1(\theta)$ with respect to rotor position along with the curve fitted function for $a_1(\theta)$. The curve fitted function is obtained using MATLAB's Curve Fitting Toolbox [105]. The function used to curve fit the FEA data for magnetizing coefficient $a_1(\theta)$ is not of the form represented by Equation 3.7, but rather a higher accuracy expression with better root mean square error bounds. The function for $a_1(\theta)$ shown in Figure 3.4 is a Fourier series containing both sine and cosine terms, in which the first two harmonics are considered. The function contains a total of six unknowns and is expressed as:

$$a_1(\theta) = f_0 + f_1 \cos(k\theta) + f_2 \sin(k\theta) + f_3 \cos(2k\theta) + f_4 \sin(2k\theta) \tag{3.8}$$

where, f_x and k are the Fourier coefficients and x is a whole number ranging from: $0 \leq x \leq 4$.

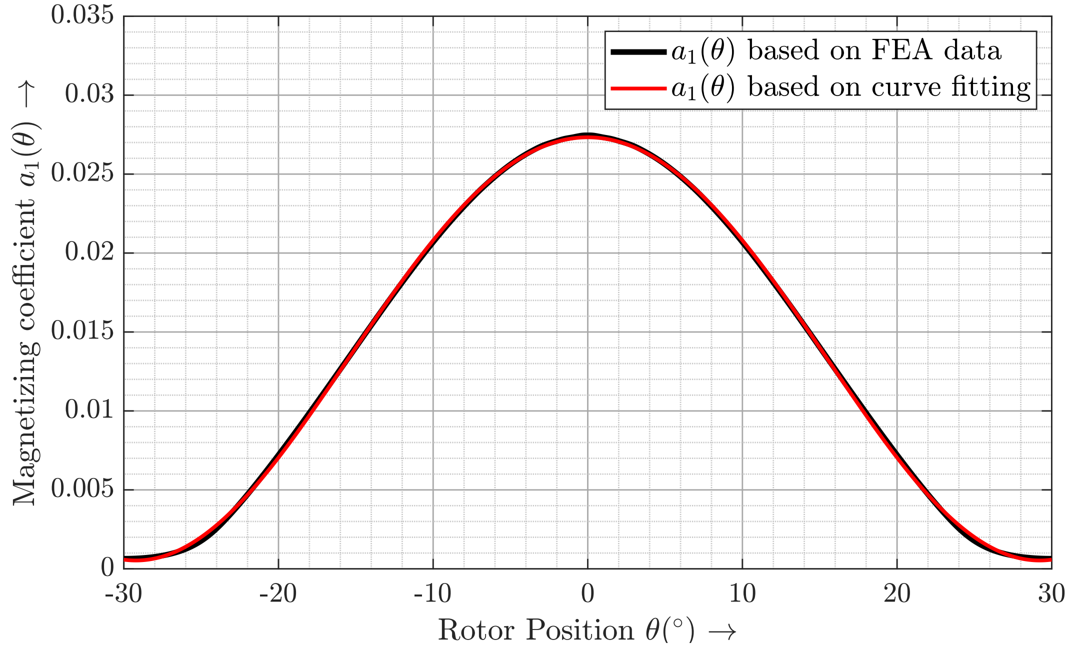

Figure 3.4: Variation of magnetizing coefficient $a_1(\theta)$ with respect to rotor position

Similarly, Figure 3.5 shows the variation of magnetizing coefficient $a_2(\theta)$ with respect to rotor position along with the curve fitted function for $a_2(\theta)$. The curve fitted function is obtained using MATLAB's Curve Fitting Toolbox [105]. Again, the function used to curve fit the FEA data for magnetizing coefficient $a_2(\theta)$ is not of the form represented by Equation 3.7, but rather a higher accuracy expression with better root mean square error bounds. The function for $a_2(\theta)$ used in Figure 3.5 is a Gaussian function with 24 unknowns and expressed as:

$$a_2(\theta) = g_1 e^{-\left(\frac{\theta - h_1}{i_1}\right)^2} + \cdots + g_8 e^{-\left(\frac{\theta - h_8}{i_8}\right)^2} \tag{3.9}$$

where, g_x, h_x, and i_x are the Gaussian regression coefficients and x is a whole number ranging from: $1 \leq x \leq 8$.

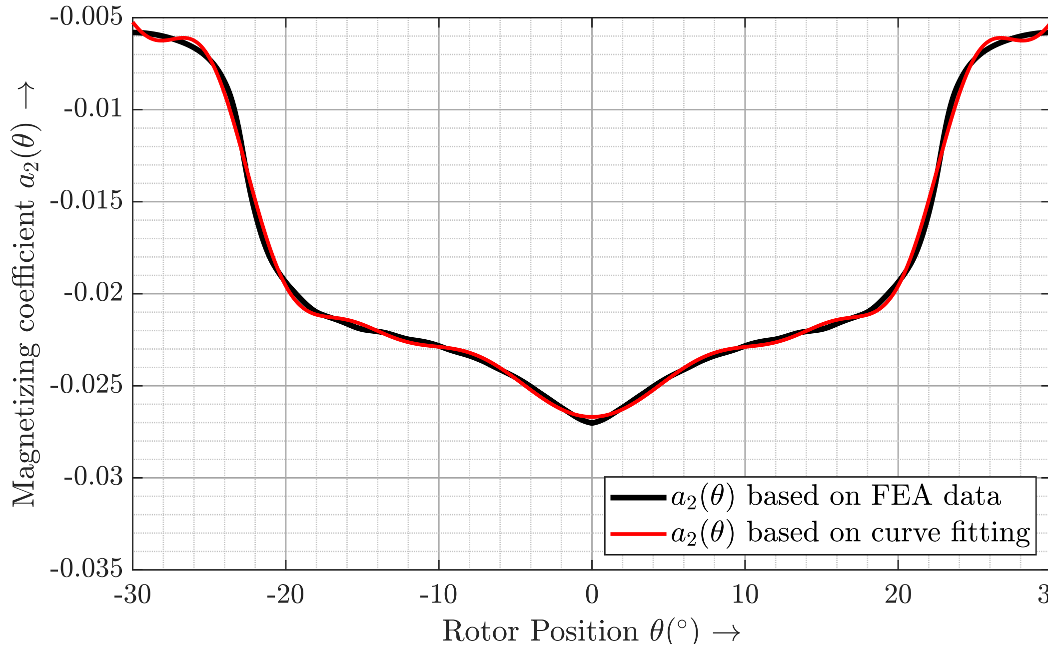

Figure 3.5: Variation of magnetizing coefficient $a_2(\theta)$ with respect to rotor position

Lastly, Figure 3.6 shows the variation of magnetizing coefficient $a_3(\theta)$ with respect to rotor position along with the curve fitted function for $a_3(\theta)$. Once again, the function used to curve fit the FEA data for magnetizing coefficient $a_3(\theta)$ is not of the form represented by Equation 3.7, but rather a higher accuracy expression with better root mean square error bounds. The function for $a_3(\theta)$ shown in Figure 3.6 is a Fourier series containing both sine and cosine terms, in which the first eight harmonics are considered. The function contains a total of 18 unknowns and is expressed as:

$$a_3(\theta) = p_0 + \sum_{x=1}^{8} q_x \cos(xu\theta) + \sum_{x=1}^{8} r_x \sin(xu\theta) \tag{3.10}$$

where, p_0, q_x, r_x, and u are the Fourier coefficients and x is a whole number ranging from: $1 \leq x \leq 8$. Functions with a high number of unknowns are assigned to the magnetizing coefficients to minimize the error between the curve fit and original data. The flux based model

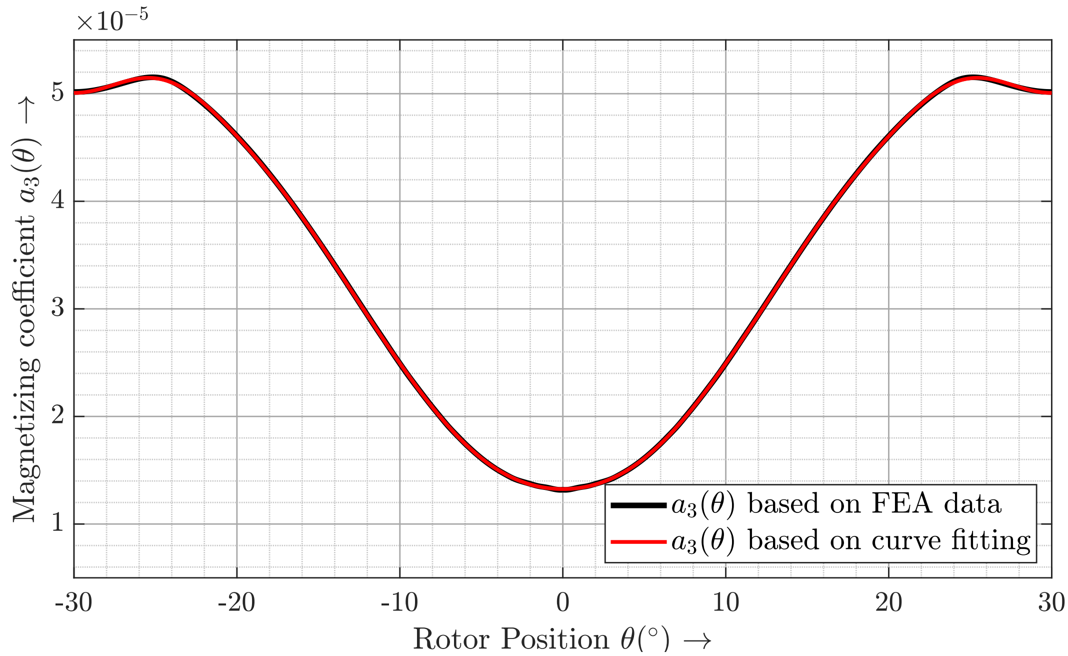

Figure 3.6: Variation of magnetizing coefficient $a_3(\theta)$ with respect to rotor position

is eventually be compared to the proposed model presented in this dissertation. Therefore, to cast away any doubts suggesting that the flux based model is compromised in any way, an overdesigned flux based model is considered. Based on the data gathered from the FEA tool, the behavior and variation of the magnetizing coefficients are consistent with the previous analysis and the description shown in Figure 3.3.

The goal of the flux based model is to reproduce the magnetization curves of a switched reluctance machine. The reconstructed magnetization curves of the switched reluctance machine considered (through the flux based model) are placed over the curves generated from the FEA data and are presented in Figure 3.7. The magnetization curves shown in the figure represent three different rotor positions, i.e., the aligned position, the midpoint position between the aligned and unaligned positions, and lastly the unaligned position. From Figure 3.7, it is observed that the chosen curve fit candidate represented by Equation 3.1 resembles the shape of the magnetization curves constructed using the FEA data; however, there is a difference between the two sets of curves.

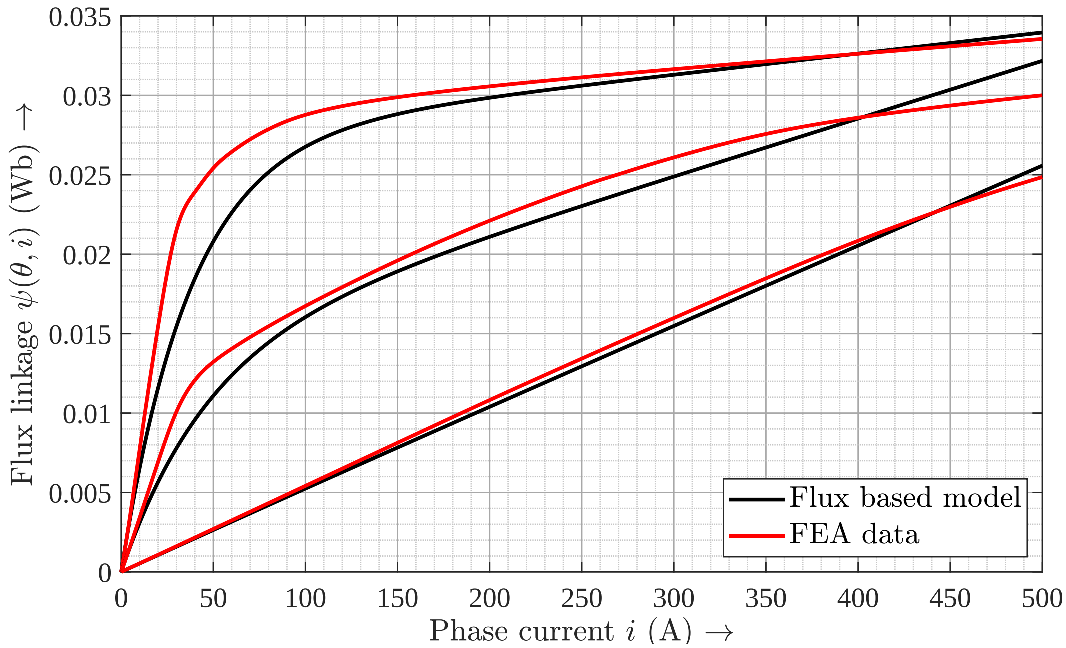

Figure 3.7: Comparison of magnetization curves obtained from the flux based model and the FEA data. The topmost curves are for the aligned position ($\theta = 0°$), the curves in the middle are for the midpoint position between the aligned and unaligned positions ($\theta = 15°$), and the bottommost curves are for the unaligned position ($\theta = 30°$)

The results presented in [11] and [104] show a very close match to the measured data; however, when the same modeling technique is replicated with even higher accuracy functions for the magnetizing coefficients, the results are not as close as the ones presented by the authors. The reason for the difference can be explained by two factors. The first one being the obvious one, a different switched reluctance machine is considered in this dissertation compared to the one presented in [11] and [104]. The shape of the magnetization curves play a very important role in calculating the magnetizing coefficients. The magnetization curves belonging to the machine specified in Table A.1 in Appendix A are more nonlinear (this is evident by inspecting the middle set of curves in Figure 3.7) compared to the ones belonging to the machine considered in [11] and [104]. As a result, a certain degree of error is observed in Figure 3.7. The second factor, which is not apparent at first, is the way the authors originally suggested calculating the magnetizing coefficients. The magnetizing coefficient

$a_2(\theta)$ is what gives the magnetization curve its *knee*, i.e., the orange points in Figure 3.3. However, the expression for magnetizing coefficient $a_2(\theta)$ from Equation 3.6 is derived from the previous equation, i.e., Equation 3.3, in which phase current tends to zero. As a result, $a_2(\theta)$ is unable to effectively capture the behavior of the magnetization curves for higher values of phase current, where saturation becomes prominent. Equation 3.6 clearly indicates that magnetizing coefficient $a_2(\theta)$ is a function of the unsaturated phase inductance $L(\theta)$. Because of the method used to calculate magnetizing coefficient $a_2(\theta)$, a potential flaw in the modeling design flow is uncovered.

Better results are obtained by calculating the magnetizing coefficients using a *brute force* approach involving regression techniques made easily possible by the availability of significant computing resources, especially the advanced toolboxes available in MATLAB [105] and are shown in Figure 3.8. The candidate to model the machine's flux linkage of course remains the same, i.e., represented by Equation 3.1.

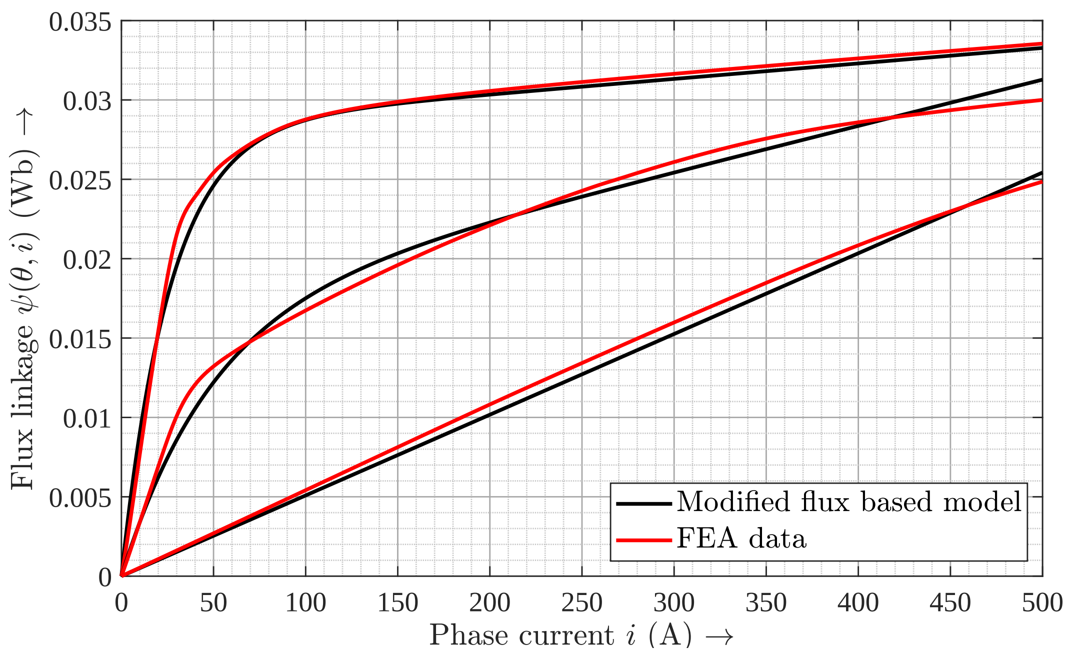

Figure 3.8: Comparison of magnetization curves obtained from the modified flux based model and the FEA data. The topmost curves are for the aligned position ($\theta = 0°$), the curves in the middle are for the midpoint position between the aligned and unaligned positions ($\theta = 15°$), and the bottommost curves are for the unaligned position ($\theta = 30°$)

The coefficients of Equations 3.7, 3.8, 3.9, and 3.10 are listed in Appendix B, and using their values, the magnetization curves for the flux based model shown in Figures 3.7 and 3.8 were created. This concludes the first modeling scheme, i.e., the flux based model. This scheme is helpful in cultivating a deeper understanding of a switched reluctance machine's operation and its modeling approach. It also helps unearth the effects of mathematical approximations in terms the system's accuracy. The data extracted from the FEA tool served as a sandbox wherein further simulations were performed.

So far, the flux based model has been presented, which uses a grey box approach to model the machine's flux linkage. With an expression for phase flux linkage, other parameters such as the instantaneous phase inductance and torque can be obtained using the electrical, magnetic and mechanical knowledge of the machine. For instance, the torque is obtained (in accordance with Equations 2.27 and 2.33) by calculating the rate of change of the co-energy with respect to rotor position using the following expression:

$$T = \frac{\partial}{\partial \theta} \int \psi di \tag{3.11}$$

Many modeling schemes have taken a similar approach and modeled the machine's nonlinear flux linkage using different candidates and regression techniques, resulting in different expressions for flux linkage. Some modeling schemes use piece wise linear segments [106–108], while others use piece wise nonlinear curves [109, 110] to model the machine's flux linkage. Another example models flux linkage using gage curves [111]. Neural networks [112] and artificial intelligence [113] based techniques have also been presented to model the machine's nonlinear flux linkage. The next section discusses another possible modeling scheme, i.e., the inductance based model.

3.1.2 The Inductance Based Model

The second modeling scheme presented is the inductance based model, which was first presented in 1998 by Fahimi et al. [114]. This work modeled the nonlinearities in the inductance profile of a switched reluctance machine. For the remainder of this dissertation, this work will be referred to as the inductance based model. Since the inductance profile of a switched reluctance machine is periodic in nature, it can be approximated using a Fourier series. A function $f(x)$ defined over the range: $-p \leq x \leq p$, belonging to the set of real numbers $\mathbb{R}$, is an even function if: $f(-x) = f(x)$. Such functions can be represented by the cosine Fourier series expressed as:

$$f(x) = \sum_{n=0}^{\infty} f_n \cos\left(\frac{n\pi x}{p}\right) \tag{3.12}$$

where, n is an integer and f_n represents the Fourier coefficients which are evaluated using the following expressions:

$$f_n = \begin{cases} \dfrac{1}{2p}\displaystyle\int_{-p}^{p} f(x)dx & ;\ n = 0 \\ \\ \dfrac{1}{p}\displaystyle\int_{-p}^{p} f(x)\cos\left(\frac{n\pi x}{p}\right)dx & ;\ n \neq 0 \end{cases} \tag{3.13}$$

Due to the geometry of a switched reluctance machine, its phase inductance is an even function, where its periodicity is defined by the rotation of the rotor as it rotates from its unaligned position on one side to its aligned position and then to its other unaligned position on the other side, as depicted by rotor pole R_2 in Figure 2.3. Therefore, the range of the function is defined from: $[-\pi/N_r\ ,\ +\pi/N_r]$. Since the phase inductance satisfies the listed requirements, better known as Dirichlet conditions, it is possible to use a Fourier cosine series to represent it. Changing the notation of Equation 3.12 (i.e., using $p = \pi/N_r$), the following Fourier series representation for the machine's unsaturated phase inductance is obtained:

$$L(\theta) = \sum_{n=0}^{\infty} L_n \cos\left(nN_r\theta\right) \tag{3.14}$$

where, $L(\theta)$ represents unsaturated phase inductance and L_n represents its Fourier coefficients. However, because of saturation, phase inductance is not only a function of rotor position (θ), but also of phase current (i). As a result, the dependency of phase inductance on phase current is introduced in the Fourier coefficients, making the coefficients functions of phase current, i.e., $L_n(i)$. Therefore, the updated expression for saturated phase inductance is expressed as:

$$L(\theta, i) = \sum_{n=0}^{\infty} L_n(i) \cos(nN_r\theta) \tag{3.15}$$

For phase inductance to be represented perfectly by the Fourier cosine series, infinite terms on the right hand side of Equation 3.15 must be considered; however, doing so is futile and impractical. In [114], three Fourier terms are considered (i.e., the average value along with the first two harmonics). Though the truncated series does introduce a certain amount of error into the model, the expressions are more manageable to work with. Figure 3.9 shows the effect of a truncated series while trying to replicate an ideal triangular phase inductance.

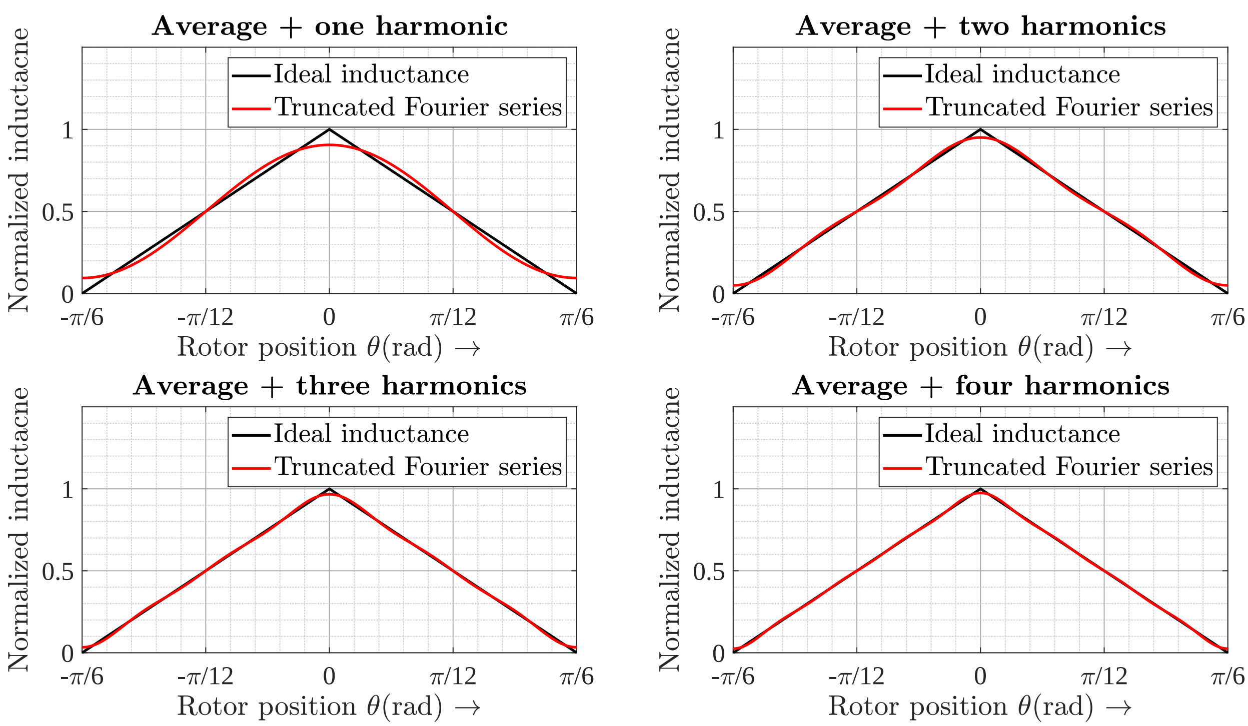

Figure 3.9: Comparison of an ideal phase inductance and a truncated Fourier series. The vertical axis represents a normalized value of phase inductance between 0 and 1. The machine considered has six rotor poles, hence the unaligned positions occur at ($\pm\pi/6$)

From Figure 3.9, it is observed that, while trying to replicate an ideal triangular phase inductance (as depicted by Figure 2.4), a three term truncated Fourier cosine series seems to be adequate without adding unnecessary mathematical overhead. Similarly, the expression for phase inductance of the inductance based model is given as:

$$L(\theta, i) = L_0(i) + L_1(i)\cos(N_r\theta) + L_2(i)\cos(2N_r\theta) \tag{3.16}$$

As stated earlier, due to saturation, the phase current and phase inductance share an inversely proportional relationship (as is evident from Figure 2.11). The interdependence between the phase current and phase inductance is extremely prominent at the aligned position and becomes less significant as the rotor rotates towards the unaligned position. The Fourier cosine series representing the phase inductance, accounts for its dependency on phase current by means of its Fourier coefficients, i.e., $L_n(i)$.

The Fourier coefficients $L_0(i)$, $L_1(i)$, and $L_2(i)$ are calculated based on three data points sampled from the inductance profile of the machine. The three points are the aligned position (at which the inductance is represented by $L_a(i)$), an intermediate position between the aligned position and unaligned positions, preferably the midpoint between the two (at which the inductance is represented by $L_m(i)$), and lastly the unaligned position (at which the inductance ought to be represented by $L_u(i)$). However, since the unaligned position does not suffer from magnetic saturation, the phase inductance at the unaligned position is independent of phase current and is represented by a constant inductance value instead, i.e., L_u. The three points considered are shown in Figure 3.10. The expression for the aligned position phase inductance ($L_a(i)$) is obtained by substituting $\theta = 0$ in Equation 3.16. Similarly, the expressions for midpoint position phase inductance ($L_m(i)$) and unaligned position phase inductance (L_u) are obtained by substituting values of $\theta = \pi/2N_r$ and $\theta = \pi/N_r$ in Equation 3.16, respectively.

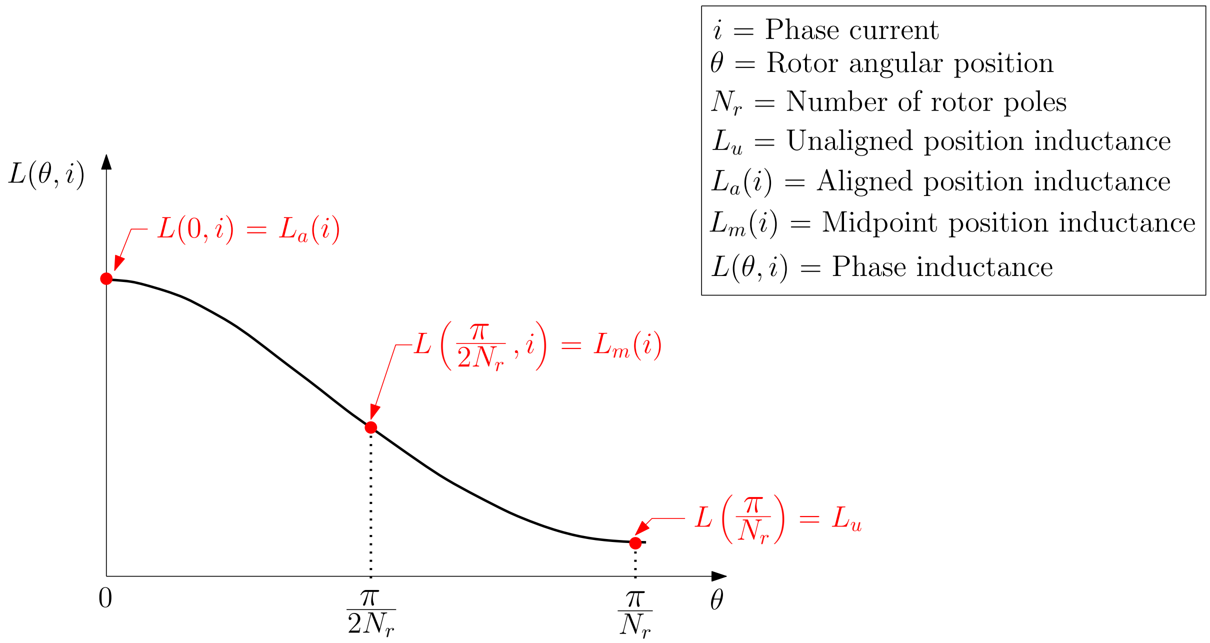

Figure 3.10: Variation of the phase inductance with respect to rotor position at a particular phase current value i

After substituting the values of rotor position (θ) for $L_a(i)$, $L_m(i)$, and L_u in Equation 3.16, the following expressions, forming a system of equations are obtained:

$$L_a(i) = L_0(i) + L_1(i) + L_2(i) \tag{3.17}$$

$$L_m(i) = L_0(i) - L_2(i) \tag{3.18}$$

$$L_u = L_0(i) - L_1(i) + L_2(i) \tag{3.19}$$

Solving the above system of equations for the Fourier coefficients $L_0(i)$, $L_1(i)$, and $L_2(i)$, results in the following expressions:

$$L_0(i) = \frac{1}{2}\left[\frac{1}{2}(L_a(i) + L_u) + L_m(i)\right] \tag{3.20}$$

$$L_1(i) = \frac{1}{2}(L_a(i) - L_u) \tag{3.21}$$

$$L_2(i) = \frac{1}{2}\left[\frac{1}{2}(L_a(i) + L_u) - L_m(i)\right] \tag{3.22}$$

The next step involves defining the functions $L_a(i)$ and $L_m(i)$ in terms of phase current (i). This is performed by collecting all the points corresponding to $L_a(i)$ at different values of phase current, i.e., the red points shown in Figure 3.11.Polynomial regression is applied to fit all the collected red points, resulting in an expression for $L_a(i)$ in terms of phase current is obtained as:

$$L_a(i) = \sum_{n=0}^{k} a_n i^n \tag{3.23}$$

where, a_n represents the polynomial regression coefficients of $L_a(i)$.

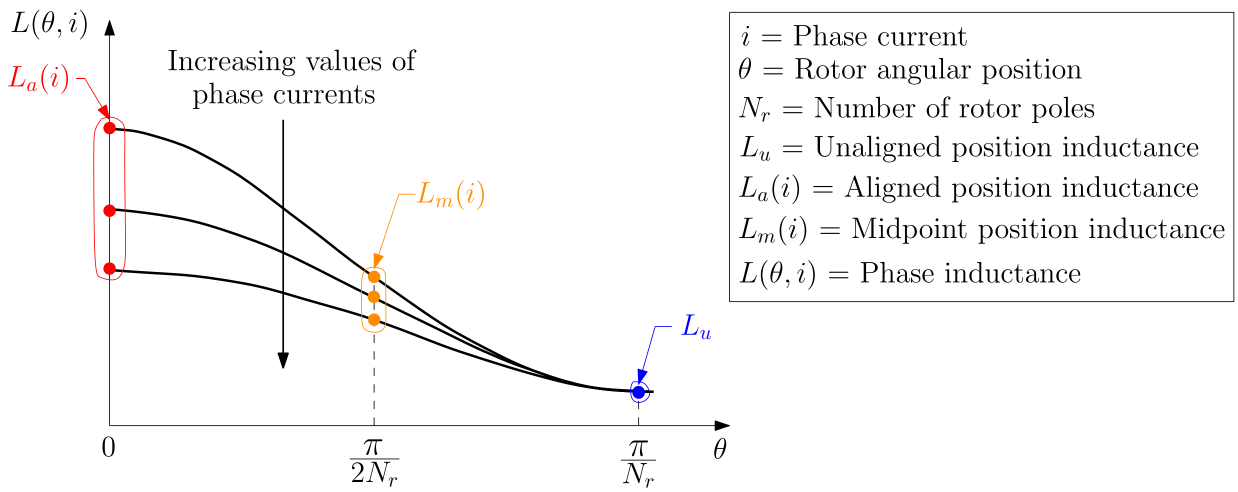

Figure 3.11: Variation of phase inductance with respect to rotor position for different values of phase current

Similarly, by collecting all the points corresponding to $L_m(i)$ at different values of phase current, i.e., the orange points shown in Figure 3.11 and applying polynomial regression to fit the collected points, an expression for $L_m(i)$ in terms of phase is obtained as:

$$L_m(i) = \sum_{n=0}^{k} b_n i^n \tag{3.24}$$

where, b_n represents the polynomial regression coefficients of $L_m(i)$. Observing the collection of points corresponding to the unaligned phase inductance L_u, i.e., the blue points shown in Figure 3.11, it appears that all the points (for different values of phase currents) lie at the same location, which is indicative of the fact that, phase inductance is independent of phase current at the unaligned position and is a constant. The idea remains consistent with earlier analysis and results shown in Figure 2.11.

Figure 3.12 depicts the variation of phase inductance with respect to rotor position. The figure is similar to Figure 3.11 except that, it is constructed using the actual data extracted from the FEA tool based on the machine specifications listed in Table A in Appendix A.

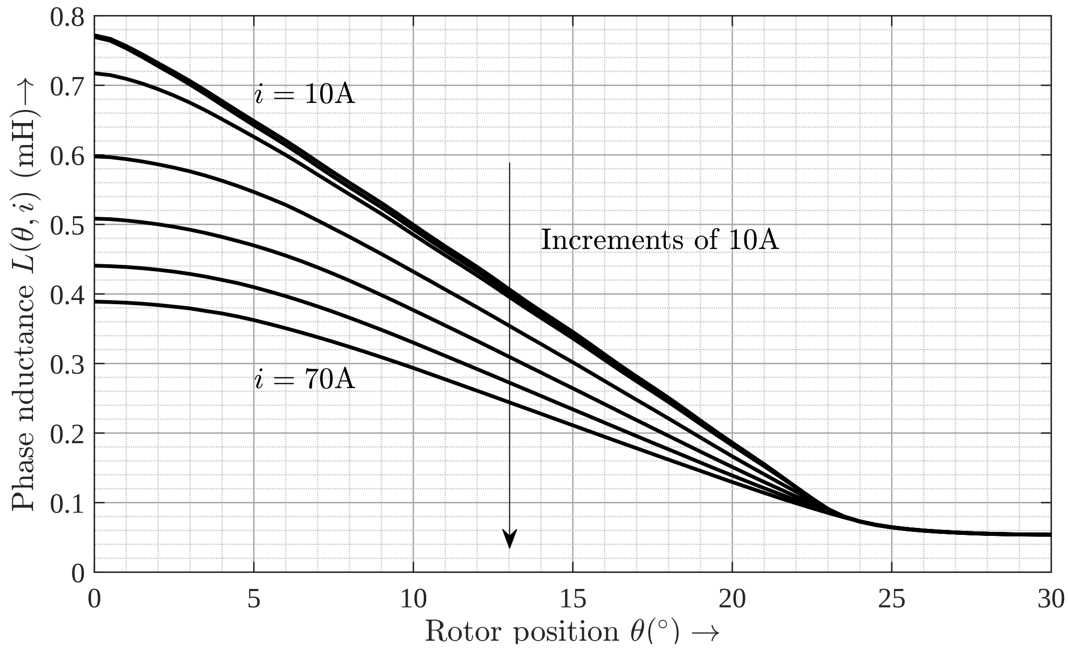

Figure 3.12: Variation of phase inductance with respect to rotor position for different values of phase current. Obtained using ANSYS Maxwell [9]

The aligned position phase inductance ($L_a(i)$) is plotted with respect to phase current and shown in Figure 3.13. A polynomial regression based curve described by Equation 3.23, where k is set to five is also plotted in the figure. Similarly, the midpoint position phase inductance ($L_m(i)$) is plotted with respect to phase current and shown in Figure 3.14. A polynomial regression based curve described by Equation 3.24, where k is set to five is also plotted in the figure. Lastly, the unaligned position phase inductance (L_u) is plotted with respect to phase current and shown in Figure 3.15. Since the unaligned position phase inductance variation is negligible, it is considered as a constant.

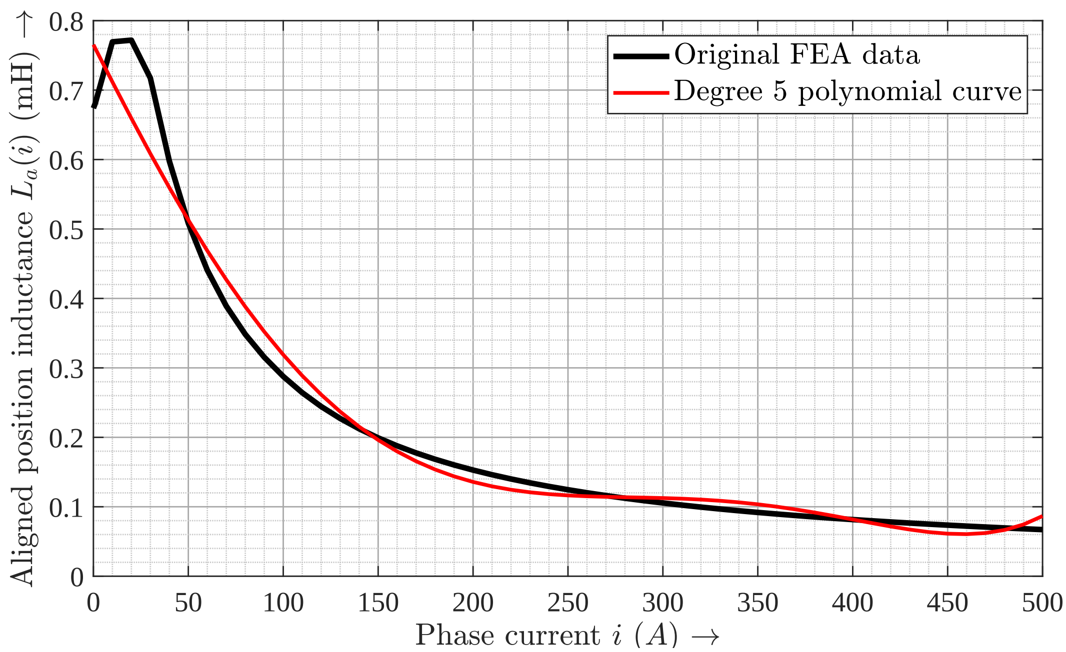

Figure 3.13: Variation of aligned position phase inductance with respect to phase current, i.e., $L_a(i)$. The red curve shows a certain amount of *ripple* at high current values. k of Equation 3.23 is set to 5

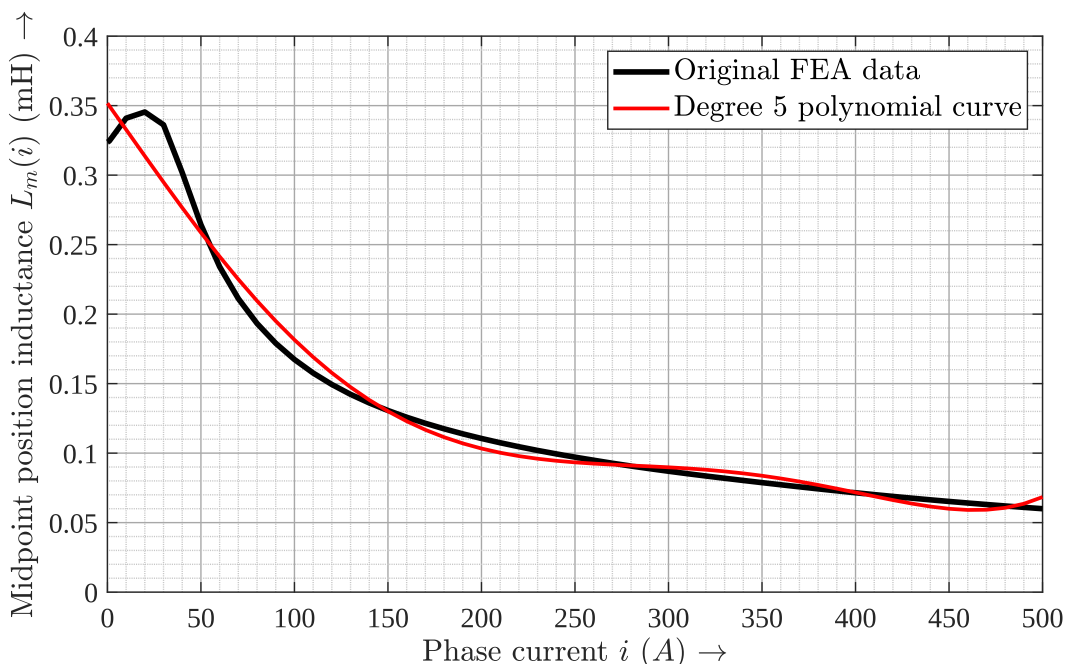

Figure 3.14: Variation of midpoint position phase inductance with respect to phase current, i.e., $L_m(i)$. The red curve shows a certain amount of *ripple* at high current values. k of Equation 3.24 is set to 5

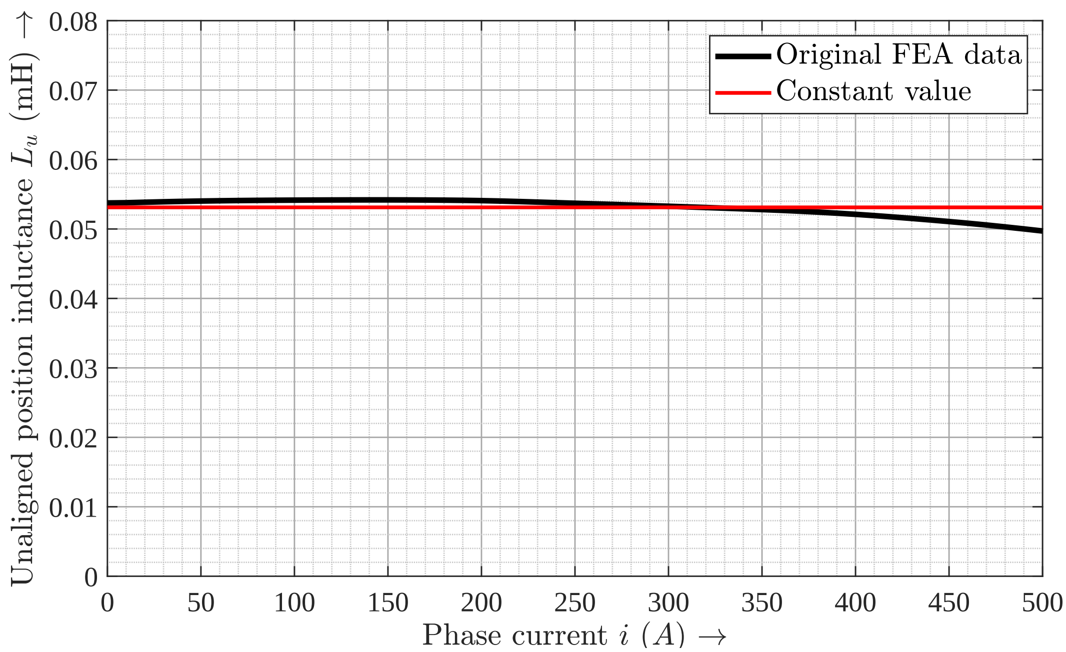

Figure 3.15: Variation of unaligned position phase inductance with respect to phase current. The red curve represents a constant value, i.e., $L_u = constant$

The coefficients a_n and b_n from Equations 3.23 and 3.24, respectively are listed in Appendix B, and using their values, the machine's magnetization curves using the inductance based model along with the magnetization curves obtained from the FEA tool are shown in Figure 3.16. In Figure 3.16, there is a considerable amount of deviation between the curves obtained from the inductance based model (depicted in red) and the curves obtained from the FEA data (depicted in black). The *ripple* observed in the magnetization curves of the inductance based model, at the aligned and midpoint rotor positions, is due to ripple in functions $L_a(i)$ and $L_m(i)$ as shown in Figures 3.13 and 3.14, respectively. Just as $L_a(i)$ and $L_m(i)$ exhibit ripple at high values of phase current, so do the magnetization curves, at high values of phase current as well (since the error propagates throughout the model). The *ripple* in the modeled magnetization curves can be overcome by considering a higher value of k in Equations 3.23 and 3.24, using $k = 10$, the results are presented in Figures 3.17, 3.18, and 3.19.

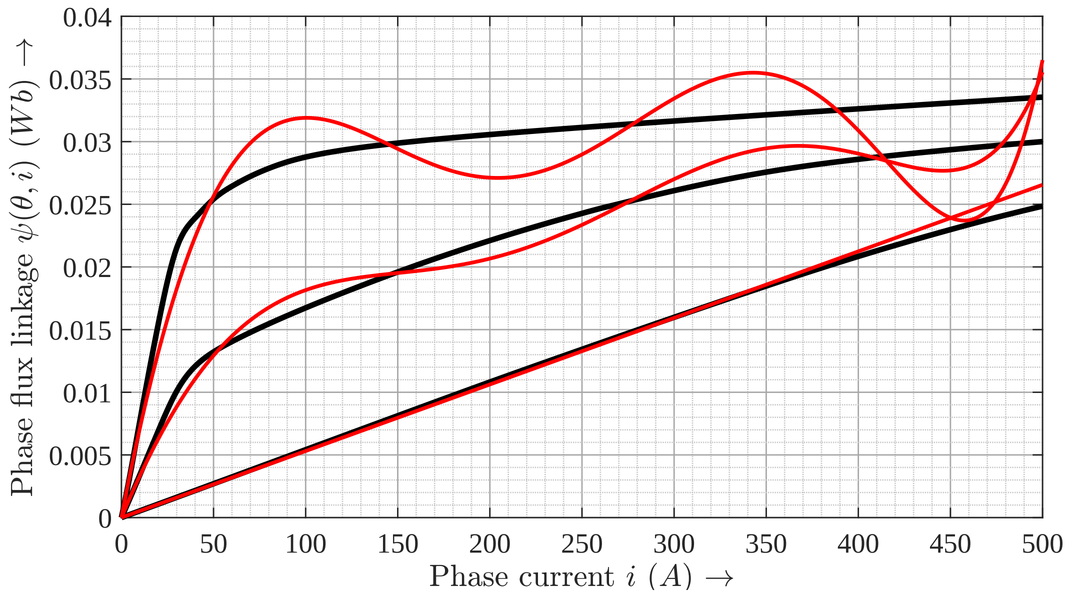

Figure 3.16: Comparison of magnetization curves obtained from the inductance based model (depicted in red) and the FEA data (depicted in black). The topmost curves are for the aligned position ($\theta = 0°$), the curves in the middle are for the midpoint position between the aligned and unaligned positions ($\theta = 15°$), and the bottommost curves are for the unaligned position ($\theta = 30°$). k of Equations 3.23 and 3.24 is set to 5

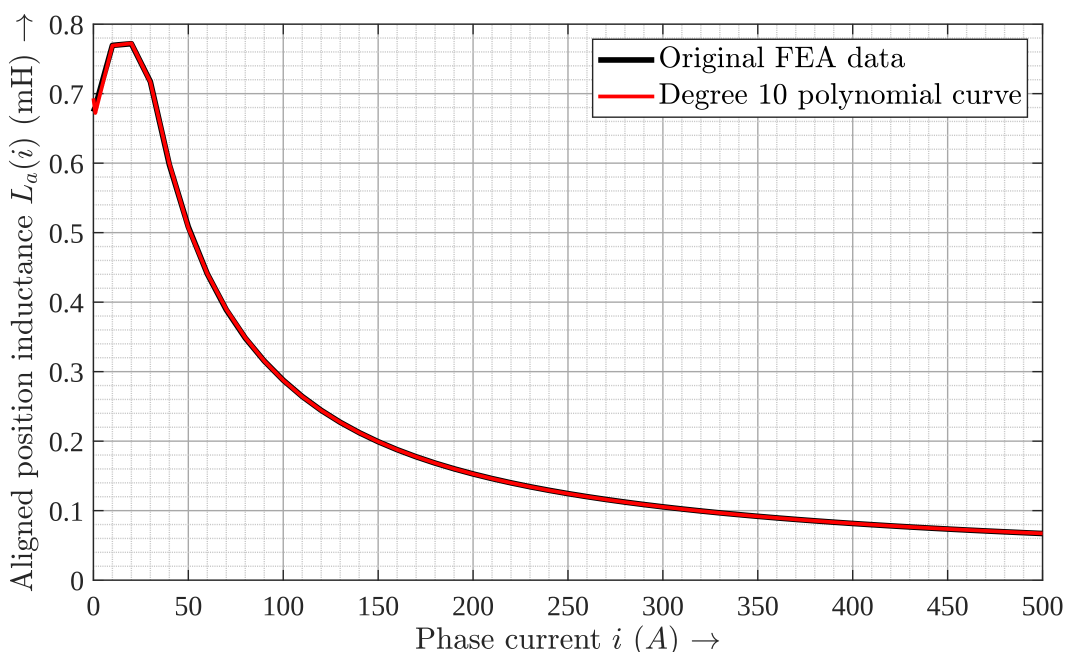

Figure 3.17: Variation of aligned position phase inductance with respect to phase current, i.e., $L_a(i)$. The red curve closely matches the FEA data. k of Equation 3.23 is set to 10

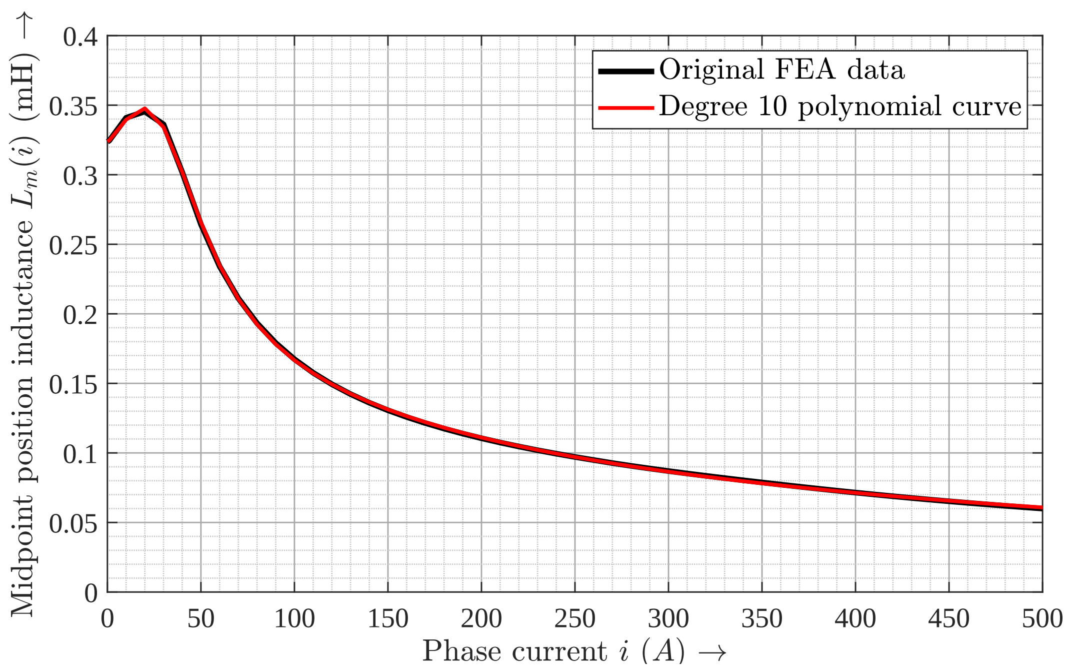

Figure 3.18: Variation of midpoint position phase inductance with respect to phase current, i.e., $L_m(i)$. The red curve closely matches the FEA data. k of Equation 3.24 is set to 10

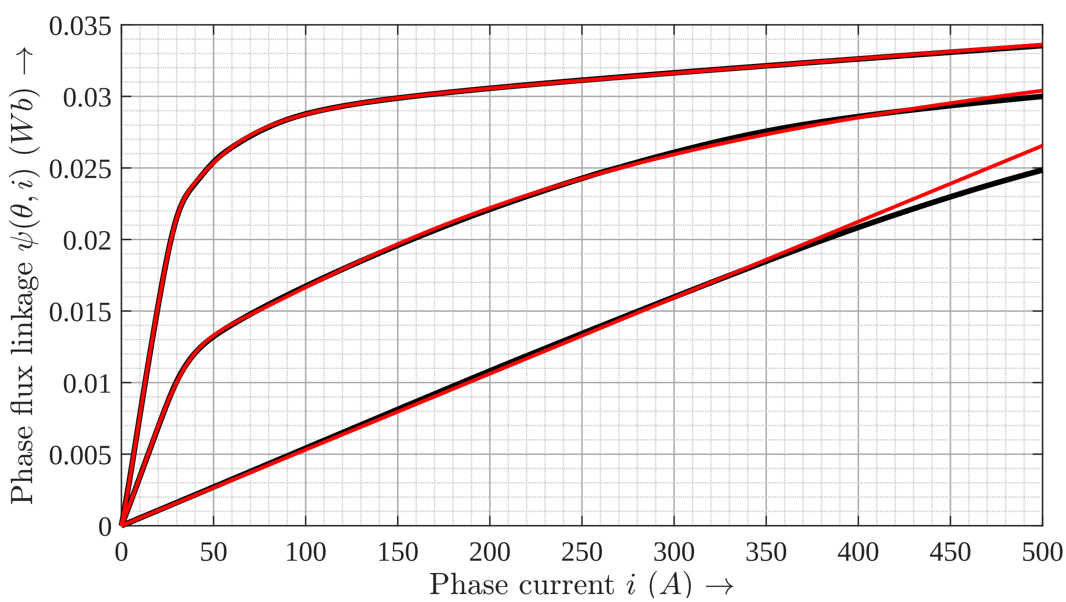

Figure 3.19: Comparison of magnetization curves obtained from the inductance based model (depicted in red) and the FEA data (depicted in black). The topmost curves are for the aligned position ($\theta = 0°$), the curves in the middle are for the midpoint position between the aligned and unaligned positions ($\theta = 15°$), and the bottommost curves are for the unaligned position ($\theta = 30°$). k of Equations 3.23 and 3.24 is set to 10

It is worth noting that the power rating of the machine designed in ANSYS Maxwell [9] (specified in Table A.1 in Appendix A) is around 2.3 kW and its rated voltage is around 48 V, implying that the current rating is close to 50 A. However, the figures shown in this section, model the machine for phase current values of upto 500 A. By doing so, most of the modeling error (i.e., ripple) occurs at current values greater than 50 A. By adopting such an approach, it is possible to push the modeling error way beyond the operating region of the machine, thus maintaining an error free model at the lower phase current values, where the machine is likely to operate. Based on the 50 A current rating, the inductance based model shown in Figure 3.16 is acceptable as there is not much deviation between the modeled and FEA curves upto 50 A.

Clearly, increasing the mathematical complexity results in better curve matching. However, it is upto the designer to tackle the problem from a practical engineering standpoint rather than from a mathematical standpoint. There is more leeway when machine dynamics and operating regions are introduced into the modeling and design process. The inductance based model is accompanied by its own sets of limitations as it uses two approximations, the first one being the use of a truncated Fourier cosine series to represent the machine's phase inductance and the second one being the use of polynomial regression to introduce the phase current dependency in the Fourier coefficients (this is similar to a *Taylor series expansion* of a function). Once again, when the grey box method of system identification is complete and the model is constructed, other parameters such as torque can be calculated in the same way as expressed in earlier sections. The torque of a machine is calculated using co-energy relations, similar to the one described by Equation 3.11 or by using Equation 2.38. Another example using the Fourier series approach to model phase inductance of a switched reluctance machine is also presented in [115]. This concludes the analysis on the inductance based modeling scheme. The results of both the flux and inductance based modeling schemes [11, 104, 114] are fairly accurate, as seen in Figures 3.8 and 3.19, respectively and are well recognized and widely used.

3.2 Limitations of the Existing Modeling Schemes

The flux based model and the inductance based model provide a high level of insight into the modeling process of a switched reluctance machine. Using either the flux linkage expression from Equation 3.1 or the phase inductance expression from Equation 3.16, a designer is free to proceed in computing other parameters of the machine. The goal of this dissertation is to effectively obtain a method to reconstruct the phase current in the phase windings of the machine. Finding a solution to the current differential equation of a switched reluctance machine is a daunting task, the equation is highly nonlinear and there is a strong interdependency between the instantaneous inductance and the instantaneous phase current. This interdependency exists due to the effect of saturation of flux linkage in the machine. The solution to the current differential equation can have various expressions depending on the way the machine is modeled. An age old trade-off is once again encountered between the accuracy of the modeling scheme and the mathematical complexities of the expressions used. Since two modeling schemes with different flavors have been presented so far, it would only be right to consider them as the starting point in reconstructing the phase current before presenting the proposed scheme. The next section attempts to reconstruct the phase current of a switched reluctance machine using the flux based model.

3.2.1 Limitation of the Flux Based Model

While considering the flux based model, the analysis begins with the expression for the machine's flux linkage, i.e., Equation 3.1, which is rewritten as:

$$\psi(\theta, i) = a_1(\theta)(1 - e^{a_2(\theta)i}) + a_3(\theta)i \tag{3.25}$$

where, the magnetizing coefficients are expressed by Equation 3.7 and are rewritten as:

$$a_m(\theta) = \sum_{k=0}^{\infty} A_{mk}\cos(kN_r\theta) \tag{3.26}$$

The authors of [104] suggest using nine Fourier coefficients (i.e., A_{m0} to A_{m8}). However, to exhibit the complexity of this approach, even considering just two Fourier terms (i.e., A_{m0} and A_{m1}) is sufficient. The magnetizing coefficients $a_1(\theta)$, $a_2(\theta)$ and $a_3(\theta)$ with two unknowns are expressed as:

$$a_1(\theta) = A_{10} + A_{11}\cos(N_r\theta) \tag{3.27}$$

$$a_2(\theta) = A_{20} + A_{21}\cos(N_r\theta) \tag{3.28}$$

$$a_3(\theta) = A_{30} + A_{31}\cos(N_r\theta) \tag{3.29}$$

Using the expressions for magnetizing coefficients $a_1(\theta)$, $a_2(\theta)$, and $a_3(\theta)$ in Equation 3.25, the machine's flux linkage is expressed as:

$$\psi(\theta, i) = [A_{10} + A_{11}\cos(N_r\theta)][1 - e^{(A_{20}+A_{21}\cos(N_r\theta))i}] + [A_{30} + A_{31}\cos(N_r\theta)]i \tag{3.30}$$

To obtain an expression for phase current, a solution to Equation 2.16 or Equation 2.17 must be obtained. Since Equation 2.17 contains the derivative of phase inductance with respect to rotor position, the first step involves computing the value of phase inductance ($L(\theta, i)$) and its derivative with respect to rotor position $dL(\theta, i)/d\theta$. Using the expression from Equation 3.30, the machine's phase inductance is obtained though the nonlinear relationship (i.e., including saturation) among flux linkage, phase current, and phase inductance, which is expressed as:

$$\begin{aligned}
L(\theta, i) &= \frac{d\psi}{di} \\
&= -a_1(\theta)a_2(\theta)e^{a_2(\theta)i} + a_3(\theta) \\
&= -[A_{10} + A_{11}\cos(N_r\theta)][A_{20} + A_{21}\cos(N_r\theta)]e^{[A_{20}+A_{21}\cos(N_r\theta)]i} + [A_{30} + A_{31}\cos(N_r\theta)]
\end{aligned} \tag{3.31}$$

Substituting the expression for phase inductance from Equation 3.31 in Equation 2.17, the current differential equation is expressed as:

$$\frac{di}{d\theta} = \frac{V - \omega i \dfrac{d}{d\theta}\left\{\begin{array}{r} -[A_{10} + A_{11}\cos(N_r\theta)][A_{20} + A_{21}\cos(N_r\theta)]e^{[A_{20}+A_{21}\cos(N_r\theta)]i} + \\ [A_{30} + A_{31}\cos(N_r\theta)] \end{array}\right\}}{-\omega[A_{10} + A_{11}\cos(N_r\theta)][A_{20} + A_{21}\cos(N_r\theta)]e^{[A_{20}+A_{21}\cos(N_r\theta)]i} + [A_{30} + A_{31}\cos(N_r\theta)]} \tag{3.32}$$

Based on Equation 3.32, it is extremely improbable that a closed form analytical expression for the phase current exists, as that would require integrating Equation 3.32 with respect to rotor position, which seems like an extremely daunting task. Unfortunately, the mathematical complexity of Equation 3.32 does not allow for any further analysis in obtaining an analytical closed form expression for the phase current using the flux based modeling scheme. As a result, the research is focused in another direction. The next section discusses the inductance based modeling scheme and its limitations in obtaining a closed form analytical expression for phase current.

3.2.2 Limitation of the Inductance Based Model

Considering the inductance based model (i.e., using the expression for phase inductance from Equation 3.16 in Equation 2.17), a switched reluctance machine's current differential equation is expressed as:

$$\frac{di}{d\theta} = \frac{V - \omega i \dfrac{d}{d\theta}\left[L_0(i) + L_1(i)\cos(N_r\theta) + L_2(i)\cos(2N_r\theta)\right]}{\omega[L_0(i) + L_1(i)\cos(N_r\theta) + L_2(i)\cos(2N_r\theta)]} \tag{3.33}$$

Furthermore, considering the polynomial expressions of degree five, for $L_a(i)$ and $L_m(i)$ from Equations 3.23 and 3.24, respectively, the following expressions are obtained:

$$L_a(i) = \sum_{n=0}^{5} a_n i^n = a_0 + a_1 i + a_2 i^2 + a_3 i^3 + a_4 i^4 + a_5 i^5 \tag{3.34}$$

$$L_m(i) = \sum_{n=0}^{5} b_n i^n = b_0 + b_1 i + b_2 i^2 + b_3 i^3 + b_4 i^4 + b_5 i^5 \tag{3.35}$$

Substituting the values of $L_a(i)$ and $L_m(i)$, and using the constant value of L_u in Equation 3.33, yields an extremely unwieldy expression. The set of equations listed above are an indication of the complexities that present themselves in the phase current differential equation of a switched reluctance machine. Once again, based on complexities involved in Equation 3.33, it is extremely improbable that a closed form analytical expression for the phase current exists. The current differential equations described by Equations 3.32 and 3.33 are quite complex. At this stage, in nonlinear system analysis, the next step would be to check the stability of the system and obtain some meaningful information. However, due to the electrical and mechanical knowledge of the machine, this information is already known. During the motoring mode of operation, the current can always be controlled (i.e., increased or decreased) by applying a positive, zero or negative voltage across the terminals of the phase windings. While in the generation mode of operation, under the condition when the phase voltage is less than the established back emf, the machine's phase current enters into a state of positive feedback and it can no longer be controlled. Such a scenario would be catastrophic from a nonlinear control point of view.

Since the analysis of the flux based and inductance based models do not lead to a closed form analytical solution for the phase current, the available options are to either consider a different modeling scheme for the machine or to make some meaningful compromises and approximations which yield a fruitful result. Before exploring either option, mathematics offers a solution to tackle extremely complex differential equations through *Numerical methods of integration*, which are presented next.

3.3 Numerical Methods of Integration

Nonlinear differential equations, such as Equations 3.32 and 3.33 do not necessarily have to have solutions in the first place, even if they do, the probability of finding their solutions can be close to zero. It was best put by Hungarian mathematician George Pólya, who stated that *"In order to solve this differential equation you look at it until a solution occurs to you"* [116]. As a result, spending significant amounts of time and resources may not be the best practice. As one begins to delve deeper into the world of nonlinear differential equations, just finding out whether a solution exists is a challenge in itself. Once the existence of a solution is known, actually finding the solution requires a lot more effort. Typically, a nonlinear system is analyzed for stability and as long as the stability of the system is verified, i.e., once it is known that the system is free from positive feedback, there is no explicit need to find the system's solution (as an appropriate control scheme will be capable of regulating the system). On the other hand, in systems containing positive feedback, the local stability is analyzed, i.e., whether the system is stable in and around a certain operating point. In the case of a switched reluctance generator, there are two scenarios in which the generator does not exhibit positive feedback; however, there is one scenario in which the machine exhibit positive feedback and also happens to provide the best returns.

Problems like analyzing nonlinear differential equations for stability, and also finding their solution have existed for an extremely long time. A brief look into the history [117] and evolution of differential equations provides a new found respect and appreciation towards the techniques used to find their solutions. In 1666, a twenty four year old Isaac Newton, after having pushed the bounds of calculus and discovering the laws of optics and universal gravitation, decided to explain the planetary orbits. At the time, astronomer Johannes Kepler had already improved the work of Nicolaus Copernicus and had observed the elliptical orbits of the planets in the solar system. However, Newton explained the planetary orbits using calculus, universal gravitation and his three laws of motion. He had, at that stage solved the *two body problem* which dealt with a single planet traveling in its orbit due to the gravitational pull of the sun (ignoring all other surrounding bodies present in the universe). He then wanted to extend his theory to include another planetary body, giving rise to the *three body problem* (Newton called it the *problem of the moon*) and scale the theory to accommodate more variables, i.e., the *n body problem*. However, the two body problem left Newton perplexed and for hundreds of years, the problem remained unsolved. Till the late 1800's there was no update on the three body problem in spite of efforts from Swiss mathematician Leonhard Euler and German mathematician Johann Carl Friedrich Gauss. It was finally explained by French mathematician Jules Henri Poincarè that the three body problem was in fact, unsolvable. Poincarè geometrically proved that it was not possible to obtain a closed form analytical expression to the *three body problem*. Through his work, where he used geometry and visualization techniques rather than mathematical equations, Poincarè encountered what is presently referred to as *chaos*. Chaos is a phenomenon that occurs in deterministic systems, i.e., systems that are governed by strict rules without any stochastic phenomenon associated with them. Deterministic systems are systems, where the present state determines the next state of the system; however, their behavior only seems to be nonrepetitive and unpredictable, i.e., their behavior is hard to predict. Deterministic systems also have a sensitive dependence on initial conditions, which means that small errors get amplified extremely quickly, making long term predictions impossible, though short term predictions are still possible as long as the errors are within reason. A lot of similarities can be made to a switched reluctance machine as well. A switched reluctance machine is a deterministic system in which the next state of the phase current depends on its present state, as a result, predictions are hard to make. However, the close inter dependencies between numerous variables, seemingly make the behavior of the machine appear chaotic.

When solutions to complex differential equations cannot be discovered, then one is forced to adopt numerical methods of integration to predict the behavior of the differential equation's solution. Numerous methods of numerical integration have been extensively presented in the past, of which a few of them are listed below [118] and are briefly explained:

- Euler's method (or, the method of tangent lines)
- Taylor's method
- The Runge-Kutta method
- Adams-Bashforth/Adams-Moulton method

3.3.1 Euler's Method

The simplest technique to approximate the solution to a differential equation is by using Euler's method. The Euler method is briefly explained in this section. Consider the following differential equation:

$$\frac{dy}{dx} = y' = f(x, y) \tag{3.36}$$

with the following initial condition:

$$y(x_0) = y_0 \tag{3.37}$$

Consider h to be a defined interval of x, as shown in Figure 3.20, such that $(x_1, y_1) = (x_0+h, y_1)$. If the first point on the actual solution is known, i.e., the initial condition (x_0, y_0), then using the slope of the line tangent to the point (x_0, y_0), the behavior of the solution $y = f(x)$ can be predicted. The slope of the tangent is easily obtained by substituting the values of $x = x_0$ and $y = y_0$ in Equation 3.36, resulting in the following expression:

$$\left.\frac{dy}{dx}\right|_{(x_0,y_0)} = y_0' = f(x_0, y_0) = slope \tag{3.38}$$

Next, using the point slope form of the tangent, the value of y_1 is computed as:

$$slope = \frac{y_1 - y_0}{x_1 - x_0} \tag{3.39}$$

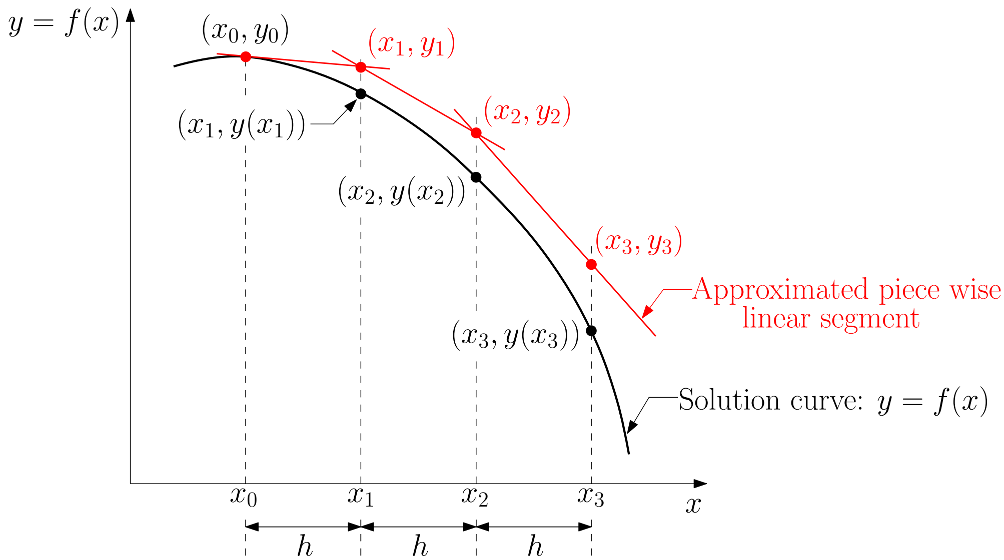

Figure 3.20: Curve $y = f(x)$ along with its approximated piece wise linear segments computed using Euler's method

Using the value of *slope* from Equation 3.38 in Equation 3.39, the following expression is obtained:

$$y'_0 = \frac{y_1 - y_0}{(x_0 + h) - x_0} \tag{3.40}$$

Rearranging Equation 3.40, the following expression is obtained:

$$y_1 = y_0 + hy'_0 \tag{3.41}$$

Therefore, the coordinate y_1 is known and is approximately equal to the value of the solution curve at x_1, i.e., $y = f(x_1)$ or $y(x_1)$. The approximation $\Delta y|_{x_1} = [y(x_1) - y_1] \to 0$ as $h \to 0$. A *reasonably small* value of h will result in $y_1 \approx y(x_1)$. Using the information of (x_1, y_1), the next approximate value, i.e., y_2 is computed in a similar manner. The iterative process is carried out till the desired value of x_n is reached and its corresponding y_n is computed. The actual deviation between the solution $y = f(x)$ and the approximated values could become significant if h is too large. From Figure 3.20, it is clear that $\Delta y|_{x_3} > \Delta y|_{x_2} > \Delta y|_{x_1}$. In general, the expression for the next value of the function is defined as:

$$\begin{aligned} y_{n+1} &= y_n + hf(x_n, y_n) \\ &= y_n + hy'_n \end{aligned} \tag{3.42}$$

where, y_{n+1} is the next value of the function definition and y_n is the present value of the function definition. Using the Euler method, reconstruction of a switched reluctance machine's phase current is presented next. With the knowledge of the reconstructed phase current ahead of time, predictive control over the machine can be applied. Using a variation of Equation 2.15, the current differential equation of a switched reluctance machine is expressed as:

$$V_{bus} = iR + L\frac{di}{dt} + \omega i\frac{dL}{d\theta} \tag{3.43}$$

Rearranging Equation 3.43 and changing L to $L(\theta, i)$, the following expression is obtained:

$$\frac{di}{dt} = \frac{1}{L(\theta, i)}\left[V_{bus} - iR - \omega i\frac{dL(\theta, i)}{d\theta}\right] \tag{3.44}$$

Using i'_n to represent the time derivative of the phase current at $\theta = \theta_n$ and $i = i_n$, the following expression is obtained:

$$i'_n = \frac{1}{L(\theta_n, i_n)}\left[V_{bus} - i_nR - \omega i_n\frac{dL(\theta_n, i_n)}{d\theta}\right] \tag{3.45}$$

By replacing y by i, and h by T_s in Equation 3.42, the following expression is obtained:

$$i_{n+1} = i_n + T_s i'_n \tag{3.46}$$

Substituting the value of i'_n from Equation 3.45 in Equation 3.46, results in the following expression:

$$i_{n+1} = i_n + \frac{T_s}{L(\theta_n, i_n)}\left[V_{bus} - i_nR - \omega i_n\frac{dL(\theta_n, i_n)}{d\theta}\right] \tag{3.47}$$

It is worth noting that the rotor position is changed from θ to θ_n, because rotor position directly relates to time (t) through the relation for angular velocity, i.e., $\omega = d\theta/dt$, and time is equivalent to x in the Euler method example. Replacing $\omega/d\theta$ of Equation 3.47 by $1/dt$, the following expression is obtained:

$$i_{n+1} = i_n + \frac{T_s}{L(\theta_n, i_n)} \left[V_{bus} - i_n R - i_n \frac{dL(\theta_n, i_n)}{dt} \right] \tag{3.48}$$

The time derivative of phase inductance is also represented as:

$$\frac{dL(\theta_n, i_n)}{dt} = \frac{L(\theta_n, i_n) - L(\theta_{n-1}, i_{n-1})}{T_s} \tag{3.49}$$

Substituting the expression for the derivative of phase inductance from Equation 3.49 in Equation 3.48, the following result is obtained:

$$i_{n+1} = i_n + \frac{T_s}{L(\theta_n, i_n)} \left\{ V_{bus} - i_n R - i_n \left[\frac{L(\theta_n, i_n) - L(\theta_{n-1}, i_{n-1})}{T_s} \right] \right\} \tag{3.50}$$

The value of phase inductance $L(\theta, i)$ in Equation 3.50 can be computed either using Equation 3.2 or Equation 3.16. Therefore, phase current can be predicted accurately enough, provided the value of T_s is reasonably small.

Using the Euler method, the first thing that comes to mind is the intense computation required to map the phase current trajectory when trying to determine its value a few time steps into the future, i.e., at some instance kT_s in the future. This is of significant importance, especially during the generating mode of operation in positive feedback, during which the magnitude of phase voltage (V) is lesser than the magnitude of the established back EMF (e) at the turn-off angle, due to which the phase current continues to increase after the phase is switched off. Consider Figure 3.21, in which the phase current is plotted with respect to time and assume that an observer observes its value at time instance nT_s, at which the phase current value corresponds to the value at point A. Also assume, it is desired to predict the phase current value four time instances into the future at time instance $(n + 4)T_s$ (i.e., a general time instance in the future denoted as kT_s).

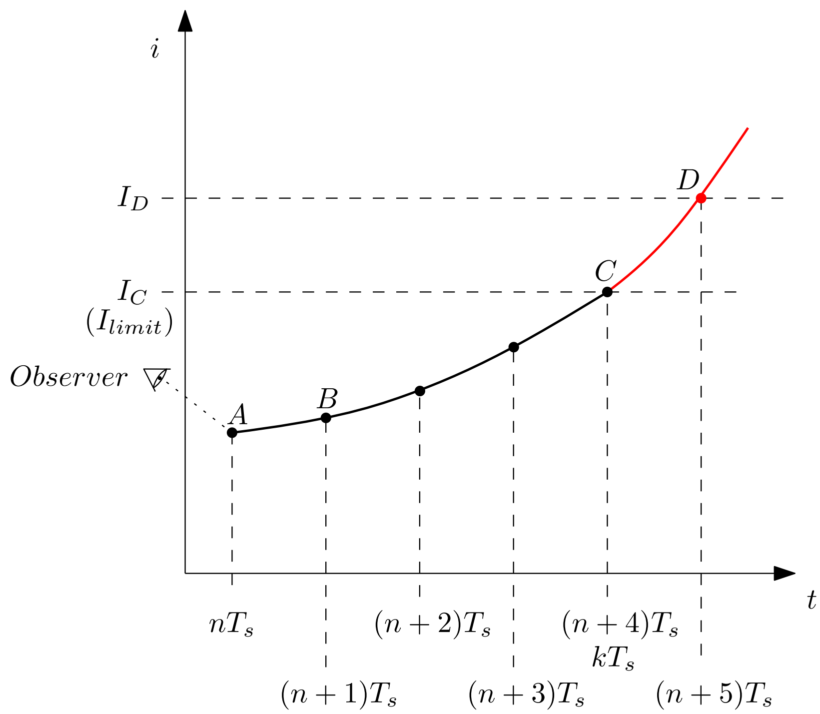

Figure 3.21: Predicting generating phase current of a switched reluctance machine

In an ideal world with infinite computing resources and no time delays, it can be assumed that after using the Euler method with initial conditions corresponding to point A, the predicted phase current four time instances in the future corresponding to the value at point C (I_C) is known at time instance nT_s. Assume that I_C is also the current limit of the system, i.e., I_{limit}.

However, in reality, such a computation takes a certain amount of time, i.e., a computational delay. Exaggerating the computational delay for the purpose of analysis, assume that the computation of the Euler method completes only at time instance $(n+1)T_s$. Due to the elapsed computational delay, the observer moves to time instance $(n+1)T_s$, still predicting I_{limit} as the phase current value four time instances in the future. However, there is a change in the initial conditions to the Euler method, i.e., from the values corresponding to point A to the values corresponding to point B. As a result, instead of predicting the value of phase current corresponding to point C (I_{limit}), its value needs to be updated to the value corresponding to point D (I_D), as that is the value of phase current four time instances in the future (from $(n+1)T_s$). As a result, due to the computational delay, the actual value of phase current (I_D) can exceed the current limit of the system (I_{limit}). Practically, due to the computational delay, the Euler method is unable to account for the change in the initial conditions, resulting in an underestimated value for the predicted phase current. The flaw however, by no means, can be attributed towards the Euler method of numerical integration. In order to minimize the error while predicting the value of phase current, it is imperative to perform the calculations as quickly as possible, which can be achieved by selecting fewer steps in the Euler method, i.e, by increasing the sampling time (T_s). However, by increasing the sampling time, the error inherent to the Euler method increases. As a result, increasing or decreasing the sampling time, both lead to an increase in the error while predicting the phase current (i.e., reducing the sampling time increases the accuracy of the Euler method but increases the computational delay and prediction error, on the other hand, increasing the sampling time reduces the accuracy of the Euler method, thereby increasing the prediction error).

The scenario presented using Figure 3.21, does not address whether or not the phase current starts decreasing at time instance kT_s when the phase is switched off at instance nT_s, as the predicted value reaches the threshold value I_{limit} at time instance kT_s. It just sheds light on the effects of computational delays while using numerical methods of integration.

The explanation for other numerical methods of integration is similar to the Euler method and does not lie within the scope of this dissertation. The idea behind all the methods remains the same, i.e., to obtain the solution to a differential equation by iterative numerical steps. The major concern in adopting such a scheme into real time control, lies in the computational delay and its effects on the result (due to the change in the initial conditions). Practically, the time steps should be reduced in order to speed up the calculations; however, theoretically the time steps must be increased for better accuracy. They all suffer from the same inherent issues, namely:

- Iterative processes
- Trade-off between the number of steps (smaller h) and the accuracy (smaller Δy)
- Requirement of high computing resources
- Time consuming

However, for the sake of completeness, the expressions for other numerical methods of integration are listed below.

3.3.2 Taylor's method

$$y_{n+1} = y_n + hy'_n + y''_n \frac{h^2}{2} \tag{3.51}$$

where, y''_n is the second derivative of y_n and is calculated by differentiating $y' = f(x, y)$.

3.3.3 The Runge-Kutta method

$$y_{n+1} = y_n + \frac{1}{6}(k_1 + 2k_2 + 2k_3 + k_4) \tag{3.52}$$

where,

$$k_1 = hf(x_n, y_n) \tag{3.53}$$

$$k_2 = hf\left(x_n + \frac{1}{2}h, y_n + \frac{1}{2}k_1\right) \tag{3.54}$$

$$k_3 = hf\left(x_n + \frac{1}{2}h, y_n + \frac{1}{2}k_2\right) \tag{3.55}$$

$$k_4 = hf(x_n + h, y_n + k_3) \tag{3.56}$$

This method comes with a high degree of accuracy but suffers from significant computational overhead as k_2 depends on k_1, k_3 depends on k_2 and k_4 depends on k_3, implying that the calculations must all be made in a sequential manner rather than simultaneously, because of which, the computational time of the model adds up.

3.3.4 Adams-Bashforth/Adams-Moulton method

This method is a two step method in which, first the *Adams-Bashforth* formula is applied, which is then followed by the *Adams-Moulton* formula. The Adams-Bashforth formula is expressed as:

$$y_{n+1}^{*} = y_n + \frac{h}{24}(55y_n' - 59y_{n-1}' + 37y_{n-2}' - 9y_{n-3}') \tag{3.57}$$

where,

$$y_n' = f(x_n, y_n) \tag{3.58}$$

$$y_{n-1}' = f(x_{n-1}, y_{n-1}) \tag{3.59}$$

$$y_{n-2}' = f(x_{n-2}, y_{n-2}) \tag{3.60}$$

$$y_{n-3}' = f(x_{n-3}, y_{n-3}) \tag{3.61}$$

For values of $n \geq 3$, the second formula is applied, i.e., the Adams-Moulton formula, which is expressed as:

$$y_{n+1} = y_n + \frac{h}{24}(9y_{n+1}' + 19y_n' - 5y_{n-1}' + y_{n-2}') \tag{3.62}$$

where,

$$y_{n+1}' = f(x_{n+1}, y_{n+1}^{*}) \tag{3.63}$$

In summary, it is clear that the modeling schemes (either the flux based or inductance based modeling) result in extremely complex nonlinear expressions. Directly working with such expressions (i.e., Equation 3.32 and Equation 3.33) did not prove to be fruitful for the purpose of reconstructing the phase current in a switched reluctance drive. Therefore, the focus shifted towards numerical methods of integration [52, 53, 119]. However, while using the numerical methods of integration, computational delays factor in, and pose a significant challenge. This challenge could be overcome by just *waiting it out*, as it is inevitable that the control cards and digital signal processors will eventually become fast enough to be able to handle the computations within a satisfactory amount of time. The theory developed and presented so far is absolutely sound, but would benefit further if it were supported by an elegant one step solution in determining the phase current value rather than an iterative one. In a nutshell, the complexities of a switched reluctance machine are encapsulated by the three dimensional plot shown in Figure 3.22, which represents the variation of phase inductance with respect to rotor position and phase current. The individual curves representing the

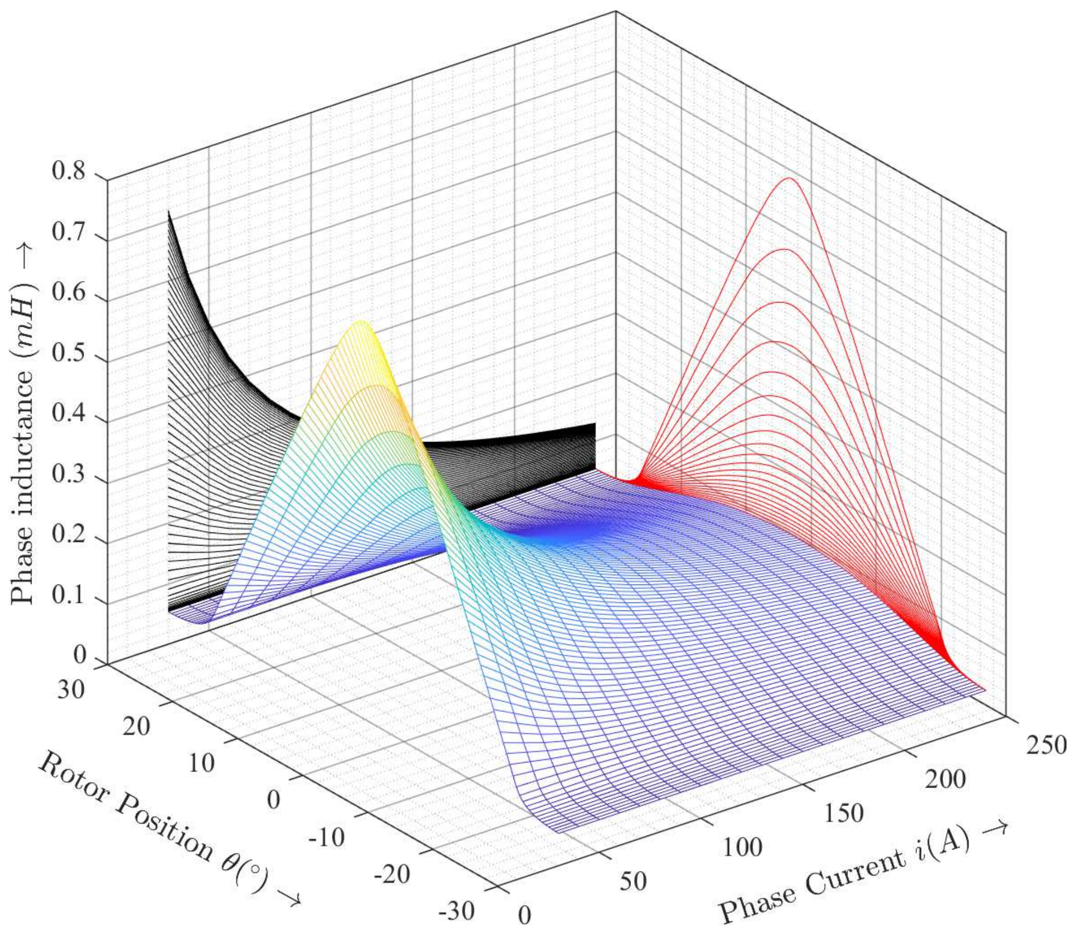

Figure 3.22: Variation of phase inductance $L(\theta, i)$ with respect to rotor position θ and phase current i

variation of phase inductance with respect to phase current are projected onto the plane on the left (curves shown in black). These curves are similar to the ones shown in Figures 3.13, 3.14, and 3.15. Similarly, the individual curves representing the variation of phase inductance with respect to rotor position are projected onto the plane on the right (curves shown in red). These curves are similar to the ones shown in Figure 3.12.

3.4 Proposed Modeling Scheme

Obtaining a closed form analytical solution for phase current, using the work presented in [11, 104, 114] is near impossible. Using the next available option, i.e., numerical methods of integration, obtaining the phase current trajectory is an iterative process and resource intensive. However, with a few reasonable approximations and trade-offs, a closed form analytical solution for phase current can be obtained. To do so, one of the parameters of a switched reluctance machine must be modeled, after which other parameters can be derived from the original one, i.e., using the grey box approach of system identification.

3.4.1 Premise for the Proposed Modeling Scheme

The work presented in this section models phase inductance in the absence of saturation using a simpler describing expression. Even though the effects of saturation are not included, a nonlinear function representing phase inductance is still considered, encapsulating the essential dynamics and behavior of the machine. The reasons for excluding saturation in the modeling of phase inductance are carefully analyzed and are three fold (especially while the machine is operated in its generating mode, where positive feedback is prevalent):

- The operating region of the machine
- The effect of permeability
- Frequency scaling and phase shifting of the inductance profile

Next, the three reasons for excluding saturation are presented, beginning with the operating region of the machine.

The Operating Region of the Machine

This section presents the typical operating region of a switched reluctance machine. As shown in Figure 3.23, a switched reluctance machine's flux linkage experiences saturation when its rotor is at the aligned position ($\theta = 0$) and when phase current is high.

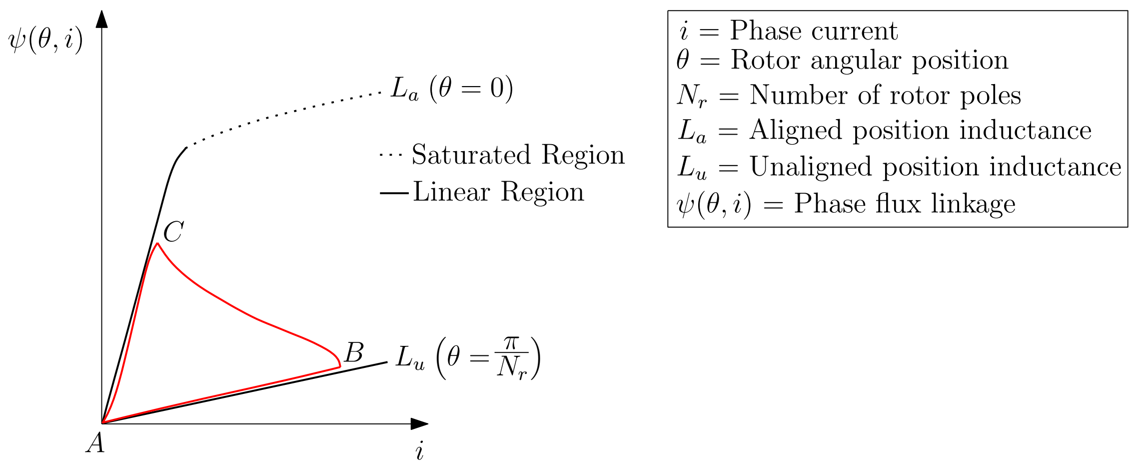

Figure 3.23: Plot of phase flux linkage $\psi(\theta, i)$ with respect to phase current i of a typical SRM. The machine operates along loop $ACBA$ during generation and along loop $ABCA$ during high-speed motoring. The locus remains in the linear region

At the aligned position, saturation occurs because the reluctance of the flux path is minimum, thereby, causing the flux lines to saturate through the rotor and stator poles. However, as shown in Figure 3.24, the machine is not operated at high current levels at the aligned position. During the motoring mode of operation, the phase current must be reduced to zero at the aligned position or else the tailing phase current produces undesirable negative torque. Similarly, during the generating mode of operation, the phase current is made to increase (by applying a positive phase voltage) during the region where the slope of phase inductance is negative. This implies that the phase current increases after the aligned

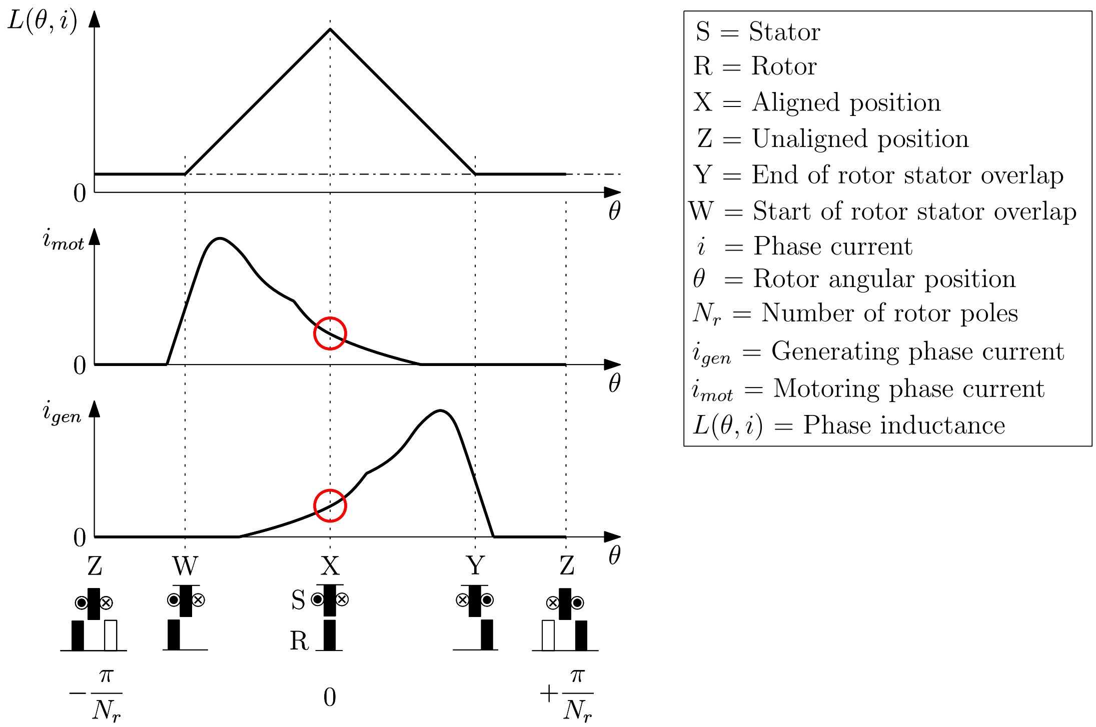

Figure 3.24: Nature of the phase current during motoring and generating. The encircled region shows low values of current. Adapted from [12], © 2002 IEEE

position. During generation, techniques such as *phase advancing* [62] may also be employed, wherein the phase current is allowed to reach a certain value at the aligned position (this is achieved by applying a positive phase voltage during the region where the slope of the phase inductance is positive). Phase advancing is achieved by switching on the machine's phase before the rotor pole aligns itself with the stator pole. By employing phase advancing, the phase current is at a non-zero value at the aligned position, which gives rise to a different set of initial conditions for the current trajectory. A non-zero value of phase current at the aligned position is helpful during generation as it allows the phase current to reach a higher value during the generating cycle, as a result, higher charge and output power is generated. However, the value of phase current is still relatively small (i.e., within the linear region of Figure 3.23) when compared to its maximum value during the generating cycle. Due to the zero or small values of phase current at the aligned position, a fair assumption is made to exclude the effects of saturation in the proposed model.

Since the analysis of the machine is carried out from an *engineering* standpoint rather than a from a *mathematical* standpoint (i.e., on the basis of the operating region of the machine), the effects of saturation are intentionally excluded, thereby easing up the mathematical complexities. Therefore, the phase inductance of a switched reluctance machine is modeled using a Fourier cosine series which is *not* a function of phase current as discussed in [114]. For the sake of simplicity, while deriving the analytical expression for phase current using the expression of the modeled phase inductance, only one cosine term for the phase inductance is considered and is shown in Figure 3.25. However, the analytical expression using an entire Fourier cosine series is also provided.

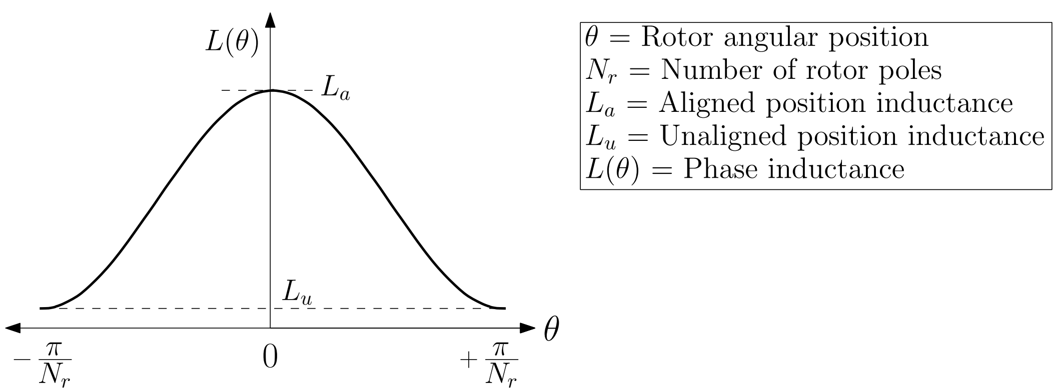

Figure 3.25: Phase inductance profile of an SRM using a single cosine term

Considering only one cosine term describing the phase inductance profile (as shown in Figure 3.25), the equation for phase inductance is expressed as:

$$L(\theta) = \left(\frac{L_a + L_u}{2}\right) + \left(\frac{L_a - L_u}{2}\right)\cos(N_r\theta) \tag{3.64}$$

where, L_a represents the phase inductance value at the aligned position, L_u represents the phase inductance value at the unaligned position, and N_r represents the number of rotor poles. Intuitively, the term: $(L_a + L_u)/2$ of Equation 3.64 represents the vertical offset of the cosine function shown in Figure 3.25 and the term: $(L_a - L_u)/2$ represents the peak to peak amplitude of the cosine function shown in Figure 3.25. Equation 3.64 represents the average value plus the first cosine term (i.e., the first harmonic) of a Fourier cosine series. The average value is represented by the expression:

$$L_0 = \frac{L_a + L_u}{2} \tag{3.65}$$

Similarly, the peak to peak amplitude of the phase inductance is represented as:

$$L_1 = \frac{L_a - L_u}{2} \tag{3.66}$$

The derivation details for coefficients L_0 and L_1 are provided in Appendix D. The phase inductance in Equation 3.64 can also be expressed in its Fourier representation, as:

$$L(\theta) = L_0 + L_1 \cos(N_r\theta) \tag{3.67}$$

The phase inductance in Equation 3.67 may also include a frequency scaling and/or a phase shift term as desired, to closely match the linear region phase inductance of a machine. The exclusion of saturation in the modeled phase inductance is analyzed from the standpoint of permeability and presented next.

The Effect of Permeability

This section presents the effect of permeability on the variation of phase inductance with respect to phase current. Consider the BH curve for an arbitrary inductor shown in Figure 3.26, in which magnetic flux density B relates to magnetic field intensity H through the following expression:

$$B = \mu H \tag{3.68}$$

where, μ is the permeability of the material and represents the slope of the curve shown in Figure 3.26. Three regions with different values of magnetic permeability are highlighted in

Figure 3.26. As magnetic field intensity (H) increases, the material's permeability begins with a medium value μ_1, then reaches its maximum value μ_2, before finally reaching its minimum value μ_3.

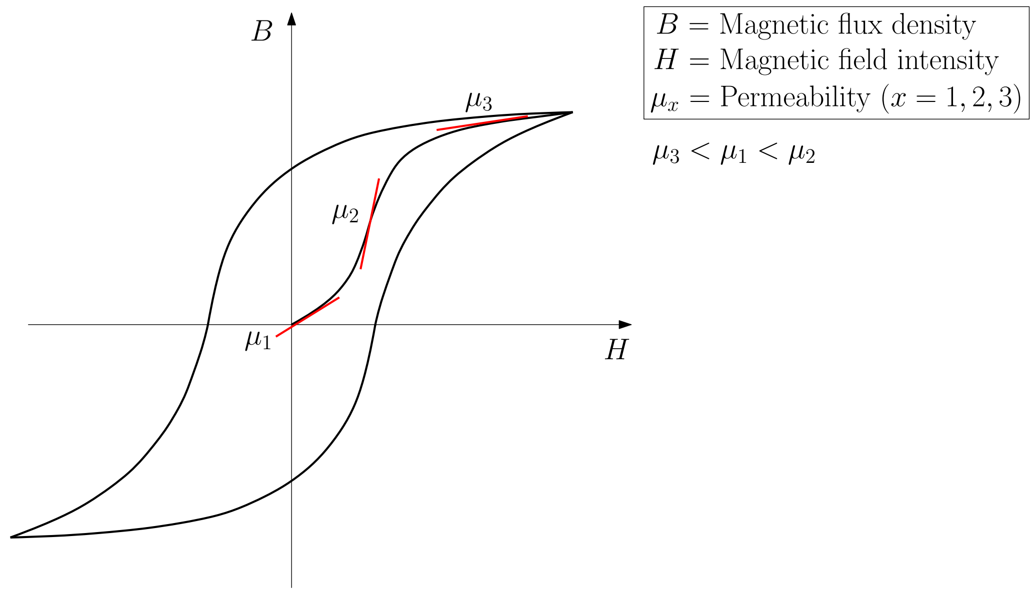

Figure 3.26: BH curve highlighting different values of material permeability

The reluctance $\Re$ of an inductor is expressed as:

$$\Re = \frac{l}{\mu A} \tag{3.69}$$

where, l represents the length of an inductor and A represents its cross sectional area. From Equation 3.69, it is observed that the reluctance of an inductor is inversely proportional to the permeability of the material. On the other hand, the inductance is inversely proportional to the reluctance, as a result, the inductance is directly proportional to the permeability of the material:

$$L \propto \mu \tag{3.70}$$

Also, the magnetic field intensity (H) is directly proportional to current (i):

$$H \propto i \tag{3.71}$$

Since $L \propto \mu$ and $H \propto i$, the plot for inductance versus current is generated, and using the properties presented, the curve starts off at a medium value (corresponding to μ_1), then reach its maximum value (corresponding to μ_2), before finally reaching its minimum value (corresponding to μ_3). The effect of this phenomenon using Equation 3.70 is shown in Figure 3.27.

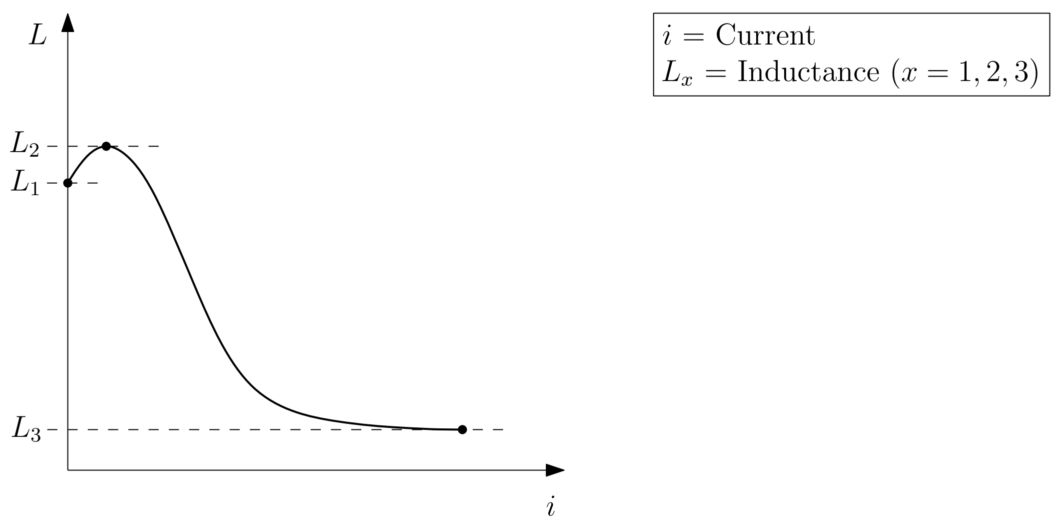

Figure 3.27: Variation of inductance with current

The same phenomenon is applicable to a switched reluctance machine as well and also explains the shape of the curves in Figures 3.17 and 3.18 (i.e., the initial *bump* in the curves). In the case of a switched reluctance machine, as the rotor rotates from its aligned position to its unaligned position, different phase inductance variations with the phase current are observed (for example, Figure 3.17 depicts the phase inductance at the aligned position, while Figure 3.18 depicts the phase inductance at the midpoint position). Stacking up a few of the phase inductance curves for positions close to each other around the aligned position are shown in Figure 3.28. As phase current increases and rotor position changes, the shape of the inductance profile (described by the red points in the figure) begins to resemble a cosine function (when the argument of the cosine function is close to zero). It is worth noting that the red points represent the variation of phase inductance with rotor position for increasing values of phase current.

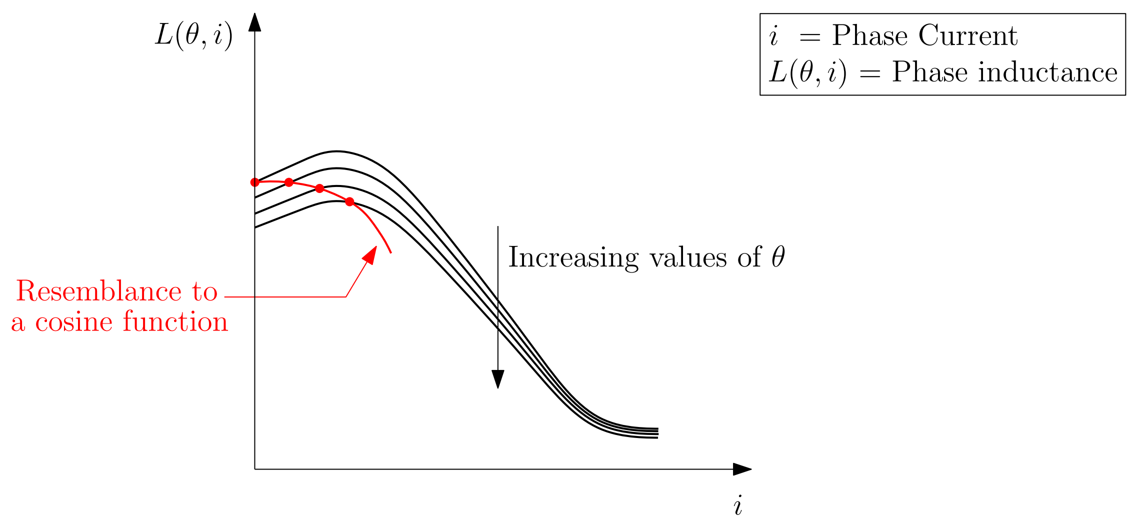

Figure 3.28: Variation of phase inductance with increasing phase current for different values of rotor position

Similarly, Figure 3.29 shows a few more of the phase inductance curves for rotor positions closer to the unaligned position. During generation, when the phase is switched off and the current begins to drop, the variation of phase inductance with rotor position is shown by the blue dots in Figure 3.29. The phase inductance resembles a *somewhat* linear profile. Collecting all the red and blue dots from Figures 3.28 and 3.29 and plotting them against rotor position (rather than phase current) results in the plot shown in Figure 3.30, which resembles a frequency scaled version of a cosine function.

As a result, the effect of permeability (i.e., the initial bump shown in Figure 3.27) reinforces the design choice of selecting Equation 3.67 with the inclusion of a frequency scaling term as the inductance profile of a switched reluctance generator, especially because of its resemblance to the cosine function when the argument of the cosine function is close to and around zero.

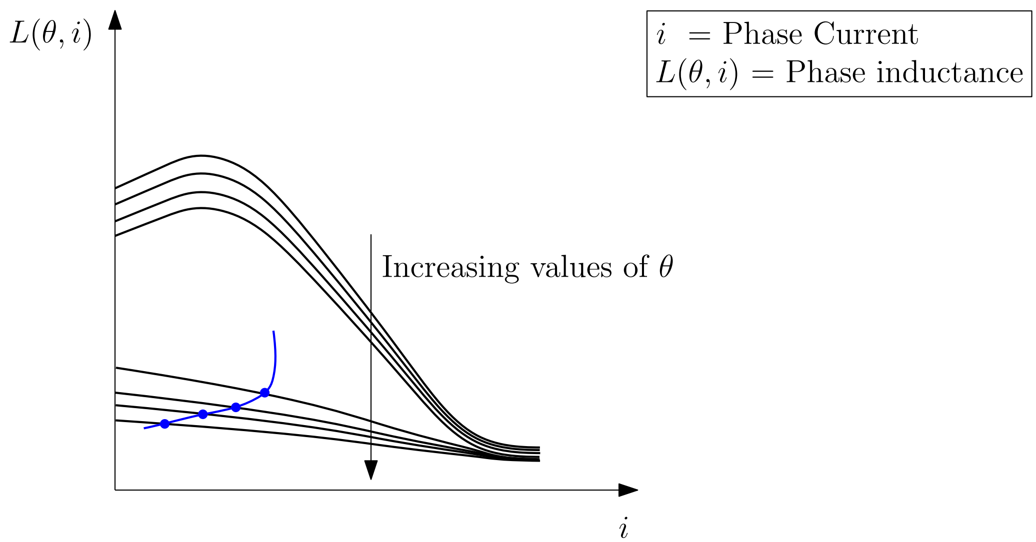

Figure 3.29: Variation of phase inductance with decreasing phase current for different values of rotor position

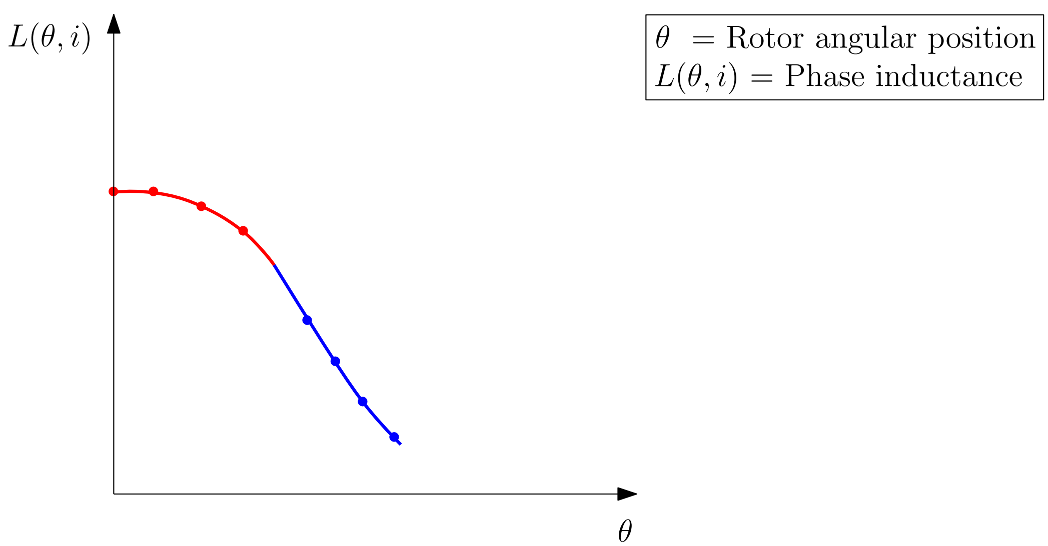

Figure 3.30: Variation of phase inductance with rotor position (exaggerated for effect)

Frequency Scaling and Phase Shifting of the Inductance Profile

This section introduces a frequency scaling term κ and a phase shift term ϕ, which when included in the inductance profile described by Equation 3.67, provides an added option of fine tuning the inductance profile to match the selected machine. One way to increase the resemblance between the modeled inductance profile and the actual machine data is by increasing the number of Fourier terms; however, that comes at the expense of increased mathematical complexity which is an undesirable side effect. On the other hand, fine tuning the inductance profile using a frequency scaling term and a phase shift term is accompanied with much less overhead. From Figure 3.30, it is clear that the initial portion of the curve highlighted in red, resembles the initial portion of a cosine function $\cos(\theta)$ (i.e., for values of θ close to $0°$); however, the portion of the curve highlighted in blue falls rather slowly compared to a cosine function shown in Figure 3.25. To better fit the curve described by Equation 3.67 to the curve shown in Figure 3.30, a frequency scaling term controlling the shape of the function can be introduced as desired.

This section provides a method of changing the shape of the inductance profile described by Equation 3.67. Other methods to compute the frequency scaling and phase shift terms can be tailor made to best suit the selected machine. The method provided in this section does not make use of a phase shift term, it only introduces a frequency scaling term. The method is best explained by considering different cases, based on which, the generalized expressions is developed. The modified version of Equation 3.67 which includes a frequency scaling term (κ) is expressed as:

$$L(\theta) = L_0 + L_1 \cos(\kappa N_r \theta) \tag{3.72}$$

Before proceeding further, it is worth mentioning the range of the frequency scaling term. The minimum value of the frequency scaling term must be greater than 0, this is because if its value were 0, then the phase inductance would be represented as a constant value defined by: $L_0 + L_1$. On the other hand, the maximum value of the frequency scaling term cannot exceed 1, this is because if it did, then the portion of the cosine function after its minima would get included in the inductance profile (i.e., the portion of a cosine function $\cos(\theta)$ after $\theta = \pi$), which would indicate that phase inductance begins to increase when the rotor is still heading towards the unaligned position, which is physically impractical. Therefore, the range of the frequency scaling term (κ) is defined as: $0 < \kappa \leq 1$.

Consider a case wherein the frequency scaling term is equal to $1/N_r$ (assuming $N_r \geq 1$). Using Equation 3.72, the inductance profile can then be described as:

$$L(\theta) = L_0 + L_1 \cos(\theta) \tag{3.73}$$

The inductance profile described by Equation 3.73 is shown in Figure 3.31, which also shows the range where the function ought to lie in, i.e., $0 \leq \theta \leq (\pi/N_r)$.

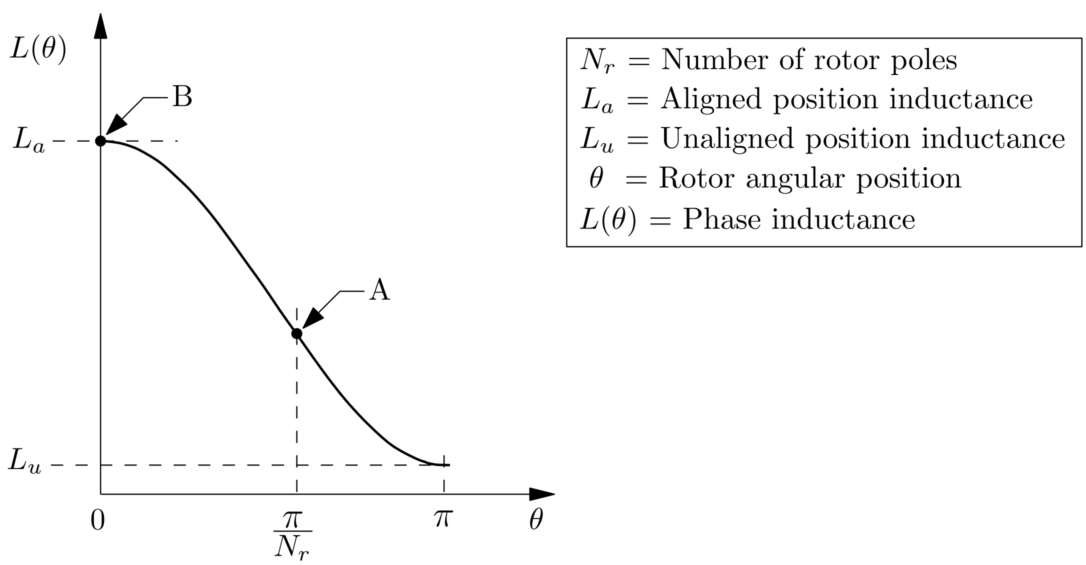

Figure 3.31: Inductance profile when $\kappa = 1/N_r$

To ensure that point A shown in the figure coincides with the unaligned inductance value (L_u) at the unaligned position (π/N_r), a few changes need to be made to Equation 3.73. To achieve the desired result, the Fourier coefficients of Equation 3.73 need to be adjusted. From Equations 3.65 and 3.66, the Fourier coefficients are adjusted by changing either the value of L_a or L_u. From Figure 3.31, it is clear that only point A needs to be shifted whereas point B can remain as is, as a result, changing the value of L_u in Equations 3.65 and 3.66 will help achieve the desired result. Therefore, assume a new L_u value, i.e., L_u^* for the purpose of modifying Equations 3.65 and 3.66, and eventually Equation 3.73. The scaled value of the unaligned inductance (L_u^*) has no physical bearing or intuitive correlation to the machine, it is just used to modify the equation describing the inductance profile. The graphical interpretation of L_u^* is presented in Figure 3.32. From Figure 3.32, it is observed that the inductance profile has the desired shape in the region defined by $0 \leq \theta \leq \pi/N_r$, with the curve lining up with L_a at the aligned position ($\theta = 0$) and with L_u at the unaligned position ($\theta = \pi/N_r$).

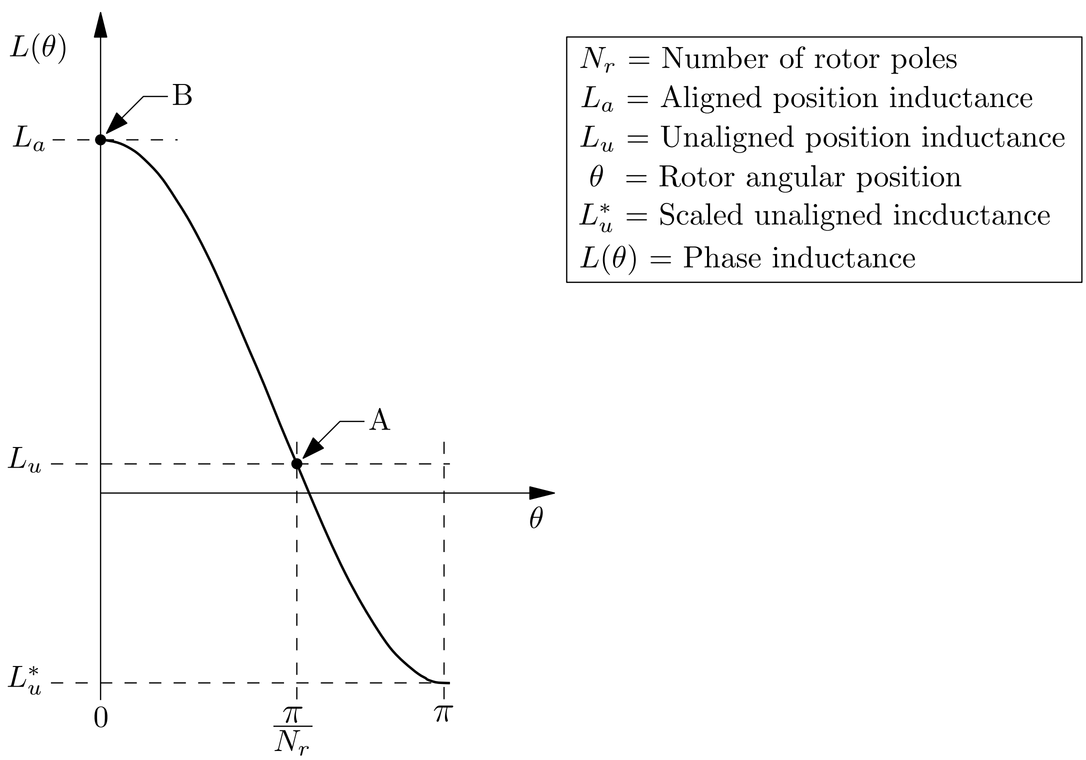

Figure 3.32: The effect of the scaled unaligned inductance (L_u^*)

The next step involves obtaining an expression for the scaled unaligned inductance (L_u^*). The expression is obtained by forcing the function described by Equation 3.73 to pass through the point ($\pi/N_r, L_u$), as a result, the expression defined by Equation 3.73 becomes:

$$L_u = L_0 + L_1 \cos\left(\frac{\pi}{N_r}\right) \tag{3.74}$$

Using the expressions for the Fourier coefficients (L_0 and L_1) from Equations 3.65 and 3.66, after having replaced the unaligned inductance (L_u) with the scaled unaligned inductance (L_u^*) in Equation 3.74, the following expression is obtained:

$$\begin{aligned} L_u &= \left(\frac{L_a + L_u^*}{2}\right) + \left(\frac{L_a - L_u^*}{2}\right)\cos\left(\frac{\pi}{N_r}\right) \\ &= \frac{L_a}{2}\left[1 + \cos\left(\frac{\pi}{N_r}\right)\right] + \frac{L_u^*}{2}\left[1 - \cos\left(\frac{\pi}{N_r}\right)\right] \end{aligned} \tag{3.75}$$

After rearranging Equation 3.75 and making L_u^* the subject of the formula, the following expression (when $\kappa = \pi/N_r$) is obtained:

$$L_u^* = \frac{2L_u - L_a\left[1 + \cos\left(\dfrac{\pi}{N_r}\right)\right]}{1 - \cos\left(\dfrac{\pi}{N_r}\right)} \tag{3.76}$$

Similarly, consider a case wherein the frequency scaling term is equal to $2/N_r$ (assuming $N_r \geq 2$). Using Equation 3.72, the inductance profile is described as:

$$L(\theta) = L_0 + L_1\cos(2\theta) \tag{3.77}$$

The inductance profile described by Equation 3.77 is shown in Figure 3.33, which also shows the range where the function ought to lie in, i.e., $0 \leq \theta \leq (\pi/N_r)$.

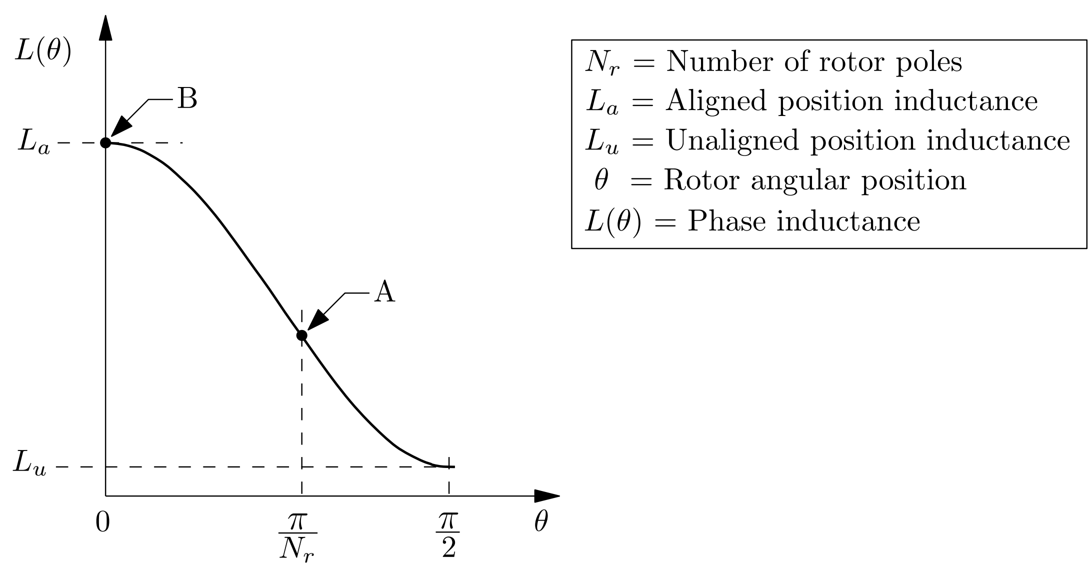

Figure 3.33: Inductance profile when $\kappa = 2/N_r$

Once again, to obtain the expression for the scaled unaligned inductance (L_u^*), the function described by Equation 3.77 is forced to pass through the point ($\pi/N_r, L_u$), as a result, the expression defined by Equation 3.77 becomes:

$$L_u = L_0 + L_1 \cos\left(\frac{2\pi}{N_r}\right) \tag{3.78}$$

Using the expressions for the Fourier coefficients (L_0 and L_1) from Equations 3.65 and 3.66, after having replaced the unaligned inductance (L_u) with the scaled unaligned inductance (L_u^*) in Equation 3.78, the following expression is obtained:

$$\begin{aligned} L_u &= \left(\frac{L_a + L_u^*}{2}\right) + \left(\frac{L_a - L_u^*}{2}\right) \cos\left(\frac{2\pi}{N_r}\right) \\ &= \frac{L_a}{2}\left[1 + \cos\left(\frac{2\pi}{N_r}\right)\right] + \frac{L_u^*}{2}\left[1 - \cos\left(\frac{2\pi}{N_r}\right)\right] \end{aligned} \tag{3.79}$$

After rearranging Equation 3.79 and making L_u^* the subject of the formula, the following expression (when $\kappa = 2\pi/N_r$) is obtained:

$$L_u^* = \frac{2L_u - L_a\left[1 + \cos\left(\frac{2\pi}{N_r}\right)\right]}{1 - \cos\left(\frac{2\pi}{N_r}\right)} \tag{3.80}$$

Based on Equations 3.76 and 3.80, a generalized expression for the scaled unaligned inductance is obtained and is expressed as:

$$L_u^* = \frac{2L_u - L_a\left[1 + \cos(\kappa\pi)\right]}{1 - \cos(\kappa\pi)} \tag{3.81}$$

The frequency scaling technique presented in this section is only one of many possible techniques to fine tune the inductance profile described by Equation 3.67. Based on the geometry of the machine, the designer must develop a scaling technique suitable for their selected machine. In general, also including a phase shift (ϕ) term in the inductance profile (for the sake of completeness), a fine tuned version of Equation 3.67 is expressed as:

$$L(\theta) = L_0 + L_1 \cos[\kappa N_r(\theta + \phi)] \tag{3.82}$$

3.4.2 Theoretical Derivation of Phase Current (Excluding Winding Resistance)

This section presents a technique to obtain an analytical closed form expression for phase current of a switched reluctance machine, based on the expression for the inductance profile presented in Section 3.4.1. The derivation to follow, starts with the basic equation of the current differential equation, which is rewritten as:

$$\frac{di}{d\theta} = \frac{V - \omega i \frac{dL(\theta)}{d\theta}}{\omega L(\theta)} \tag{3.83}$$

Since the derivation in this section does not include the winding and parasitic resistances (R), the voltage (V) refers to the machine's phase voltage. Using Equation 3.82, the expression for the derivative of phase inductance with respect to rotor position is expressed as:

$$\frac{dL(\theta)}{d\theta} = -L_1 \kappa N_r \sin(\kappa N_r \theta + \kappa N_r \phi) \tag{3.84}$$

Substituting the expression for the slope of phase inductance from Equation 3.84 in Equation 3.83, the following expression is obtained:

$$\frac{di}{d\theta} = \frac{V + \omega i L_1 \kappa N_r \sin(\kappa N_r \theta + \kappa N_r \phi)}{\omega[L_0 + L_1 \cos(\kappa N_r \theta + \kappa N_r \phi)]} \tag{3.85}$$

Equation 3.85 is then rewritten as:

$$\frac{di}{d\theta} + \frac{-L_1 \kappa N_r \sin(\kappa N_r \theta + \kappa N_r \phi)}{L_0 + L_1 \cos(\kappa N_r \theta + \kappa N_r \phi)} i - \frac{V}{\omega[L_0 + L_1 \cos(\kappa N_r \theta + \kappa N_r \phi)]} = 0 \tag{3.86}$$

To obtain an analytical expression for phase current, Equation 3.86 must be integrated with respect to rotor position θ. Equation 3.86 is similar to the general equation which has the *integrating factor* form [118] described by:

$$\frac{di}{d\theta} + p(\theta) i - f(\theta) = 0 \tag{3.87}$$

where, $p(\theta)$ is defined by the following expression:

$$p(\theta) = \frac{-L_1 \kappa N_r \sin(\kappa N_r \theta + \kappa N_r \phi)}{L_0 + L_1 \cos(\kappa N_r \theta + \kappa N_r \phi)} \tag{3.88}$$

and, $f(\theta)$ is defined by the following expression:

$$f(\theta) = \frac{V}{\omega[L_0 + L_1 \cos(\kappa N_r \theta + \kappa N_r \phi)]} \tag{3.89}$$

The integrating factor $\mu(\theta)$[2] is expressed in terms of $p(\theta)$ from Equation 3.88 and is expressed by the following relation:

$$\mu(\theta) = \exp\left[\int p(\theta)\ d\theta\right] \tag{3.90}$$

Considering only the exponent of Equation 3.90, the following expression is obtained:

$$\int p(\theta)\ d\theta = \int \frac{-L_1 \kappa N_r \sin(\kappa N_r \theta + \kappa N_r \phi)}{L_0 + L_1 \cos(\kappa N_r \theta + \kappa N_r \phi)}\ d\theta \tag{3.91}$$

To solve for $p(\theta)$, let:

$$L_0 + L_1 \cos(\kappa N_r \theta + \kappa N_r \phi) = x \tag{3.92}$$

Considering the derivative of Equation 3.92 with respect to θ, the following expression is obtained:

$$-L_1 \kappa N_r \sin(\kappa N_r \theta + \kappa N_r \phi)\ d\theta = dx \tag{3.93}$$

Using the expressions of Equations 3.92 and 3.93, the variable θ of Equation 3.91 is changed to x, resulting in the following expression:

$$\begin{aligned} \int p(\theta)\ d\theta &= \int \frac{1}{x}\ dx \\ &= \ln(x) \end{aligned} \tag{3.94}$$

[2]Integrating factor $\mu(\theta)$ not to be confused with permeability of a material μ presented in Section 3.4.1.

Using the result from Equation 3.94 in Equation 3.90, the following expression for the integrating factor is obtained:

$$\mu(\theta) = x \tag{3.95}$$

The solution to Equation 3.87 has the following form [118]:

$$i = \frac{1}{\mu(\theta)} \int \mu(\theta) f(\theta)\ d(\theta) + \frac{C_1}{\mu(\theta)} \tag{3.96}$$

where, C_1 is an integration constant. Using the expression of the integrating factor form Equation 3.95 in Equation 3.96, the following expression is obtained:

$$i = \frac{1}{x} \int x f(\theta)\ d\theta + \frac{C_1}{x} \tag{3.97}$$

Substituting the values of $f(\theta)$ and x (from by Equations 3.89 and 3.92, respectively) in Equation 3.97, the following expression is obtained:

$$i = \frac{V\theta}{\omega[L_0 + L_1 \cos(\kappa N_r \theta + \kappa N_r \phi)]} + \frac{C_1}{L_0 + L_1 \cos(\kappa N_r \theta + \kappa N_r \phi)} \tag{3.98}$$

Since angular velocity (ω) is a slow varying parameter, it is considered as a constant in a commutation cycle, as a result, ωC_1 is absorbed into another constant, i.e., C_2, resulting in a more compact equation, which has the following form:

$$i = \frac{V\theta + C_2}{\omega[L_0 + L_1 \cos(\kappa N_r \theta + \kappa N_r \phi)]} \tag{3.99}$$

Equation 3.99 describes the phase current equation of a switched reluctance machine when a single cosine term along with the average value and fine tuning coefficients κ and ϕ are used. However, if instead of the fine tuning approach (i.e., the inductance profile defined by Equation 3.82), the entire Fourier series is considered, the solution for the phase current can be obtained using the following set of equations:

$$L(\theta) = \sum_{n=0}^{\infty} L_n \cdot \cos(nN_r\theta) \tag{3.100}$$

where, n represents the number of Fourier terms considered and L_n represents the n^{th} Fourier coefficient. The solution for the phase current is obtained by repeating the steps performed earlier for Equation 3.99. Using, Equation 3.100, the derivative of phase inductance is:

$$\frac{dL(\theta)}{d\theta} = -N_r \sum_{n=1}^{\infty} n \cdot L_n \cdot \sin(nN_r\theta) \tag{3.101}$$

Performing similar steps as presented earlier, the expression for phase current results in:

$$i = \frac{V\theta}{\omega \left[\sum_{n=0}^{\infty} L_n \cdot \cos(nN_r\theta) \right]} + \frac{C_1}{\left[\sum_{n=0}^{\infty} L_n \cdot \cos(nN_r\theta) \right]} \tag{3.102}$$

Assuming that ωC_1 gets absorbed into another constant, i.e., C_2, a more compact equation is obtained and has the following form:

$$i = \frac{V\theta + C_2}{\omega \left[\sum_{n=0}^{\infty} L_n \cdot \cos(nN_r\theta) \right]} \tag{3.103}$$

Figures 3.34 and 3.35 present the motoring simulation results of the flux based model, the inductance based model, the proposed model, along with the FEA data. The figures show simulation results for two different operating points of the machine, indicating that the phase current trajectories remain close to each other for a wide range of operating points. The machine model is based on the specifications listed in Appendix A, which suggest that the rated current of the machine is close to 50 A, as a result, the simulations are pushed to that limit. Similarly, Figures 3.36 and 3.37 present the generating simulation results. The current trajectories for the flux and inductance based models are constructed using a numerical method of integration (i.e., Euler method) with 1000 steps. The FEA data is plotted using a look up table approach. On the other hand, the current trajectory for the proposed model is computed in two steps (one for magnetization and one for demagnetization), making it computationally efficient. The values of error indicated in the figures represent the maximum instantaneous error between the model and the FEA data.

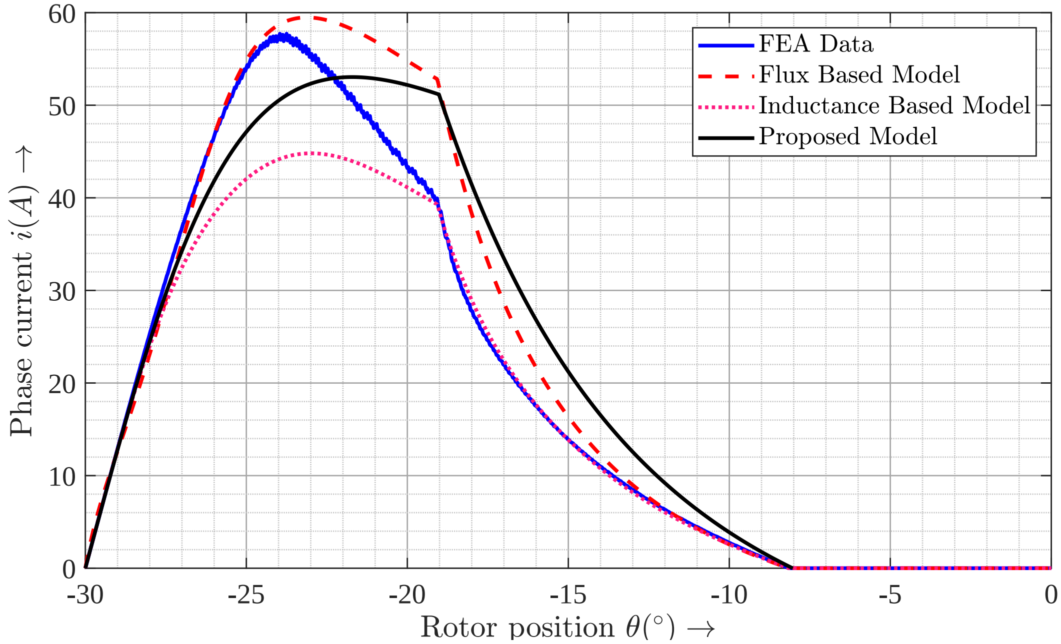

Figure 3.34: Motoring simulation results with angular velocity: $\omega = 4,800$ rpm, phase voltage: $V = 20$ V, and turn-off angle: $\theta_{off} = -19°$. The error in the models: Flux based model = 26%, Inductance base model = 27% and Proposed model = 23%

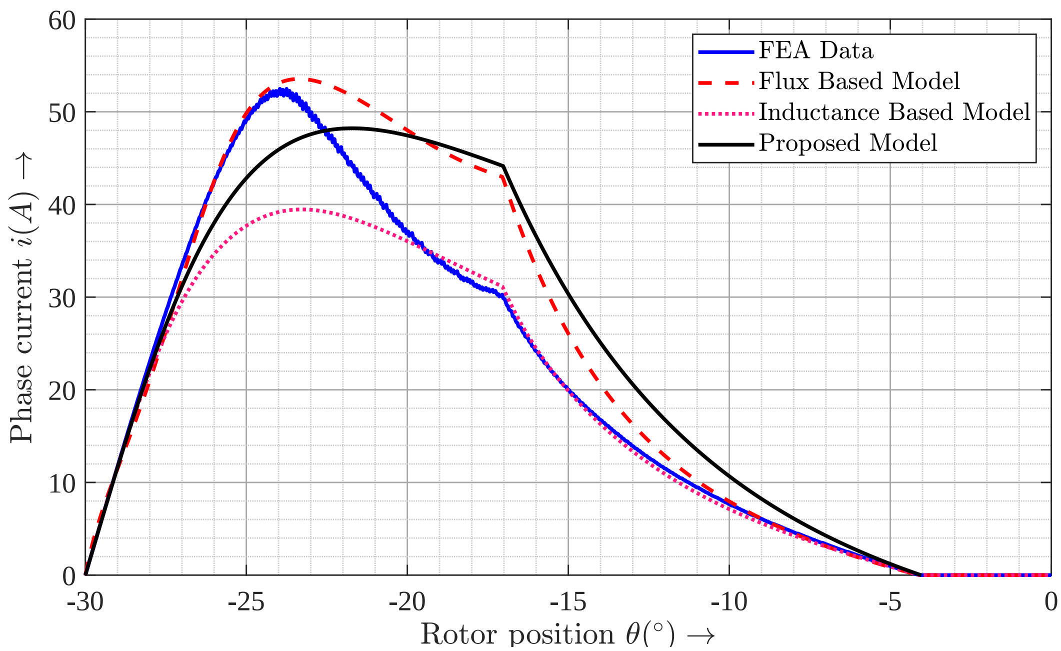

Figure 3.35: Motoring simulation results with angular velocity: $\omega = 10,000$ rpm, phase voltage: $V = 40$ V, and turn-off angle: $\theta_{off} = -17°$ The error in the models: Flux based model = 29%, Inductance base model = 29% and Proposed model = 32%

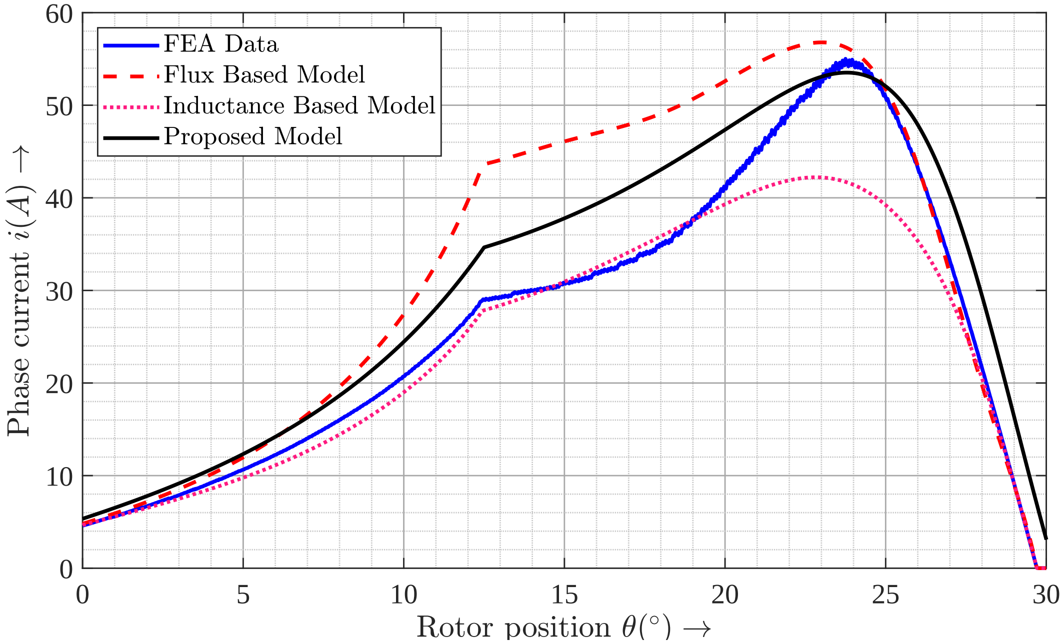

Figure 3.36: Generating simulation results with angular velocity: $\omega = 5,800$ rpm, phase voltage: $V = 24$ V, and turn-off angle: $\theta_{off} = 12.5°$. The error in the models: Flux based model = 42%, Inductance base model = 25% and Proposed model = 22%

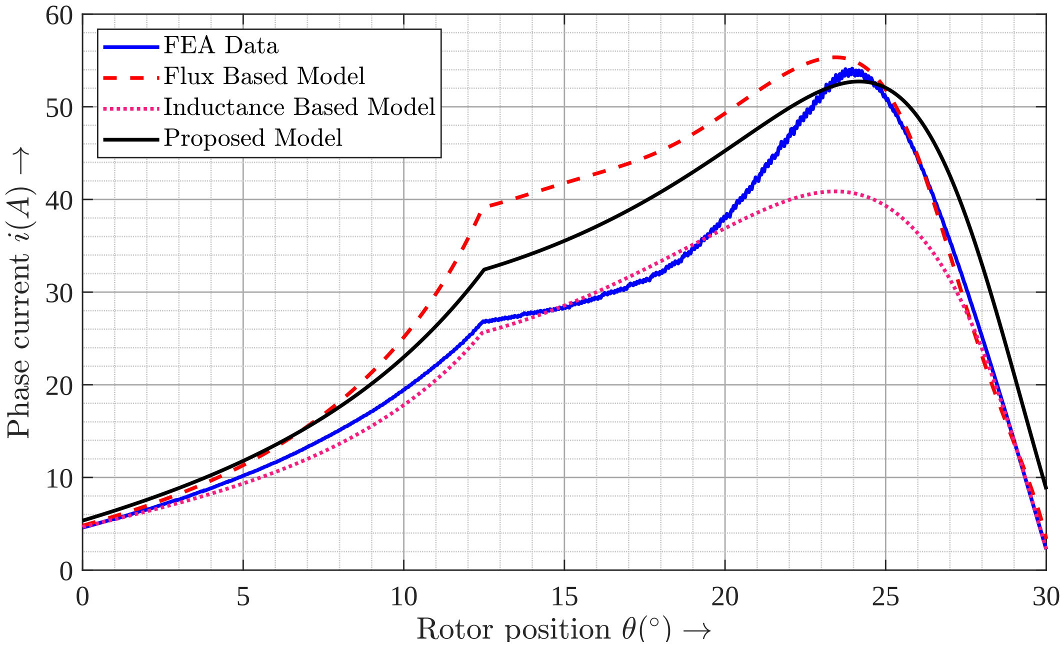

Figure 3.37: Generating simulation results with angular velocity: $\omega = 10,000$ rpm, phase voltage: $V = 40$ V, and turn-off angle: $\theta_{off} = 12.5°$. The error in the models: Flux based model = 38%, Inductance base model = 25% and Proposed model = 22%

3.4.3 Theoretical Derivation of Phase Current (Including Winding Resistance)

This section presents an analytical expression for the phase current including winding resistance and any other parasitic resistance, all captured by the term: R. The winding resistance cannot just be factored into Equations 3.99 or 3.103 at the very end using the expression: $V = (V_{bus} - iR)$, from Equation 2.5. This is because $(V_{bus} - iR)$ is not a constant, but in fact a function of the phase current. The voltage drop across the winding resistance is due to the phase current flowing through it, as a result, as phase current begins to increase, the voltage drop also increases, and thus the term: $(V_{bus} - iR)$, reduces (assuming that the bus voltage V_{bus} is a constant). If the machine's phase voltage V drops, the slope of the phase current also drops. To accommodate the winding resistance, it must be included at the very beginning of the derivation, i.e., in Equation 3.83, resulting in the following expression:

$$\frac{di}{d\theta} = \frac{(V_{bus} - iR) - \omega i \dfrac{dL(\theta)}{d\theta}}{\omega L(\theta)} \tag{3.104}$$

Rewriting the above equation in the integrating factor form, the following expression is obtained:

$$\frac{di}{d\theta} + \left(\frac{R}{\omega} \frac{1}{L(\theta)} + \frac{1}{L(\theta)} \frac{dL(\theta)}{d\theta} \right) i - \frac{V_{bus}}{\omega} \frac{1}{L(\theta)} = 0 \tag{3.105}$$

On comparing the above equation with the integrating factor form of Equation 3.87, the following expressions for $p(\theta)$ and $f(\theta)$ are obtained:

$$p(\theta) = \frac{R}{\omega} \frac{1}{L(\theta)} + \frac{1}{L(\theta)} \frac{dL(\theta)}{d\theta} \tag{3.106}$$

$$f(\theta) = \frac{V_{bus}}{\omega} \frac{1}{L(\theta)} \tag{3.107}$$

In Equation 3.106, let $R/\omega = \tau$. Since $p(\theta)$ contains two separate terms, it is rewritten as: $p(\theta) = \tau p_1(\theta) + p_2(\theta)$, where the terms $p_1(\theta)$ and $p_2(\theta)$ are defined as:

$$p_1(\theta) = \frac{1}{L(\theta)} \tag{3.108}$$

$$p_2(\theta) = \frac{1}{L(\theta)}\frac{dL(\theta)}{d\theta} \tag{3.109}$$

The solution to Equation 3.105 is given by the following expression:

$$i = \frac{1}{\mu(\theta)}\int \mu(\theta) f(\theta)\ d\theta + \frac{C_3}{\mu(\theta)} \tag{3.110}$$

where, C_3 is an integration constant and $\mu(\theta)$[3] is the integrating factor, which is expressed as:

$$\begin{aligned}\mu(\theta) &= \exp\left[\int p(\theta)\ d\theta\right]\\ &= \exp\left[\int \tau p_1(\theta)\ d\theta + \int p_2(\theta)\ d\theta\right]\end{aligned} \tag{3.111}$$

In order to solve Equation 3.110, first the expression for the integrating factor expressed by Equation 3.111 needs to be solved. Substituting the expressions for $p_1(\theta)$ and $p_2(\theta)$ from Equations 3.108 and 3.109, respectively results in:

$$\begin{aligned}\mu(\theta) &= \exp\left[\tau\int \frac{1}{L(\theta)}\ d\theta + \int \frac{1}{L(\theta)}\ dL(\theta)\right]\\ &= \exp\left[\tau\int \underbrace{\frac{1}{L(\theta)}}_{p_1(\theta)}\ d\theta + \ln(L(\theta))\right]\end{aligned} \tag{3.112}$$

Considering only the integral of $p_1(\theta)$ and using the expression for the inductance profile from Equation 3.82, the following expressions is obtained:

$$\int p_1(\theta)\ d\theta = \int \frac{1}{L_0 + L_1\cos(\kappa N_r\theta + \kappa N_r\phi)}\ d\theta \tag{3.113}$$

[3]Integrating factor $\mu(\theta)$ not to be confused with permeability of a material μ presented in Section 3.4.1.

Replacing $(\kappa N_r \theta + \kappa N_r \phi)$ with u and considering its derivative with respect to θ, results in: $\kappa N_r d\theta = du$. Using these substitutions in Equation 3.113, the following expression is obtained:

$$\int p_1(\theta)\ d\theta = \frac{1}{\kappa N_r} \int \frac{1}{L_0 + L_1 \cos(u)}\ du \tag{3.114}$$

Next, using the trigonometric identity: $\cos(u) = [1 - \tan^2(u/2)]/[1 + \tan^2(u/2)]$, in Equation 3.114, the following expression is obtained:

$$\int p_1(\theta)\ d\theta = \frac{1}{\kappa N_r} \int \frac{1 + \tan^2(u/2)}{L_0[1 + \tan^2(u/2)] + L_1[1 - \tan^2(u/2)]}\ du \tag{3.115}$$

Using another trigonometric identity: $\sec^2(u/2) = 1 + \tan^2(u/2)$, in Equation 3.115, along with replacing $\tan(u/2)$ by v, where its derivative with respect to u is $(1/2)\sec^2(u/2)du = dv$, the following expression is obtained:

$$\begin{aligned} \int p_1(\theta)\ d\theta &= \frac{1}{\kappa N_r} \int \frac{\sec^2(u/2)}{L_0[1 + \tan^2(u/2)] + L_1[1 - \tan^2(u/2)]}\ du \\ &= \frac{1}{\kappa N_r} \int \frac{2}{L_0(1 + v^2) + L_1(1 - v^2)}\ dv \\ &= \frac{2}{\kappa N_r} \int \frac{1}{(L_0 - L_1)v^2 + (L_0 + L_1)}\ dv \end{aligned} \tag{3.116}$$

Substituting the values of L_0 and L_1 from Equations 3.65 and 3.66, respectively in Equation 3.116 the following expression is obtained:

$$\int p_1(\theta)\ d\theta = \frac{2}{\kappa N_r} \int \frac{1}{[(L_a + L_u)/2 - (L_a - L_u)/2]v^2 + [(L_a + L_u)/2 + (L_a - L_u)/2]}\ dv \tag{3.117}$$

Rearranging Equation 3.117 and solving the integral results in the following expression:

$$\begin{aligned}
\int p_1(\theta)\ d\theta &= \frac{2}{\kappa N_r} \int \frac{1}{L_u v^2 + L_a}\ dv \\
&= \frac{2}{\kappa N_r L_u} \int \frac{1}{v^2 + L_a/L_u}\ dv \\
&= \frac{2}{\kappa N_r L_u} \int \frac{1}{v^2 + (\sqrt{L_a/L_u})^2}\ dv \\
&= \frac{2}{\kappa N_r L_u} \frac{\tan^{-1}(v/\sqrt{L_a/L_u})}{\sqrt{L_a/L_u}} + C_4 \\
&= \frac{2}{\kappa N_r \sqrt{L_a L_u}} \tan^{-1}\left(\frac{v}{\sqrt{L_a/L_u}}\right) + C_4
\end{aligned} \tag{3.118}$$

where, C_4 is a constant of integration. Replacing the value of v by $\tan(u/2)$, the following expression is obtained:

$$\int p_1(\theta)\ d\theta = \frac{2}{\kappa N_r \sqrt{L_a L_u}} \tan^{-1}\left(\frac{\tan(u/2)}{\sqrt{L_a/L_u}}\right) + C_4 \tag{3.119}$$

Also, replacing u by $(\kappa N_r \theta + \kappa N_r \phi)$, the following expression is obtained:

$$\int p_1(\theta)\ d\theta = \frac{2}{\kappa N_r \sqrt{L_a L_u}} \tan^{-1}\left\{\frac{\tan[(\kappa N_r \theta + \kappa N_r \phi)/2]}{\sqrt{L_a/L_u}}\right\} + C_4 \tag{3.120}$$

To obtain an expression for the integrating factor ($\mu(\theta)$) from Equation 3.112, the expression for the integral of $p_1(\theta)$ obtained in Equation 3.120 must be used. However, if that substitution is made, it will result in an extremely complex equation, eventually making it impossible to obtain the solution for phase current. Therefore, a curve fitting expression for the integral of $p_1(\theta)$ is used, in order to simplify the process of solving Equation 3.112. After examining Equation 3.112, it is observed that if the integral of $p_1(\theta)$ is replaced by an expression that contains a natural logarithmic function, the solution would be easier to compute (since the integral of $p_1(\theta)$ is raised to the power of the exponent). The selection of the exact candidate which can replace the integral of $p_1(\theta)$ is presented next.

The goal here is to replace the expression for the integral of $p_1(\theta)$ with a logarithmic curve fitting function; however, a single logarithmic function is unable to fit the integral of $p_1(\theta)$ over its entire range, which is defined by: $-\pi/N_r \leq \theta \leq +\pi/N_r$. Therefore, to overcome this obstacle, two logarithmic candidates are selected, one for the range defined by: $-\pi/N_r \leq \theta \leq 0$, and another for the range defined by: $0 \leq \theta \leq +\pi/N_r$. This implies that essentially, one logarithmic candidate is used during the motoring operation and one is used during the generating operation. After extensive tries, the following logarithmic based candidates were used:

$$\lambda_m(\theta) = \alpha_m \Big[\ln(\beta_m + \theta) + \gamma_m \Big] \tag{3.121}$$

$$\lambda_g(\theta) = \alpha_g \left[\ln\left(\frac{1}{\beta_g - \theta}\right) + \gamma_g \right] \tag{3.122}$$

where, $\lambda_m(\theta)$ represents the curve fitting expression for the integral of $p_1(\theta)$ during the motoring operation and α_m, β_m, and γ_m represent its constant coefficients. Similarly, $\lambda_g(\theta)$ represents the curve fit expression for the integral of $p_1(\theta)$ during the generating operation and α_g, β_g, and γ_g represent its constant coefficients. The analysis has been split up for the motoring and generating operations. The motoring phase current analytical expression is presented next.

Phase Current Expression During Motoring

Equating the integral of $p_1(\theta)$ to the curve fitting expression $\lambda_m(\theta)$, the following expression (which is valid for $-\pi/N_r \leq \theta \leq 0$) is obtained:

$$\int p_1(\theta)\ d\theta = \lambda_m(\theta) \tag{3.123}$$

Substituting the value of $\lambda_m(\theta)$ from Equation 3.121 in Equation 3.112 and using the expression from Equation 3.123 for the integral of $p_1(\theta)$, the following sets of equations are

obtained:

$$\mu(\theta) = \exp\left[\tau\lambda_m(\theta) + \ln(L(\theta))\right]$$
$$= \exp\left[\tau\alpha_m \ln(\beta_m + \theta) + \tau\alpha_m\gamma_m + \ln(L(\theta))\right]$$
$$= \exp\left[\ln(\beta_m + \theta)^{\tau\alpha_m} + \tau\alpha_m\gamma_m + \ln(L(\theta))\right]$$
$$= (\beta_m + \theta)^{\tau\alpha_m} \cdot \exp(\tau\alpha_m\gamma_m) \cdot L(\theta) \tag{3.124}$$

In Equation 3.124, assigning $\exp(\tau\alpha_m\gamma_m) = \zeta_m$, the expression for the integrating factor (μ) becomes:

$$\mu(\theta) = \zeta_m L(\theta)(\beta_m + \theta)^{\tau\alpha_m} \tag{3.125}$$

Substituting the value of $\mu(\theta))$ from Equation 3.125 and the value of $f(\theta)$ from Equation 3.107 in Equation 3.110, the following expression for the solution to the phase current is obtained:

$$i = \frac{\zeta_m^{-1}(\beta_m + \theta)^{-\tau\alpha_m}}{L(\theta)} \int \left[\zeta_m L(\theta)(\beta_m + \theta)^{\tau\alpha_m} \cdot \frac{V_{bus}}{\omega L(\theta)}\right] d\theta + C_3 \left[\frac{(\beta_m + \theta)^{-\tau\alpha_m}}{\zeta_m L(\theta)}\right]$$
$$= \frac{V_{bus}(\beta_m + \theta)^{-\tau\alpha_m}}{\omega L(\theta)} \int (\beta_m + \theta)^{\tau\alpha_m}\, d\theta + C_3 \left[\frac{(\beta_m + \theta)^{-\tau\alpha_m}}{\zeta_m L(\theta)}\right]$$
$$= \frac{V_{bus}(\beta_m + \theta)^{-\tau\alpha_m}}{\omega L(\theta)} \frac{(\beta_m + \theta)^{(\tau\alpha_m + 1)}}{(\tau\alpha_m + 1)} + C_3 \left[\frac{(\beta_m + \theta)^{-\tau\alpha_m}}{\zeta_m L(\theta)}\right]$$
$$= \frac{V_{bus}(\beta_m + \theta)}{\omega L(\theta)(\tau\alpha_m + 1)} + C_3 \left[\frac{(\beta_m + \theta)^{-\tau\alpha_m}}{\zeta_m L(\theta)}\right] \tag{3.126}$$

To calculate the value of C_3, the initial conditions must be applied, i.e., $i = i_{initial}$ at $\theta = -\pi/N_r$, at which position, the phase inductance value is defined by its unaligned value L_u. Therefore, using the values of $i = i_{initial}$, $\theta = -\pi/N_r$, and $L(-\pi/N_r) = L_u$, the following expression for C_3 is obtained:

$$C_3 = \left[i_{initial} - \frac{V_{bus}}{\omega L_u} \frac{\left(\beta_m - \frac{\pi}{N_r}\right)}{(\tau\alpha_m + 1)}\right] \left(\beta_m - \frac{\pi}{N_r}\right)^{\tau\alpha_m} \zeta_m L_u \tag{3.127}$$

Replacing the value of the integration constant C_3 in Equation 3.126, the following result for the phase current during motoring is obtained:

$$i = \frac{V_{bus}(\beta_m + \theta)}{\omega L(\theta)(\tau\alpha_m + 1)} + \left[i_{initial} - \frac{V_{bus}}{\omega L_u} \frac{\left(\beta_m - \frac{\pi}{N_r}\right)}{(\tau\alpha_m + 1)} \right] \frac{L_u \left(\beta_m - \frac{\pi}{N_r}\right)^{\tau\alpha_m}}{L(\theta)(\beta_m + \theta)^{\tau\alpha_m}} \tag{3.128}$$

As a sanity check, on replacing R by 0, i.e., $\tau = 0$ in Equation 3.128, the solution for phase current becomes:

$$\begin{aligned}
i &= \frac{V_{bus}(\beta_m + \theta)}{\omega L(\theta)} + \left[i_{initial} - \frac{V_{bus}}{\omega L_u} \left(\beta_m - \frac{\pi}{N_r}\right) \right] \frac{L_u}{L(\theta)} \\
&= \frac{V_{bus}(\beta_m + \theta)}{\omega L(\theta)} + \frac{L_u i_{initial}}{L(\theta)} - \frac{V_{bus}}{\omega L(\theta)} \left(\beta_m - \frac{\pi}{N_r}\right) \\
&= \frac{V_{bus}\beta_m}{\omega L(\theta)} + \frac{V_{bus}\theta}{\omega L(\theta)} + \frac{L_u i_{initial}}{L(\theta)} - \frac{V_{bus}\beta_m}{\omega L(\theta)} + \frac{V_{bus}\beta_m}{\omega L(\theta)} \left(\frac{\pi}{N_r}\right) \\
&= \frac{V_{bus}\theta}{\omega L(\theta)} + \frac{L_u i_{initial}\omega}{\omega L(\theta)} + \frac{V_{bus}\beta_m}{\omega L(\theta)} \left(\frac{\pi}{N_r}\right) \\
&= \frac{V_{bus}\theta + \left(\omega L_u i_{initial} + V_{bus}\beta_m \frac{\pi}{N_r}\right)}{\omega L(\theta)}
\end{aligned} \tag{3.129}$$

In Equation 3.129, the term: $\omega L_u i_{initial} + V_{bus}\beta_m(\pi/N_r)$ is assigned as a constant, i.e., C_5. Also, substituting the value of phase inductance from Equation 3.82 and replacing the value of bus voltage V_{bus} by phase voltage V (since the winding resistance is assumed to be zero) in Equation 3.129, the following expression is obtained:

$$i = \frac{V\theta + C_5}{\omega[L_0 + L_1 \cos(\kappa N_r \theta + \kappa N_r \phi)]} \tag{3.130}$$

On comparing the expressions for phase current from Equations 3.130 and 3.99, the expressions are identical barring the notation of integration constants, i.e., C_2 and C_5.

The phase current expression represented by Equation 3.128 correctly accounts for the winding resistance of the machine (along with any other parasitic resistances). On comparing the phase current equation for the two cases, where the winding resistance is excluded and included, it is evident that higher accuracy is accompanied by mathematical overhead. Figure 3.38 shows the closeness of the integral of $p_1(\theta)$ with the logarithmic curve fit expression used while operating the machine as a motor. The expressions for the coefficients of $\lambda_m(\theta)$, i.e., α_m, β_m, and γ_m are listed in Appendix E.

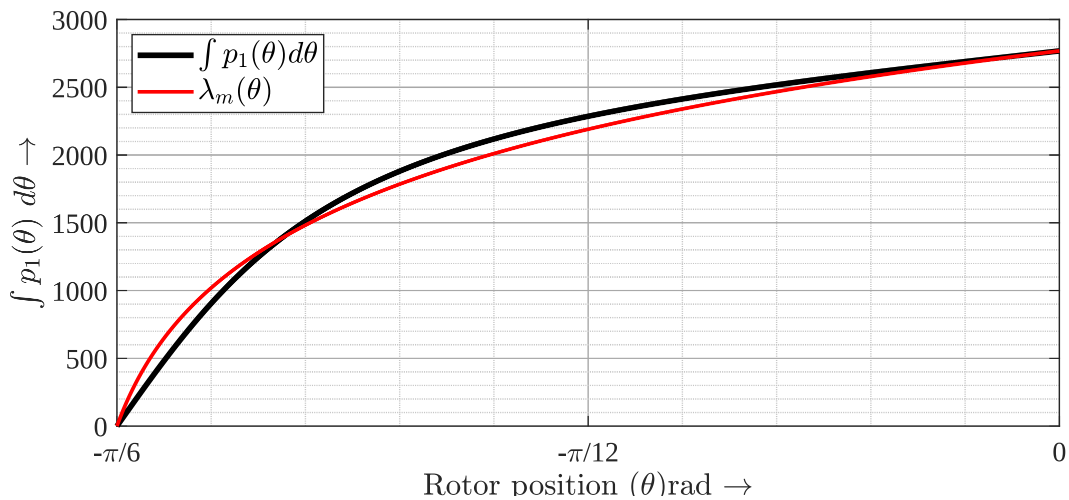

Figure 3.38: Integral of $p_1(\theta)$ and the logarithmic curve fit expression for motoring $\lambda_m(\theta)$ versus rotor position (θ)

Phase Current Expression During Generation

This section presents an analytical expression for phase current during generation when the winding resistance (along with any other parasitic resistance) is considered. The derivation is similar to the one obtained during motoring and differs because of the use of a different logarithmic curve fitting expression, i.e., $\lambda_g(\theta)$. Equating the integral of $p_1(\theta)$ to the curve fitting expression $\lambda_g(\theta)$, the following expression (which is valid for $0 \leq \theta \leq +\pi/N_r$) is obtained:

$$\int p_1(\theta)\ d\theta = \lambda_g(\theta) \tag{3.131}$$

Substituting the value of $\lambda_g(\theta)$ from Equation 3.122 in Equation 3.112 and using the expression from Equation 3.131 for the integral of $p_1(\theta)$, the following sets of equations are

obtained:

$$\begin{aligned}
\mu(\theta) &= \exp\left[\tau\lambda_g(\theta) + \ln(L(\theta))\right] \\
&= \exp\left[\tau\alpha_g \ln\left(\frac{1}{\beta_g - \theta}\right) + \tau\alpha_g\gamma_g + \ln(L(\theta))\right] \\
&= \exp\left[\ln\left(\beta_g - \theta\right)^{-\tau\alpha_g} + \tau\alpha_g\gamma_g + \ln(L(\theta))\right] \\
&= \left(\beta_g - \theta\right)^{-\tau\alpha_g} \cdot \exp(\tau\alpha_g\gamma_g) \cdot L(\theta) \qquad (3.132)
\end{aligned}$$

In Equation 3.132, assigning $\exp(\tau\alpha_g\gamma_g) = \zeta_g$, the expression for the integrating factor ($\mu(\theta)$) becomes:

$$\mu(\theta) = \zeta_g L(\theta)\left(\beta_g - \theta\right)^{-\tau\alpha_g} \qquad (3.133)$$

Substituting the value of $\mu(\theta)$ form Equation 3.133 and the value of $f(\theta)$ from Equation 3.107 in Equation 3.110, the following expression for the solution to the phase current is obtained (integration constant C_3 is changed to C_6 to avoid any confusion):

$$\begin{aligned}
i &= \frac{\zeta_g^{-1}\left(\beta_g - \theta\right)^{\tau\alpha_g}}{L(\theta)} \int \left[\zeta_g L(\theta)\left(\beta_g - \theta\right)^{-\tau\alpha_g} \cdot \frac{V_{bus}}{\omega L(\theta)}\right] d\theta + C_6\left[\frac{\left(\beta_g - \theta\right)^{\tau\alpha_g}}{\zeta_g L(\theta)}\right] \\
&= \frac{V_{bus}\left(\beta_g - \theta\right)^{\tau\alpha_g}}{\omega L(\theta)} \int \left(\beta_g - \theta\right)^{-\tau\alpha_g}\ d\theta + C_6\left[\frac{\left(\beta_g - \theta\right)^{\tau\alpha_g}}{\zeta_g L(\theta)}\right] \\
&= \frac{V_{bus}\left(\beta_g - \theta\right)^{\tau\alpha_g}}{\omega L(\theta)} \frac{\left(\beta_g - \theta\right)^{1-\tau\alpha_g}}{(\tau\alpha_g - 1)} + C_6\left[\frac{\left(\beta_g - \theta\right)^{\tau\alpha_g}}{\zeta_g L(\theta)}\right] \\
&= \frac{V_{bus}\left(\beta_g - \theta\right)}{\omega L(\theta)(\tau\alpha_g - 1)} + C_6\left[\frac{\left(\beta_g - \theta\right)^{\tau\alpha_g}}{\zeta_g L(\theta)}\right] \qquad (3.134)
\end{aligned}$$

To calculate the value of C_6, the initial conditions must be applied, i.e., $i = i_{initial}$ at $\theta = 0$, at which position, the phase inductance value is defined by its aligned value L_a. Therefore, using the values of $i = i_{initial}$, $\theta = 0$, and $L(0) = L_a$, the following eexpression for C_6 is

obtained:

$$C_6 = \left[i_{initial} - \frac{V_{bus}\beta_g}{\omega L_a(\tau\alpha_g - 1)} \right] \beta_g^{-\tau\alpha_g} \zeta_g L_a \tag{3.135}$$

Replacing the value of the integration constant C_6 in Equation 3.134, the following result for the phase current during generating is obtained:

$$i = \frac{V_{bus}\left(\beta_g - \theta\right)}{\omega L(\theta)(\tau\alpha_g - 1)} + \left[i_{initial} - \frac{V_{bus}\beta_g}{\omega L_a(\tau\alpha_g - 1)} \right] \frac{L_a\left(\beta_g - \theta\right)^{\tau\alpha_g}}{L(\theta)\beta_g^{\tau\alpha_m}} \tag{3.136}$$

As a sanity check, on replacing R by 0, i.e., $\tau = 0$ in Equation 3.136, the solution for phase current becomes:

$$\begin{aligned}
i &= -\frac{V_{bus}\left(\beta_g - \theta\right)}{\omega L(\theta)} + \left[i_{initial} + \frac{V_{bus}\beta_g}{\omega L_a} \right] \frac{L_a}{L(\theta)} \\
&= -\frac{V_{bus}\left(\beta_g - \theta\right)}{\omega L(\theta)} + \frac{L_a i_{initial}}{L(\theta)} + \frac{V_{bus}\beta_g}{\omega L(\theta)} \\
&= -\frac{V_{bus}\beta_g}{\omega L(\theta)} + \frac{V_{bus}\theta}{\omega L(\theta)} + \frac{L_a i_{initial}}{L(\theta)} + \frac{V_{bus}\beta_g}{\omega L(\theta)} \\
&= \frac{V_{bus}\theta}{\omega L(\theta)} + \frac{L_a i_{initial}\omega}{\omega L(\theta)} \\
&= \frac{V_{bus}\theta + \omega L_a i_{initial}}{\omega L(\theta)}
\end{aligned} \tag{3.137}$$

In Equation 3.137, the term $\omega L_a i_{initial}$ is assigned as a constant, i.e., C_7. Also, substituting the value of phase inductance from Equation 3.82 and replacing the value of bus voltage V_{bus} by phase voltage V (since the winding resistance is assumed to be zero) in Equation 3.137, the following expression is obtained:

$$i = \frac{V\theta + C_7}{\omega[L_0 + L_1 \cos(\kappa N_r\theta + \kappa N_r\phi)]} \tag{3.138}$$

On comparing the expressions for phase current from Equations 3.138 and 3.99, the expressions are identical barring the notation of integration constants, i.e., C_2 and C_7.

The phase current expression represented by Equation 3.136 correctly accounts for the winding resistance of the machine (along with any other parasitic resistances). On comparing the phase current equation for the two cases, where the winding resistance is excluded and included, it is evident that higher accuracy is accompanied by mathematical overhead. Figure 3.39 shows the closeness of the integral of $p_1(\theta)$ with the logarithmic curve fit expression used while operating the machine as a generator. The expressions for the coefficients of $\lambda_g(\theta)$, i.e., α_g, β_g, and γ_g are listed in Appendix F.

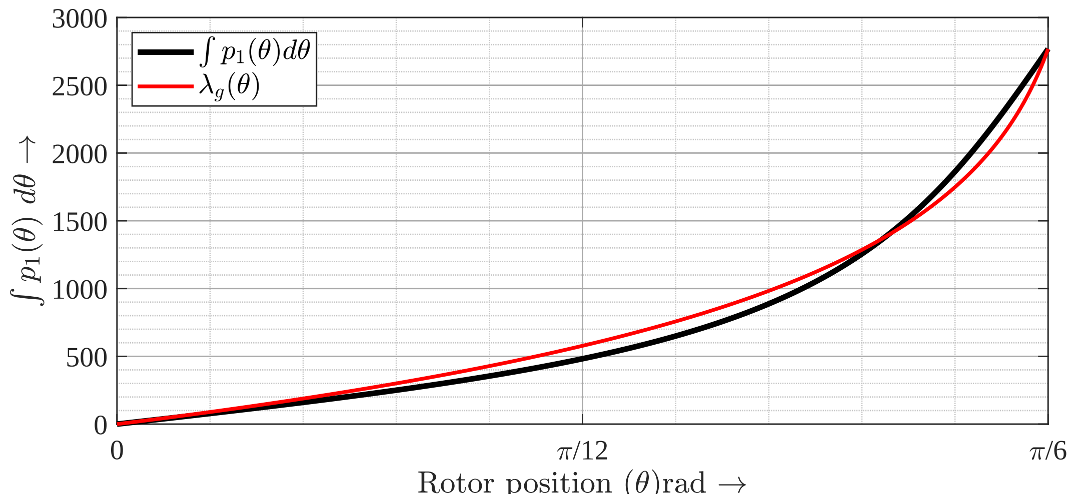

Figure 3.39: Integral of $p_1(\theta)$ and the logarithmic curve fit expression for generation $\lambda_g(\theta)$ versus rotor position (θ)

3.5 Experimental Results

This section presents experimental results recorded from the setup shown in Appendix J using the machine specified in Table A.2 in Appendix A, which is characterized in Appendix C. The experimental results are recorded for both, motoring and generating modes of operation and are compared with simulation results (based on the phase current equations including winding resistance) to verify the validity and accuracy of the analytical expression for phase current. In the generating mode, the machine is tested at its rated current value as it would, during regular operation. The results for the motoring mode of operation are presented next.

3.5.1 Motoring Results

Since the switched reluctance machine considered has six rotor poles, the unaligned position occurs at $-30°$ (i.e., position Z in Figure 2.4), while the aligned position occurs at $0°$ (i.e., position X in Figure 2.4). The first set of readings are recorded for turn-on and turn-off angles of $-30°$ and $-20°$, respectively, followed by a second set with turn-on and turn-off angles of $-30°$ and $-15°$, respectively, and finally a third set with turn-on and turn-off angles of $-30°$ and $-10°$, respectively. Essentially, the turn-off angle is incremented by $5°$ for every set of readings. The turn-off angle is not increased beyond $-10°$, as that produces a current tail which surpasses the aligned position at $0°$, producing negative torque.

The turn-on angle is not changed and is fixed at $-30°$ because during motoring, since the produced torque is directly proportional to phase current (based on Equation 2.38), it is essential to make sure that the phase current reaches its rated value as early as possible. For positions closer to the unaligned position (i.e., $\theta = -30°$), the phase inductance is low, as a result, from Equation 2.2, the phase current can reach its rated value sooner when compared to a later position at which the phase inductance is higher (i.e., a position closer to the aligned position). Delaying the turn-on angle also reduces the window in which positive torque is produced as the turn-off angle cannot be too close to the aligned position (in high-speed single pulse motoring) to avoid the current tail and consequently, negative torque.

Each combination of turn-on and turn-off angles has three readings within it, where the angular velocity of the machine is varied. The increase in the angular velocity results in an increase in back EMF, which opposes the effect of the applied voltage, thereby reducing the peak of the phase current. The experimental i_{exp} and simulated i_{sim} motoring phase currents are presented in Figures 3.40, 3.41, and 3.42. All the motoring results presented in this section show a very close match between the experimentally captured phase current and the simulated phase current.

Motoring: Turn-on Angle: $-30°$, Turn-off Angle: $-20°$

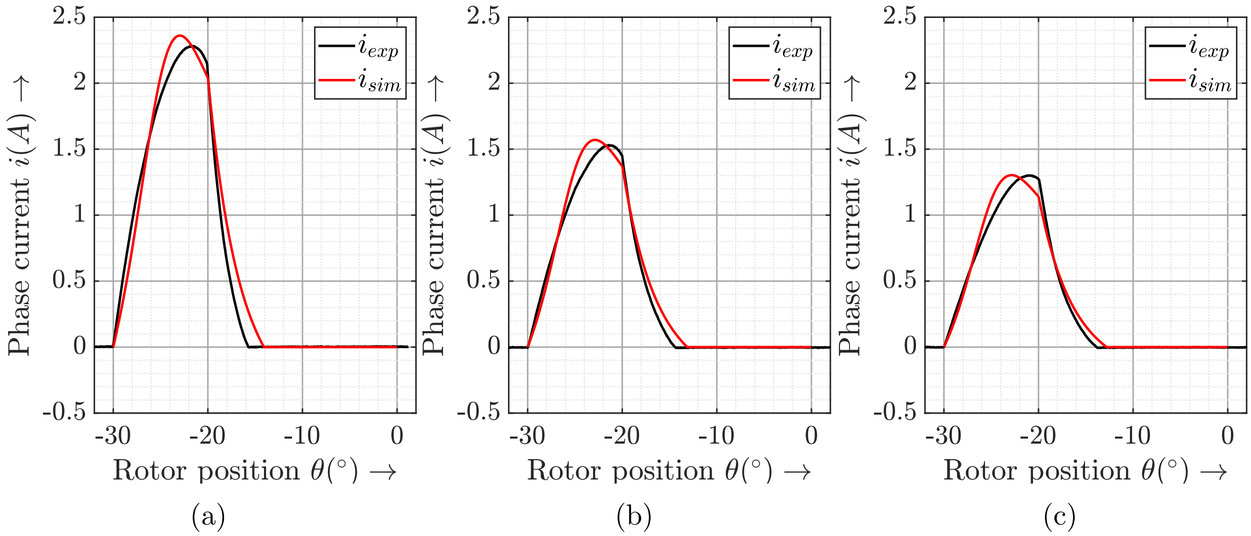

Figure 3.40: Motoring experimental (i_{exp}) and simulated (i_{sim}) phase currents versus rotor angular position (θ) with $\theta_{on} = -30°$ and $\theta_{off} = -20°$ for (a) $\omega = 160$ rpm, (b) $\omega = 281$ rpm, and (c) $\omega = 373$ rpm

Motoring: Turn-on Angle: $-30°$, Turn-off Angle: $-15°$

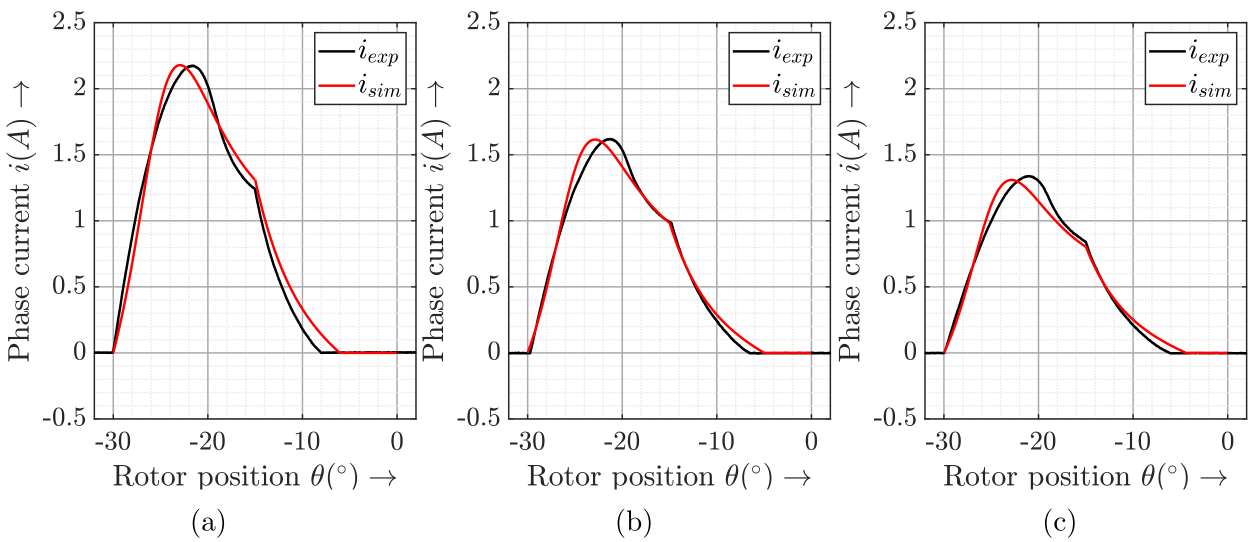

Figure 3.41: Motoring experimental (i_{exp}) and simulated (i_{sim}) phase currents versus rotor angular position (θ) with $\theta_{on} = -30°$ and $\theta_{off} = -15°$ for (a) $\omega = 180$ rpm, (b) $\omega = 271$ rpm, and (c) $\omega = 370$ rpm

Motoring: Turn-on Angle: $-30°$, Turn-off Angle: $-10°$

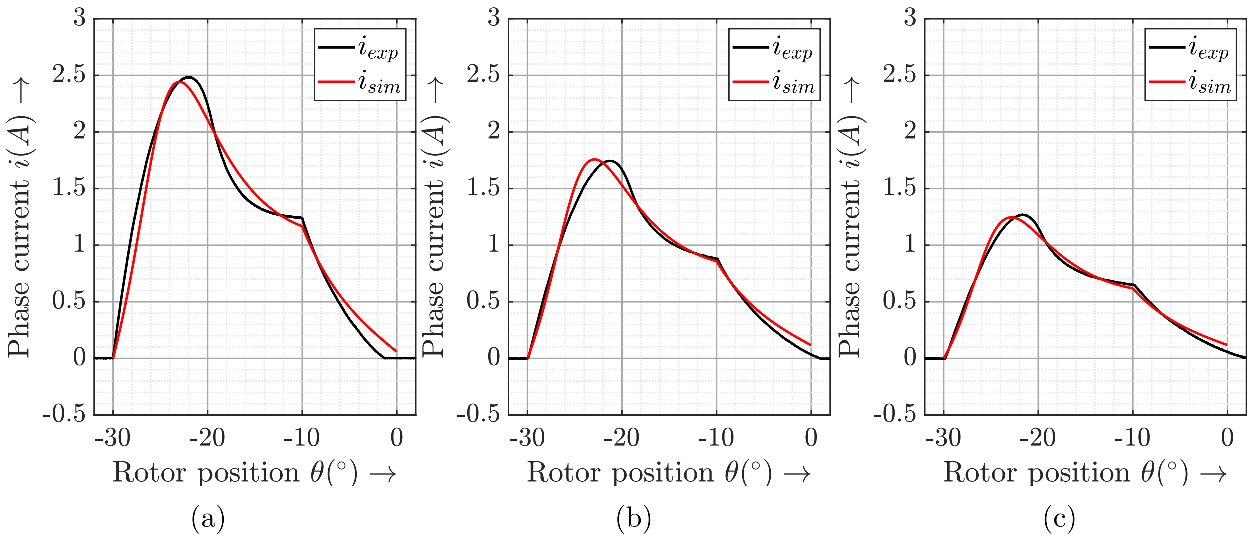

Figure 3.42: Motoring experimental (i_{exp}) and simulated (i_{sim}) phase currents versus rotor angular position (θ) with $\theta_{on} = -30°$ and $\theta_{off} = -10°$ for (a) $\omega = 140$ rpm, (b) $\omega = 260$ rpm, and (c) $\omega = 373$ rpm

3.5.2 Generating Results

Since the switched reluctance machine considered has six rotor poles, the unaligned position occurs at $+30°$ (i.e., position Z in Figure 2.4), while the aligned position occurs at $0°$ (i.e., position X in Figure 2.4). The first set of readings are recorded for turn-on and turn-off angles of $-15°$ and $+15°$, respectively, followed by a second set with turn-on and turn-off angles of $-15°$ and $+20°$, respectively, and finally a third set with turn-on and turn-off angles of $-15°$ and $+25°$, respectively. Essentially, the turn-off angle is incremented by $5°$ for every set of readings.

Each combination of turn-on and turn-off angles has three readings within it, where the angular velocity of the machine is varied and the switched reluctance generator is operated in negative feedback, zero feedback, and positive feedback single pulse mode (unless specified otherwise).

Similarly three more sets of readings are recorded with a turn-on angle of $-10°$ and the turn-off angle is incremented from $+15°$ to $+20°$ to $+25°$). Similar sets of three readings are repeated by incrementing the turn-on angle by 5°, upto the point where the turn-on angle reaches 0° (i.e., no phase advancing is employed) beyond which the net charge and output power is poor.

At lower angular velocities, the back EMF is not as high and does not oppose the applied voltage as much, as a result, the phase current has a steep initial slope reaching a high peak value compared to the other scenarios. The experimental i_{exp} and simulated i_{sim} phase currents are presented beginning at Figure 3.43 and ending at Figure 3.54. The phase current of the machine is pushed to its rated value to examine the model's integrity under regular operation. The difference between the simulated and the experimental phase currents remain within a 10% error bound and closely match each other.

Generating: Turn-on Angle: $-15°$, Turn-off Angle: 15° (With Phase Advancing)

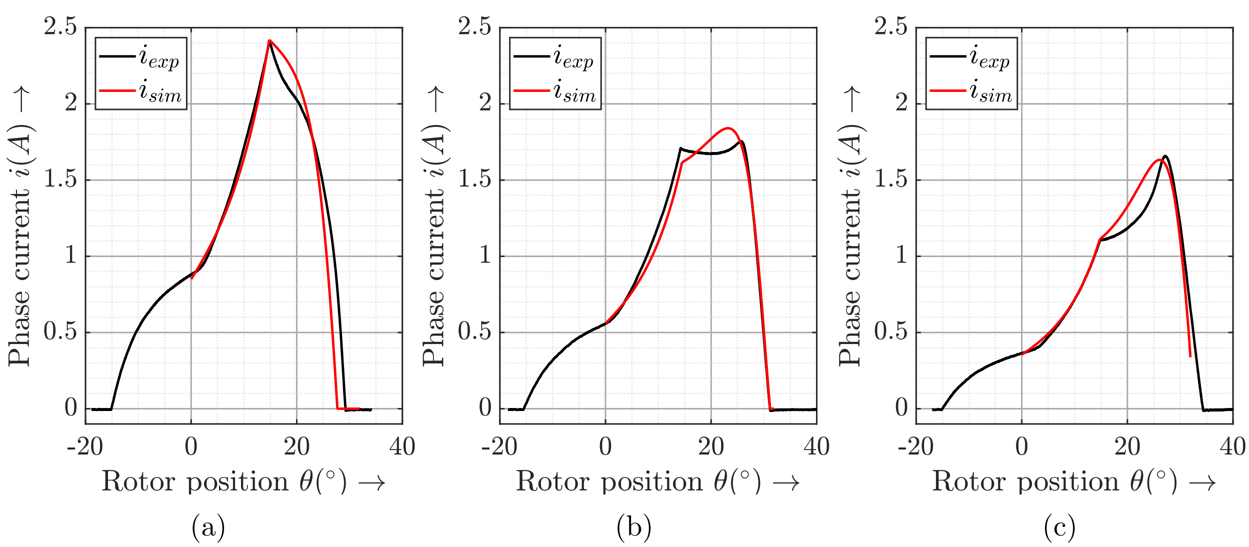

Figure 3.43: Generating experimental (i_{exp}) and simulated (i_{sim}) phase currents versus rotor angular position (θ) with $\theta_{on} = -15°$ and $\theta_{off} = 15°$ during (a) Negative feedback, (b) Zero feedback, and (c) Positive feedback

Generating: Turn-on Angle: $-15°$, Turn-off Angle: $20°$ (With Phase Advancing)

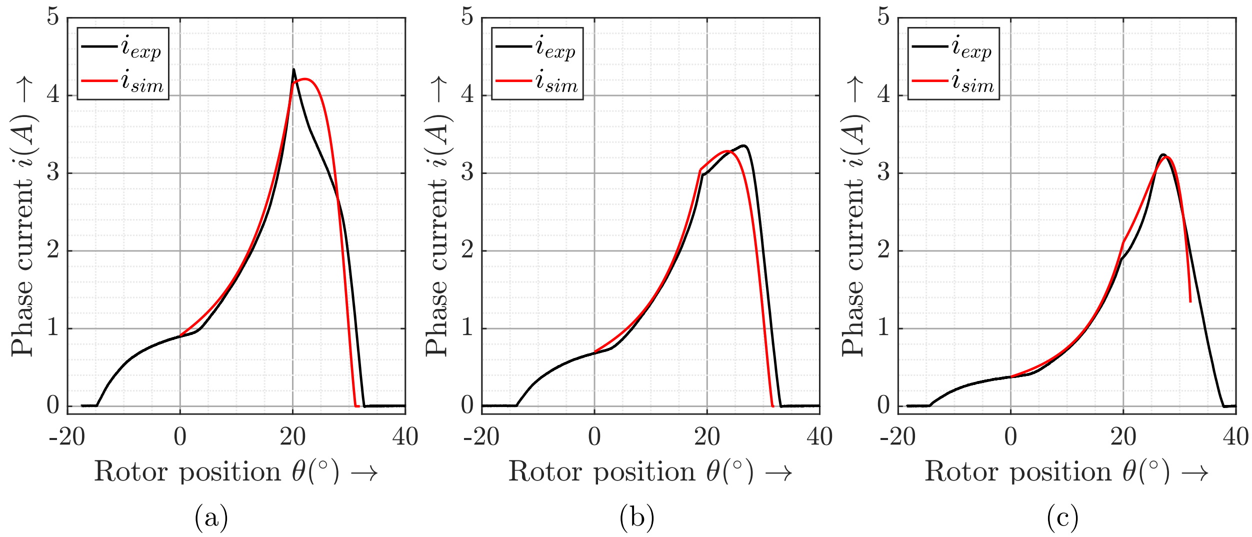

Figure 3.44: Generating experimental (i_{exp}) and simulated (i_{sim}) phase currents versus rotor angular position (θ) with $\theta_{on} = -15°$ and $\theta_{off} = 20°$ during (a) Negative feedback, (b) Zero feedback, and (c) Positive feedback

Generating: Turn-on Angle: $-15°$, Turn-off Angle: $25°$ (With Phase Advancing)

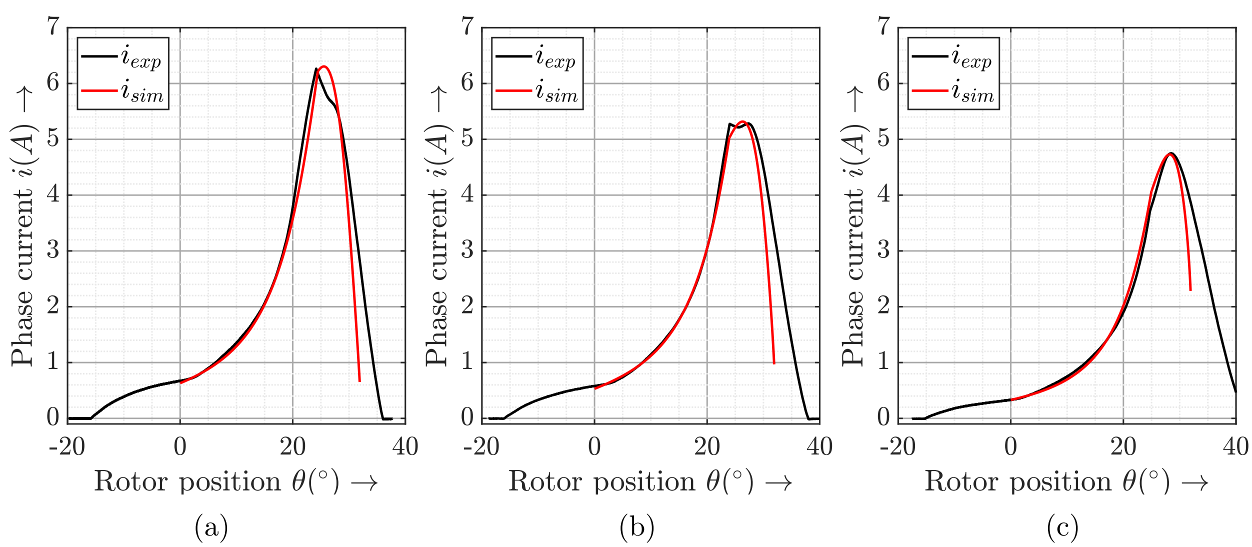

Figure 3.45: Generating experimental (i_{exp}) and simulated (i_{sim}) phase currents versus rotor angular position (θ) with $\theta_{on} = -15°$ and $\theta_{off} = 25°$ during (a) Negative feedback, (b) Zero feedback, and (c) Positive feedback

Generating: Turn-on Angle: $-10°$, Turn-off Angle: $15°$ (With Phase Advancing)

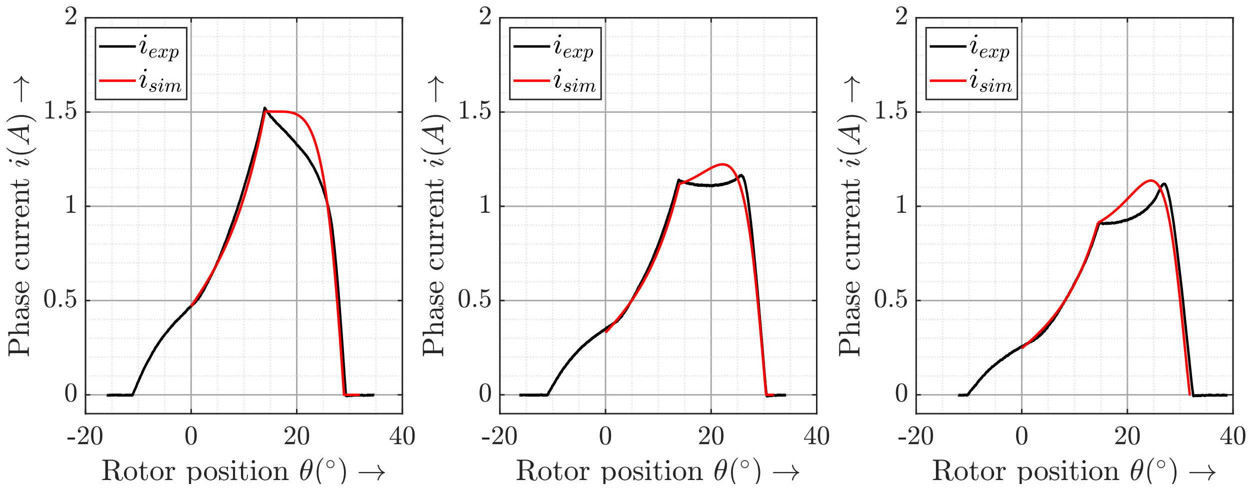

(a) (b) (c)

Figure 3.46: Generating experimental (i_{exp}) and simulated (i_{sim}) phase currents versus rotor angular position (θ) with $\theta_{on} = -10°$ and $\theta_{off} = 15°$ during (a) Negative feedback, (b) Zero feedback, and (c) Positive feedback

Generating: Turn-on Angle: $-10°$, Turn-off Angle: $20°$ (With Phase Advancing)

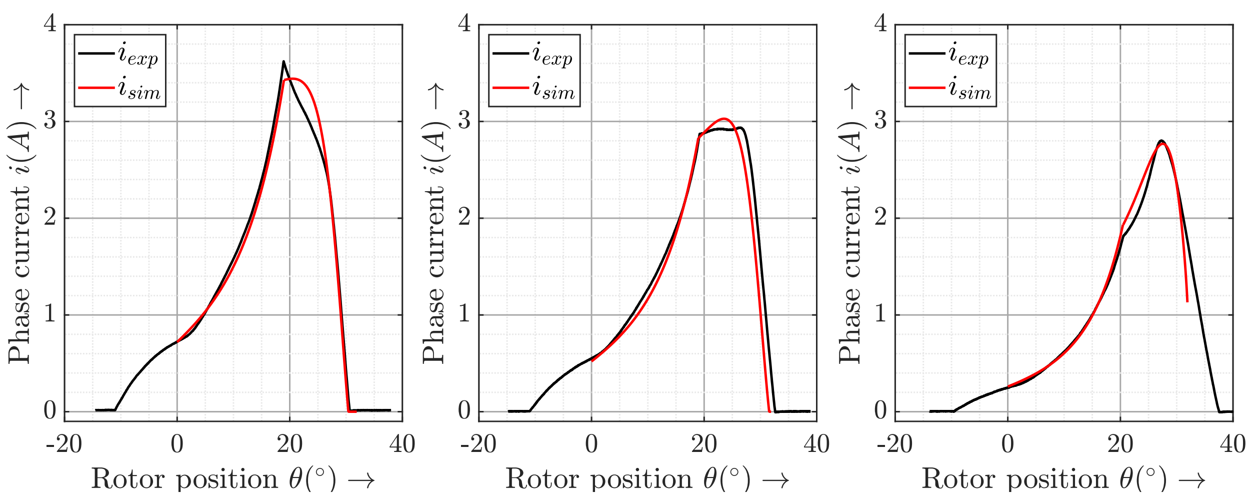

(a) (b) (c)

Figure 3.47: Generating experimental (i_{exp}) and simulated (i_{sim}) phase currents versus rotor angular position (θ) with $\theta_{on} = -10°$ and $\theta_{off} = 20°$ during (a) Negative feedback, (b) Zero feedback, and (c) Positive feedback

Generating: Turn-on Angle: $-10°$, Turn-off Angle: $25°$ (With Phase Advancing)

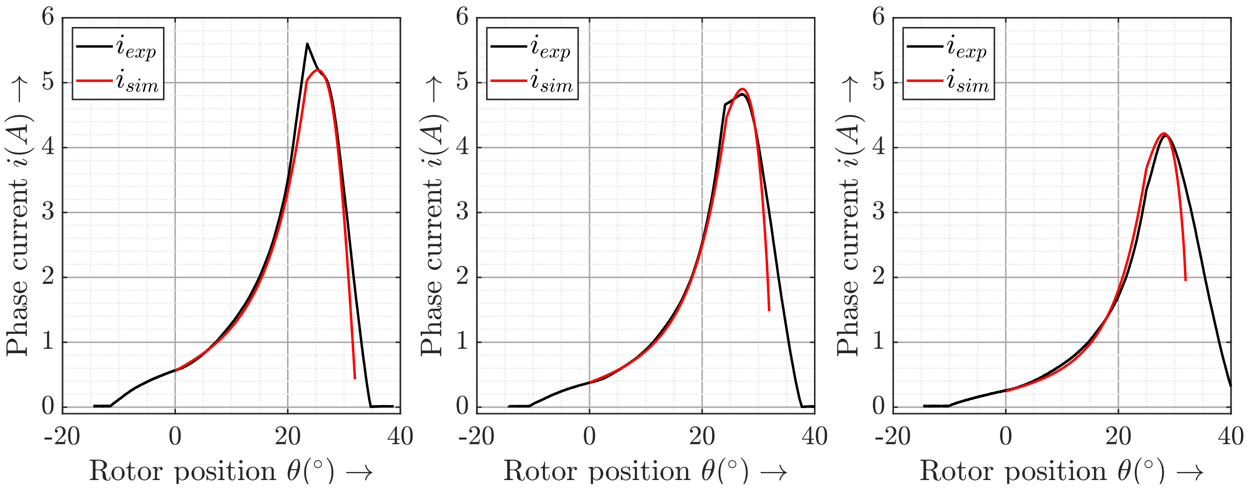

(a) (b) (c)

Figure 3.48: Generating experimental (i_{exp}) and simulated (i_{sim}) phase currents versus rotor angular position (θ) with $\theta_{on} = -10°$ and $\theta_{off} = 25°$ during (a) Negative feedback, (b) Zero feedback, and (c) Positive feedback

Generating: Turn-on Angle: $-5°$, Turn-off Angle: $15°$ (With Phase Advancing)

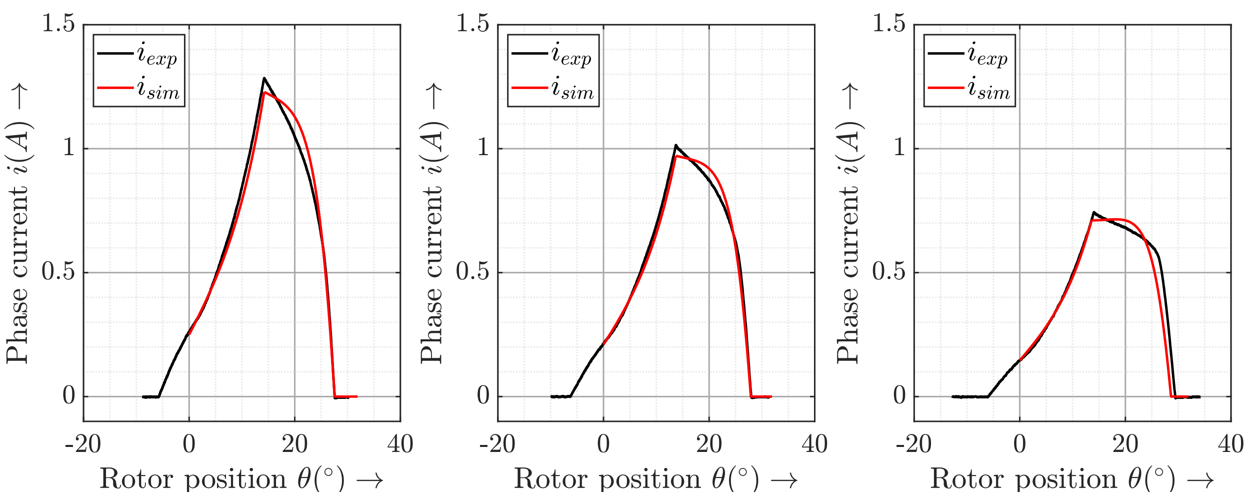

(a) (b) (c)

Figure 3.49: Generating experimental (i_{exp}) and simulated (i_{sim}) phase currents versus rotor angular position (θ) with $\theta_{on} = -5°$ and $\theta_{off} = 15°$ for (a) $\omega = 209$ rpm, (b) $\omega = 275$ rpm, and (c) $\omega = 372$ rpm

Generating: Turn-on Angle: $-5°$, Turn-off Angle: $20°$ (With Phase Advancing)

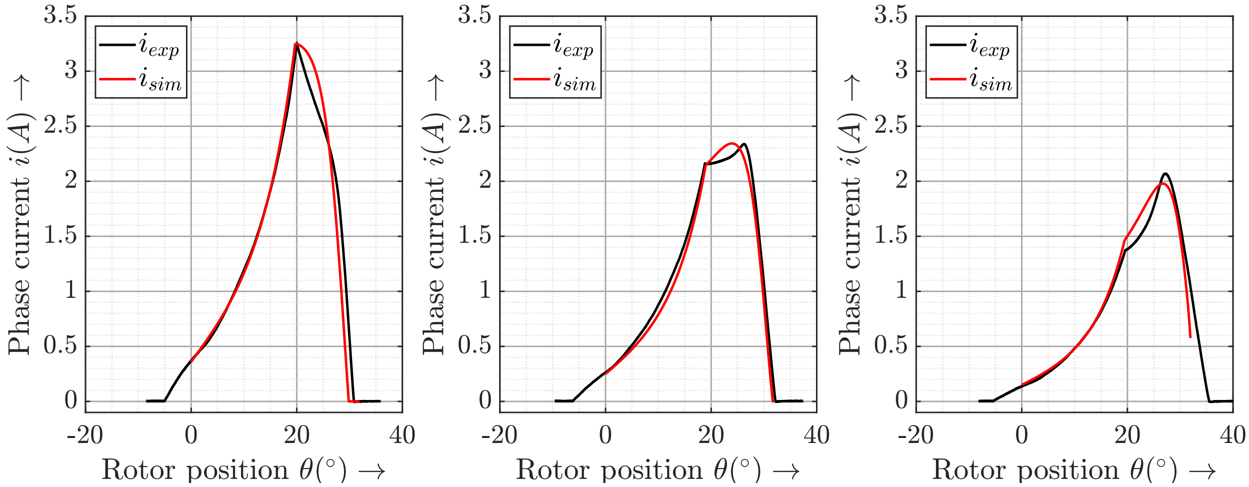

(a) (b) (c)

Figure 3.50: Generating experimental (i_{exp}) and simulated (i_{sim}) phase currents versus rotor angular position (θ) with $\theta_{on} = -5°$ and $\theta_{off} = 20°$ during (a) Negative feedback, (b) Zero feedback, and (c) Positive feedback

Generating: Turn-on Angle: $-5°$, Turn-off Angle: $25°$ (With Phase Advancing)

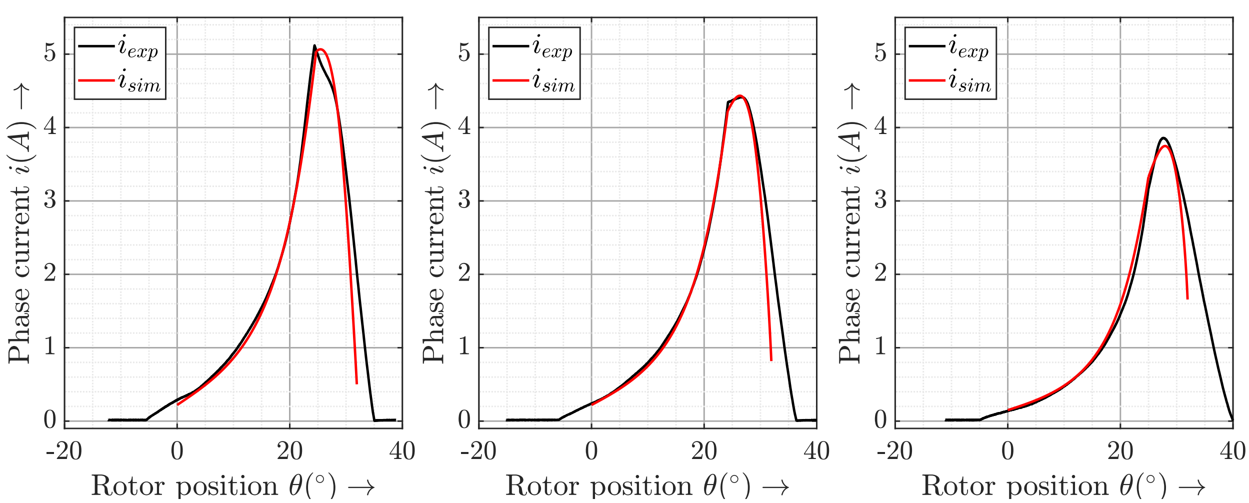

(a) (b) (c)

Figure 3.51: Generating experimental (i_{exp}) and simulated (i_{sim}) phase currents versus rotor angular position (θ) with $\theta_{on} = -5°$ and $\theta_{off} = 25°$ during (a) Negative feedback, (b) Zero feedback, and (c) Positive feedback

Generating: Turn-on Angle: 0°, Turn-off Angle: 15° (Without Phase Advancing)

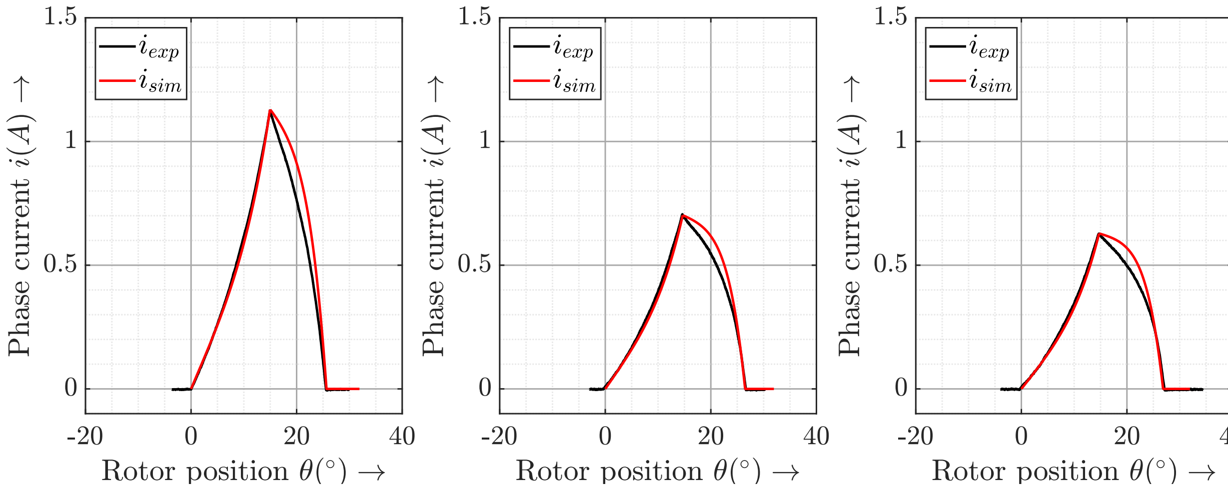

(a) (b) (c)

Figure 3.52: Generating experimental (i_{exp}) and simulated (i_{sim}) phase currents versus rotor angular position (θ) with $\theta_{on} = 0°$ and $\theta_{off} = 15°$ for (a) $\omega = 187$ rpm, (b) $\omega = 305$ rpm, and (c) $\omega = 371$ rpm

Generating: Turn-on Angle: 0°, Turn-off Angle: 20° (Without Phase Advancing)

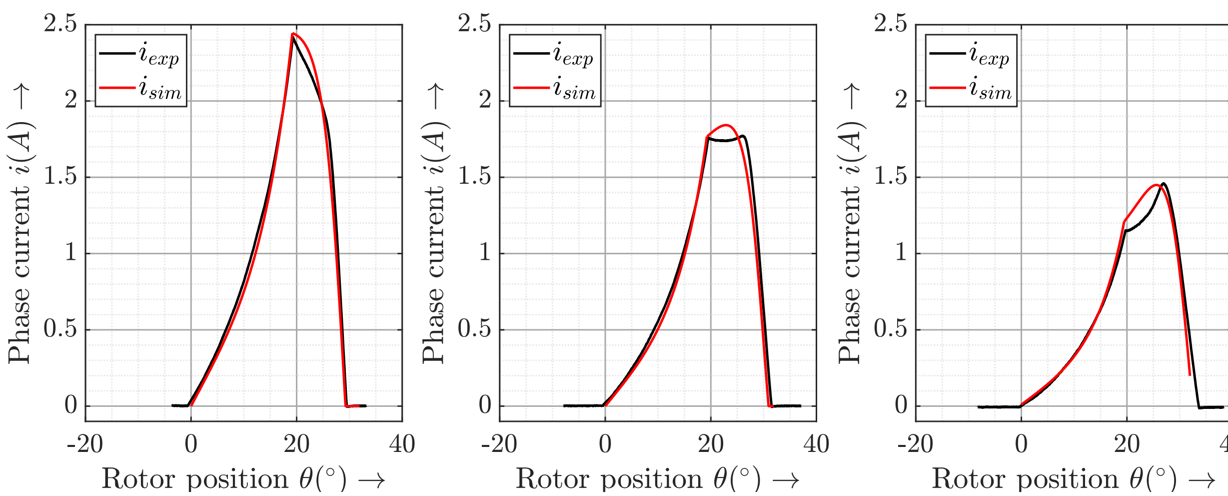

(a) (b) (c)

Figure 3.53: Generating experimental (i_{exp}) and simulated (i_{sim}) phase currents versus rotor angular position (θ) with $\theta_{on} = 0°$ and $\theta_{off} = 20°$ during (a) Negative feedback, (b) Zero feedback, and (c) Positive feedback

Generating: Turn-on Angle: 0°, Turn-off Angle: 25° (Without Phase Advancing)

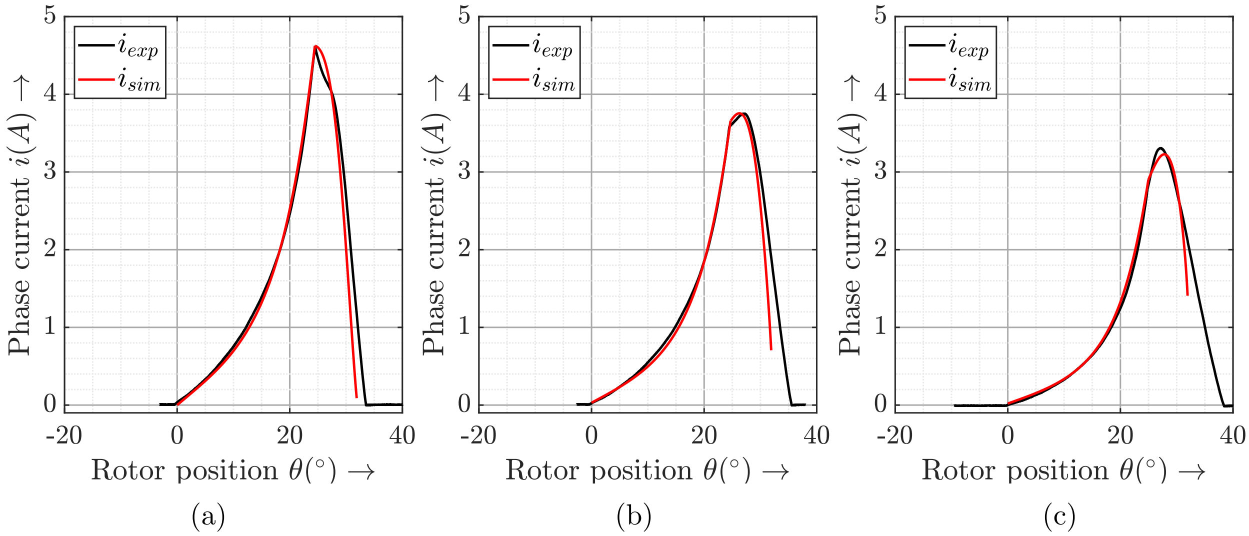

Figure 3.54: Generating experimental (i_{exp}) and simulated (i_{sim}) phase currents versus rotor angular position (θ) with $\theta_{on} = 0°$ and $\theta_{off} = 25°$ during (a) Negative feedback, (b) Zero feedback, and (c) Positive feedback

CHAPTER 4

PHASE CURRENT PEAK PREDICTION FOR SWITCHED RELUCTANCE GENERATORS

This chapter presents a technique to predict the peak value of a switched reluctance generator's phase current, while operating in positive feedback single pulse mode,[1] using which the machine is safely operated, resulting in a larger amount of harvested charge and higher output power. Safe operation of the machine ensures that the phase current's peak value does not exceed the specified rated current, thereby preserving the integrity and functionality of the drive's power converter. The prediction technique builds on the phase current expression presented in Chpater 3, specifically Equation 3.134. Two techniques to obtain the turn-off angle to predict the peak value of the phase current are presented. The first technique involves a comparative approach involving real time calculations to estimate the correct turn-off angle, while the second technique involves obtaining the correct value of the turn-off angle beforehand. The first step in estimating the correct turn-off angle involves the computation of the rotor angular position, where the phase current peak exists, which is presented next.

4.1 Estimating the Rotor Position at the Phase Current Peak

Figure 4.1 shows the phase current of a switched reluctance generator during positive feedback single pulse mode of operation, where the peak or maximum value of the phase current i_{max} occurs at θ_{max}. The goal is to have prior knowledge of i_{max} and θ_{max} in order to control the machine effectively. The value of i_{max} is obtained from the machine's datasheet and the drive power converter's peak current rating (specifically, the peak current rating of the

[1] Accepted for publication under the title: A Phase Current Peak Prediction Technique to Increase the Output Power of Switched Reluctance Generators for Wind Turbines, in the: 2019 IEEE Energy Conversion Congress and Exposition (ECCE), © 2019 IEEE.

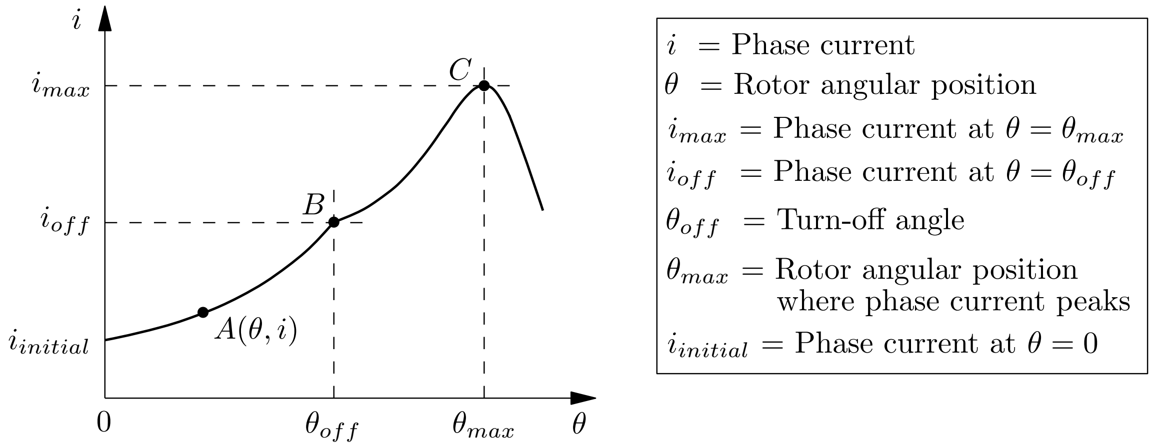

Figure 4.1: Phase current of a switched reluctance generator during positive feedback single pulse mode of operation

diodes of the asymmetric bridge converter). Since the peak value of phase current (i_{max}) is known based on the hardware used, it is used to compute the value of θ_{max}, after which the turn-off angle (θ_{off}) is calculated. Once the value of the turn-off angle is obtained, using it in the control algorithm ensures that the phase current peaks at the desired level (i_{max}), i.e., the control algorithm is capable of predicting the peak value of the phase current based on the turn-off angle. The first step in the estimation of the turn-off angle includes computing the expression for θ_{max}. The value of θ_{max} is obtained using the properties of a local maxima (i.e., at θ_{max}, the slope of phase current with respect to rotor position is zero). The phase current during generation is expressed by Equation 3.134 and is rewritten as:

$$i = \frac{V_{bus}(\beta_g - \theta)}{\omega L(\theta)(\tau\alpha_g - 1)} + C_6 \left[\frac{(\beta_g - \theta)^{\tau\alpha_g}}{\zeta_g L(\theta)}\right] \tag{4.1}$$

Therefore, equating the derivative of phase current (using Equation 4.1) with respect to the rotor position to zero at $\theta = \theta_{max}$, the following expression is obtained:

$$0 = \frac{\omega L(\theta_{max})(\tau\alpha_g - 1)(-V_{bus}) - V_{bus}(\beta_g - \theta_{max})\omega L'(\theta_{max})(\tau\alpha_g - 1)}{[\omega L(\theta_{max})(\tau\alpha_g - 1)]^2} + C_6 \left\{\frac{\zeta_g L(\theta_{max})\tau\alpha_g(\beta_g - \theta_{max})^{(\tau\alpha_g - 1)}(-1) - (\beta_g - \theta_{max})^{\tau\alpha_g}\zeta_g L'(\theta_{max})}{[\zeta_g L(\theta_{max})]^2}\right\} \tag{4.2}$$

where, $L'(\theta)$ is the derivative of the inductance profile with respect to rotor position. Obtaining the expression for θ_{max} from Equation 4.2 is not possible as the equation contains an unknown integration constant C_6, even if it were possible, due to its sheer size and complexity, it would not be very useful. As a result, another alternative ought to be explored in order to obtain the expression for θ_{max}. Consider the current differential equation given by Equation 3.104, which is rewritten as:

$$\frac{di}{d\theta} = \frac{(V_{bus} - iR) - \omega i \dfrac{dL(\theta)}{d\theta}}{\omega L(\theta)} \tag{4.3}$$

As stated earlier, during the demagnetization phase, the machine's phase voltage is negative. Thus, factoring out the negative sign from V_{bus}, the following expression is obtained:

$$\frac{di}{d\theta} = \frac{-|V_{bus}| - iR - \omega i \dfrac{dL(\theta)}{d\theta}}{\omega L(\theta)} \tag{4.4}$$

Again, in order to obtain an expression for θ_{max}, the properties of a local maxima are applied to Equation 4.4, i.e., the derivative of phase current with respect to rotor position is equated to zero at $\theta = \theta_{max}$, where $i = i_{max}$, resulting in the following expression:

$$0 = -|V_{bus}| - i_{max}R - \omega i_{max} \left. \frac{dL(\theta)}{d\theta} \right|_{\theta=\theta_{max}} \tag{4.5}$$

From Equation 3.82, the derivative of phase inductance with respect to rotor position evaluated at $\theta = \theta_{max}$ is expressed as:

$$\left. \frac{dL(\theta)}{d\theta} \right|_{\theta=\theta_{max}} = -\kappa N_r L_1 \sin(\kappa N_r \theta_{max} + \kappa N_r \phi) \tag{4.6}$$

Substituting the expression from Equation 4.6 in Equation 4.5, the following expression is obtained:

$$\sin(\kappa N_r \theta_{max} + \kappa N_r \phi) = \frac{|V_{bus}| + i_{max}R}{\omega i_{max} \kappa N_r L_1} \tag{4.7}$$

Rearranging Equation 4.7, the expression for θ_{max} is obtained as:

$$\theta_{max} = \frac{1}{\kappa N_r} \sin^{-1}\left(\frac{|V_{bus}| + i_{max}R}{\omega i_{max}\kappa N_r L_1}\right) - \phi \tag{4.8}$$

Now that the values of i_{max} and θ_{max} are known, they are used as initial conditions to solve for the integration constant C_6 of Equation 4.1. Since the calculations relate to the demagnetization phase, the machine's phase voltage is negative. Factoring out the negative sign from V_{bus} of Equation 4.1, the integration constant C_{6-max} is expressed as:

$$C_{6-max} = \left[i_{max} + \frac{|V_{bus}|(\beta_g - \theta_{max})}{\omega L(\theta_{max})(\tau\alpha_g - 1)}\right]\left[\frac{\zeta_g L(\theta_{max})}{(\beta_g - \theta_{max})^{\tau\alpha_g}}\right] \tag{4.9}$$

where, C_{6-max} is the demagnetizing integration constant calculated based on θ_{max} and i_{max} and represents the integration constant C_6 for the demagnetization phase current trajectory. The next step involves the calculation of the turn-off angle, which is presented using two techniques, the first of which uses a comparative approach and is presented next.

4.2 Estimation of the Turn-off Angle Based on a Comparative Approach

This section presents a technique of estimating the turn-off angle in real time using a comparative approach. Referring to Figure 4.1 and Equation 4.9, the demagnetizing integration constant is computed using the coordinates of point C (i.e., θ_{max} and i_{max}); however, the same value for the demagnetizing integration constant is obtained when the coordinates of point B are used instead (as the phase current trajectory during the demagnetization phase passes through both the points, i.e., point B and point C). Making use of this property, the control algorithm can determine the turn-off angle by performing real time comparisons during the magnetization phase.

Consider the portion of Figure 4.1, where the phase is magnetized, i.e., for values of rotor positions ranging from: $0 \leq \theta \leq \theta_{off}$. During this portion, i.e., point A in Figure 4.1, the controller senses the phase current's value along with the rotor position (using a position sensor) and proceeds to compute the demagnetizing integration constant (C_6) using the following expression:

$$C_6 = \left[i + \frac{|V_{bus}|(\beta_g - \theta)}{\omega L(\theta)(\tau\alpha_g - 1)}\right]\left[\frac{\zeta_g L(\theta)}{(\beta_g - \theta)^{\tau\alpha_g}}\right] \tag{4.10}$$

The expression for demagnetizing integration constant C_6 of Equation 4.10 is obtained using Equation 4.1 for the demagnetization phase, where the machine's phase voltage across is negative, as a result, the negative sign from V_{bus} is factored out. The value of C_6 from Equation 4.10 represents the expression for the demagnetizing integration constant for rotor position θ and phase current i (i.e., coordinates of point A). The value of C_6 is computed for all rotor positions (in real time, as the rotor changes its position from 0 to θ_{off}) ranging from: $0 \leq \theta \leq \theta_{off}$. When point A finally becomes point B, the C_6 value computed using Equation 4.10 matches the earlier computed value of the demagnetizing integration constant C_{6-max}. The rotor position at which the comparison between C_6 and C_{6-max} results in a match is the turn-off angle in order for the phase current to peak at desired its level, i.e., i_{max}.

This technique of computing the turn-off angle is based on a continuous comparative approach, where the controller computes the demagnetizing integration constant using Equation 4.10 at every sampled rotor position ranging from: $0 \leq \theta \leq \theta_{off}$, and compares it with the demagnetizing integration constant C_{6-max} precalculated using Equation 4.9. Since the demagnetizing integration constant C_6 is computed continuously at every sampled rotor positions, this technique is computationally demanding, which led to the development of a technique of estimating the turn-off angle beforehand rather than using a compute and compare approach.

4.3 Estimation of the Turn-off Angle Based on a One Step Approach

This section presents a technique of estimating the turn-off angle using a one step approach, wherein its value is precalculated beforehand. From Figure 4.2, the magnetization phase current trajectory (represented by i_1) and the demagnetizing phase current trajectory (represented by i_2) intersect at point B, where $i_1 = i_2$.

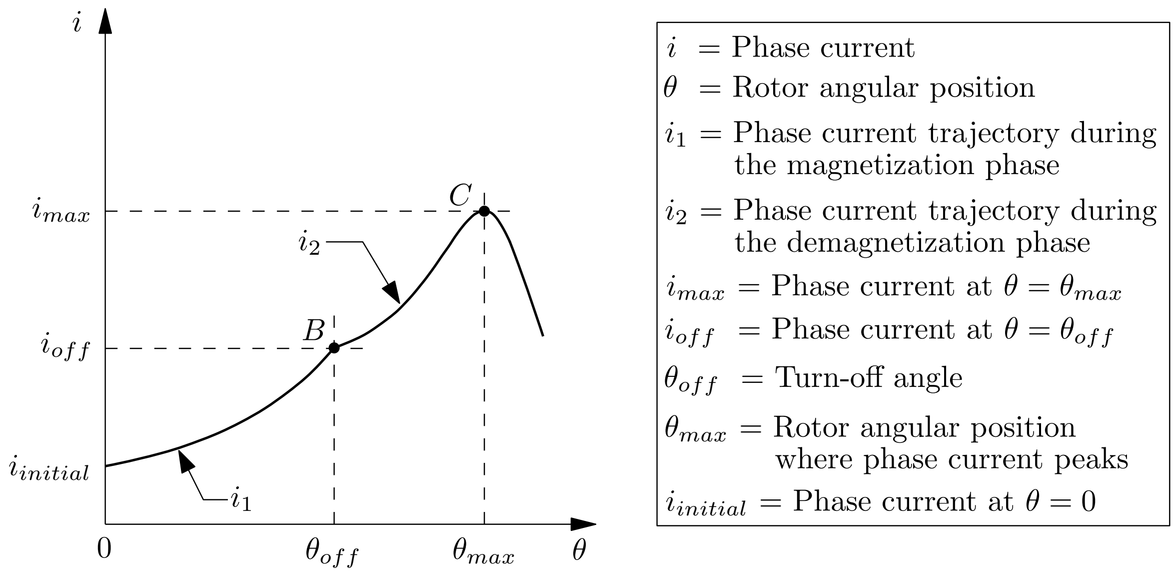

Figure 4.2: Phase current of a switched reluctance generator during positive feedback single pulse mode of operation, highlighting the magnetization i_1 and demagnetization i_2 phase currents

This technique makes use of the property that $i_1 = i_2$ at $\theta = \theta_{off}$. Using Equation 4.1, the magnetization phase current trajectory is described by the following expression:

$$i_1 = \frac{V_{bus}(\beta_g - \theta)}{\omega L(\theta)(\tau\alpha_g - 1)} + C_{6-1}\left[\frac{(\beta_g - \theta)^{\tau\alpha_g}}{\zeta_g L(\theta)}\right] \tag{4.11}$$

where, C_{6-1} represents the magnetizing integration constant, which is calculated based on the application of the initial conditions (i.e., $i = i_{initial}$ and $\theta = 0$) in Equation 4.11. The magnetizing integration constant C_{6-1} for the magnetization phase current trajectory i_1 is expressed as:

$$C_{6-1} = \left[i_{initial} - \frac{V_{bus}\beta_g}{\omega L(0)(\tau\alpha_g - 1)}\right]\left[\frac{\zeta_g L(0)}{\beta_g^{\tau\alpha_g}}\right] \tag{4.12}$$

At $\theta = 0$, the value of phase inductance is equal to the aligned position inductance, i.e., $L(0) = L_a$. Replacing the value of $L(0)$ with the aligned position inductance in Equation 4.12, the following expression is obtained:

$$C_{6-1} = \left[i_{initial} - \frac{V_{bus}\beta_g}{\omega L_a(\tau\alpha_g - 1)} \right] \left[\frac{\zeta_g L_a}{\beta_g^{\tau\alpha_g}} \right] \tag{4.13}$$

Similarly, using Equation 4.1, the demagnetization phase current trajectory is described by the following expression (after factoring out the negative sign from V_{bus}, as the machine's phase voltage during the demagnetization phase is negative):

$$i_2 = \frac{-|V_{bus}|(\beta_g - \theta)}{\omega L(\theta)(\tau\alpha_g - 1)} + C_{6-2} \left[\frac{(\beta_g - \theta)^{\tau\alpha_g}}{\zeta_g L(\theta)} \right] \tag{4.14}$$

where, C_{6-2} represents the demagnetizing integration constant, which is calculated based on the application of the initial conditions (i.e., $i = i_{max}$ and $\theta = \theta_{max}$) in Equation 4.14. The demagnetizing integration constant C_{6-2} for the demagnetization phase current trajectory i_2 is expressed as:

$$C_{6-2} = \left[i_{max} + \frac{|V_{bus}|(\beta_g - \theta_{max})}{\omega L(\theta_{max})(\tau\alpha_g - 1)} \right] \left[\frac{\zeta_g L(\theta_{max})}{(\beta_g - \theta_{max})^{\tau\alpha_g}} \right] \tag{4.15}$$

On comparing Equations 4.9 and 4.15, it turns out that the two demagnetizing integration constants C_{6-max} and C_{6-2} are equal (since they make use of the same initial conditions, i.e., $i = i_{max}$ and $\theta = \theta_{max}$).

To compute the value of the turn-off angle, the magnetization phase current from Equation 4.11 and the demagnetization phase current from Equation 4.14 are equated to each other at $\theta = \theta_{off}$, as a result, the following expression is obtained:

$$\frac{V_{bus}(\beta_g - \theta_{off})}{\omega L(\theta_{off})(\tau\alpha_g - 1)} + C_{6-1} \left[\frac{(\beta_g - \theta_{off})^{\tau\alpha_g}}{\zeta_g L(\theta_{off})} \right] = \frac{-|V_{bus}|(\beta_g - \theta_{off})}{\omega L(\theta_{off})(\tau\alpha_g - 1)} + C_{6-2} \left[\frac{(\beta_g - \theta_{off})^{\tau\alpha_g}}{\zeta_g L(\theta_{off})} \right] \tag{4.16}$$

Rearranging Equation 4.16, the following expression is obtained:

$$\frac{2|V_{bus}|(\beta_g - \theta_{off})}{\omega L(\theta_{off})(\tau\alpha_g - 1)} = \left[\frac{(\beta_g - \theta_{off})^{\tau\alpha_g}}{\zeta_g L(\theta_{off})} \right] (C_{6-2} - C_{6-1}) \tag{4.17}$$

Again, rearranging Equation 4.17, the following expression is obtained:

$$\frac{2|V_{bus}|\zeta_g}{\omega(\tau\alpha_g - 1)(C_{6-2} - C_{6-1})} = (\beta_g - \theta_{off})^{\tau\alpha_g - 1} \tag{4.18}$$

Finally, from Equation 4.18, the expression for the turn-off angle is expressed as:

$$\begin{aligned} \theta_{off} &= \beta_g - \left[\frac{2|V_{bus}|\zeta_g}{\omega(\tau\alpha_g - 1)(C_{6-2} - C_{6-1})}\right]^{\frac{1}{(\tau\alpha_g - 1)}} \\ &= \beta_g - \left[\frac{\omega(\tau\alpha_g - 1)(C_{6-2} - C_{6-1})}{2|V_{bus}|\zeta_g}\right]^{\frac{1}{(1-\tau\alpha_g)}} \end{aligned} \tag{4.19}$$

So far, two techniques of estimating the turn-off angle have been presented. However, they both assume that at the turn-off angle, the machine's phase voltage is less than the established back EMF, i.e., $V < e$, implying that the phase current is in a state of positive feedback. The next section presents a technique of estimating the turn-off angle when the phase current is in a state of zero or negative feedback during generation.

4.4 Estimation of Turn-off Angle Under Zero and Negative Feedback Operation

As stated earlier in Sections 2.5.1 and 2.5.2, the generating phase current under zero and negative feedback remains controllable and does not pose a threat to the drive's power converter or the machine itself. The negative and zero feedback scenarios occur when the established back EMF at the turn-off angle is lesser than (or equal to) the machine's phase voltage. A lower established value of back EMF does not oppose the applied bus voltage as much as a higher value does. As a result, the effective voltage across the machine's phase is higher, which assists the phase current to build up more rapidly and reach the maximum allowable peak value quicker.

In this case, a simple comparator compares the value of the phase current with the maximum allowable peak current and when the two are equal, the phase is switched off. Figure 4.3 shows the machine operating under negative feedback, where θ_{max} is the same as θ_{off} and i_{max} is the same as i_{off}. From Figure 4.3, after the phase is switched off, no local maxima is observed in the trajectory of the phase current, as a result, the controller presented so far is unable to compute the value of θ_{max} (i.e., the rotor position where the slope of the phase current is zero). Mathematically, this phenomenon manifests itself through Equation 4.8, where during the negative feedback operation, the inverse of the sine function is unable to return a valid value, as its argument exceeds the valid range for an argument x, for the inverse sine function (i.e., the valid range of x is: $0 \leq x \leq 1$). Intuitively, the negative feedback scenario occurs when the mechanical energy provided by the prime mover is low, i.e., the angular velocity (ω) is low. Since the argument of the inverse sine function in Equation 4.8 is inversely proportion to angular velocity, its value exceeds 1 for low values of angular velocity, which implies that a maxima (θ_{max}) does not exist.

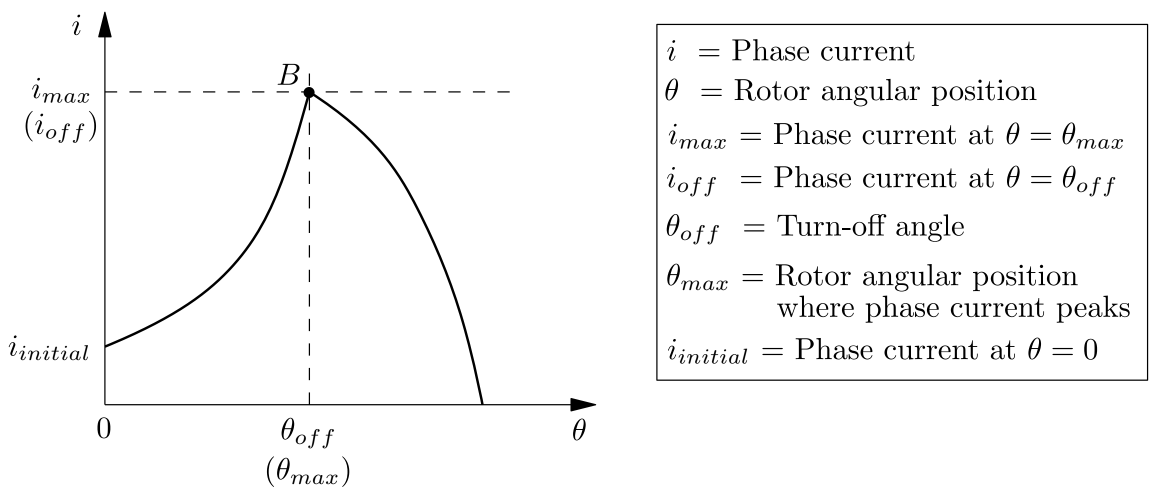

Figure 4.3: Phase current of a switched reluctance generator during negative feedback single pulse mode of operation

In the zero feedback scenario, the value of θ_{max} does exist and can be used to switch off the phase; however, the value of phase current at θ_{off} is equal to the maximum allowable level, as a result, a comparator can also be used to switch the phase off. Therefore, in the zero feedback scenario, the phase is switched off either by computing the value of θ_{max} and then using the control technique described earlier or it is switched off using a comparator when the sensed phase current reaches its maximum allowable level. To accommodate the zero and negative feedback scenarios, a comparator is enabled in the control algorithm and is shown in the flowchart of Figure 4.4. A complete detailed flowchart of the entire control algorithm is presented in Appendix I.

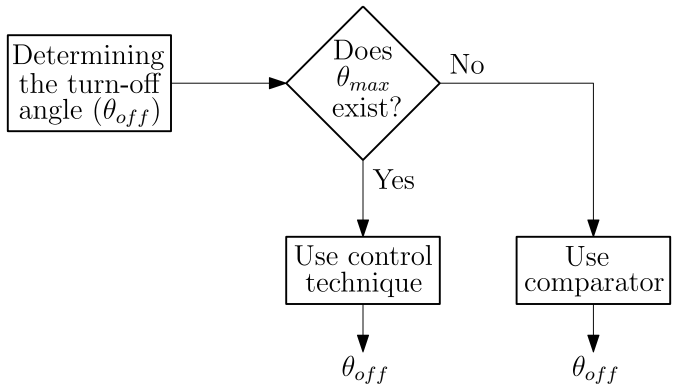

Figure 4.4: Flowchart used to estimate the turn-off angle

4.5 Experimental Results

This section presents experimental results recorded from the setup shown in Appendix J using the machine specified in Table A.2 in Appendix A, which is characterized in Appendix C. Since a technique to predict the peak value of phase current is provided in Sections 4.2 and 4.3, the experimental results presented in this section are used to verify the accuracy of the technique in determining the correct turn-off angle, such that the phase current peaks at the desired level. Two scenarios wherein the machine is operated as a generator in single pulse mode are executed, and the simulated and experimental data for both scenarios is compared. The first scenario mimics a situation, in which the angular velocity of a switched reluctance generator is maintained at a constant value with the help of a prime mover while the peak value (i_{max}) of the phase current is changed. The simulation (i_{sim}) and experimental (i_{exp}) results of the phase currents are shown in Figure 4.5. In Figure 4.5(a), the value of i_{max} is assigned as 0.5 A, which is not that high and results in a calculated turn-off angle of 7.51°. As a result, the phase current remains in a state of negative feedback as seen in Figure 4.5(a). The remaining results shown in Figure 4.5 correspond to increasing values of i_{max} (i.e., from 1.0 A to 3.5 A), during which the phase current enters into a state of positive feedback. In all the results provided in Figure 4.5, the phase current always peaks at the desired level based on the calculated turn-off angle using Equation 4.19.

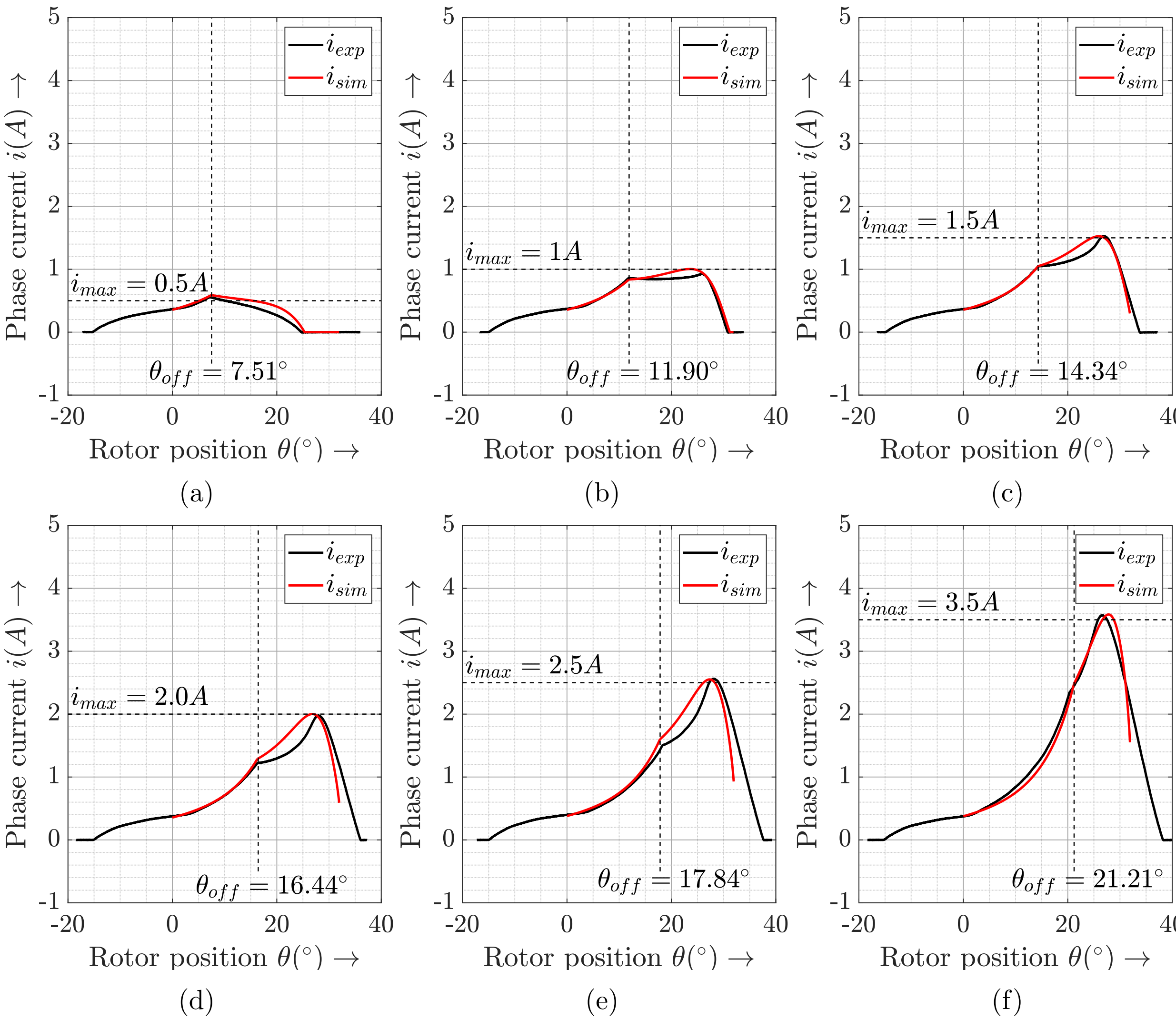

Figure 4.5: Simulation (i_{sim}) and experimental (i_{exp}) phase current results at a constant angular velocity: $\omega = 400$ rpm, with (a) $i_{max} = 0.5$ A, (b) $i_{max} = 1.0$ A, (c) $i_{max} = 1.5$ A, (d) $i_{max} = 2.0$ A, (e) $i_{max} = 2.5$ A, and (f) $i_{max} = 3.5$ A

The second scenario mimics a situation in which the angular velocity of the switched reluctance generator is varied through the prime mover and the turn-off angle is computed, ensuring that the phase current peaks at the desired i_{max} value. This scenario is similar to one experienced by a wind generator, wherein a changing wind speed causes a change in the angular velocity of the machine's shaft. Figure 4.6 presents the results of this scenario

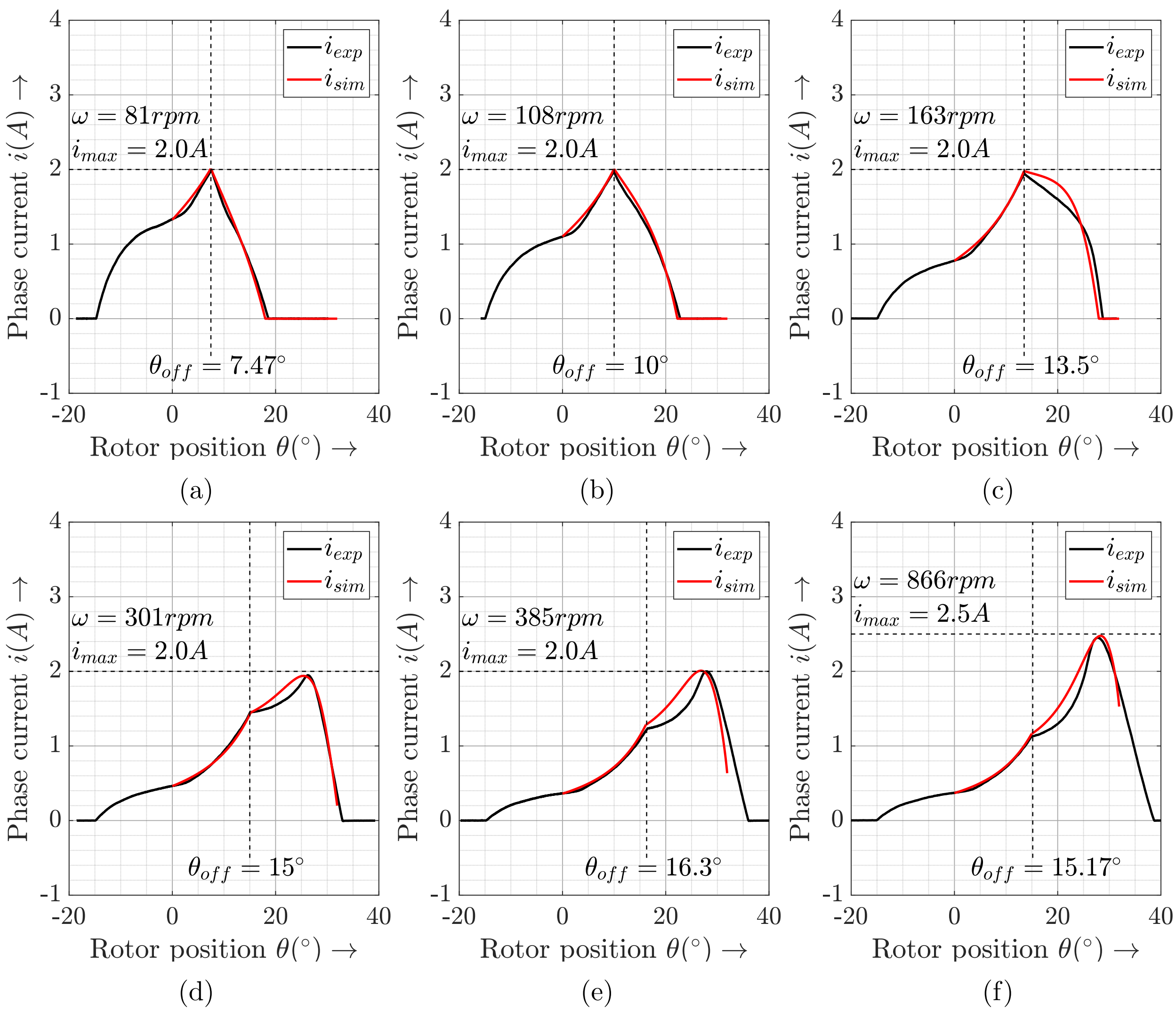

Figure 4.6: Simulation (i_{sim}) and experimental (i_{exp}) phase current results at changing angular velocities: (a) $w = 81$ rpm and $i_{max} = 2.0$ A, (b) $w = 108$ rpm and $i_{max} = 2.0$ A, (c) $w = 163$ rpm and $i_{max} = 2.0$ A, (d) $w = 301$ rpm and $i_{max} = 2.0$ A, (e) $w = 385$ rpm and $i_{max} = 2.0$ A, and (f) $w = 866$ rpm and $i_{max} = 2.5$ A

wherein the value of i_{max} is assigned as 2.0 A and the angular velocity is varied from 81 rpm in Figure 4.6(a) to 866 rpm Figure 4.6(f). In the results shown in Figure 4.6(f), the i_{max} value was also simultaneously varied to 2.5 A. Once again, in all the results provided in Figure 4.6, the phase current always peaks at the desired level based on the calculated turn-off angle using Equation 4.19.

4.6 Effect of Winding Resistance

A switched reluctance machine exhibits characteristics of a chaotic system. A chaotic system is defined as one which is deterministic in nature with a sensitive dependence on its initial conditions [117]. A deterministic system has no randomness to it, the seemingly random or irregular behavior of the system arises from its nonlinearity rather than random or noisy inputs. Sensitive dependence on the initial condition implies, trajectories close to each other separate from each other exponentially quickly.

A switched reluctance machine's flux linkage and inductance profile are highly nonlinear in nature, due to which, the machine's phase current trajectory appears to be irregular or random. However, the phase current trajectory is in fact not irregular or random, but rather, it is deterministic in nature, evolving in accordance with the characteristics of the nonlinear describing system. The phase current trajectory is also extremely sensitive to the initial conditions, i.e., a small change in the initial conditions results in a significant deviation in the current trajectory. This phenomenon is especially magnified during the positive feedback single pulse operating mode of a switched reluctance generator.

Due to the highly chaotic dynamics of a switched reluctance machine, it is imperative to model the machine's phase current accurately, capturing the effects of parameters which control the evolution of phase current and have the potential to alter the initial conditions of the system. A poor estimation of the machine's parameters gives rise to an error, which propagates throughout the model. The ripple effect of the error manifests itself through a poor reconstruction of the phase current, leading to an over or under estimated current peak, which in turn affects the turn-off angle of the phase, resulting in an incorrect estimation of the output power of the machine.

An important parameter of a switched reluctance machine is its winding resistance. This section presents the impact of the machine's winding resistance on the reconstructed phase current during single pulse mode while generating (which also serves as a comparison between the model with and without winding resistance). The expression for the phase current from Equation 3.134 is rewritten as:

$$i = \frac{V_{bus}(\beta_g - \theta)}{\omega L(\theta)(\tau\alpha_g - 1)} + C_6 \left[\frac{(\beta_g - \theta)^{\tau\alpha_g}}{\zeta_g L(\theta)} \right] \tag{4.20}$$

where, τ and ζ (defined earlier) are functions of the machine's winding resistance. The winding resistance relates to τ as follows:

$$\tau = \frac{R}{\omega} \tag{4.21}$$

The winding resistance relates to ζ as follows:

$$\begin{aligned} \zeta_g &= \tau\alpha_g\gamma_g \\ &= \frac{R}{\omega}\alpha_g\gamma_g \end{aligned} \tag{4.22}$$

From Equation 4.20, the integration constant C_6 is expressed as:

$$C_6 = \left[i - \frac{V_{bus}(\beta_g - \theta)}{\omega L(\theta)(\tau\alpha_g - 1)} \right] \frac{\zeta_g L(\theta)}{(\beta_g - \theta)^{\tau\alpha_g}} \tag{4.23}$$

Next, the effect of the machine's winding resistance is examined around a particular operating point, at which the applied bus voltage is 12 V, the turn on angle is -15° (i.e., phase advancing is employed), the turn off angle is +15°, and the angular velocity is 380 rpm. The evolution of the phase current with respect to rotor position is shown in Figure 4.7. For the switched reluctance machine setup considered and the results shown in Figure 4.7, the winding resistance (along with parasitic resistances) is 3.2 Ω (an accurate technique of estimating a machine's winding resistance is presented in Appendix G). The error between the reconstructed phase current (simulated) and the experimental phase current at the current peak lies within the ±2% error bounds, as a result, the simulated phase current is accurate enough and considered for the subsequent analysis. This is because the effects of the winding resistance below 3.2 Ω cannot be examined as that is the minimum value measured from the setup; however, for analysis regarding values of winding resistance greater than 3.2 Ω, experimental results can be obtained by adding resistance in series to the machine's terminals, though that has not been performed.

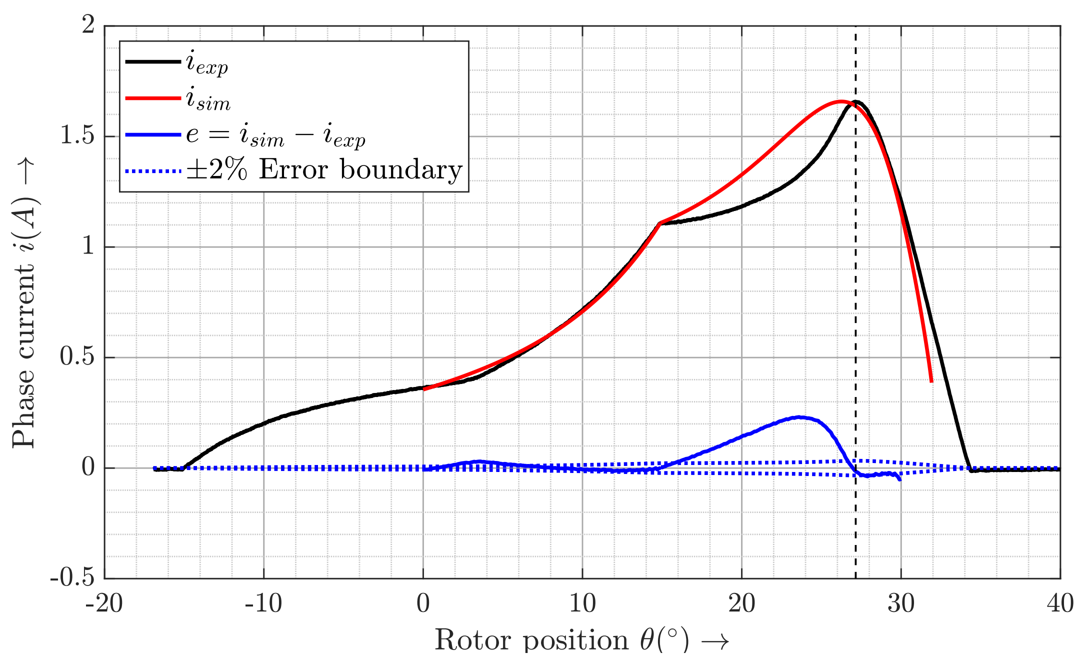

Figure 4.7: Evolution of the phase current with respect to rotor position during generation

Figure 4.8 shows the simulation result for the phase current during generation, at the operating point specified earlier, for three different values of winding resistance. From the figure, it is observed that when $R = 0\ \Omega$, the phase current peaks at a much higher value, intuitively this holds true, as there is no damping in the system. Similarly, for values of

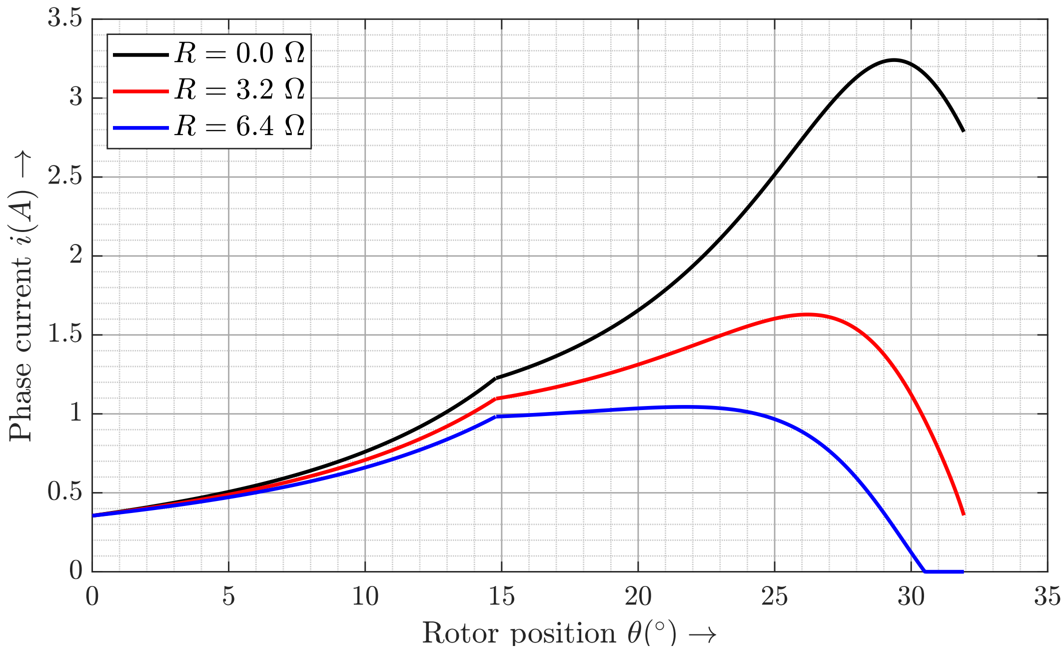

Figure 4.8: Evolution of the phase current with respect to rotor position during generation at $R = 0.0\ \Omega$, $R = 3.2\ \Omega$, and $R = 6.4\ \Omega$ ($V_{bus} = 12$V and $\omega = 380$ rpm)

$R = 3.2\ \Omega$ (the actual value of the setup's resistance) and $R = 6.4\ \Omega$ (twice the actual value of the setup's resistance), the peak of the phase current reduces.

From the standpoint of predicting the peak value of the phase current, underestimating the phase resistance is a safer option compared to overestimating it. When the winding resistance is underestimated, i.e., the winding resistance considered in the control algorithm is lesser than its true value, then the reconstructed phase current peaks at a higher value than its true value, as a result, the control algorithm switches off the phase earlier (expecting the current peak to exceed the allowable value). The downside of underestimating the winding resistance is that less charge is harvested during the demagnetization phase (due to an earlier turn off angle); however, there is no damage to the drive's power converter due to excessive current levels.

On the other hand, if the winding resistance is overestimated, it could lead to an unsafe operation of the drive and the machine. When the winding resistance is overestimated, i.e., the winding resistance considered in the control algorithm is greater than its true value, then the reconstructed phase current peaks at a lower value than its true value, as a result, the control algorithm switches off the phase later. The risk of overestimating the winding resistance is that the phase current peak exceeds the allowable level (due to a later turn off angle), which can damage the drive's power converter.

At the operating point stated earlier, a sweep of the winding resistance is performed and the peak error percentage $\delta\%$ is calculated using the following expression:

$$\delta(\%) = \frac{i_{max}(R) - i_{max}(3.2)}{i_{max}(3.2)} \times 100 \tag{4.24}$$

where, $i_{max}(R)$ represents the peak value of phase current for a winding resistance value of R and $i_{max}(3.2)$ represents the peak value of phase current for a winding resistance value of 3.2 Ω (i.e., its true value) at the operating point considered. The plot of the peak error percentage ($\delta\%$) versus the winding resistance (R) is shown in Figure 4.9. For a value of $R = 3.2\ \Omega$, the error percentage ($\delta\%$) is zero, as expected.

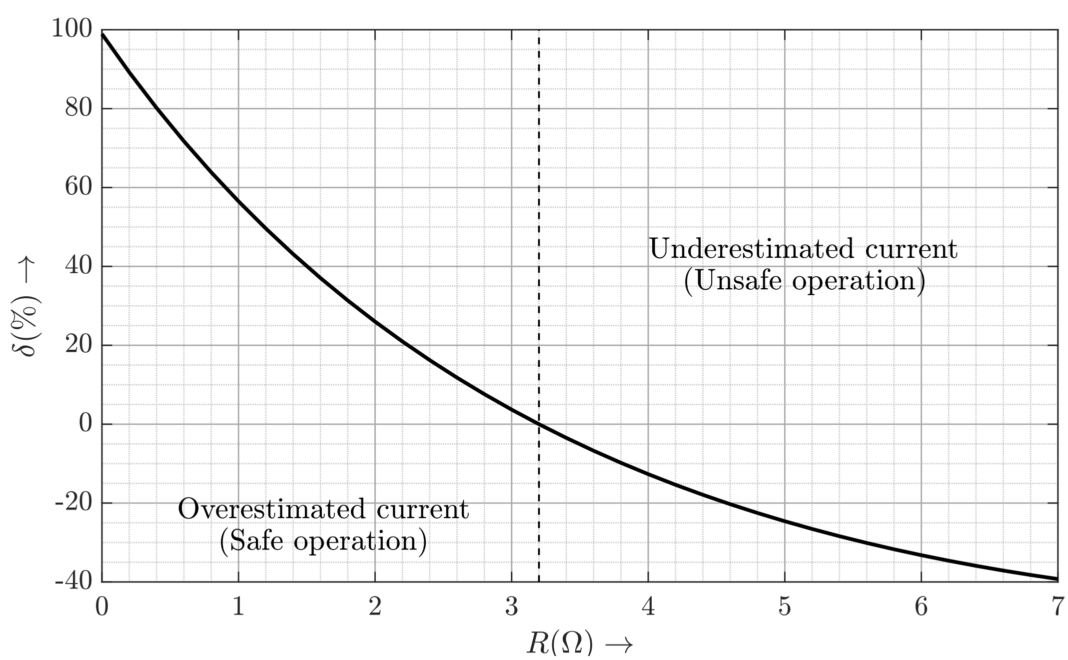

Figure 4.9: Peak error percentage ($\delta\%$) versus winding resistance (R) for $V_{bus} = 12$V and $\omega = 380$ rpm

4.6.1 Impact of Other Parameters on the Effect of Winding Resistance

So far, the effect of winding resistance has been analyzed by itself; however, other parameters can impact the degree by which the winding resistance affects the reconstruction of the phase current. The first step involves the identification of the other parameters, which is done by analyzing the analytical expression for the phase current, descibed by Equation 4.1, which is rewritten as:

$$i = \frac{V_{bus}(\beta_g - \theta)}{\omega L(\theta)(\tau\alpha_g - 1)} + C_6 \left[\frac{(\beta_g - \theta)^{\tau\alpha_g}}{\zeta_g L(\theta)} \right] \tag{4.25}$$

The constants of Equation 4.25 which impact the reconstruction of the phase current include the bus voltage (V_{bus}), the angular velocity (ω), the winding resistance (R), and the turn-on and turn-off angles θ_{on} and θ_{off}, respectively. Therefore, the phase current can be expressed by the following function:

$$i = f(V_{bus}, \omega, R, \theta_{off}, \theta_{on}) \tag{4.26}$$

At turn-on and turn-off angles defined by $\theta_{on} = -15°$ and $\theta_{off} = +15°$ (same values of turn-on and turn-off angles as the previous operating point), the effect of V_{bus}, ω, and R are examined. Consider a switched reluctance generator operated at two separate operating points, i.e., operating points 1 and 2 with bus voltages V_{bus1} and V_{bus2} along with angular velocities ω_1 and ω_2, respectively. Assume that the peak value of the phase current (i_{max}) is roughly the same at both operating points (i.e., a parameter defined by the machine and its drive hardware). If $V_{bus1} > V_{bus2}$, then to make sure that the peak value of the phase current at both operating points is the same, the angular velocity at operating point 1 must also be greater than the angular velocity at operating point 2, i.e., $\omega_1 > \omega_2$. This is because when the applied bus voltage is high, the phase current in the machine builds up rapidly unless an equally high back EMF opposes the action of the applied bus voltage, which makes sure that the peak value of the phase current reaches the desired level and does not surpass it.

Similarly if the applied bus voltage is low, the phase current does not build up as rapidly, as a result, the back EMF may also be low to ensure that the peak value of the phase current reaches the desired level. Of the two operating points, operating point 1, where the applied bus voltage is higher, is more immune to errors in the estimation of the winding resistance. This is because at operating point 1, the term $V = V_{bus1} - iR$ is greater than the term at operating point 2, i.e., $V = V_{bus2} - iR$, as a result, the impact of the iR term at operating point 1 is overshadowed by the applied bus voltage, making the operating point more immune to winding resistance estimation errors. Therefore, at the second operating point, the applied bus voltage is increased to 50 V and the angular velocity is increased to 1000 rpm (in simulations), the results of the phase current are shown in Figure 4.10. In the case of a higher applied bus voltage and a higher angular velocity, the phase currents peaks (for different values of winding resistance) are closer to each other when compared to the results shown in Figure 4.8, indicating that the error is drowned out at operating points with higher applied bus voltages and angular velocities. The case when the applied bus voltage

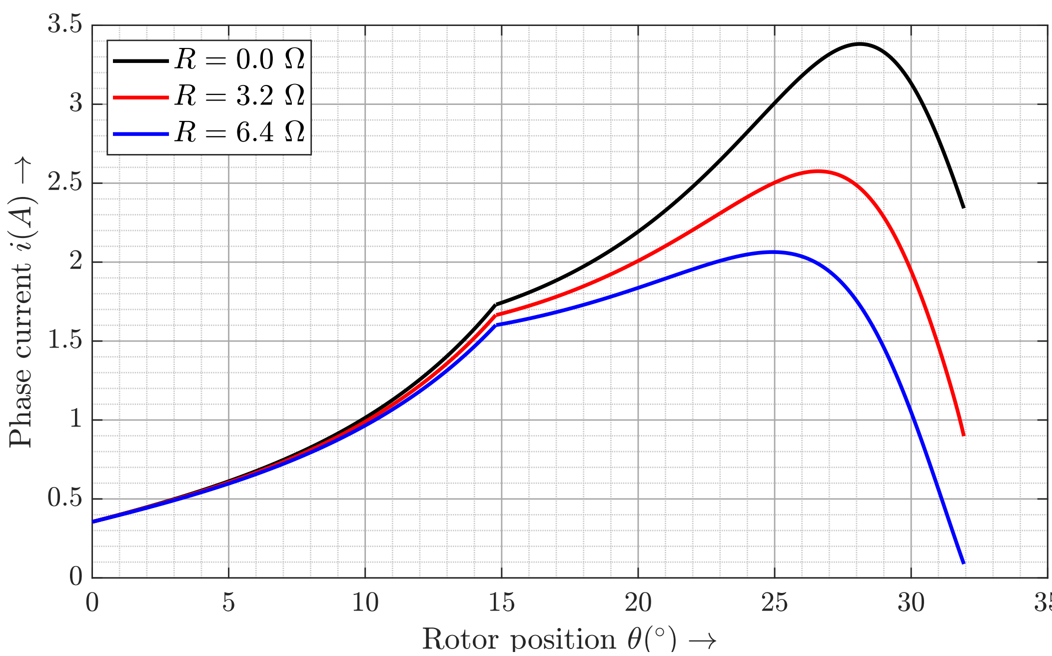

Figure 4.10: Evolution of the phase current with respect to rotor position during generation at $R = 0.0\ \Omega$, $R = 3.2\ \Omega$, and $R = 6.4\ \Omega$ ($V_{bus} = 50$V and $\omega = 1000$ rpm)

and the angular velocity is low, acts as the worst case operating point in terms of estimation errors related to the winding resistance. For the new operating point considered, the peak error percentage ($\delta\%$) versus the winding resistance (R) plot is shown in Figure 4.11.

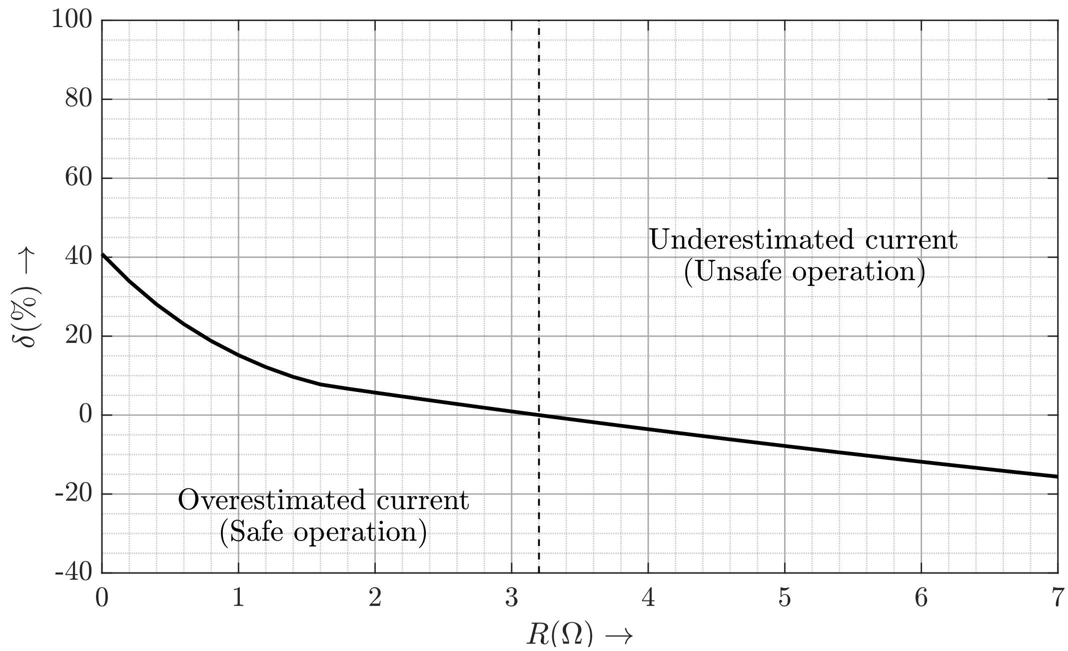

Figure 4.11: Peak error percentage ($\delta\%$) versus winding resistance (R) for $V_{bus} = 50$V and $\omega = 1000$ rpm

At the operating point where $V_{bus} = 12$ V and $\omega = 380$ rpm, the error percentage ($\delta\%$) for $R = 0\ \Omega$ is close to 100% (from Figure 4.9). On the other hand at the operating point where $V_{bus} = 50$ V and $\omega = 1000$ rpm, the error percentage ($\delta\%$) for $R = 0\ \Omega$ is close to 40% (from Figure 4.11). This proves that the estimation error related to the machine's winding resistance is not as severe for operating points with higher applied bus voltages and angular velocities. As a result, the simpler mathematical model described in Section 3.4.2 may be used when the applied bus voltage and angular velocity of the machine are high (depending on the allowable error), while the accurate model (including the machine's winding resistance) described in Section 3.4.3 must be used when the applied bus voltage and angular velocity of the machine are low (however, the mathematical complexity of the model increases).

CHAPTER 5

EFFECT OF FREEWHEELING ON HARVESTED CHARGE

In earlier chapters, a switched reluctance generator was analyzed with only two phases, i.e., a magnetization phase and a demagnetization phase (during the single pulse mode of operation). Since only two phases were considered, it resulted in only one control variable, i.e., the turn-off angle θ_{off}. At the turn-off angle, the machine's phase voltage is negative. However, there is a possibility of injecting a *freewheeling* phase between the magnetization and the demagnetization phases, where the machine's phase voltage is zero. This chapter presents an analysis of the effect of a freewheeling phase on the production of charge and compares it to the case without freewheeling.

During the freewheeling phase, the zero voltage level across the machine's phase is achieved when only one of the switches of the asymmetric bridge converter is on, while the other switch is off. This allows for the corresponding diode to turn on (as shown in Figure 2.33), allowing the current to freewheel through it, hence the name of the phase. Figure 5.1 shows a switched reluctance generator's phase current trajectory with the inclusion of a freewheeling phase. The phase voltage is switched to zero at θ_{off1} and eventually to a negative level at θ_{off2}. The slope of phase current during generation is described by Equation 2.39 and is rewritten with a zero voltage value for the freewheeling phase as:

$$\frac{di}{d\theta} = \frac{0 + \omega i \left| \dfrac{dL}{d\theta} \right|}{\omega L} \tag{5.1}$$

From Equation 5.1, it is observed that during the freewheeling phase, the slope of phase current is positive, which indicates that the phase current increases during the freewheeling phase. As a result, a benefit of adding a freewheeling phase includes an increase in the phase current without the extraction of charge from the source (as the voltage across the machine's phase is zero). During freewheeling, the phase current builds up based on the established

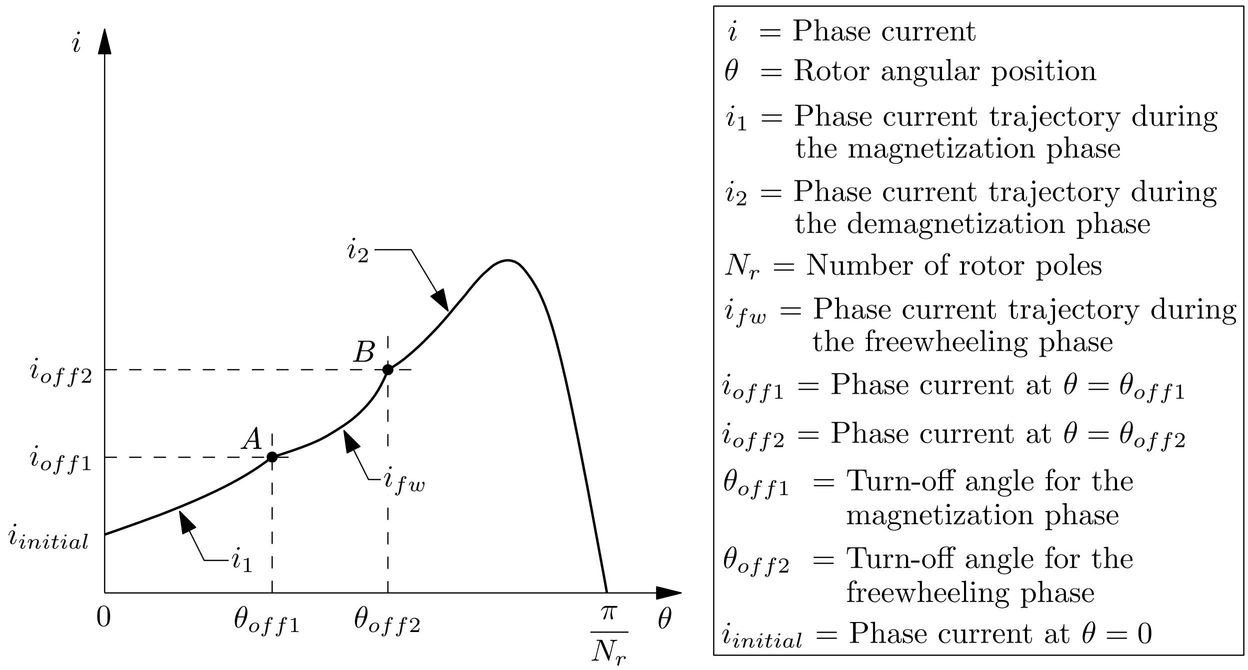

Figure 5.1: Phase current of a switched reluctance generator during positive feedback including a freewheeling phase

back EMF of the machine, i.e., the mechanical energy from the prime mover is converted into stored electrical energy within a switched reluctance generator.

Another benefit of the freewheeling phase includes a lower root mean square (RMS) value of the DC link current $i_{dc-link}$, which reduces the design constraint on the DC link capacitor absorbing the DC link current ripple. Figure 5.2 shows a single phase of an asymmetric bridge converter, highlighting the DC link current $i_{dc-link}$. During the magnetization phase, the DC link current is the same as the machine's phase current; however, during the demagnetization phase, the DC link current and the machine's phase current are equal in magnitude but have opposite polarities. Consider Figure 5.3, where a freewheeling phase is not included, the DC link current flows into the machine during the magnetization phase (same as i_1) and flows from the machine (i.e., generation) during the demagnetization phase (similar to i_2). As a result, the RMS value of the DC link current is substantial.

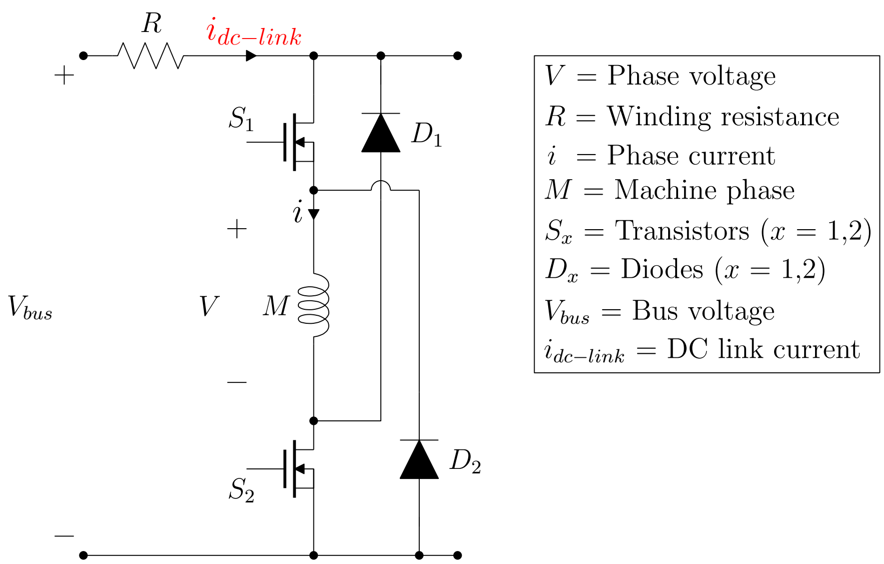

Figure 5.2: Single phase of an asymmetric bridge converter highlighting the DC link current

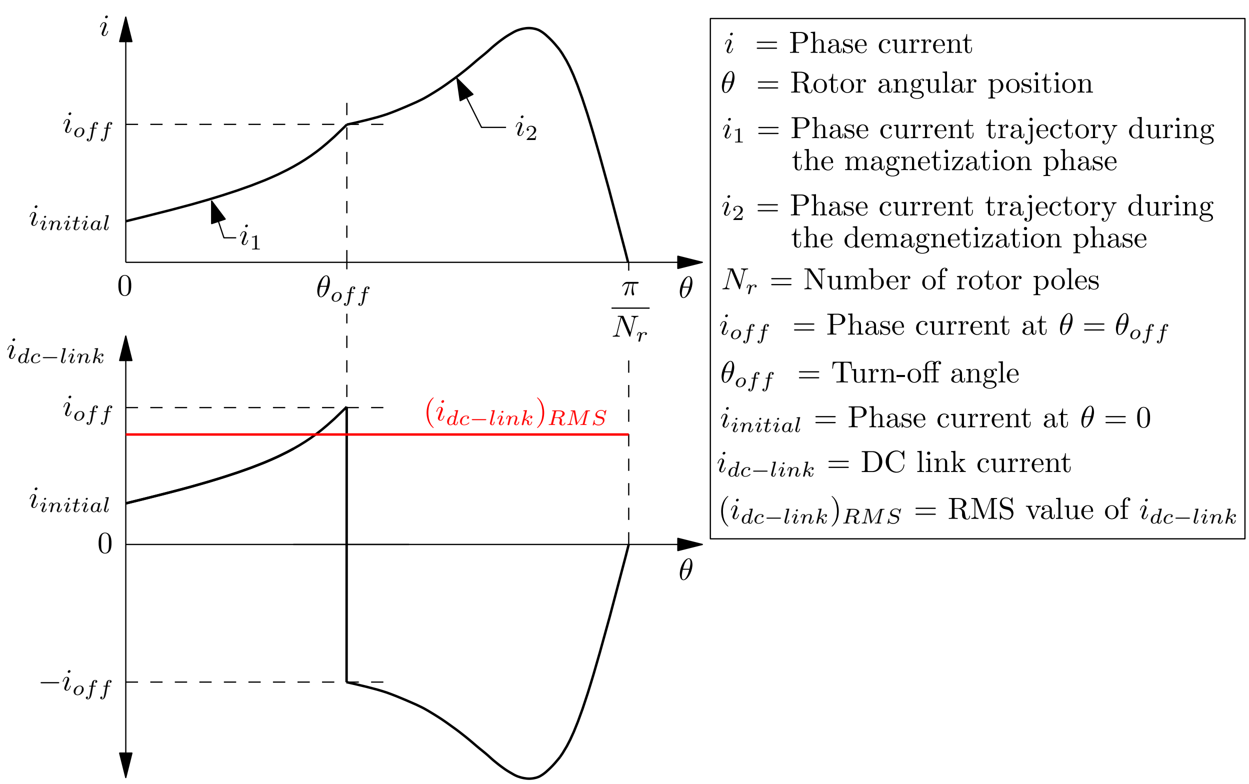

Figure 5.3: Phase current and DC link current of a switched reluctance generator during positive feedback without a freewheeling phase

On the other hand, consider Figure 5.4, where a freewheeling phase is included. The DC link current flows into the machine during the magnetization phase (same as i_1), then has a zero level during the freewheeling phase, and eventually flows from the machine during the demagnetization phase (similar to i_2). Comparing the DC link currents of the two scenarios (i.e., with and without freewheeling), the RMS value of the DC link current for the scenario with a freewheeling phase is lower, as a result, the size of the DC link capacitor can be reduced. Due to the lower RMS value of the DC link current when a freewheeling phase is included, the copper losses are also minimized.

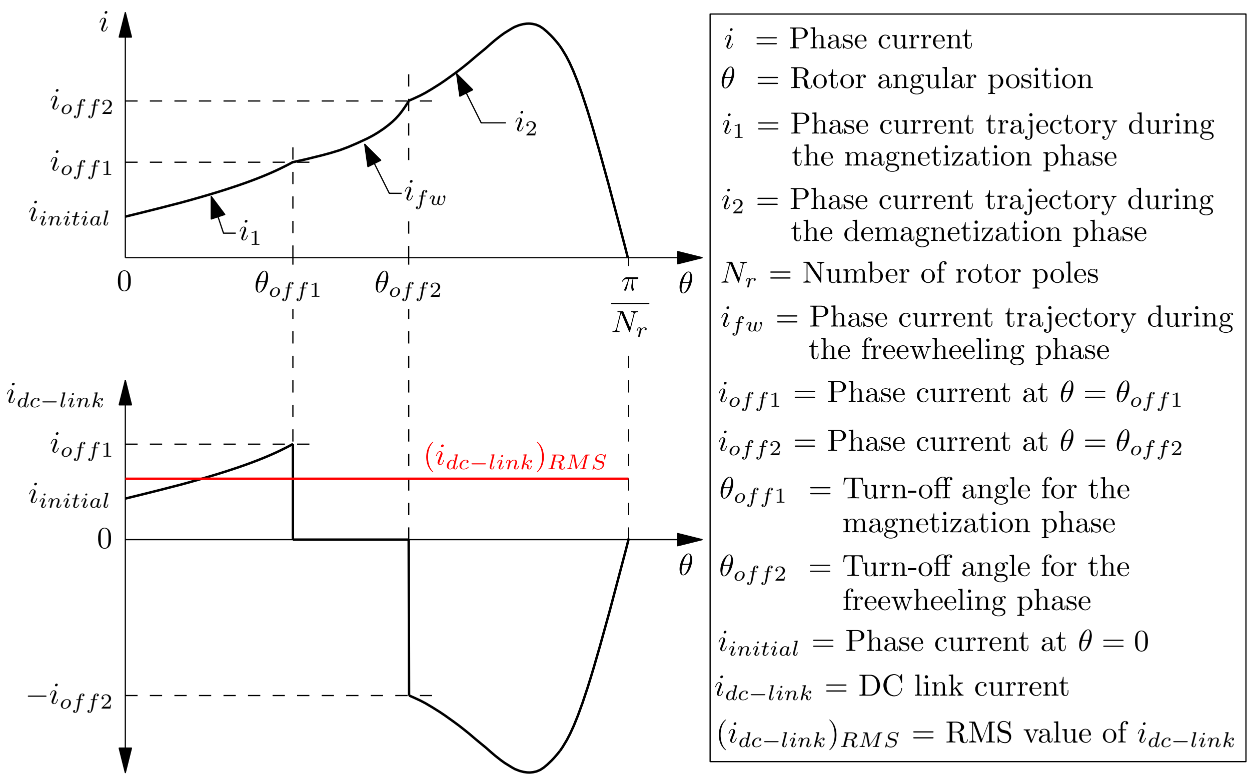

Figure 5.4: Phase current and DC link current of a switched reluctance generator during positive feedback with a freewheeling phase

There are definitely benefits to the inclusion of a freewheeling phase. Therefore, the subsequent sections of this chapter present an approach to analyze and compare the amount of charge produced with and without a freewheeling phase.

5.1 Freewheeling Phase Current Equations

In this section, the expressions for phase current during the magnetization phase, the freewheeling phase, and the demagnetization phase are presented. For the purpose of mathematical simplicity, the analytical expression for the phase current without the winding resistance is selected. The winding resistance has a damping effect on the phase current trajectory in all three phases, as a result, from a comparative standpoint, not much is lost with the exclusion of the winding resistance. Again, for mathematical simplicity, the frequency scaling term (κ) and the phase shift term (ϕ) are also excluded from the phase inductance expression of Equation 3.82. The phase current analytical expression is based on Equation 3.99 and is expressed as:

$$i = \frac{V\theta + C_x}{\omega\left[L_0 + L_1\cos(N_r\theta)\right]} \tag{5.2}$$

where, C_x represents the integration constant C_{on} during the magnetization phase, C_{fw} during the freewheeling phase, and C_{off} during the demagnetization phase. From Equation 5.2, the integration constant C_x is expressed as:

$$C_x = \omega i\left[L_0 + L_1\cos(N_r\theta)\right] - V\theta \tag{5.3}$$

Next, analytical expressions for phase currents in each of the phases (i.e., magnetization, freewheeling, and demagnetization) are analyzed.

5.1.1 Phase current Analysis During the Magnetization Phase

From Figure 5.4, during magnetization, the initial conditions used to compute integration constant C_{on} are: $i = i_{initial}$ and $\theta = 0$. Applying the magnetization phase initial conditions to Equation 5.3, the integration constant C_{on} is obtained as follows:

$$C_{on} = \omega i_{initial}\left[L_0 + L_1\right] \tag{5.4}$$

Therefore, using the integration constant from Equation 5.4, the magnetization phase current i_1 is expressed using Equation 5.2 as:

$$i_1 = \frac{V\theta + C_{on}}{\omega \left[L_0 + L1 \cos(N_r\theta)\right]} \tag{5.5}$$

From Figure 5.4, the phase current value at $\theta = \theta_{off1}$ is i_{off1}, which is a point on the magnetization phase current trajectory (i_1). Therefore, applying the coordinates of the point in Equation 5.5 and using the magnetization integration constant (C_{on}) from Equation 5.4, the following expression is obtained:

$$i_{off1} = \frac{V\theta_{off1} + C_{on}}{\omega \left[L_0 + L_1 \cos(N_r\theta_{off1})\right]} \tag{5.6}$$

Next, the phase current equations related to the freewheeling phase are examined.

5.1.2 Phase current Analysis During the Freewheeling Phase

From Figure 5.4, during freewheeling, the initial conditions used to compute integration constant C_{fw} are: $i = i_{off1}$ and $\theta = \theta_{off1}$, along with a value of zero for V. Applying the freewheeling phase initial conditions to Equation 5.3, the integration constant C_{fw} is obtained as follows:

$$C_{fw} = \omega i_{off1} \left[L_0 + L_1 \cos(N_r\theta_{off1})\right] \tag{5.7}$$

Therefore, using the integration constant from Equation 5.7, the freewheeling phase current i_{fw} is expressed using Equation 5.2 as:

$$i_{fw} = \frac{C_{fw}}{\omega \left[L_0 + L1 \cos(N_r\theta)\right]} \tag{5.8}$$

From Figure 5.4, the phase current value at $\theta = \theta_{off2}$ is i_{off2}, which is a point on the freewheeling phase current trajectory (i_{fw}). Therefore, applying the coordinates of the point in Equation 5.8, substituting i_{off1} form Equation 5.6 and freewheeling integration constant (C_{fw}) from Equation 5.7, the following expression is obtained:

$$i_{off2} = \frac{V\theta_{off1} + C_{on}}{\omega \left[L_0 + L_1 \cos(N_r \theta_{off2}) \right]} \tag{5.9}$$

Next, the phase current equations related to the demagnetization phase are examined.

5.1.3 Phase current Analysis During the Demagnetization Phase

During the demagnetization phase, the machine's phase voltage is negative, as a result, the negative sign from the voltage term is factored out in the subsequent equations. From Figure 5.4, during demagnetization, the initial conditions used to compute integration constant C_{off} are: $i = 0$ and $\theta = \pi/N_r$. Applying the demagnetization phase initial conditions to Equation 5.3, the integration constant C_{off} is obtained as follows:

$$C_{off} = |V|\frac{\pi}{N_r} \tag{5.10}$$

Therefore, using the integration constant from Equation 5.10, the demagnetization phase current i_2 is expressed using Equation 5.2 as:

$$i_2 = \frac{-|V|\theta + C_{off}}{\omega \left[L_0 + L1 \cos(N_r \theta) \right]} \tag{5.11}$$

From Figure 5.4, the phase current value at $\theta = \theta_{off2}$ is i_{off2}, which is a point on the demagnetization phase current trajectory (i_2). Therefore, applying the coordinates of the point in Equation 5.11 and using the demagnetization integration constant (C_{off}) from Equation 5.10, the following expression is obtained:

$$i_{off2} = \frac{-|V|\theta_{off2} + |V|(\pi/N_r)}{\omega \left[L_0 + L_1 \cos(N_r \theta_{off2}) \right]} \tag{5.12}$$

Next, using the equations presented in this section, a relationship between the turn-off angles (θ_{off1} and θ_{off2}) is established.

5.1.4 Relationship Between the Turn-off Angles

This section presents the relationship between the turn-off angles θ_{off1} and θ_{off2} shown in Figure 5.4. The first step involves equating the expressions described by Equations 5.9 and 5.12, resulting in the following expression:

$$V\theta_{off1} + C_{on} = -|V|\theta_{off2} + |V|(\pi/N_r) \tag{5.13}$$

Rearranging Equation 5.13, the following expression is obtained:

$$\begin{aligned}\theta_{off1} + \theta_{off2} &= \frac{|V|(\pi/N_r) - C_{on}}{|V|} \\ &= \frac{\pi}{N_r} - \frac{C_{on}}{|V|}\end{aligned} \tag{5.14}$$

Assigning the terms on the right hand side of Equation 5.14 as a constant x, the following expression is obtained:

$$\theta_{off1} + \theta_{off2} = x \tag{5.15}$$

From Equation 5.15, it is observed that the relationship between θ_{off1} and θ_{off2} is linear (as shown in Figure 5.5). Therefore, if θ_{off1} is reduced by a small amount Δx, then θ_{off2} must increase by the same amount Δx to ensure that their sum remains a constant, i.e., x.

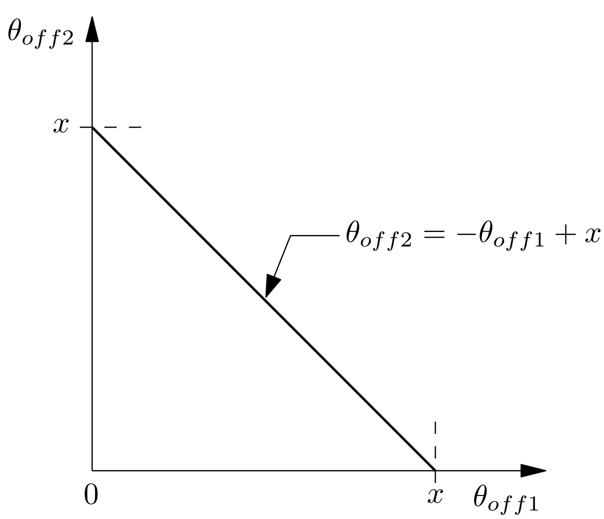

θ_{off1} = Turn-off angle for the magnetization phase

θ_{off2} = Turn-off angle for the freewheeling phase

$x = \left(\dfrac{\pi}{N_r} - \dfrac{C_{on}}{|V|}\right)$

Figure 5.5: Graphical representation between θ_{off1} and θ_{off2}

If $\theta_{off1} = \theta_{off2} = \theta_{off}$, then using Equation 5.15, the following expression is obtained:

$$\theta_{off} = \frac{x}{2} \tag{5.16}$$

The condition: $\theta_{off1} = \theta_{off2} = \theta_{off}$, implies that the freewheeling phase is absent, i.e., while referring to Figure 5.4, if the turn-off angles θ_{off1} and θ_{off2} are equal to each other, then the trajectory of the phase current will resemble the one shown in Figure 5.3 with only one turn-off angle θ_{off}. As a result, the turn-off angles θ_{off1} and θ_{off2} either symmetrically diverge from $x/2$ (i.e., the freewheeling phase increases) or symmetrically converge to $x/2$ (i.e., the freewheeling phase decreases, eventually becoming completely absent at $x/2$). This phenomenon is graphically expressed in Figure 5.6.

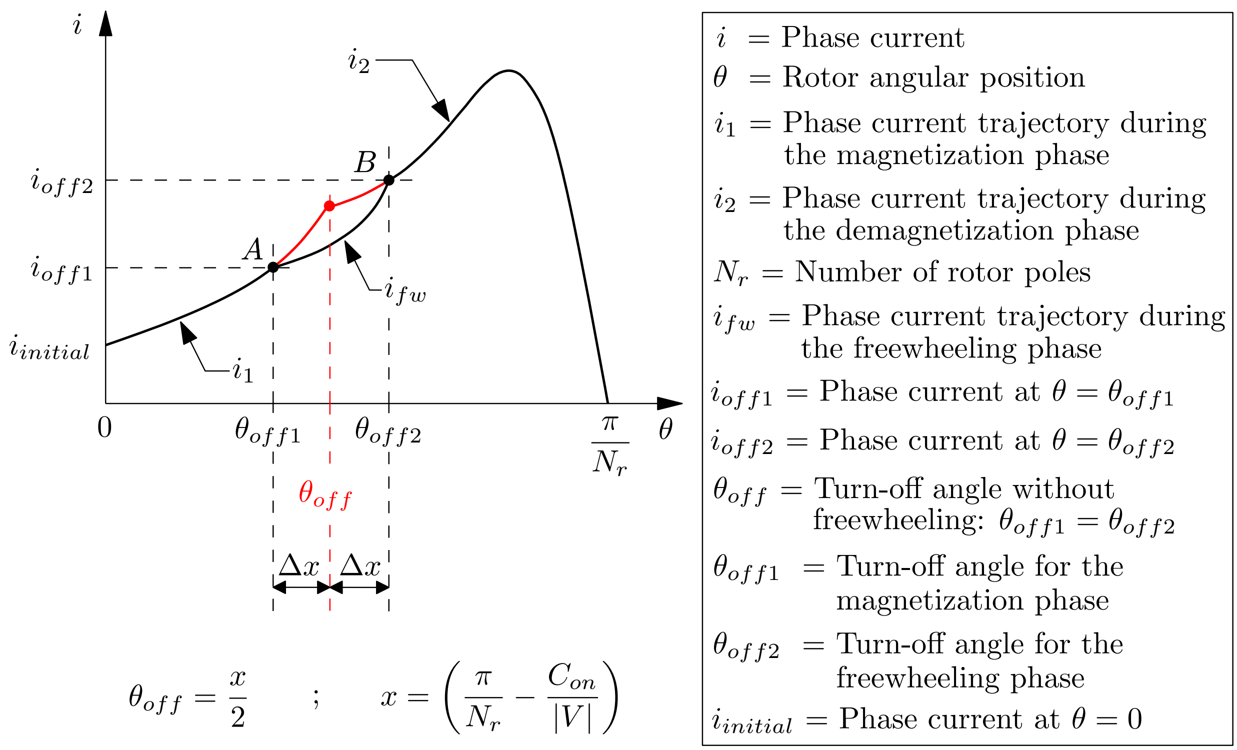

Figure 5.6: Phase current trajectory with and without a freewheeling phase (highlighting the linear relationship between θ_{off1} and θ_{off2})

Using the linear relationship between θ_{off1} and θ_{off2}, more specifically, any change in θ_{off1} results in an equal and opposite change in θ_{off2}, an analysis related to the amount of net charge in the two scenarios, i.e., with and without freewheeling is presented next.

5.2 Electrical Charge Harvested With and Without Freewheeling

Analyzing the amount of charge produced with a freewheeling phase and comparing it to the amount of charge produced without a freewheeling phase is mathematically extremely intensive, as a result, a graphical approach is chosen to perform the analysis. In the absence of a freewheeling phase, the amount of charge invested by the source is higher, consequently the amount of charge harvested from the machine is also higher. However, in the presence of freewheeling, the amount of charge invested by the source is lesser, but it is allowed to *accrue* before it is harvested from the machine (as shown in Figure 5.6). There seems to be an unfair advantage towards the scenario in which freewheeling is included, the advantage being the extra time (which translates to a longer commutation cycle in terms of θ) which is provided for the charge to accrue. By intuition, it is more advantageous to invest, allow for growth, and extract over an extended period rather than investing and extracting over a shorter period. Therefore, in order to perform a fair comparison between the two scenarios, the period for both the scenarios is kept the same, i.e., for both the scenarios the phase current must be made zero at the unaligned position (π/N_r).

When the phase current is nonzero (i.e., $i_{initial}$) at the aligned position (i.e., $\theta = 0$), then the integration constant C_{on} described by Equation 5.4 is also a nonzero positive quantity. As a result, the value of x defined by Equations 5.14 and 5.15, is less than π/N_r, i.e., when $i_{initial} \neq 0$, then $x < \pi/N_r$. When $i_{initial} \neq 0$ and freewheeling is not included, the value of θ_{off} described by Equation 5.16 turns out to be less than $\pi/2N_r$ as shown in Figure 5.7. The area enclosed by the phase current trajectory and the θ axis is proportional to electrical charge, as the rotor position (θ) directly relates to time (t) through angular velocity (ω).[1] The difference between the charge harvested and the charge invested, i.e., net charge or charge produced is proportional to: area B - area A.

[1]Electrical charge is defined as the product of current and time. The area under the phase current (in A) curve with respect to rotor position needs to be divided by the angular velocity (in $^\circ\,\mathrm{s}^{-1}$) in order to represent charge (in C).

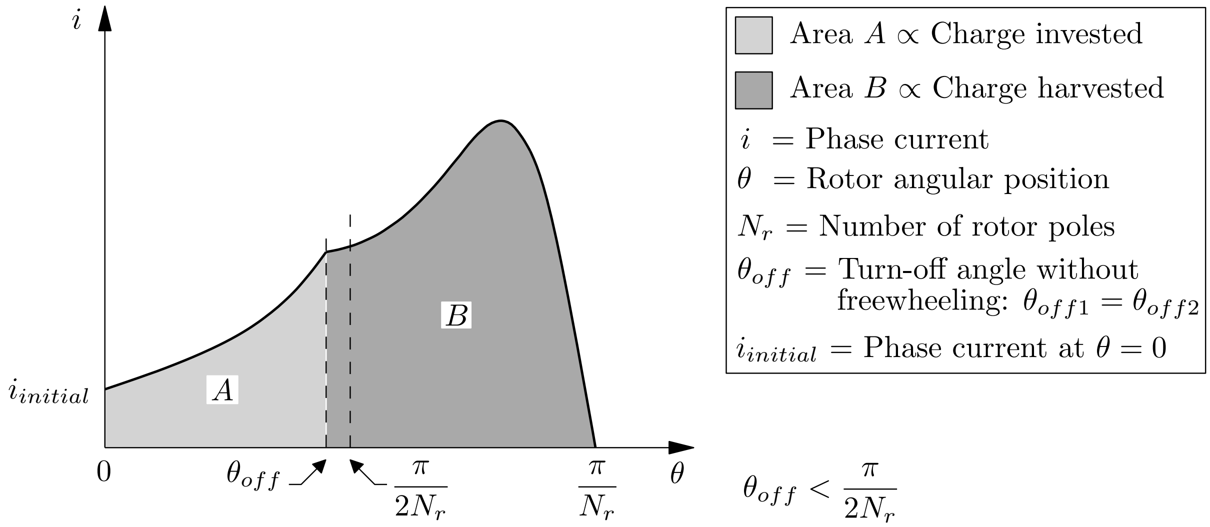

Figure 5.7: Phase current trajectory without a freewheeling phase

In order to analyze the areas related to the invested and harvested charge more effectively, the magnetization phase current trajectory is folded about the line: $\theta = \theta_{off}$, as shown in Figure 5.8. It is worth noting that since $\theta_{off} \leq \pi/2N_r$, the following relationship also holds true: $2\theta_{off} \leq \pi/N_r$.

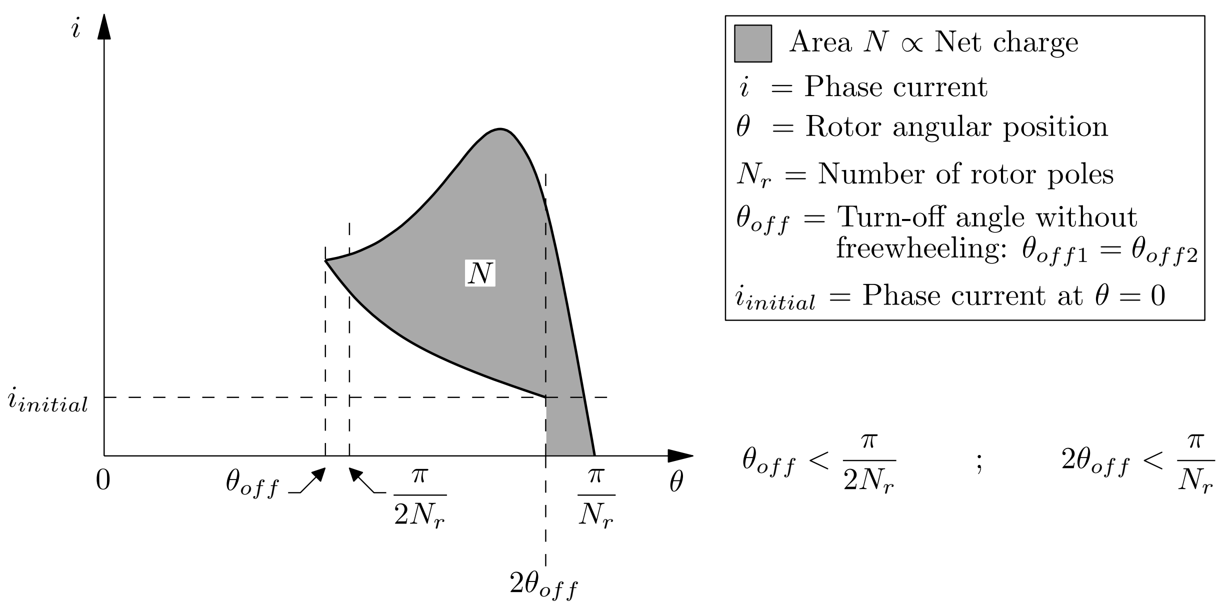

Figure 5.8: Magnetization phase current trajectory (without a freewheeling phase) folded about the line: $\theta = \theta_{off}$

The net charge (i.e., proportional to area B - area A in Figure 5.7) is represented by area N in Figure 5.8. The next step involves analyzing the net charge produced when a freewheeling phase is included during the generation process. Figure 5.9 shows the phase current trajectory with a freewheeling phase along with the areas proportional to invested, freewheeling, and harvested charge.

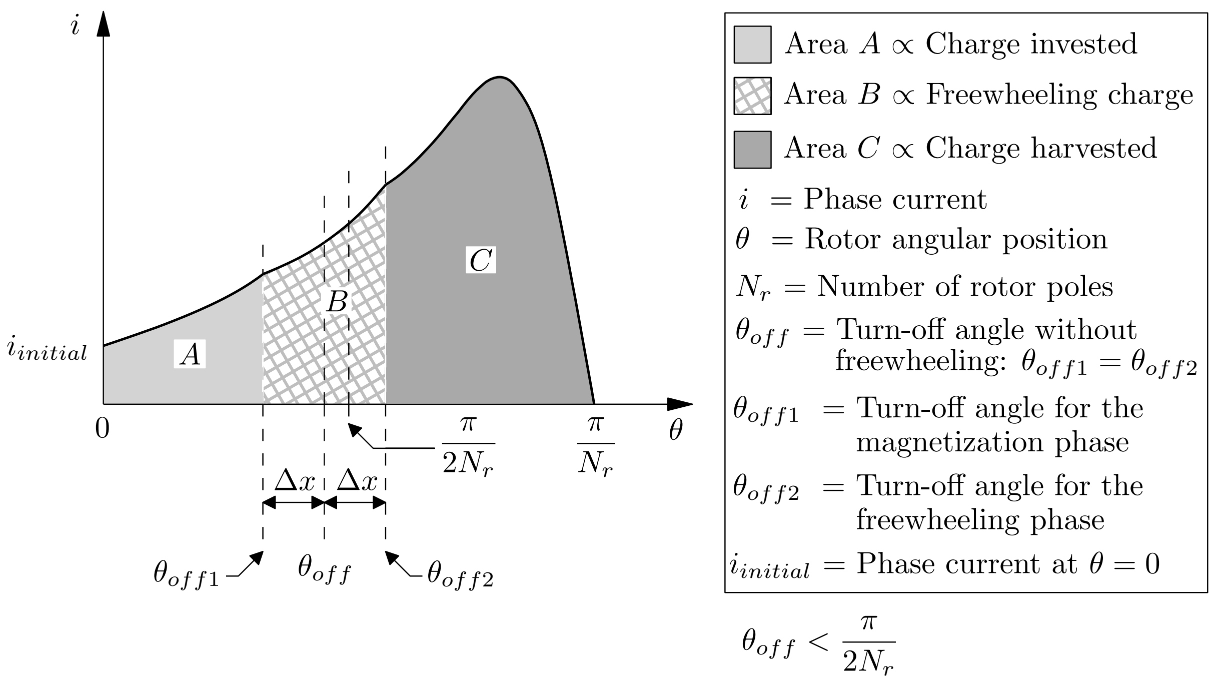

Figure 5.9: Phase current trajectory with a freewheeling phase

Again, in order to analyze the net charge more effectively, the phase current is folded about the line: $\theta = \theta_{off}$ and is shown in Figure 5.10. Since the relationship between θ_{off1} and θ_{off2} is linear (as described by Equation 5.15), when the phase current trajectory shown in Figure 5.9 is folded about the line: $\theta = \theta_{off}$, the lines: $\theta = \theta_{off1}$ and $\theta = \theta_{off2}$, perfectly line up with each other as shown in Figure 5.10. On comparing the net charge without a freewheeling phase (i.e., as shown in Figure 5.8) to the net charge with a freewheeling phase (i.e., as shown in Figure 5.10), it is clear that the net charge is greater in the scenario without a freewheeling phase. This is graphically proven using Figure 5.10, where area *abcea* represents the charge which is taken away from the harvesting current trajectory due to the inclusion of a freewheeling phase, while area *abdea* represents the charge which is taken away from the investing charge trajectory due to the inclusion of a freewheeling phase. Due to the inclusion of a freewheeling phase, the following must hold true: $d \leq b \leq c$, as a result, area *abcea* is always greater than area *abdea*, implying that the net charge without a freewheeling phase is always greater than the net charge with a freewheeling phase (by area *bcdb*), provided, the phase current is made zero at the unaligned position (π/N_r).

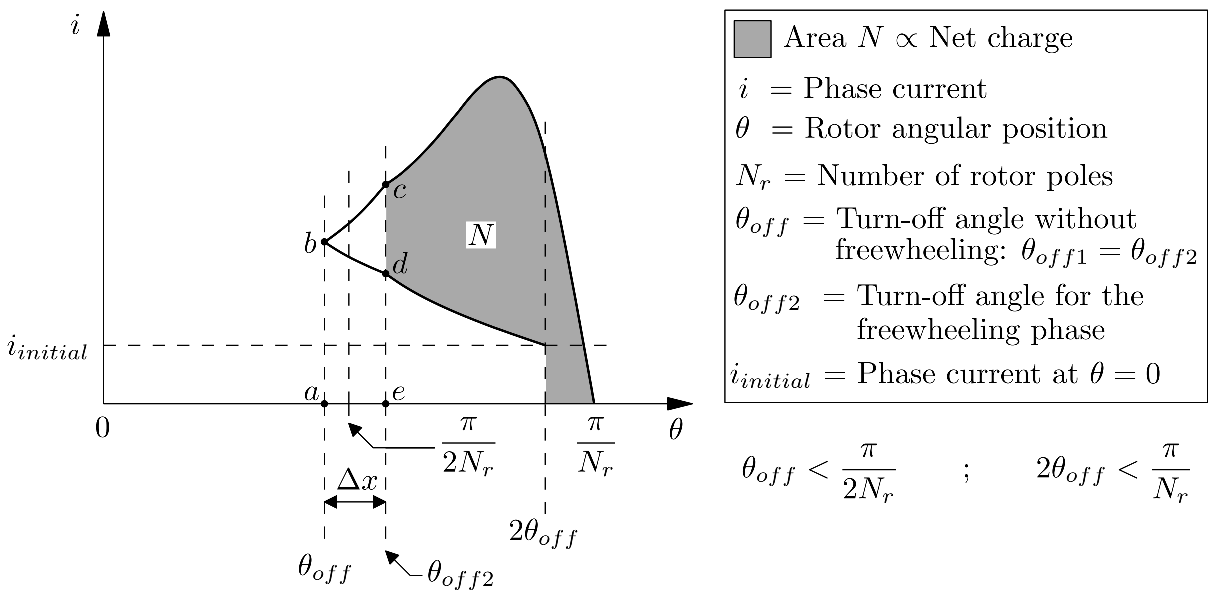

Figure 5.10: Phase current trajectory (with a freewheeling phase) folded about the line: $\theta = \theta_{off}$

Similar results have been presented based on experimental measurements [120]; however, no theoretical proof was provided to support the results and behavior of the machine. From the proof provided in this chapter it is clear that from a net charge standpoint, when a switched reluctance generator is operated in single pulse positive feedback mode, the inclusion of a freewheeling phase causes the net charge to drop, provided the phase current is made zero at the unaligned position. Some previous research [121, 122] suggests that the net charge is greater with a freewheeling phase when compared to a scenario without freewheeling;

however, the comparison does not ensure that the phase current is made zero at the same rotor position in both cases, as a result, the scenario with a freewheeling phase gets an unfair advantage. The freewheeling phase has its own merit, as it reduces the RMS value of the DC link current, which in turn reduces the constraints on the DC link capacitor; however, it reduces the output power generated by the machine as well. This concludes the analysis of the effect of a freewheeling phase on the net charge or charge produced by the machine.

CHAPTER 6

CONCLUSION AND FUTURE RESEARCH

This chapter presents concluding remarks on the work presented in earlier chapters of this dissertation and its contribution towards the study of switched reluctance machines. It also provides a direction for future research work, related to the modeling of switched reluctance machines.

6.1 Conclusion

This dissertation presented an approach for modeling and reconstructing the phase current of a switched reluctance machine. With the availability of an analytical expression for the phase current, significant improvements in a switched reluctance machine's control are achieved. Its benefits are observed during the generating mode, as the phase current can be controlled as desired. The accuracy of the proposed predictive modeling scheme when compared to finite element analysis data (i.e., a look up table) is reasonably high and acceptable, considering the simple inductance function used. Prior modeling schemes ([11, 104, 114], among others) are analytically extremely complex and require a much higher number of calculation steps in order to describe the trajectory of the machine's phase current (as they make use of numerical methods of integration in order to obtain the solution). The proposed model requires only two two steps to describe the entire phase current trajectory, one step during the magnetization phase and the second step during the demagnetization phase, making it computationally efficient. The proposed method provides the option for a higher accuracy model by considering a more extensive inductance function; however, that would result in increased mathematical complexities while describing the phase current trajectory. The proposed model is not immune to the trade-off of computational speed versus accuracy but greatly reduces the complexity compared to the existing methods.

A first of its kind control strategy for switched reluctance generators is also presented. Conventionally, a switched reluctance generator is not operated in single pulse positive feedback due to the phase current's uncontrollable behavior. The challenge of operating the machine in single pulse positive feedback lies in the ability to limit the phase current's peak value below the maximum allowable value after the phase is switched off. If the current exceeds the maximum allowable value, the diodes of an asymmetric bridge converter are at a risk of getting damaged, which can compromise the functionality of the entire drive. The attraction towards operating the machine in single pulse positive feedback is due to its ability to produce more charge; however, it is accompanied by control challenges. The predictive control model presented in this dissertation provides a technique, which allows for a safe operation of the machine in single pulse positive feedback.

Due to a switched reluctance generator's sensitive dependence on its initial conditions and measured parameters, an extensive and comprehensive model including the machine's winding resistance was also presented. The presented predictive control model was implemented in hardware and tested (in Chapter 4) at various operating points simulating real world operating scenarios for a switched reluctance generator. Scenarios including varying wind speeds and its effects on the peak value of phase currents of a switched reluctance generator used in wind turbine applications were simulated and experimentally verified. Another scenario with a varying value for the maximum allowable current level was also simulated and experimentally verified. In all test cases, the simulation and experimental data closely matched each other.

The work presented in this dissertation is especially targeted towards the operation of a switched reluctance generator in single pulse mode with positive feedback. Since a switched reluctance generator does not operate at high current levels at the aligned position, the effects of saturation are not as prominent and are excluded in the proposed predictive model. The next section provides direction for future research work in order to include saturation in the modeling and reconstruction of phase current for a switched reluctance machine.

6.2 Future Research

This section provides direction for future research work, to further improve the techniques presented in this dissertation. The inclusion of the effect of saturation in the analytical expression for the machine's phase current is worth looking into.

6.2.1 Linear Saturation Model of a Switched Reluctance Machine

A linear model including saturation is presented in this section, which may be further improved by considering segments forming a piecewise linear theory. It is worth noting that since two points are sufficient to describe the equation of a line, the linear model only considers two points, i.e., the aligned rotor position (θ_a) and the unaligned rotor position (θ_u), as a result, the phase inductances only at the aligned and unaligned rotor positions are considered. To begin with, consider the variation of phase inductance with rotor position curves shown in Figure 3.12, which are approximated by the lines shown in Figure 6.1.

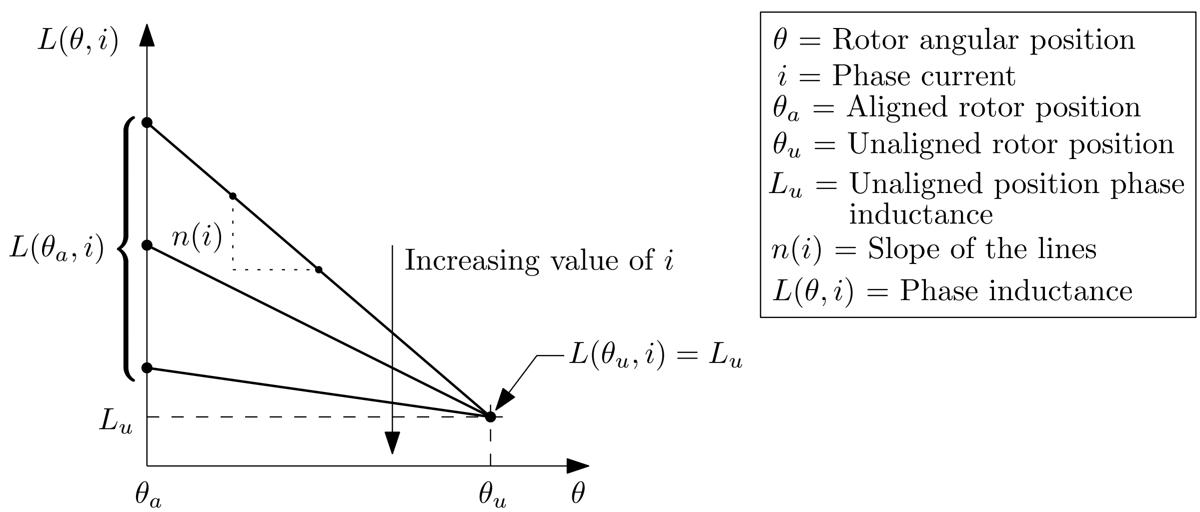

Figure 6.1: Linear approximation of phase inductance with rotor position

From Figure 6.1, since only two points are needed to describe the equation of a line, the phase inductance at the aligned position, i.e., $L(\theta_a, i)$ is used as the first point, while the phase inductance at the unaligned position, i.e., $L(\theta_u, i)$ is used as the second point. However, even in a model with saturation, due to the geometry of the machine among other factors, the value of phase inductance at the unaligned position is immune to saturation (i.e., is not a function of phase current) and is represented as a constant, i.e., L_u. On the other hand, the aligned position phase inductance ($L(\theta_a, i)$) is indeed a function of the phase current, which begins to drop towards the unaligned position phase inductance (L_u), as phase current increases (as shown in Figure 6.1). As a result, the slope of the lines, defined by $n(i)$, also change based on the value of phase current, due to which it is also assigned as a function of the phase current. Using the phase inductance values at the aligned and unaligned rotor positions, the following expression for the slope of phase inductance with respect to rotor position is obtained:

$$n(i) = \frac{L(\theta_a, i) - L_u}{\theta_a - \theta_u} \tag{6.1}$$

Using the expression for the slope from Equation 6.1, the equation for the variation of phase inductance with respect to rotor position, shown in Figure 6.1 is expressed as:

$$\begin{aligned} L(\theta, i) &= n(i)\ \theta + L(\theta_a, i) \\ &= \left[\frac{L(\theta_a, i) - L_u}{\theta_a - \theta_u}\right] \theta + L(\theta_a, i) \end{aligned} \tag{6.2}$$

The next step involves obtaining an expression for the aligned position phase inductance ($L(\theta_a, i)$). Consider the variation of the aligned position phase inductance with phase current as shown in Figure 3.17, which is also linearly approximated as shown in Figure 6.2, where the slope of the line is defined by m, which is the slope of the line curve fitting the data either obtained through an FEA tool or through experimental measurements. From Figure 6.2, the expression for the aligned position phase inductance, i.e., $L(\theta_a, i)$ is expressed as:

$$L(\theta_a, i) = m\ i + L_a \tag{6.3}$$

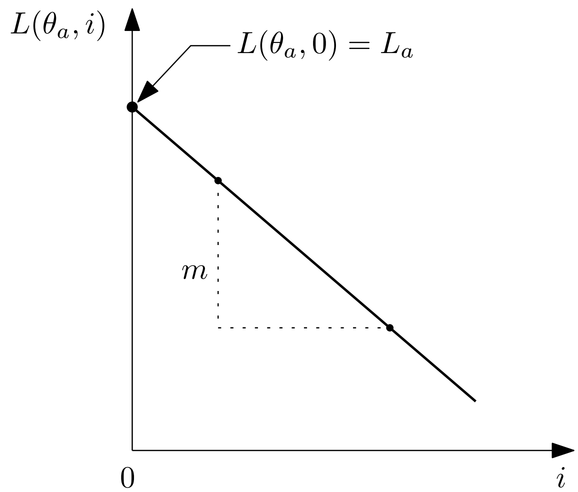

i = Phase current
m = Slope of the line
θ_a = Aligned rotor position
L_a = Aligned position phase inductance
$L(\theta_a, i)$ = Phase inductance at θ_a

Figure 6.2: Linear approximation of phase inductance with phase current

Substituting the expression of $L(\theta_a, i)$ from Equation 6.3 in Equation 6.2, the following expression is obtained:

$$L(\theta, i) = \left[\frac{(mi + L_a) - L_u}{\theta_a - \theta_u}\right]\theta + (mi + L_a) \tag{6.4}$$

Assigning the term: $\theta_a - \theta_u$, as a constant K_1 in Equation 6.4, the following expression is obtained:

$$\begin{aligned} L(\theta, i) &= \left[\frac{(mi + L_a) - L_u}{K_1}\right]\theta + (mi + L_a) \\ &= \frac{1}{K_1}\Big(L_a\theta - L_u\theta + mi\theta + miK_1 + L_aK_1\Big) \end{aligned} \tag{6.5}$$

Now that the expression for phase inductance is obtained, the current differential equation of a switched reluctance machine is considered (i.e., the one specified by Equation 2.16) and rewritten as:

$$\frac{di}{d\theta} = \frac{V - \omega i \dfrac{dL(\theta, i)}{d\theta}}{\omega L(\theta, i)} \tag{6.6}$$

Equation 6.6 makes use of the derivative of phase inductance with respect to rotor position, which is obtained using Equation 6.5 (it is worth noting that the product rule of differential calculus is used on terms containing the product of phase current and rotor position) and is expressed as:

$$\frac{dL(\theta,i)}{d\theta} = \frac{1}{K_1}\left[L_a - L_u + \left(mi + m\theta\frac{di}{d\theta}\right) + \left(mK_1\frac{di}{d\theta}\right)\right] \tag{6.7}$$

Substituting the expressions from Equations 6.5 and 6.7 in Equation 6.6, the following expression is obtained:

$$\frac{di}{d\theta} = \frac{V - \omega i\frac{1}{K_1}\left[L_a - L_u + mi + \left(m\theta + mK_1\right)\frac{di}{d\theta}\right]}{\omega\frac{1}{K_1}\left(L_a\theta - L_u\theta + mi\theta + miK_1 + L_aK_1\right)} \tag{6.8}$$

Equation 6.8 represents the linear saturation model of a switched reluctance machine. The next section presents a technique of obtaining a solution to Equation 6.8.

6.2.2 An Analytical Expression for Phase Current Using a Linear Model

This section presents a technique to obtain an analytical expression for phase current of a switched reluctance machine, modeled using the linear saturation model presented in Section 6.2.1. Rearranging Equation 6.8, the following expression is obtained:

$$\begin{aligned}\frac{\omega}{K_1}\left(L_a\theta - L_u\theta + mi\theta + miK_1 + L_aK_1\right)\frac{di}{d\theta} &= \\ V - \omega i\frac{1}{K_1}\left[L_a - L_u + mi + \left(m\theta + mK_1\right)\frac{di}{d\theta}\right]\end{aligned} \tag{6.9}$$

Separating out some of the terms of Equation 6.9, the following expression is obtained:

$$\begin{aligned}\frac{\omega}{K_1}\left(L_a\theta - L_u\theta + mi\theta + miK_1 + L_aK_1\right)\frac{di}{d\theta} &= \\ V - \omega i\frac{1}{K_1}\left(L_a - L_u + mi\right) - \frac{\omega}{K_1}\left(mi\theta + miK_1\right)\frac{di}{d\theta}\end{aligned} \tag{6.10}$$

Rearranging Equation 6.10, results in the following:

$$\frac{\omega}{K_1}\left(L_a\theta - L_u\theta + 2mi\theta + 2miK_1 + L_aK_1\right)\frac{di}{d\theta} = V - \omega i\frac{1}{K_1}\left(L_a - L_u + mi\right) \tag{6.11}$$

Multiplying Equation 6.11 by K_1/ω and replacing the term: VK_1/ω, by another constant K_2, the following expression is obtained:

$$\left(L_a\theta - L_u\theta + 2mi\theta + 2miK_1 + L_aK_1\right)\frac{di}{d\theta} = K_2 - L_ai + L_ui - mi^2 \tag{6.12}$$

Replacing $di/d\theta$ by i' and rearranging Equation 6.12 results in the following expression:

$$(L_ai - L_ui + mi^2 - K_2) + (L_a\theta - L_u\theta + 2mi\theta + 2miK_1 + L_aK_1)\ i' = 0 \tag{6.13}$$

The solution to the differential equation expressed by Equation 6.13 is obtained using the technique of solving exact differential equations [118]. The first step in solving for the phase current involves rewriting Equation 6.13 using functions: $M(\theta, i)$ and $N(\theta, i)$, resulting in:

$$M(\theta, i) + N(\theta, i)\ i' = 0 \tag{6.14}$$

where,

$$M(\theta, i) = (L_ai - L_ui + mi^2 - K_2) \tag{6.15}$$

and,

$$N(\theta, i) = (L_a\theta - L_u\theta + 2mi\theta + 2miK_1 + L_aK_1) \tag{6.16}$$

Next, the partial derivatives of $M(\theta, i)$ and $N(\theta, i)$ with respect to i and θ, respectively are checked for *exactness*. Using Equation 6.15, the partial derivative of $M(\theta, i)$ with respect to i is expressed as:

$$\frac{\partial M(\theta, i)}{\partial i} = L_a - L_u + 2mi \tag{6.17}$$

Similarly, using Equation 6.16, the partial derivative of $N(\theta, i)$ with respect to θ is expressed as:

$$\frac{\partial N(\theta, i)}{\partial \theta} = L_a - L_u + 2mi \tag{6.18}$$

From Equations 6.17 and 6.18, it is observed that the differential equation described by Equation 6.13 are indeed exact equations. Since the differential equation is exact, there exists a function $f(\theta, i)$, where:

$$\frac{\partial f(\theta, i)}{\partial \theta} = M(\theta, i) \tag{6.19}$$

and,

$$\frac{\partial f(\theta, i)}{\partial i} = N(\theta, i) \tag{6.20}$$

Integrating Equation 6.19 with respect to rotor position (θ) using the expression for $M(\theta, i)$ from Equation 6.15, the following expression is obtained:

$$f(\theta, i) = L_a i\theta - L_u i\theta + mi^2\theta - K_2\theta + g(i) \tag{6.21}$$

where, the function $g(i)$ acts as a *constant* of integration (since it is only a function of i and not θ). Next, considering the partial derivative of Equation 6.21 with respect to i and using the relationship from Equation 6.20, i.e., equating it to the expression for $N(\theta, i)$ from Equation 6.16, the resultant expression is:

$$L_a\theta - L_u\theta + 2mi\theta + g'(i) = L_a\theta - L_u\theta + 2mi\theta + 2miK_1 + L_aK_1 \tag{6.22}$$

where, $g'(i)$ represents the derivative of the function $g(i)$ with respect to i. Rearranging Equation 6.22, the following expression for $g'(i)$ is obtained:

$$g'(i) = 2miK_1 + L_aK_1 \tag{6.23}$$

To obtain an expression for the function $g(i)$, Equation 6.23 is integrated with respect to i, resulting in the following expression:

$$g(i) = mi^2K_1 + L_aiK_1 \tag{6.24}$$

Using $g(i)$ from Equation 6.24 in Equation 6.21, the following expression for $f(\theta, i)$ is obtained:

$$f(\theta, i) = L_a i\theta - L_u i\theta + mi^2\theta - K_2\theta + mi^2 K_1 + L_a i K_1 \tag{6.25}$$

According to the exact equation technique for solving differential equations, the solution of Equation 6.25 is: $f(\theta, i) = K_3$, where, K_3 is a constant solved using a set of initial conditions. As a result, Equation 6.25 finally becomes:

$$(m\theta + mK_1)i^2 + (L_a\theta - L_u\theta + L_a K_1)i - (K_2\theta + K_3) = 0 \tag{6.26}$$

Applying the formula used to solve quadratic equations[1] on Equation 6.26, the expression for the phase current of a switched reluctance machine using a linear saturation model is expressed as:

$$i = \frac{-(L_a\theta - L_u\theta + L_a K_1) \pm \sqrt{(L_a\theta - L_u\theta + L_a K_1)^2 + 4(m\theta + mK_1)(K_2\theta + K_3)}}{2(m\theta + mK_1)} \tag{6.27}$$

where, $K_1 = (\theta_a - \theta_u)$ and $K_2 = VK_1/\omega$.

Prior work using piecewise linear and nonlinear modeling techniques have been previously presented; however, this section also provided an analytical closed form expression for the phase current of a switched reluctance machine using a linear saturation model. The presented approach can be extended and applied to piecewise (i.e., multiple segments) linear/nonlinear function of the phase inductance depicted in Figures 6.1 and 6.2 in order to better match the dynamics of a switched reluctance machine. This concludes this section regarding future research work relating to the modeling and reconstruction of the phase current of a switched reluctance machine.

---

[1]The solution to a quadratic equation: $ax^2 + bx + c = 0$, where x is an unknown variable and a, b, and c are constants is defined by the following roots: $x = \frac{-b \pm \sqrt{b^2 - 4ac}}{2a}$.

APPENDIX A

SWITCHED RELUCTANCE MACHINE SPECIFICATIONS

This appendix presents the specifications of the switched reluctance machine used for the flux based model and the inductance based model and also the specifications of the switched reluctance machine used to record the experimental data.

Table A.1: SRM specifications for the flux and inductance based models

Parameter	**Value**
Number of rotor poles	6
Number of stator poles	8
Number of windings per pahse	8
Stator outer diameter	130 mm
Stator inner diameter	106 mm
Rotor diameter	69.5 mm
Stack length	70 mm
Stator arc	22.9°
Rotor arc	23.0°
Air gap length	0.25 mm
shaft diameter	25 mm

Table A.2: SRM specifications for experimentally tested machine

Parameter	**Value**
Number of rotor poles	6
Number of stator poles	8
Number of windings per phase	120
Stator outer diameter	130 mm
Stator inner diameter	106 mm
Rotor diameter	69.5 mm
Stack length	70 mm
Stator arc	22.9°
Rotor arc	23.0°
Air gap length	0.25 mm
shaft diameter	25 mm

Figure A.1 shows the three dimensional CAD model of the switched reluctance machine based on the specifications listed in Tables A.1 and A.2. The three dimensional structure on the right represents the rotor of the machine, while the three dimensional structure on the left represents the stator of the machine.

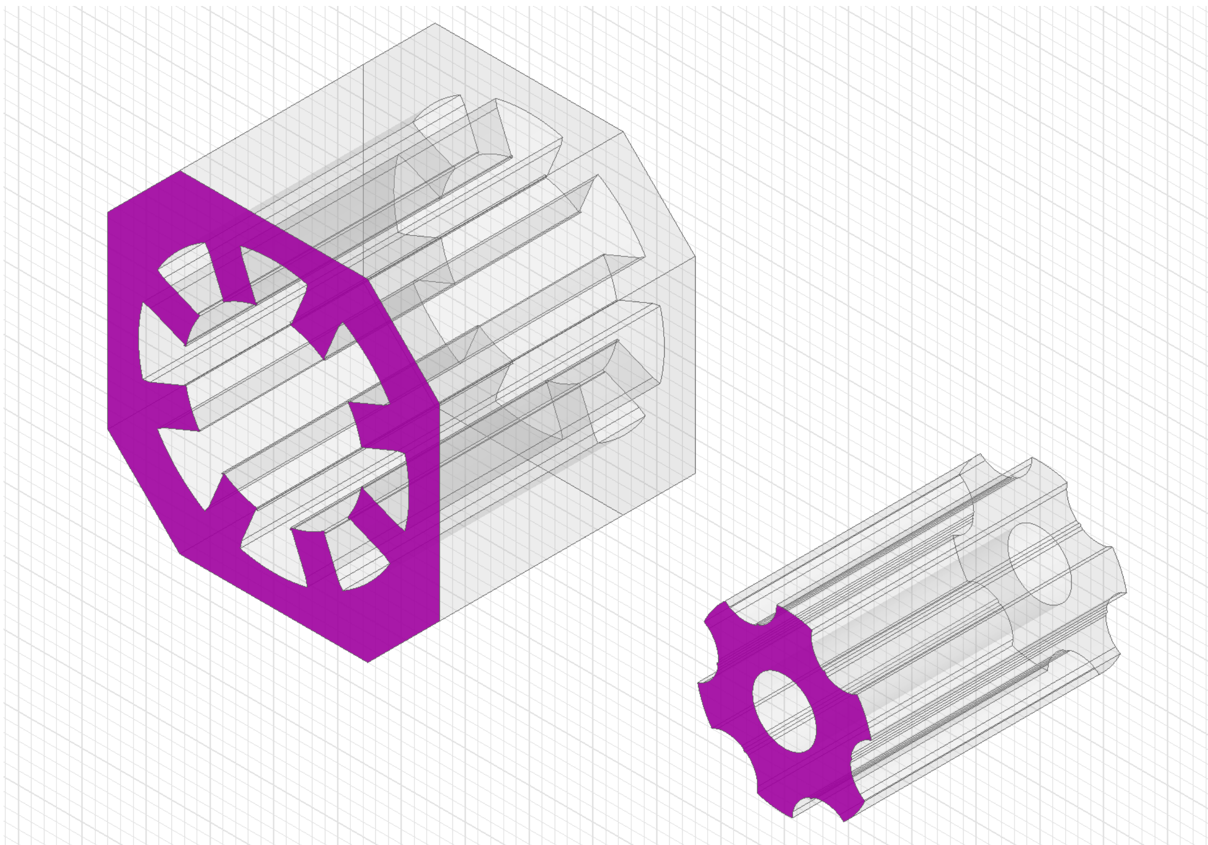

Figure A.1: A three Dimensional view of the SRM's stator (left) and rotor (right) modeled in ANSYS Maxwell [9]

APPENDIX B

COEFFICIENTS OF THE FLUX AND INDUCTANCE BASED MODELS

This appendix lists the values of the constants used in Chapter 3 of this dissertation. The following constant values pertain to the magnetizing coefficients of the flux based model specified in Section 3.1.1. The coefficients of Equation 3.7 are listed below (for $k = 8$) and are used to construct the magnetization curves shown in Figure 3.7:

- $A_{10} = +0.0139$
- $A_{11} = +0.01358$
- $A_{12} = -7.734 \times 10^{-5}$
- $A_{13} = +4.632 \times 10^{-5}$
- $A_{14} = -0.0001248$
- $A_{15} = +8.562 \times 10^{-5}$
- $A_{16} = -4.642 \times 10^{-5}$
- $A_{17} = +1.636 \times 10^{-5}$
- $A_{18} = +1.546 \times 10^{-6}$
- $A_{20} = -0.01873$
- $A_{21} = -0.008976$
- $A_{22} = +0.003469$
- $A_{23} = -0.00127$
- $A_{24} = +0.0006183$
- $A_{25} = -0.0008737$
- $A_{26} = +0.000344$
- $A_{27} = -6.282 \times 10^{-5}$
- $A_{28} = -0.0002695$
- $A_{30} = +3.442 \times 10^{-5}$
- $A_{31} = -1.985 \times 10^{-5}$
- $A_{32} = -2.134 \times 10^{-6}$
- $A_{33} = +2.473 \times 10^{-7}$
- $A_{34} = +4.186 \times 10^{-7}$
- $A_{35} = -2.107 \times 10^{-7}$
- $A_{36} = +1.253 \times 10^{-7}$
- $A_{37} = -2.89 \times 10^{-8}$
- $A_{38} = -7.156 \times 10^{-9}$

The following constant values pertain to the coefficients of the flux based model specified in Section 3.1.1. The coefficients of Equations 3.8, 3.9, and 3.10 are listed below and are used to construct the magnetization curves shown in Figure 3.8:

- $f_0 = +0.01425$
- $f_1 = +0.0134$
- $f_2 = +5.349 \times 10^{-21}$
- $f_3 = -0.0003204$
- $f_4 = -1.148 \times 10^{-20}$
- $k = +0.1075$
- $g_1 = -0.005607$
- $h_1 = -28.83$
- $i_1 = +3.555$
- $g_2 = -0.01146$
- $h_2 = -20.54$
- $i_2 = +4.364$
- $g_3 = -0.01269$
- $h_3 = -14.42$
- $i_3 = +6.545$
- $g_4 = -0.01571$
- $h_4 = -4.504$
- $i_4 = +10.85$
- $g_5 = -0.01575$
- $h_5 = +4.499$
- $i_5 = +10.86$
- $g_6 = -0.01268$
- $h_6 = +14.42$
- $i_6 = +6.545$
- $g_7 = -0.01146$
- $h_7 = +20.54$
- $i_7 = +4.363$
- $g_8 = -0.005607$
- $h_8 = +28.83$
- $i_8 = +3.555$
- $p_0 = +3.442 \times 10^{-5}$
- $q_1 = -1.985 \times 10^{-5}$
- $q_2 = -2.127 \times 10^{-6}$
- $q_3 = +9.004 \times 10^{-7}$
- $q_4 = -4.04 \times 10^{-7}$
- $q_5 = +4.171 \times 10^{-7}$
- $q_6 = -2.059 \times 10^{-7}$
- $q_7 = +1.229 \times 10^{-7}$
- $q_8 = -2.281 \times 10^{-8}$
- $r_1 = -3.821 \times 10^{-25}$
- $r_2 = +2.197 \times 10^{-24}$
- $r_3 = -3.319 \times 10^{-24}$
- $r_4 = +4.967 \times 10^{-24}$
- $r_5 = -6.208 \times 10^{-24}$
- $r_6 = +7.641 \times 10^{-24}$
- $r_7 = -1.012 \times 10^{-23}$
- $r_8 = +1.07 \times 10^{-23}$
- $u = 0.1047$

The following constant values pertain to the inductance based model specified in Section 3.1.2. The coefficients of Equations 3.23 and 3.24 for $k = 5$ are listed below and are used to construct the magnetization curves shown in Figure 3.16:

- $a_0 = +0.765378078420070 \times 10^{-3}$
- $a_1 = -0.005412448241577 \times 10^{-3}$
- $a_2 = +0.000003897192706 \times 10^{-3}$
- $a_3 = +0.000000079196518 \times 10^{-3}$
- $a_4 = -0.000000000256260 \times 10^{-3}$
- $a_5 = +0.000000000000229 \times 10^{-3}$
- $b_0 = +0.351693238339206 \times 10^{-3}$
- $b_1 = -0.001885774189798 \times 10^{-3}$
- $b_2 = -0.000001413682877 \times 10^{-3}$
- $b_3 = +0.000000044095081 \times 10^{-3}$
- $b_4 = -0.000000000126439 \times 10^{-3}$
- $b_5 = +0.000000000000109 \times 10^{-3}$

The following constant values pertain to the inductance based model specified in Section 3.1.2. The coefficients of Equations 3.23 and 3.24 for $k = 9$ are listed below and are used to construct the magnetization curves shown in Figure 3.19:

- $a_0 = +0.0006754$
- $a_1 = +1.554 \times 10^{-5}$
- $a_2 = -7.862 \times 10^{-7}$
- $a_3 = +1.241 \times 10^{-8}$
- $a_4 = -1.024 \times 10^{-10}$
- $a_5 = +4.98 \times 10^{-13}$
- $a_6 = -1.475 \times 10^{-15}$
- $a_7 = +2.615 \times 10^{-18}$
- $a_8 = -2.552 \times 10^{-21}$
- $a_9 = +1.054 \times 10^{-24}$
- $b_0 = +0.0003204$
- $b_1 = +4.921 \times 10^{-6}$
- $b_2 = -2.449 \times 10^{-7}$
- $b_3 = +3.658 \times 10^{-9}$
- $b_4 = -2.872 \times 10^{-11}$
- $b_5 = +1.337 \times 10^{-13}$
- $b_6 = -3.818 \times 10^{-16}$
- $b_7 = +6.564 \times 10^{-19}$
- $b_8 = -6.237 \times 10^{-22}$
- $b_9 = +2.517 \times 10^{-25}$

APPENDIX C

SWITCHED RELUCTANCE MACHINE CHARACTERIZATION

This appendix provides an overview on the characterization process for the switched reluctance machine specified in Table A.2 in Appendix A. The characterization process of a switched reluctance machine involves alignment of the rotor with respect to the stator, application of an appropriate voltage signal across the terminals of the machine, and sensing of the induced phase current. This appendix also describes the magnetic saturation of the phase inductance and provides inferences regarding the characterization of the collected and processed data. The first step while operating a switched reluctance machine involves its alignment procedure and is presented next.

C.1 Alignment of the Machine's Rotor

Alignment is the process of identifying the angular position (in terms of degrees or radians) of the machine's reference rotor pole with respect to a reference stator pole and positioning the rotor in such a way that the reference rotor and stator poles perfectly align with each other. Any one of the machine's rotor poles can be selected and assigned as the reference rotor pole (or primary rotor pole) R_p, similarly any one of the machine's stator poles can be selected and assigned as the reference stator pole (or primary stator pole) S_p. The reference rotor and stator poles of an 8/6 switched reluctance machine are shown in Figure C.1. In Figure C.1, assuming that the rotor rotates in the clockwise direction and based on the technique of determining the reference rotor pole's position described in Section 2.1.1, the reference rotor pole's (R_p) position makes an angle of $-\theta^\circ$ with respect to the reference stator pole (S_p). The first step before operating the machine involves determining the unknown rotor position. The rotor position is typically obtained using a shaft encoder, which as the name suggests, monitors the shaft position of the machine (which is the same as the machine's

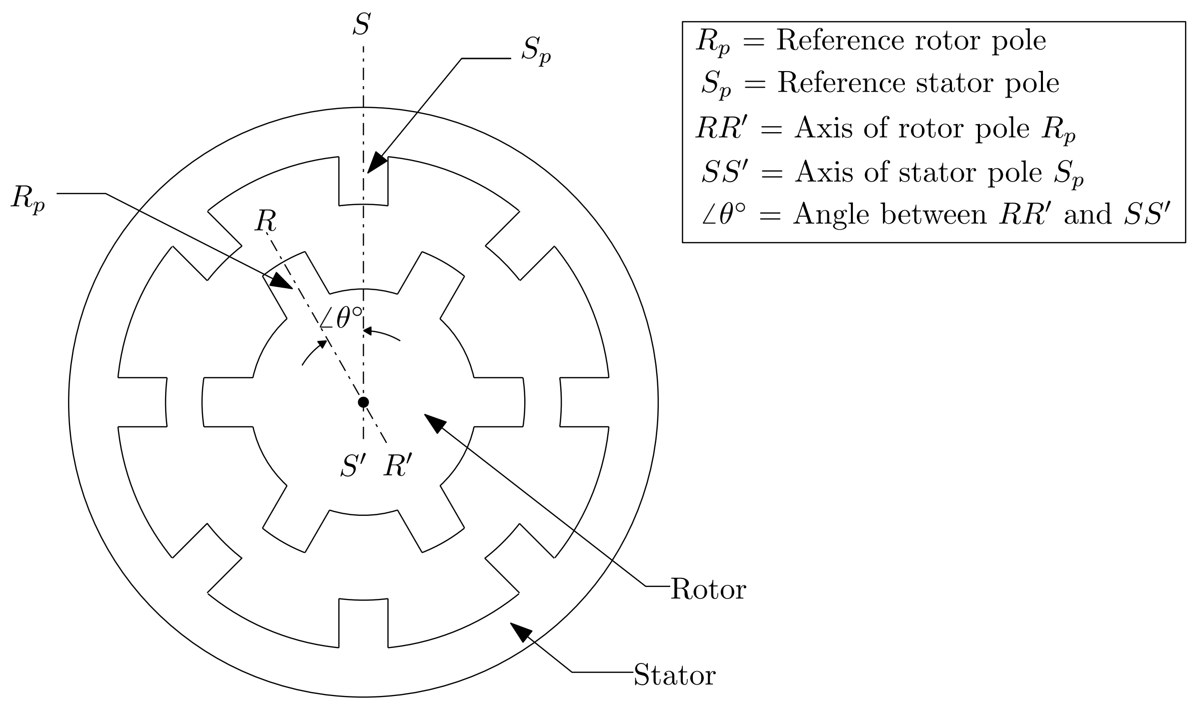

Figure C.1: A two dimensional cross sectional view of an 8/6 SRM

rotor position). It is not necessary to use an external shaft encoder to obtain the rotor's position, there are switched reluctance drive configurations without shaft encoders known as *sensorless* switched reluctance drive configurations [92–94]. However, such sensorless switched reluctance drives and their operation lie outside the scope of this dissertation and are not presented. Figure C.2 shows a block diagram of a typical switched reluctance machine and its controller. The rotor's position is a measured state of the machine and is required to effectively control the dynamics of the machine, as a result, having an initial accurate rotor position is extremely important. At start up, the shaft encoder is unaware of the rotor's position, as a result, it appears to have the state shown in Figure C.3. At that point the alignment procedure is then executed, which when completed, aligns the reference rotor pole (R_p) with the reference stator pole (S_p). After the alignment procedure is complete, the value of the shaft encoder is initialized to zero using software and the machine is ready for operation.

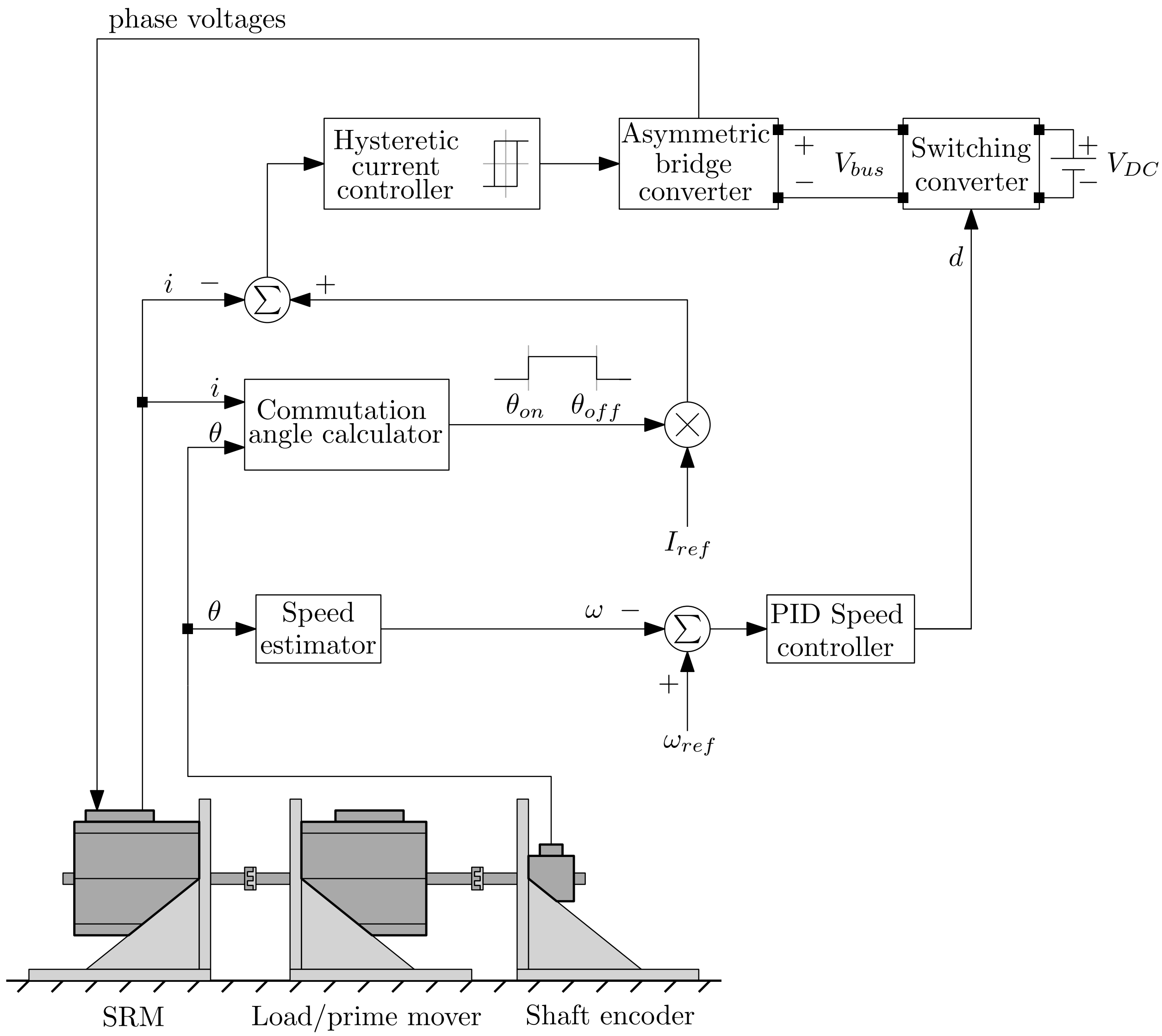

i = Phase current	θ_{off} = Turn-off angle
ω = Rotor angular velocity	I_{ref} = Phase current reference
d = Duty cycle	ω_{ref} = Rotor angular velocity reference
θ = Rotor angular position	V_{bus} = Bus voltage
θ_{on} =Turn-on angle	V_{DC} = DC voltage
PID = Proportional Integral Derivative	

Figure C.2: Block diagram of a switched reluctance machine with a hyesteretic current controller, a commutation angle calculator, a speed loop, a shaft encoder, a load/prime mover, and an asymmetric bridge converter

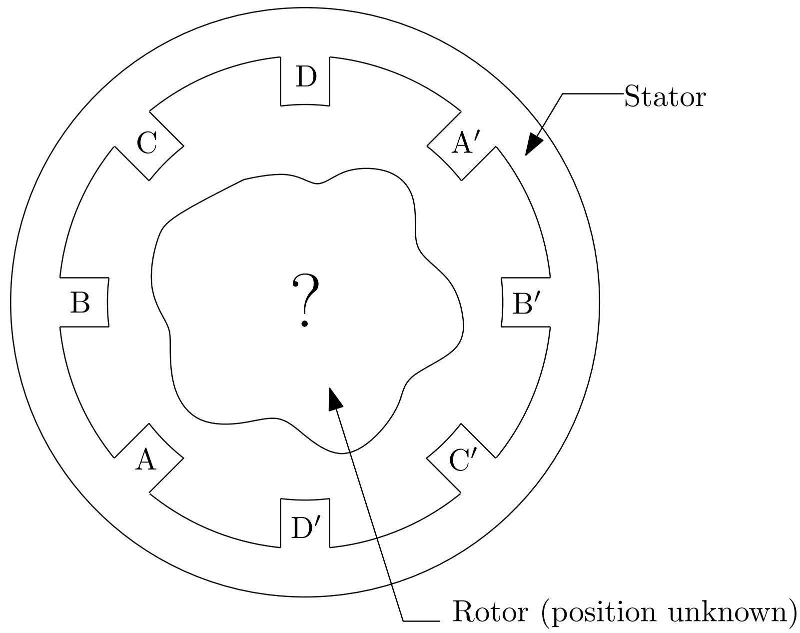

Figure C.3: Unknown rotor position before the alignment procedure

The alignment procedure employed is fairly straightforward, it involves the excitation of the stator phase windings in a particular order for a short duration of time; however, long enough to overcome the mechanical time constant of the rotor shaft to rotate to its new position based on the excited phase. The phase excitation order during the alignment procedure is as follows: phase $A \rightarrow$ phase $B \rightarrow$ phase $C \rightarrow$ phase D. Phase A represents the windings associated with stator poles A and A′, Phase B represents the windings associated with stator poles B and B′, Phase C represents the windings associated with stator poles C and C′, and Phase D represents the windings associated with stator poles D and D′. As a result, in Figure C.3, the stator's rotating magnetic field rotates in the clockwise direction. To complete the alignment procedure, the excitation order is executed only once, by the end of which, the position of the rotor is known. During the alignment procedure, the output values of the shaft encoder are of no importance and are considered as garbage values, only at the end of the alignment procedure is the value of the shaft encoder initialized and utilized from there on.

Consider an 8/6 machine, where the rotor is in an initial unknown position as shown in Figure C.4(a). The alignment procedure is then executed. The first phase excited is the phase associated with stator poles A and A′, due to which rotor poles R_1 and R_1' experience a torque and rotate in the clockwise direction, thereby aligning themselves with stator poles A and A′, respectively. The rotor then takes on the position shown in Figure C.4(b), at which point the phase associated with stator poles B and B′ is excited, causing rotor poles R_2 and R_2' to experience a torque and rotate in the counterclockwise direction in order to align themselves with stator poles B and B′, respectively. The rotor then takes on the position shown in Figure C.4(c). Similarly at that point, the phase associated with stator poles C and C′ is excited, causing rotor poles R_3 and R_3' to experience a torque and rotate in the counterclockwise direction in order to align themselves with stator poles C and C′, respectively. The rotor then takes on the position shown in Figure C.4(d). Finally at that point, the phase associated with stator poles D and D′ is excited, once again causing rotor poles R_1 and R_1' to experience a torque and rotate in the counterclockwise direction in order to align themselves with stator poles D and D′, respectively.

Similarly if the rotor is in an initial unknown position as shown in Figure C.5(a) and the alignment procedure is executed, the first phase excited is the phase associated with stator poles A and A′, due to which rotor poles R_1 and R_1' experience a torque and rotate in the counterclockwise direction, thereby aligning themselves with stator poles A and A′, respectively. The rotor then takes on the position shown in Figure C.5(b). After this stage the steps are similar to the to the ones presented for Figure C.4. Therefore, at the end of the alignment procedure, the rotor always appears to be in the position as shown in Figure C.6, i.e., R_p is aligned with S_p.

The excitation period (i.e., the duration for which a positive voltage is applied across the machine's windings) for each of the phases during the alignment procedure is set to 1 s, which is a sufficient amount of time for the machine and load considered (specified in Table A.1 in

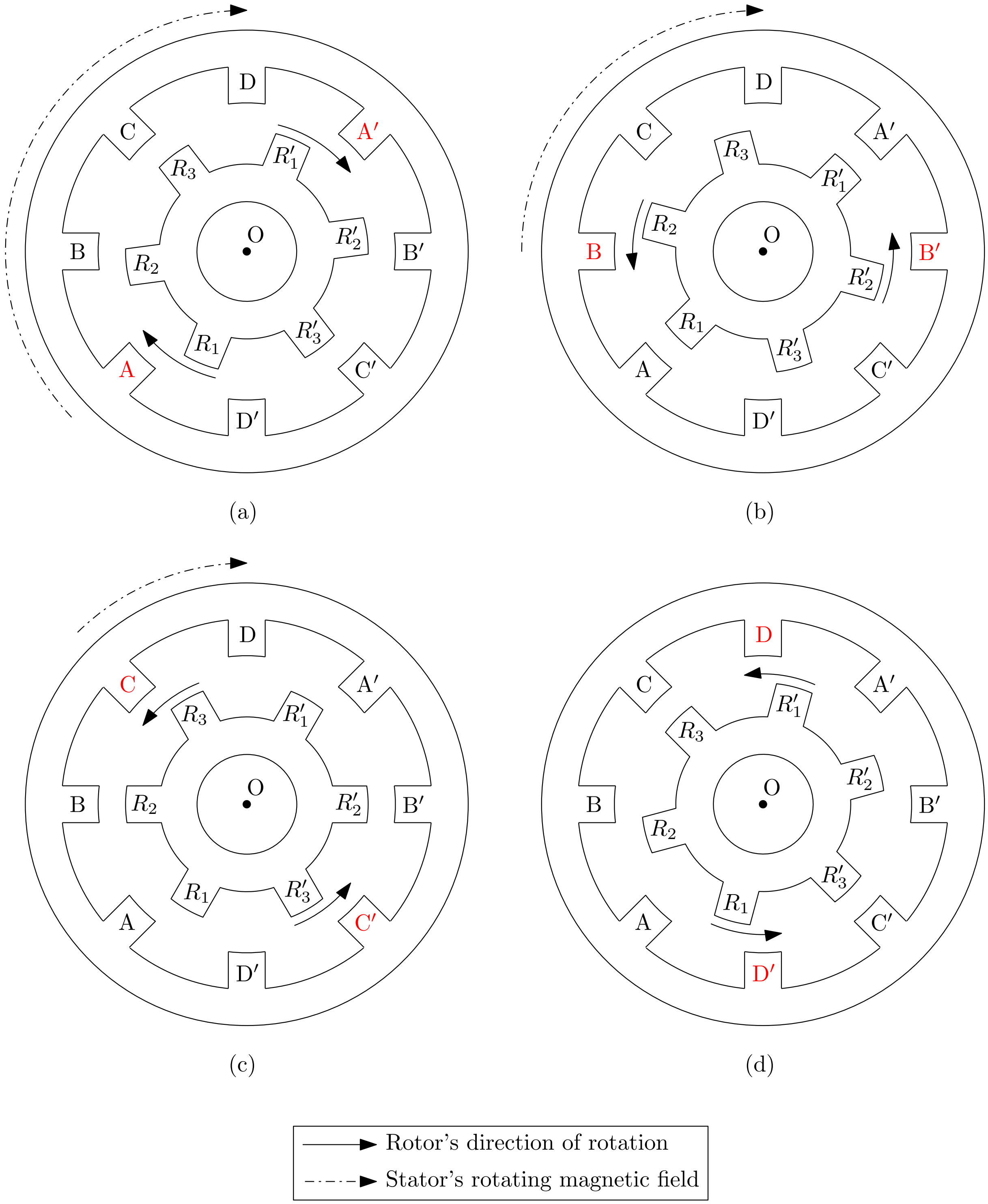

Figure C.4: Alignment process when rotor pole R_1 initially lies in sector AOD′. Rotor initially rotates in the clockwise direction and then in the counterclockwise direction

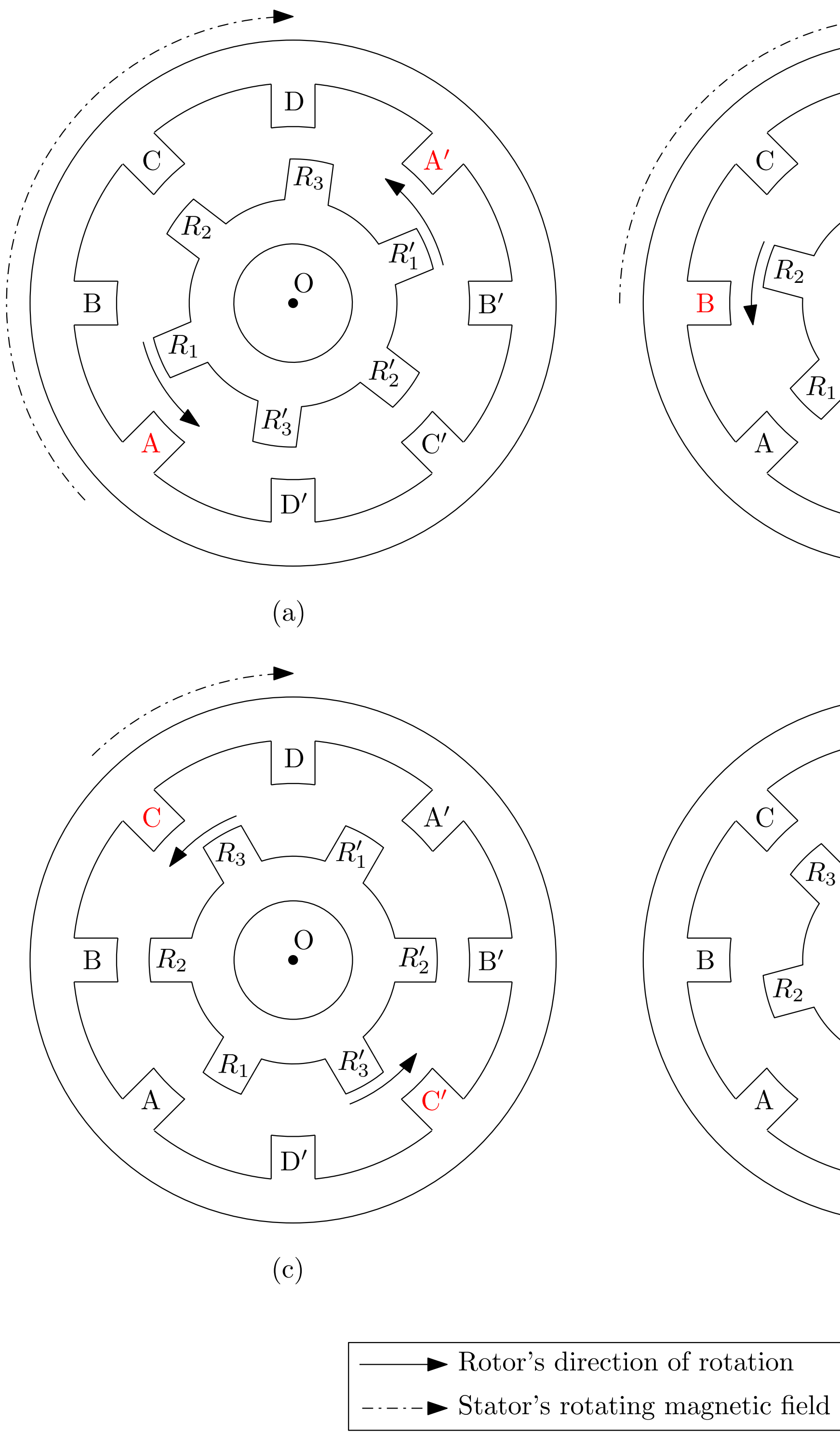

Figure C.5: Alignment process when rotor pole R_1 initially lies in sector BOA. Rotor always rotates in the counterclockwise direction

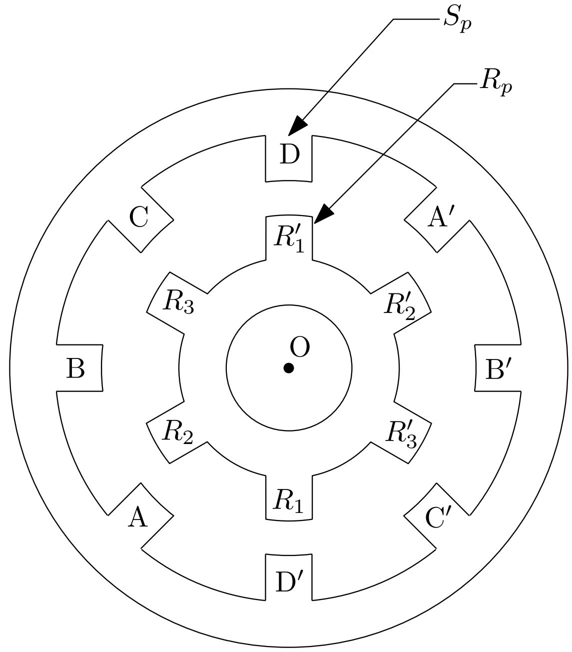

Figure C.6: Rotor position at the end of the alignment procedure

Appendix A). It is worth noting that the speed loop can be disabled during the alignment procedure; however, a current controller is required, or else, depending on the applied bus voltage, the machine's phase could easily saturate in 1 s. The current controller used during the alignment procedure is a simple hysteretic controller (as shown in Figure C.2) with a reference current value of 1 A (i.e., $I_{ref} = 1$ A). For reference, the 8/6 switched reluctance machine is controlled using a Texas Instruments C2000 F28035 isolated Piccolo control card [123]. Based on the alignment procedure described, it is observed that at the end of the alignment procedure, the reference rotor pole (R'_1 in Figure C.6) always aligns itself with the reference stator pole (D in Figure C.6). All possible initial unknown rotor positions are encapsulated into either the scenario similar to the one represented by Figure C.4(a) or the one represented by Figure C.5(a) and need not be explicitly elaborated. The alignment procedure can also be extended to a switched reluctance machine with a higher number of rotor and stator poles.

C.2 Saturation of Phase Flux Linkage

This section of the appendix presents the effect of saturation in an inductor followed by its correlation to a switched reluctance machine. Figure C.7 shows flux linkage through the inductor core for different values of inductor current.

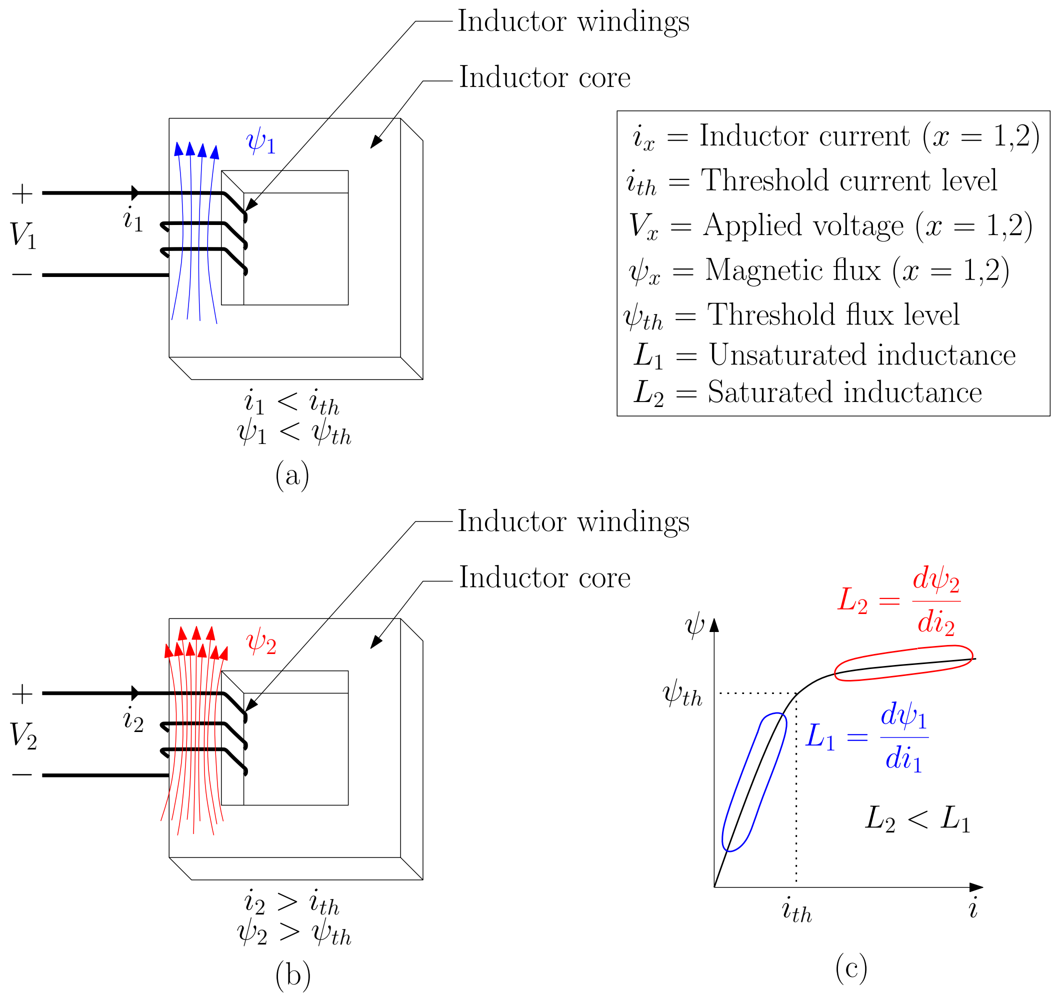

Figure C.7: Saturation in an inductor from a magnetic standpoint: (a) Flux linkage for lower values of inductor current (b) Flux linkage for higher values of inductor current (c) Magnetic flux linkage versus inductor current

Figure C.7(a) shows the magnetic flux linkage ψ_1 due to current i_1 flowing through the inductor. The assumption is that the current i_1 through the inductor is below a certain threshold current level i_{th}, i.e., the current level above which the inductor begins to saturate.

Similarly, it is also assumed that the flux linkage ψ_1 is less than the threshold flux level ψ_{th}, i.e., the flux level where the inductor begins to saturate. As a result, the plot of flux linkage versus the inductor current shown in Figure C.7(c) exhibits linear characteristics upto values of i_{th} and ψ_{th}. The inductance L_1 of the inductor is estimated by calculating the slope of the plot in the linear region. Since the plot is linear, the inductance L_1 is a constant. On the other hand, figure C.7(b) shows the magnetic flux linkage ψ_2 due to current i_2 flowing through the inductor. The assumption is that the current i_2 through the inductor is above the threshold current level. Similarly, it is also assumed that the flux linkage ψ_2 is greater than the threshold flux level. Intuitively, this means that the current is proportionally trying to squeeze in a lot more flux lines through the inductor core. The issue being, the carrying capacity of the core begins to act as a bottleneck, implying that an increasing inductor current is no longer capable of causing an increase in the flux linkage, as a result, the inductor begins to saturate. For higher levels of inductor current and flux linkage, the inductance L_2 of the inductor no longer exhibits a constant value but rather a reduced value, as shown by the slope of the flux linkage versus inductor current plot of Figure C.7(c). The point to take away from the above description is that the value of the inductor begins to drop as the current flowing through it exceeds a certain threshold level.

Since the terminals of a switched reluctance machine act as an inductive load, the machine also suffers from a similar saturation phenomenon. While trying to characterize a switched reluctance machine, only the electrical terminals of the machine are accessible. The description provided for Figure C.7, analyzed saturation from a magnetic standpoint; however, the phenomenon of saturation can also be viewed from an electrical standpoint, which is presented next through Figure C.8. Figure C.8 shows the voltage signal V_L, measured across the terminals of an inductor L along with the evolution of its inductor current i_L, whose rate of change with respect to time is defined by the following expression:

$$\frac{di_L}{dt} = \frac{V_L}{L} \tag{C.1}$$

$$V_L = L\frac{di_L}{dt}$$

$$\frac{di_L}{dt} = \frac{V_L}{L}$$

L = Inductor's inductance value
t = Time
t_x = Time instances (x = 1,2,3,4,5,6)
i_L = Current through the inductor
V_L = Voltage measured across the inductor
V_{dc} = DC level of the applied inductor voltage
i_{th} = Threshold current level
$\Delta T_1 = (t_2 - t_1) = (t_3 - t_2)$
$\Delta T_2 = (t_5 - t_4) = (t_6 - t_5)$

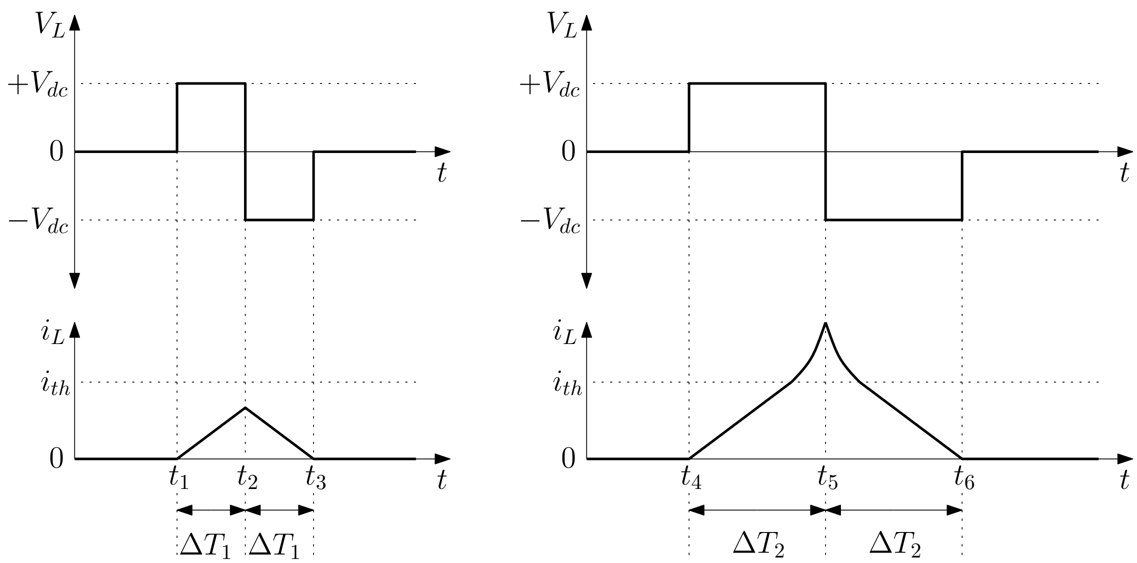

(a) $\Delta T_2 > \Delta T_1$ (b)

Figure C.8: Saturation in an inductor from an electrical standpoint: (a) Lower values of current at which the inductor value is constant (b) Higher values of current at which the inductor value starts reducing

In Figure C.8(a), when a positive voltage, i.e., $+V_{dc}$ is applied for a short duration, i.e., $\Delta T_1 = (t_2 - t_1)$, the inductor current does not have sufficient time to cross the threshold current level. As a result, the inductor does not saturate and has a constant value. Based on Equation C.1, the rate of change of the inductor current is also a constant value, as shown in Figure C.8(a), as a result of which, the current rises and falls in a linear manner.

However, in Figure C.8(b), when a positive voltage, i.e., $+V_{dc}$ is applied for a longer duration, i.e., $\Delta T_2 = (t_5 - t_4)$, the inductor current does in fact have sufficient time to cross the threshold current level. As a result, the inductor begins to saturate and its inductance value begins to drop. Based on Equation C.1, the rate of change of inductor current starts increasing, and as shown in Figure C.8(b), the current starts to rise in a nonlinear manner (for values greater than the threshold current level). When the applied voltage is negative, i.e., $-V_{dc}$, the inductor current begins to fall in a nonlinear manner as well (as long as its above the threshold current level). As long as the current remains below the threshold current level, it follows a linear trajectory whereas when it is greater than the threshold current level, it follows a nonlinear trajectory. To characterize a switched reluctance machine, the plot shown in Figure C.8 is obtained and the data is then processed.

From a pratical standpoint, care should be taken while operating the system in its saturation region, because the currents could reach high damaging levels quite rapidly (from Equation C.1, when the inductance value begins to drop, the current increases even more rapidly, i.e., positive feedback). Care should be taken by increasing the time period (from ΔT_1 to ΔT_2) extremely gradually and also by selecting a low value of V_{dc}, all while closely monitoring the current.

C.3 Experimental Setup

This section of the appendix presents the steps in setting up a laboratory testbed for characterizing a switched reluctance machine. Earlier sections of this appendix describe the alignment procedure and what to expect in terms of phase current through the terminals of a machine when it saturates. The process of characterizing the machine begins with the execution of the alignment procedure, at the end of which, the rotor is at a position, where $\theta = 0°$. After the alignment procedure is complete, a protractor (printed on a piece of paper) is attached to the face of the switched reluctance machine (the orientation of the protractor is unimportant at this stage; however, it is preferable to have the 0° marking on top) and a key stock (or some form of marking) is attached to the shaft of the machine (on the surface of the shaft with the help of some tape) such that, the key stock points to the 0° marking on the protractor. Figure C.9 shows the setup of a switched reluctance machine with a protractor and key stock attached as mentioned, after the execution of the alignment process, by the end of which the rotor is at its aligned position (i.e., $\theta = 0°$).

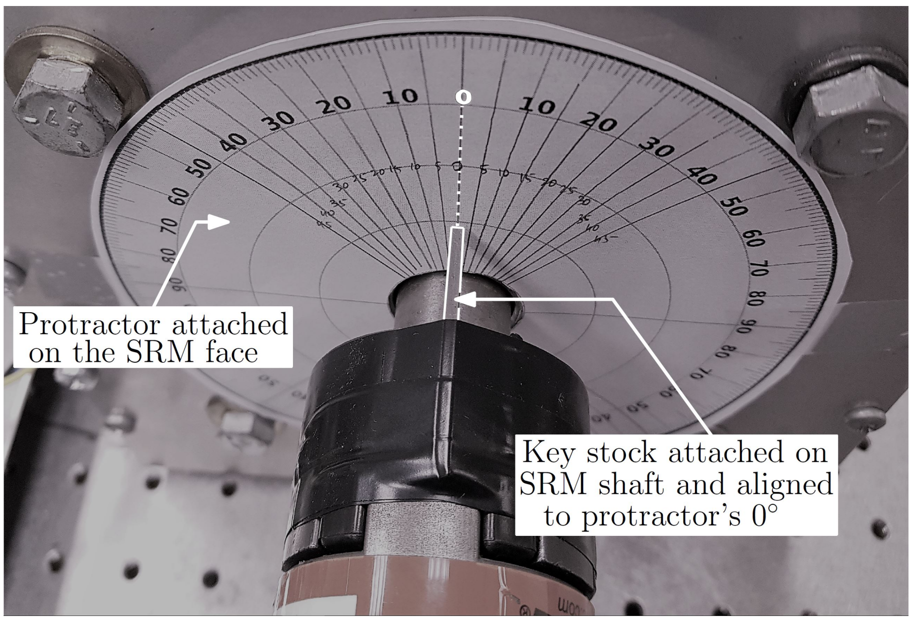

Figure C.9: The SRM with the attached protractor and the shaft key stock. The rotor is at its aligned position (i.e., $\theta = 0°$)

The next step in the characterization process involves providing a voltage pulse as shown in Figure C.8. However, before a voltage is applied across the terminals of the machine, the machine's rotor is locked in its place to prevent it from changing its position (θ). Since the rotor is connected to the shaft of the machine, locking the machine's shaft ensures that the rotor remains locked as well. The shaft position of the switched reluctance machine is locked using a locking pinch off plier which is held in place with a flat drill press vise (which is screwed down to the testbed). The locking setup is shown in Figure C.10.

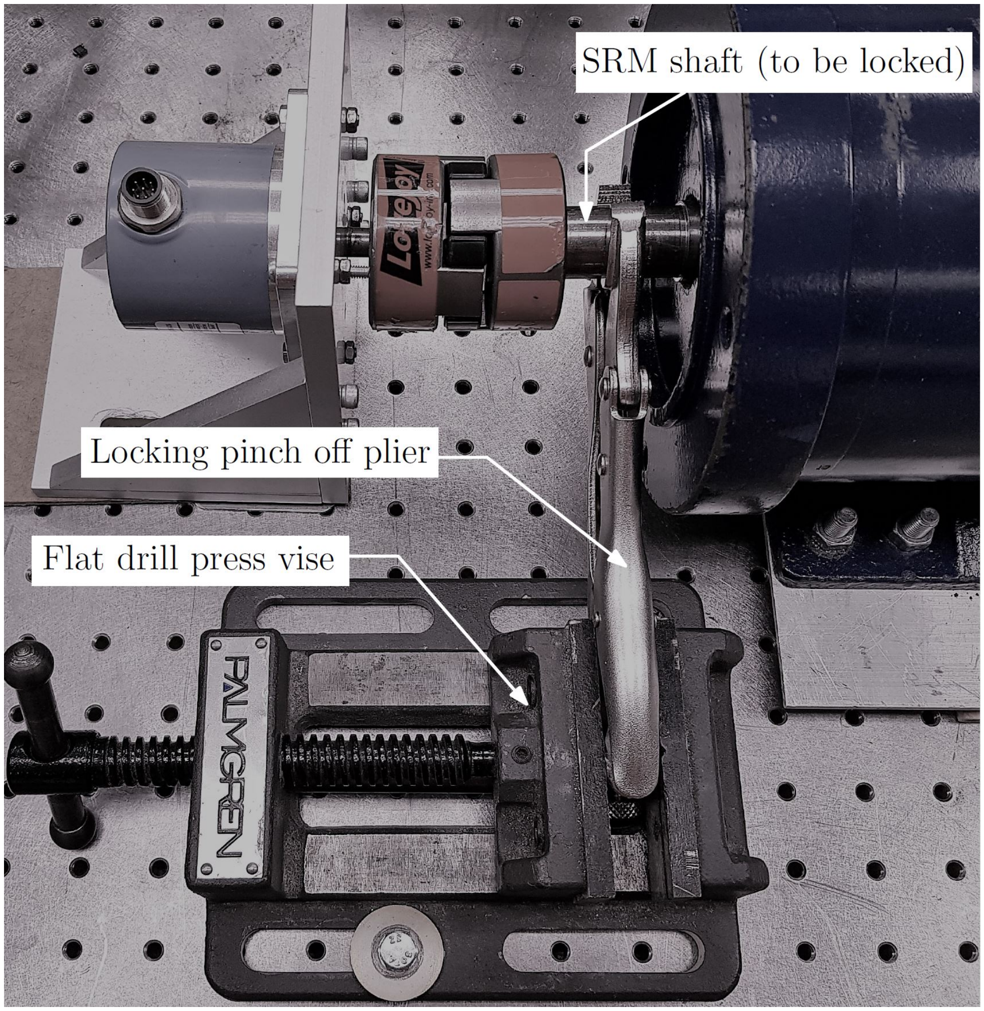

Figure C.10: Locking mechanism for a switched reluctance machine's shaft (in turn, its rotor)

It is worth noting that, locking the rotor at positions other than the aligned position is of higher importance and necessary because at positions other than the aligned position (especially the positions still relatively close to the aligned position), the rotor tends to realign itself with the stator phase when the voltage pulse is applied (i.e., the stator phase is excited). This is because the aligned position acts as the rotor's stable equilibrium point. Therefore, locking the rotor at the aligned position is theoretically not required, but is preferred as the shaft vibrations can lead to erroneous readings.

Since the aligned position experiences the maximum amount of saturation, the phase current exhibits its maximum nonlinearity at the aligned position (as shown in Figure C.8). Next, a voltage pulse is applied across the terminals of a switched reluctance machine, resulting in the evolution of its phase current. The applied voltage pulse and the sensed phase current waveforms are captured using an oscilloscope and are shown in Figure C.11. The time period for the positive voltage pulse was gradually increased from a value of 0.5 ms to a value 1.8 ms. During this test, the current controller is disabled (as the current needs to be unregulated), as a result, the magnetizing time period must be very small and increased in small increments. The selected magnetizing time period allows the phase current to reach a value of 3.5 A, a value below the machine's rated current level of 4.0 A.

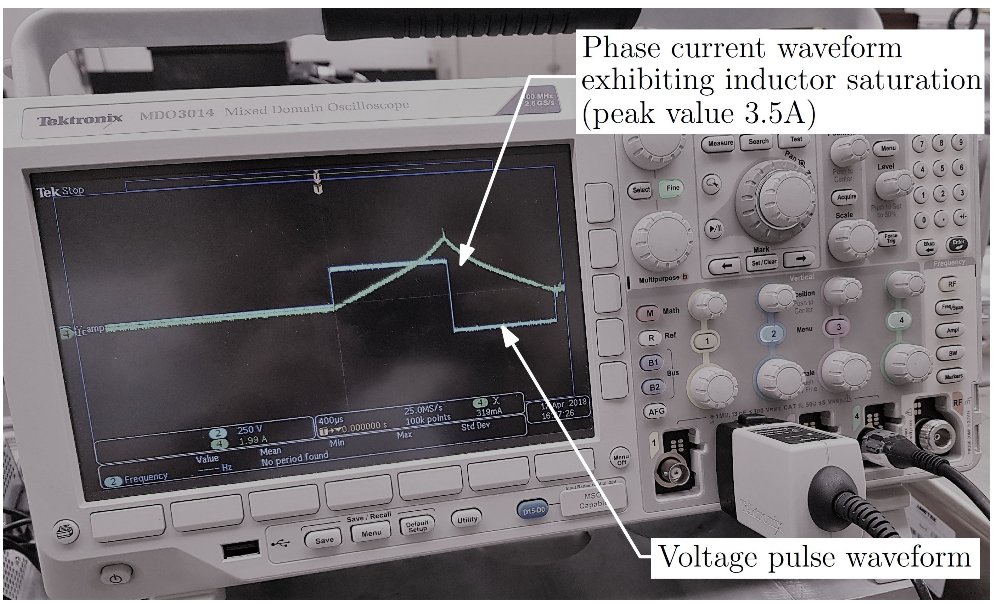

Figure C.11: Captured voltage signal and phase current at the aligned position ($\theta = 0°$)

After successfully recording the results at the aligned position, the rotor is manually turned in either the positive or the negative direction by a certain amount $\Delta\theta$ and the test is repeated. Figure C.12 shows the rotor position manually set to the $\theta = -20°$ position (in the counterclockwise direction). At the new position, the next set of results are then recorded. For a symmetric switched reluctance machine, theoretically the results for $\pm\theta$ should be identical; however, it is best to verify the results experimentally. The process is iteratively performed for different values of θ ranging from: $-(\pi/N_r) \leq \theta \leq +(\pi/N_r)$. In this manner, all the characterization data of a switched reluctance machine is gathered. A smaller value of $\Delta\theta$ results is a larger collection of characterization data and a finer resolution.

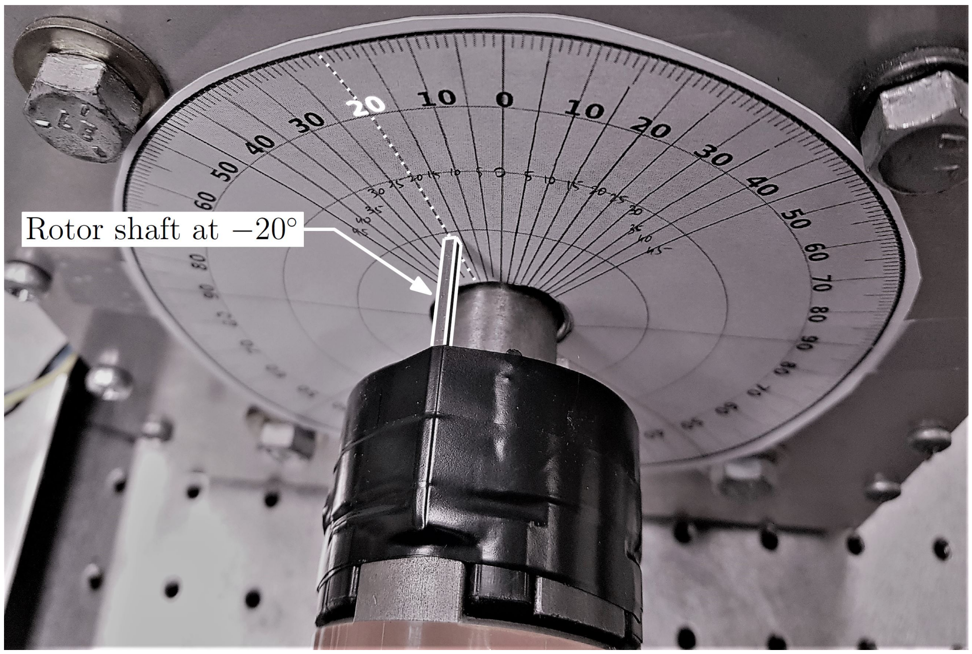

Figure C.12: The rotor locked at position: $\theta = -20°$

C.4 Experimental Measurements

This section of the appendix presents the results recorded at different rotor positions based on the technique specified in Section C.3. For a switched reluctance machine with six rotor poles (i.e., $N_r = 6$), the value of the rotor position (θ) ranges from: $-(\pi/N_r) \leq \theta \leq +(\pi/N_r)$, i.e., $-30° \leq \theta \leq +30°$. The experimental data is collected for rotor positions separated by: $\Delta\theta = \pm 5°$, i.e., for rotor positions corresponding to $0°$, $\pm 5°$, $\pm 10°$, $\pm 15°$, $\pm 20°$, $\pm 25°$, and $\pm 30°$. However, the results reported are in steps of: $\Delta\theta = \pm 15°$ as shown in Figure C.13, i.e., for the rotor at its aligned position ($0°$), midpoint positions ($\pm 15°$), and unaligned positions $\pm 30°$. From Figure C.13, it is observed that at the aligned position ($\theta = 0°$) the

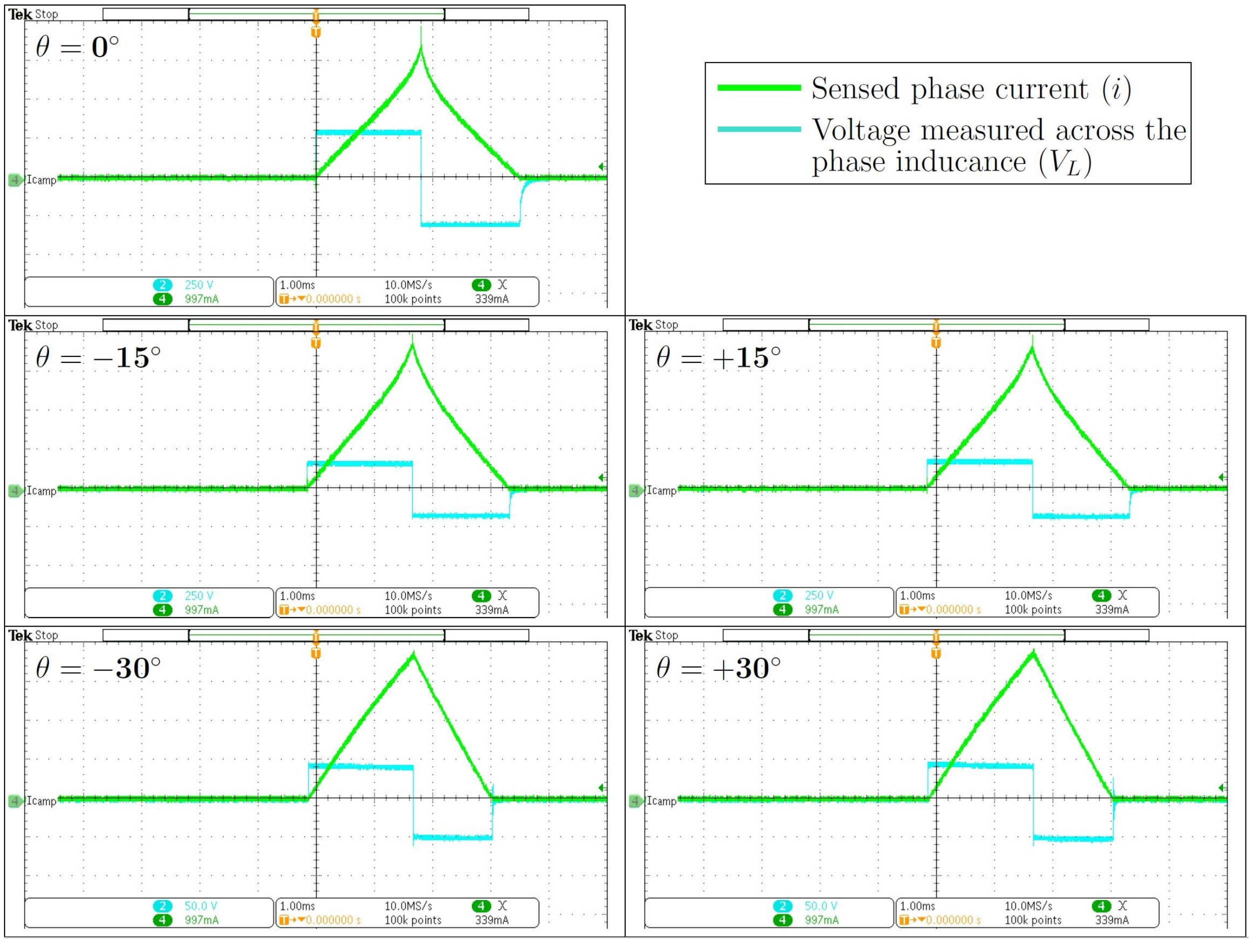

Figure C.13: Oscilloscope results displaying the applied voltage signal and the sensed phase current. The displayed results are 15° apart in both, the positive and the negative directions

phase current experiences the maximum saturation, while at the midpoint ($\theta = \pm 15°$) and unaligned ($\theta = \pm 30°$) positions, the effect of saturation is not as prominent (as is evident from the sensed phase current's reducing nonlinearity, as the rotor position is changed from the aligned position to the unaligned position in Figure C.13). The phase current waveform is more or less linear at the unaligned positions ($\theta = \pm 30°$), indicating no saturation and a constant value for the machine's phase inductance (based on Equation C.1).

It is worth noting that at each rotor position, the DC value of the applied voltage ($\pm V_{dc}$) must be reduced if the magnetizing time period (i.e., $\Delta T_2 = t_5 - t_4$ of Figure C.8(b)) is kept constant. This is because the phase inductance of the machine for positions closer to the unaligned position begins to drop, as a result, from Equation C.1, the phase current rises rapidly and hits the machine's rated current level quicker. Either the magnetizing time period or the applied DC voltage ($\pm V_{dc}$) must be reduced in order to keep the phase current peak below the machine's rated level. For the results shown in Figure C.13, the magnetizing time period was kept constant while the applied DC voltage ($\pm V_{dc}$) was changed accordingly.

C.5 MATLAB Post Processing

This section presents the post processing steps applied on the experimentally gathered data, based on techniques specified in earlier sections of this appendix. The first step of post processing involves averaging the results shown in Figure C.13, which is performed using MATLAB [124]. Consider a sequence $\{a_j\}_{j=1}^{N}$, where j represents the indices of the elements belonging to the sequence, a_j represents the j^{th} element of the sequence, and N represents the total number of elements in the sequence. Depending on the signal to be averaged, a_j is replaced either with the phase inductance voltage V_L or the sensed phase current i. From figure C.13, it is observed that the oscilloscope has a sampling rate of 10 M Samples s^{-1} and the time period captured by the oscilloscope is 10 ms. As a result, the total number of samples (or elements of the sequence) contained in the V_L and i sequence is 100 k samples. Therefore, the value of N is equal to 100 k. An n sized moving average window is then applied to the sequence $\{a_j\}_{j=1}^{N}$, which results in a new sequence $\{s_j\}_{j=1}^{N}$, where s_j represents the new moving averaged sequence, which is computed using the following expression:

$$s_j = \frac{1}{n} \sum_{k=j-x}^{j+y} a_k \tag{C.2}$$

where,

$$x = \begin{cases} \dfrac{n-1}{2} & ;\ n = \text{odd} \\ \\ \dfrac{n}{2} & ;\ n = \text{even} \end{cases} \tag{C.3}$$

and,

$$y = \begin{cases} \dfrac{n-1}{2} & ; \ n = \text{odd} \\ \\ \dfrac{n}{2} - 1 & ; \ n = \text{even} \end{cases} \tag{C.4}$$

Figure C.14 and Figure C.15 show an example of the moving average filter applied to a sequence $\{a_j\}$. It is worth noting that the window size is automatically truncated at the endpoints when there are not enough elements to fill the window. When the window is truncated, the average is taken only over the elements that do fill the window. This way, the number of elements in the resultant sequence $\{s_j\}$ remains the same as those in the original sequence $\{a_j\}$, i.e., N.

$$\{a_j\}_{j=1}^{6} = \begin{array}{|c|c|c|c|c|c|}\hline a_1 & a_2 & a_3 & a_4 & a_5 & a_6 \\ \hline\end{array} \quad (\text{with } \overbrace{a_2 \; a_3 \; a_4}^{n=3})$$

N = 6
n = 3
j = 3

$$x, y = \left(\frac{n-1}{2}\right) = 1$$

$$s_j = \frac{1}{n} \sum_{k=j-x}^{j+y} a_k \quad \Rightarrow s_3 = \frac{1}{3} \sum_{k=2}^{4} a_k \quad \Rightarrow s_3 = \left(\frac{a_2+a_3+a_4}{3}\right)$$

$$\{s_j\}_{j=1}^{6} = \begin{array}{|c|c|c|c|c|c|}\hline s_1 & s_2 & s_3 & s_4 & s_5 & s_6 \\ \hline\end{array}$$

Figure C.14: An odd sized moving average filter applied to a sequence $\{a_j\}$

$$\{a_j\}_{j=1}^{6} = \begin{array}{|c|c|c|c|c|c|}\hline a_1 & a_2 & a_3 & a_4 & a_5 & a_6 \\ \hline\end{array} \quad (\text{with } \overbrace{a_1 \; a_2 \; a_3 \; a_4}^{n=4})$$

N = 6
n = 4
j = 3

$$x = \frac{n}{2} = 2$$

$$y = \left(\frac{n}{2} - 1\right) = 1$$

$$s_j = \frac{1}{n} \sum_{k=j-x}^{j+y} a_k \quad \Rightarrow s_3 = \frac{1}{4} \sum_{k=1}^{4} a_k \quad \Rightarrow s_3 = \left(\frac{a_1+a_2+a_3+a_4}{4}\right)$$

$$\{s_j\}_{j=1}^{6} = \begin{array}{|c|c|c|c|c|c|}\hline s_1 & s_2 & s_3 & s_4 & s_5 & s_6 \\ \hline\end{array}$$

Figure C.15: An even sized moving average filter applied to a sequence $\{a_j\}$

Figure C.16, shows the normalized phase inductance voltage (V_L) and the sensed phase current (i), along with the post processed averaged values of the normalized phase inductance voltage $V_{L(avg)}$ and the phase current i_{avg}. The averaged values $V_{L(avg)}$ and i_{avg} are essentially low pass filtered values of V_L and i, respectively.

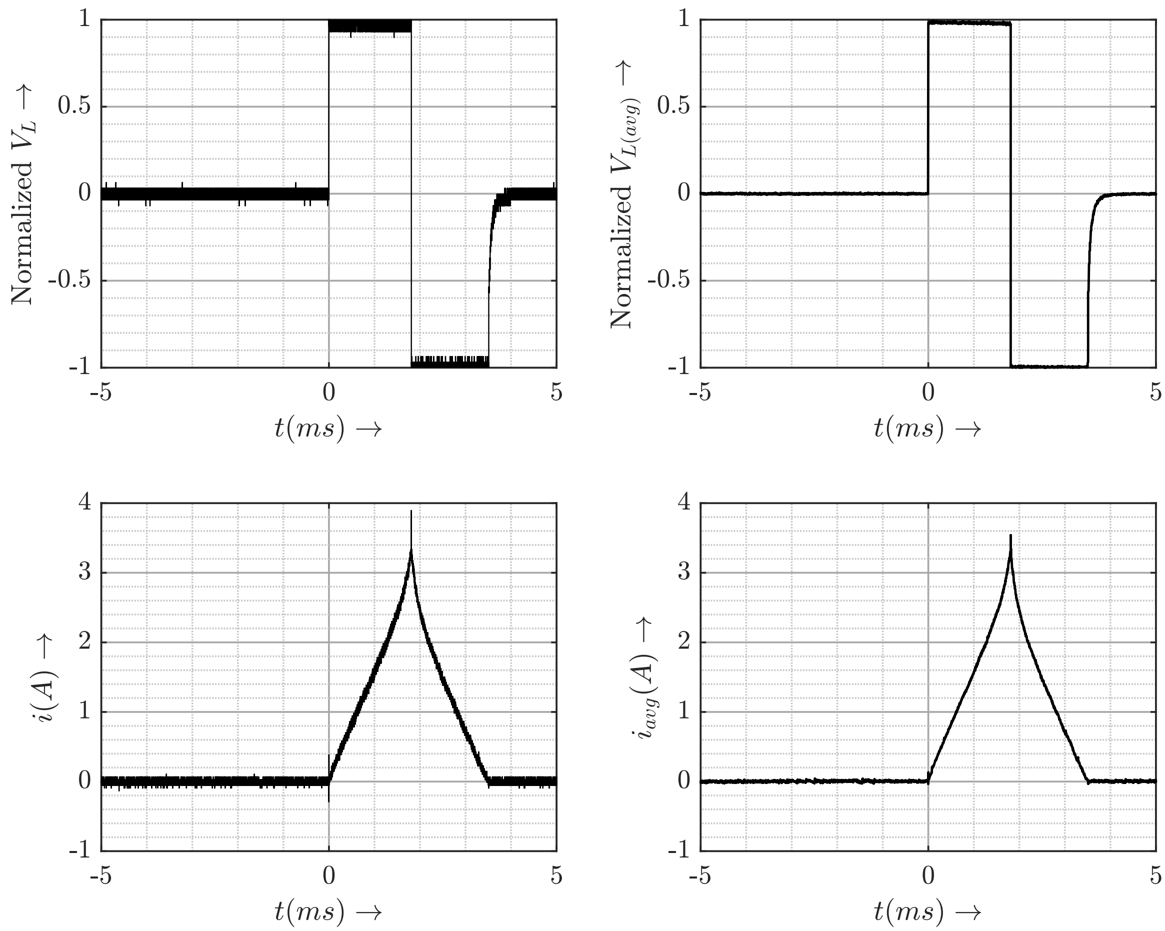

Figure C.16: Aligned position (i.e., $\theta = 0°$) normalized phase inductance voltage (V_L) and sensed phase current (i) along with their averaged values $V_{L(avg)}$ and i_{avg}, respectively

The signals $V_{L(avg)}$ and i_{avg} shown in Figure C.16 are computed with a moving average window size of 50, i.e., $n = 50$. The characterization process of a switched reluctance machine involves obtaining the plot of the phase inductance (L) versus the phase current (i) at different rotor positions (θ). Therefore, at a particular rotor position (i.e., $\theta = \theta_x$ and a particular value of phase current (i.e., $i = i_x$), the instantaneous phase inductance is calculated in accordance with Equation C.1 and is expressed as:

$$L(\theta_x, i_x) = \frac{V_L}{\left.\dfrac{di}{dt}\right|_{i=i_x}} \tag{C.5}$$

Figure C.17 provides a graphical representation of calculating the inductance of a switched reluctance machine at different current levels (i.e., i_1 and i_2), at a particular rotor position (θ_x).

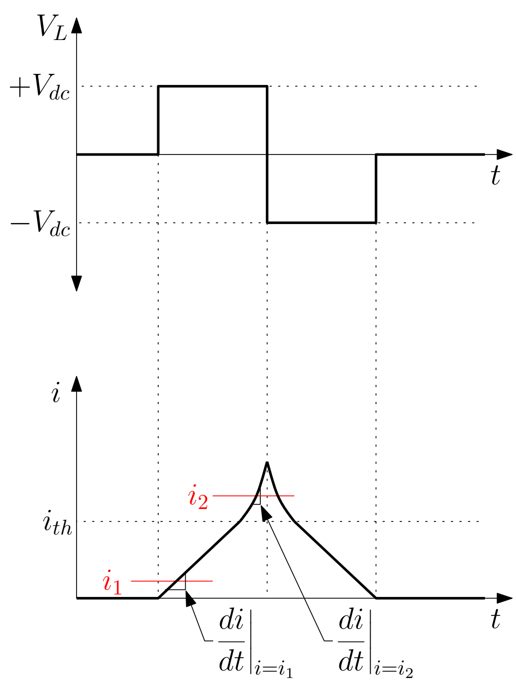

i = Phase current
t = Time
i_x = A particular phase current value
θ_x = A particular rotor angular position
i_{th} = Threshold current level
V_L = Phase inductance voltage
V_{dc} = DC level of the applied inductor voltage
$L(\theta_x, i_x)$ = Instantaneous phase inductance at $\theta = \theta_x$ and $i = i_x$

$$\Rightarrow V_L = L(\theta_x, i_x)\left.\frac{di}{dt}\right|_{i\,=\,i_x}$$

$$\Rightarrow L(\theta_x, i_x) = \frac{V_L}{\left.\dfrac{di}{dt}\right|_{i=i_x}}$$

Figure C.17: Inductance calculation at different current levels i_1 and i_2 at a particular rotor position

Figure C.18(a), shows the averaged normalized phase voltage ($V_{L(avg)}$) and the averaged sensed current (i_{avg}) at the aligned rotor position ($\theta = 0°$). Due to the high saturation experienced at the aligned rotor position, the phase current exhibits a high degree of non-linearity, which is clearly visible from the averaged phase current waveform (i_{avg}), especially for higher values of phase current, as that is where the machine begins to saturate. The instantaneous phase inductance ($L(\theta_x, i_x)$) is iteratively calculated using Equation C.5 (i.e., shown in Figure C.17) for all the values of phase current, and the resultant values are plotted in Figure C.18(b). The calculated aligned position phase inductance $L(0, i)$ appears to have a lot of ripple and noise in it (due to the noise picked up in the sensed phase current), which is removed in the averaged aligned position phase inductance curve represented by $L_{avg}(0, i)$.

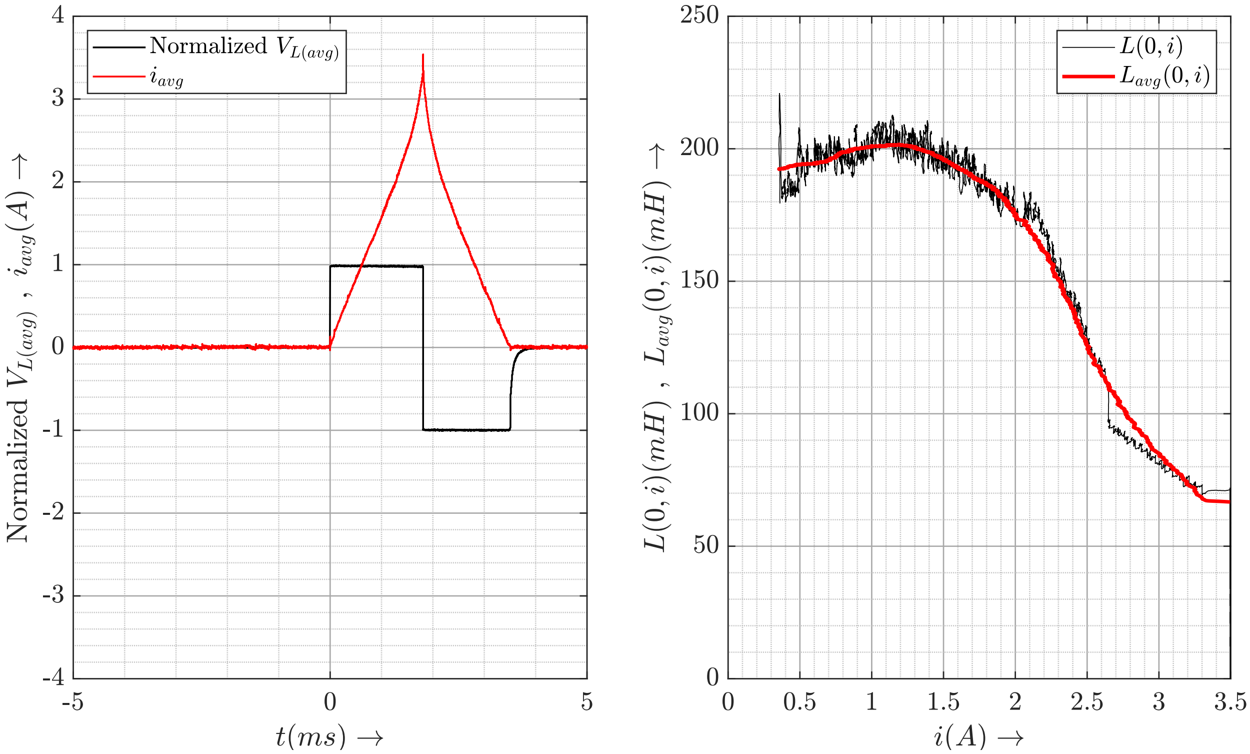

(a) (b)

Figure C.18: SRM characterization data at the aligned position, i.e., $\theta = 0°$ (a) Normalized $V_{L(avg)}$ and i_{avg} versus time t (b) Aligned position saturated inductance $L(0, i)$ and its average $L_{avg}(0, i)$ versus phase current i

Figure C.19(a), shows the averaged normalized phase voltage ($V_{L(avg)}$) and the averaged sensed current (i_{avg}) at the positive midpoint rotor positions ($\theta = +15°$), while Figure C.19(b), shows the averaged normalized phase voltage ($V_{L(avg)}$) and the averaged sensed current (i_{avg}) at the negative midpoint rotor positions ($\theta = -15°$). Due to the medium saturation experienced at the midpoint rotor positions, the phase current exhibits a lower degree of nonlinearity (compared to the aligned rotor position), which is visible in both the

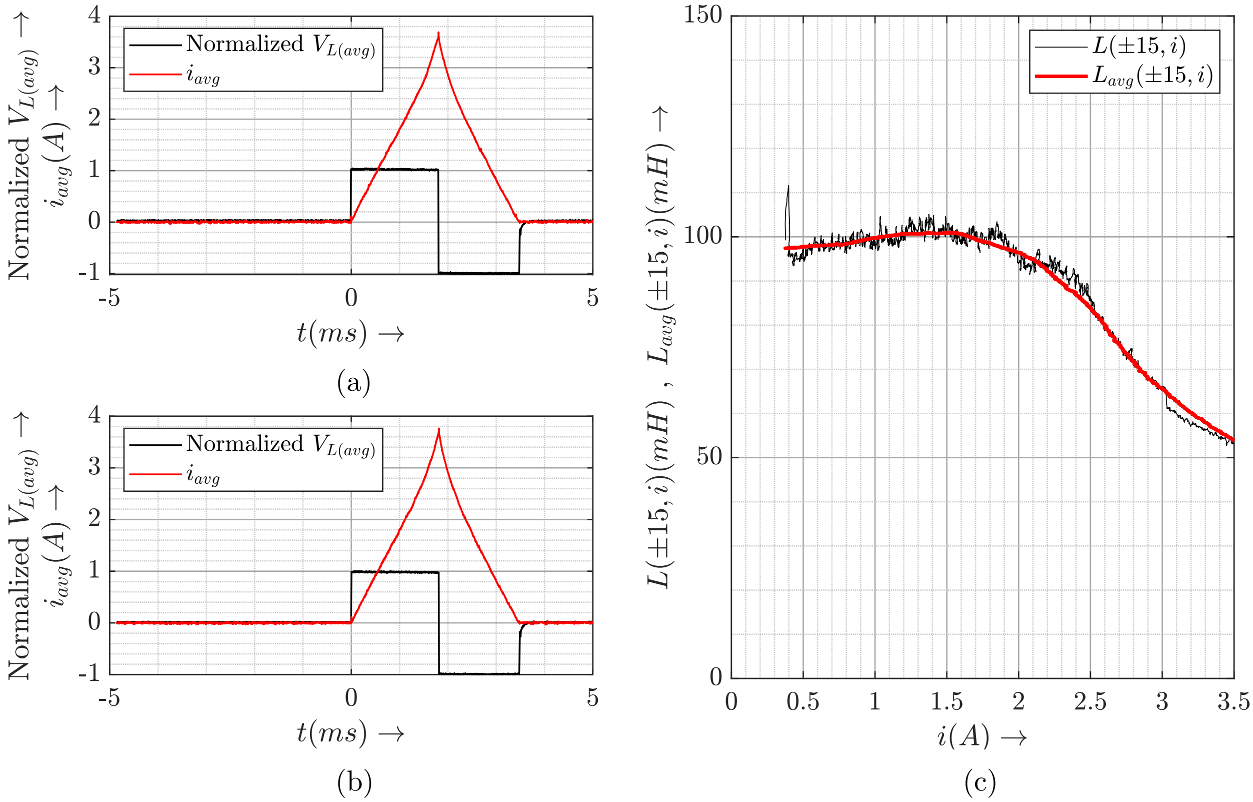

Figure C.19: SRM characterization data at the midpoint positions, i.e., $\theta = \pm15°$ (a) Normalized $V_{L(avg)}$ and i_{avg} at $\theta = +15°$ versus time t (b) Normalized $V_{L(avg)}$ and i_{avg} at $\theta = -15°$ versus time t (c) Mean midpoint position saturated inductance $L(\pm15, i)$ and its average $L_{avg}(\pm15, i)$ versus phase current i

averaged phase current waveform, especially for higher values of phase current where the machine begins to saturate. Since two different rotor positions ($\theta = \pm15°$) are considered as midpoint positions, two different phase inductance data sets are obtained. Theoretically, the data sets should be identical due to the geometrical symmetry in the switched reluctance machine under test. However, the measurements show a slight difference in the values of the inductance at $\theta = \pm15°$. Figure C.19(c) shows only the mean of the two data sets belonging to $\theta = \pm15°$. The instantaneous phase inductance ($L(\theta_x, i_x)$) is iteratively calculated using Equation C.5 (i.e., shown in Figure C.17) for all the values of phase current, and the resultant values are plotted in Figure C.19(c). The calculated mean of the two midpoint position phase inductances $L(\pm15, i)$ appears to have a lot of ripple and noise in it (due to the noise picked up in the sensed phase current), which is removed in the averaged mean midpoint position phase inductance curve represented by $L_{avg}(\pm 15, i)$.

Similarly, Figure C.20(a), shows the averaged normalized phase voltage ($V_{L(avg)}$) and the averaged sensed current (i_{avg}) at the positive unaligned rotor positions ($\theta = +30°$), while Figure C.20(b), shows the averaged normalized phase voltage ($V_{L(avg)}$) and the averaged sensed current (i_{avg}) at the negative unaligned rotor positions ($\theta = -30°$). Since there is no saturation at the unaligned rotor positions, the phase current exhibits no nonlinearity (as a result, the phase inductance is a constant), which is visible in both the averaged phase current waveform, even at higher values of phase current. Since two different rotor positions ($\theta = \pm 30°$) are considered as unaligned positions, two different phase inductance data sets are

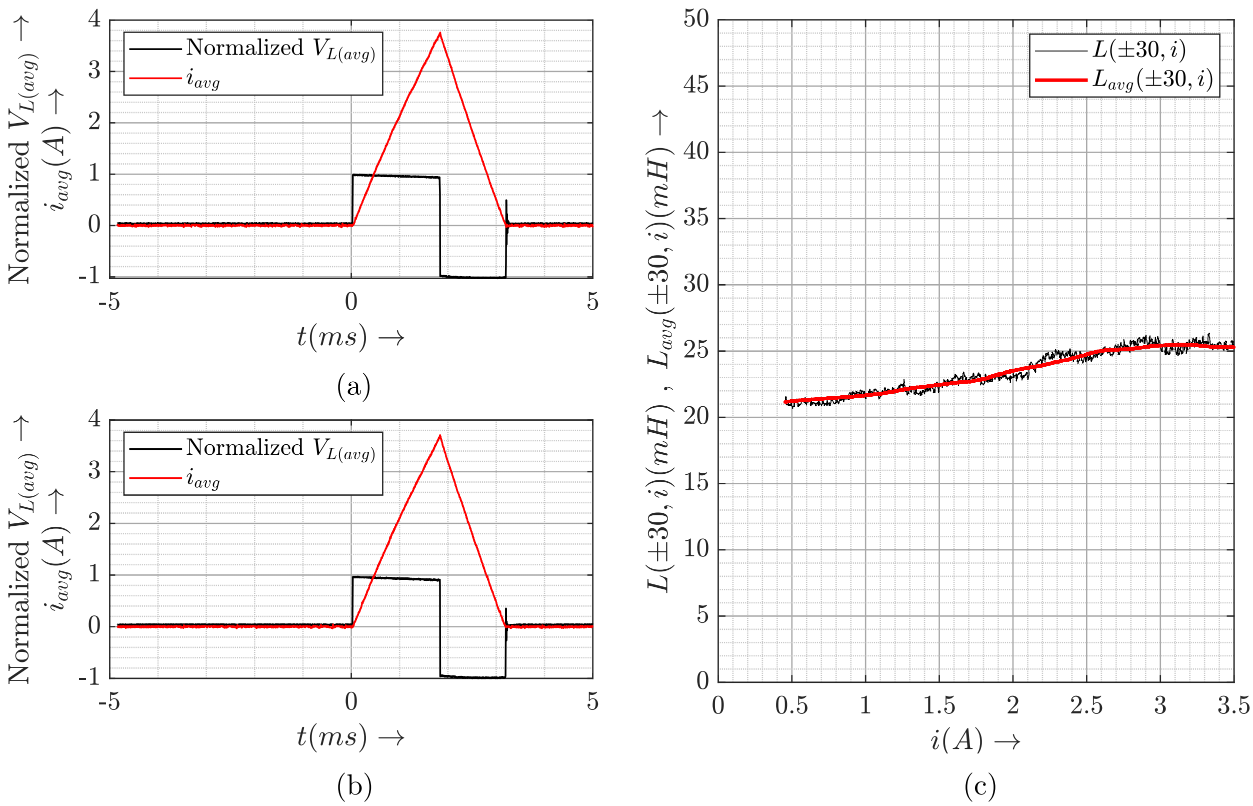

Figure C.20: SRM characterization data at the unaligned positions, i.e., $\theta = \pm 30°$ (a) Normalized $V_{L(avg)}$ and i_{avg} at $\theta = +30°$ versus time t (b) Normalized $V_{L(avg)}$ and i_{avg} at $\theta = -30°$ versus time t (c) Mean unaligned position saturated inductance $L(\pm 30, i)$ and its average $L_{avg}(\pm 30, i)$ versus phase current i

obtained. Theoretically, the data sets should be identical due to the geometrical symmetry in the switched reluctance machine under test. However, the measurements show a slight difference in the values of the inductance at $\theta = \pm 30°$. Figure C.20(c) shows only the mean of the two data sets belonging to $\theta = \pm 30°$. The instantaneous phase inductance ($L(\theta_x, i_x)$) is iteratively calculated using Equation C.5 (i.e., shown in Figure C.17) for all the values of current, and the resultant values are plotted in Figure C.20(c). The calculated mean of the two unaligned position phase inductances $L(\pm 15, i)$ appears to have a lot of ripple and noise in it (due to the noise picked up in the sensed phase current), which is removed in the averaged mean midpoint position phase inductance curve represented by $L_{avg}(\pm 30, i)$.

Figure C.21 shows the variation of the phase inductance (L) versus the phase current (i) for different values of the rotor position (θ). The measurements shown in the figure are for rotor positions separated by 5° (i.e., $\Delta\theta = 5°$). The curves in the figure are also extrapolated to meet the vertical axis of the plot. The values of phase inductance at different rotor positions (at current values of 0 A) are compared to measurements made using an LCR meter as well, which are shown in Figure C.22.

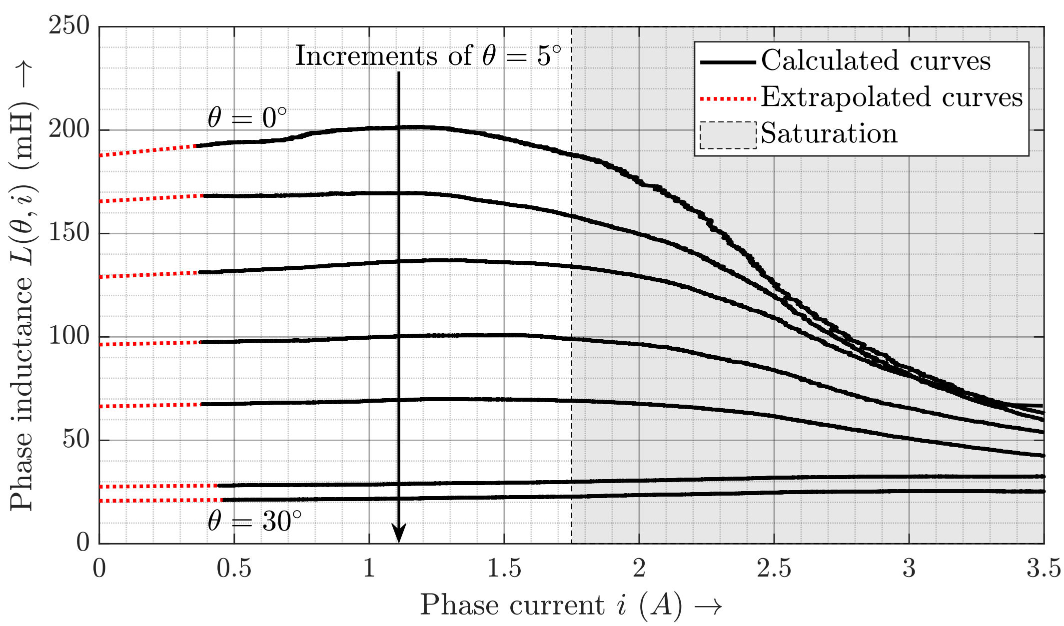

Figure C.21: Variation of the phase inductance with phase current at different rotor positions

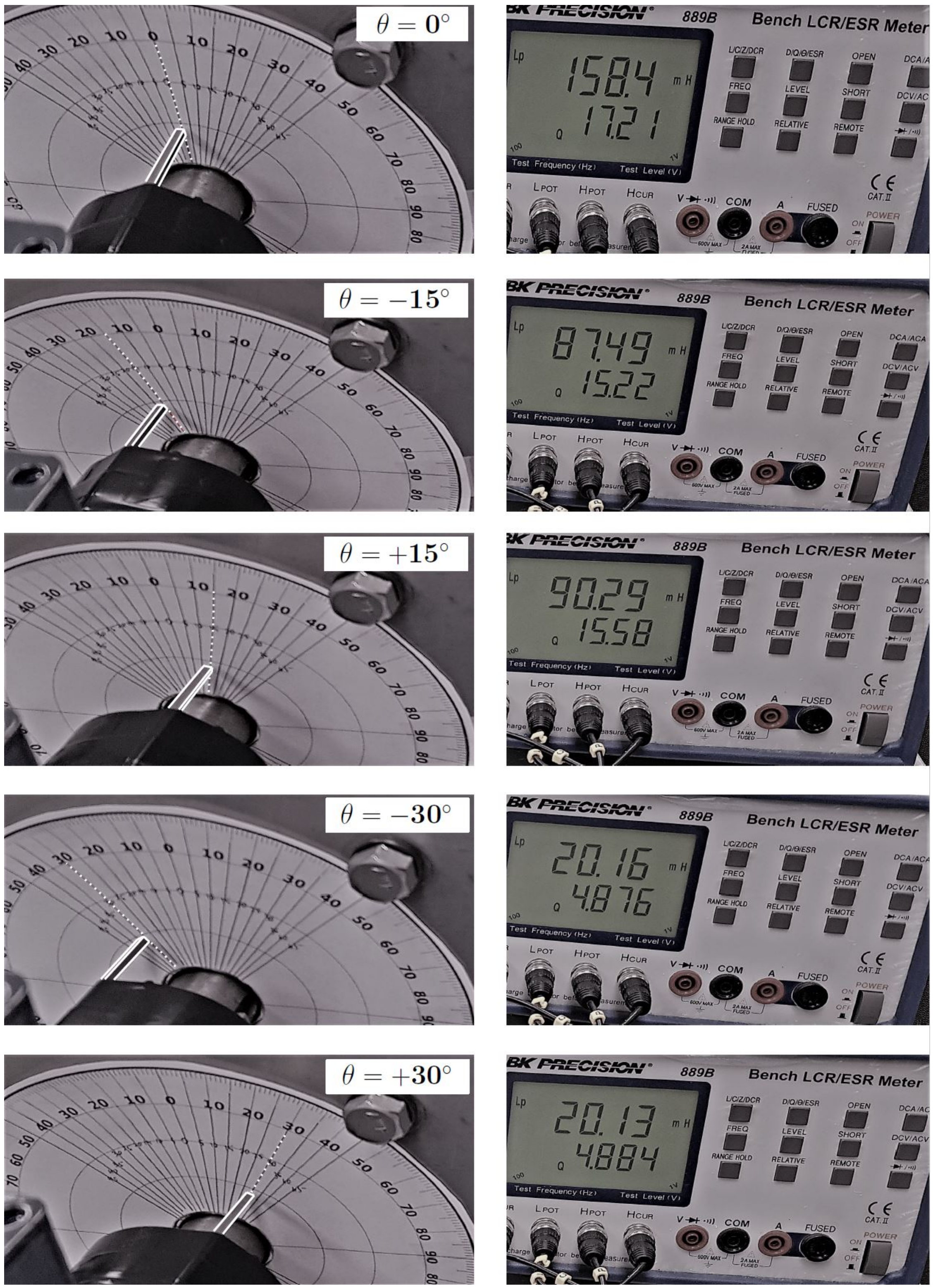

Figure C.22: Measured inductance at different rotor positions (θ) using an LCR meter

It is worth noting that, since the inductance values are relatively high, the parallel mode of an LCR meter is selected (i.e., L_p) along with a low frequency injected signal (i.e., 100 Hz). The calculated inductance values and the ones obtained using an LCR meter have been compared in Table C.1, and they are comparable to each other.

Table C.1: Comparison of the calculated inductance and the measured inductance at different rotor positions. The values are the mean values of the $\pm\theta$ positions (except for the case when $\theta = 0°$)

Rotor Position $\theta(°)$	**Calculated Inductance** $L(\theta, 0)$ (mH)	**Measured Inductance** $L(\theta, 0)$ (mH)
0	187.7	158.4
± 5	165.5	140.6
± 10	128.9	115.8
± 15	96.28	88.89
± 20	66.37	68.06
± 25	27.56	25.32
± 30	20.73	20.15

This concludes the characterization process of a switched reluctance machine. The machine's data was experimentally obtained and then post-processed using MATLAB. The data is also compared with measurements made using an LCR meter. Overall, both the data sets lie within an acceptable margin of error; however, there is a slight difference between the calculated and measured inductance values, especially at the aligned position. From Figure C.21, the saliency (i.e., the ratio of the aligned position inductance to the unaligned position inductance) of the machine at lower values of phase current (0.5 A) is ≈ 9, while for higher values of phase current (3.5 A) its close to ≈ 3 (i.e., indicative of significant saturation).

APPENDIX D

FOURIER COEFFICIENTS OF THE PROPOSED MODEL'S PHASE INDUCTANCE

This appendix presents the derivation for the Fourier coefficients of the proposed model's phase inductance specified in Section 3.4 by Equations 3.65 and 3.66. In the proposed model, only one cosine term (i.e., the average value and the first harmonic) for phase inductance is considered as shown in Figure D.1.

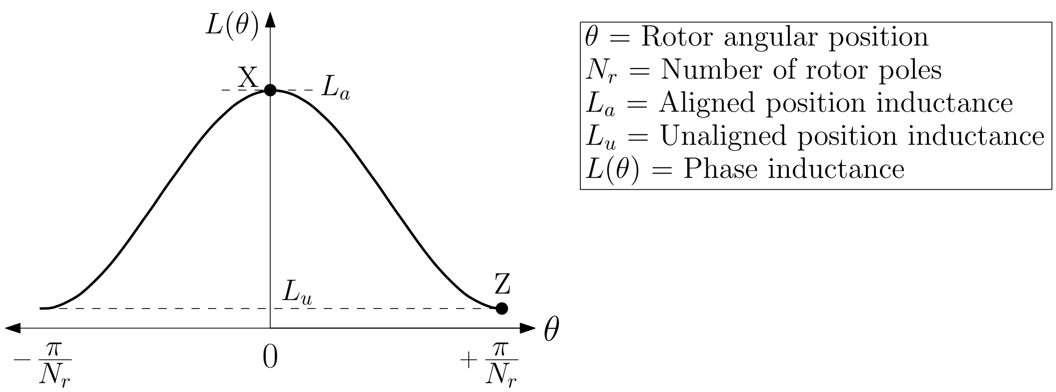

Figure D.1: Phase inductance profile of an SRM using a single cosine term. X and Z represent the aligned and unaligned positions, respectively

The cosine function shown in Figure D.1, in its Fourier representation is expressed as:

$$L(\theta) = L_0 + L_1 \cos(N_r\theta) \tag{D.1}$$

To obtain expressions for the Fourier coefficients L_0 and L_1, two points on the curve shown in Figure D.1 are selected and their coordinates are substituted in Equation D.1, creating a system of equations. The first coordinate selected is the aligned position X, at which $\theta = 0$ and $L(\theta) = L_a$. Substituting the coordinates of the first point in Equation D.1, the following expression is obtained:

$$L_a = L_0 + L_1 \tag{D.2}$$

The second coordinate selected is the unaligned position Z, at which $\theta = \pi/N_r$ and $L(\theta) = L_u$. Substituting the coordinates of the second point in Equation D.1, the following expression is obtained:

$$L_u = L_0 - L_1 \tag{D.3}$$

Solving the system of equations (i.e., defined by Equations D.2 and D.3) results in the following expression for L_0:

$$L_0 = \frac{L_a + L_u}{2} \tag{D.4}$$

and the following expression for L_1:

$$L_1 = \frac{L_a - L_u}{2} \tag{D.5}$$

Similarly, in order to model a phase inductance profile using n Fourier coefficients, n points are selected from the inductance profile and their respective coordinates are used to build a system of equations (i.e., n equations), which can then be solved for in order to obtain the expressions for the n Fourier coefficients.

APPENDIX E

MOTORING LOGARITHMIC FUNCTION COEFFICIENT ESTIMATION

This appendix presents a method of computing the expressions for the coefficients (α_m, β_m, γ_m) of the logarithmic curve fitting function $\lambda_m(\theta)$, which is used during motoring. The logarithmic function is used to curve fit the integral of $p_1(\theta)$ (expressed by Equation 3.123), which is rewritten as:

$$\int p_1(\theta)\ d\theta = \lambda_m(\theta) \tag{E.1}$$

where, $\lambda_m(\theta) = \alpha_m[\ln(\beta_m + \theta) + \gamma_m]$. Since there are three unknowns to be solved for (i.e., α_m, β_m, γ_m), three points which lie on the function must be used. The first step involves obtaining the coordinates of the three points to be used. Since the expression for the original function (i.e., the integral of $p_1(\theta)$) that is being curve fit by $\lambda_m(\theta)$ is known, the coordinates are obtained based on the original function, which are then used to solve for the three unknowns of the logarithmic curve fitting function. To obtain the coordinates of the three points, consider the expression for the integral of $p_1(\theta)$ (from Equation 3.120), which is rewritten as:

$$\int p_1(\theta)\ d\theta = \frac{2}{\kappa N_r\sqrt{L_a L_u}} \tan^{-1}\left\{\frac{\tan[(\kappa N_r\theta + \kappa N_r\phi)/2]}{\sqrt{L_a/L_u}}\right\} + C_4 \tag{E.2}$$

However, the integration constant in Equation E.2, i.e., C_4, first needs to be computed for the motoring scenario. This is done by considering the θ coordinate of the first point as: $-\pi/N_r$, as that represents where the rotor pole begins to align itself with the stator pole during motoring. From Figure E.1, at $\theta = -\pi/N_r$, the value of the corresponding vertical axis coordinate (i.e., the value of the integral of $p_1(\theta)$) is zero, using the coordinates of the first point, i.e., $(-\pi/N_r, 0)$, the value of the integration constant C_4 is computed by substituting the coordinate values in Equation E.2, which results in the following expression:

$$0 = \frac{2}{\kappa N_r\sqrt{L_a L_u}} \tan^{-1}\left\{\frac{\tan[(-\kappa\pi + \kappa N_r\phi)/2]}{\sqrt{L_a/L_u}}\right\} + C_4 \tag{E.3}$$

From Equation E.3, the integration constant is expressed as:

$$C_4 = -\frac{2}{\kappa N_r \sqrt{L_a L_u}} \tan^{-1}\left\{\frac{\tan[(-\kappa\pi + \kappa N_r \phi)/2]}{\sqrt{L_a/L_u}}\right\} \tag{E.4}$$

With the value of the integration constant (C_4) known, the θ coordinate of the second point, i.e., 0 is considered and its corresponding vertical axis coordinate, i.e., the value of the integral of $p_1(0)$, represented by y_2 (shown in Figure E.1),[1] is computed by substituting $(0, y_2)$ in Equation E.2 and is expressed as:

$$y_2 = \frac{2}{\kappa N_r \sqrt{L_a L_u}} \tan^{-1}\left\{\frac{\tan[(\kappa N_r \phi)/2]}{\sqrt{L_a/L_u}}\right\} + C_4 \tag{E.5}$$

Finally, a third point with its θ coordinate lying in the range: $-\pi/N_r \leq \theta \leq 0$, is considered (represented by x_1[2]). The point is selected such that its corresponding vertical axis coordinate (i.e., the value of the integral of $p_1(\theta)$), represented as y_1 is equal to $y_2/2$ (the reason for this selection will become apparent later in the derivation). Therefore, the coordinates of the third point (x_1, y_1) are substituted in Equation E.2, resulting in the following expression:

$$y_1 = \frac{2}{\kappa N_r \sqrt{L_a L_u}} \tan^{-1}\left\{\frac{\tan[(\kappa N_r x_1 + \kappa N_r \phi)/2]}{\sqrt{L_a/L_u}}\right\} + C_4 \tag{E.6}$$

After rearranging Equation E.6, using the relation: $y_1 = y_2/2$, and making x_1 the subject of the formula, the following expression is obtained:

$$x_1 = \frac{2}{\kappa N_r} \tan^{-1}\left\{\sqrt{\frac{L_a}{L_a}} \tan\left[\frac{\kappa N_r \sqrt{L_a L_u}\ (y_2/2 - C_4)}{2}\right]\right\} - \phi \tag{E.7}$$

Now that all the coordinates of the three points are known, the coefficients of the logarithmic curve fitting function (α_m, β_m, γ_m) can be computed. This is because ideally, the logarithmic curve fitting function ($\lambda_m(\theta)$) must also pass through the same points that the original

[1]The vertical axis represents the integral of $p_1(\theta)$ and not the variable y; however, due to the common convention of assigning the variable y to the vertical axis, the same is done in this situation, i.e., y_2.

[2]The horizontal axis represents θ and not the variable x; however, due to the common convention of assigning the variable x to the horizontal axis, the same is done in this situation, i.e., x_1.

curve described by the integral of $p_1(\theta)$ passes through. To summarize, the three points considered are: $(-\pi/N_r, 0)$, $(0, y_2)$, and (x_1, y_1). The expressions for x_1 and y_2 are defined by Equation E.7 and Equation E.5, respectively and $y_1 = y_2/2$. The coordinates also use an integration constant C_4, which is defined by Equation E.4.

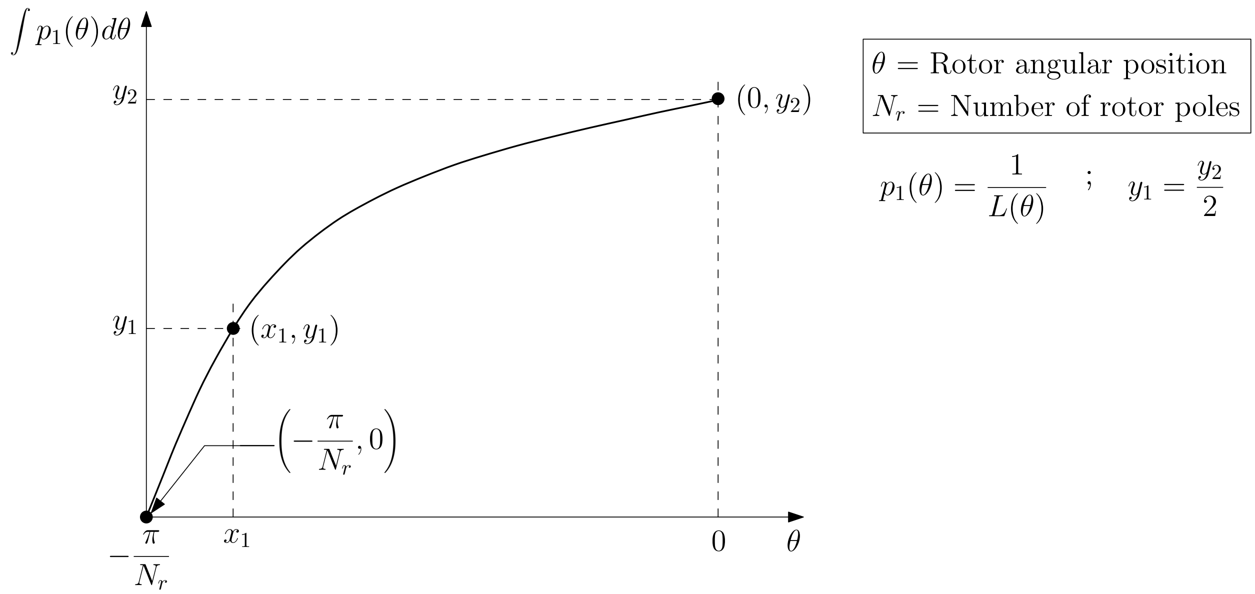

Figure E.1: Integral of $p_1(\theta)$ versus the rotor position (θ) during motoring

The next step involves using the three points in the expression for the motoring logarithmic curve fitting function $\lambda_m(\theta)$, which is defined by Equation 3.121 and is rewritten as:

$$\lambda_m(\theta) = \alpha_m \Big[\ln(\beta_m + \theta) + \gamma_m \Big] \tag{E.8}$$

Applying the coordinates of the first point, i.e., $(-\pi/N_r, 0)$ to Equation E.8, the following expression is obtained:

$$0 = \alpha_m \Big[\ln(\beta_m - \pi/N_r) + \gamma_m \Big] \tag{E.9}$$

From Equation E.9, the expression for the coefficient γ_m is obtained as:

$$\gamma_m = -\ln(\beta_m - \pi/N_r) \tag{E.10}$$

Using the expression of γ_m from Equation E.10 and substituting it in Equation E.8, the following expression is obtained:

$$\begin{aligned}\lambda_m(\theta) &= \alpha_m\Bigg[\ln(\beta_m+\theta)-\ln(\beta_m-\pi/N_r)\Bigg]\\ &= \alpha_m\Bigg[\ln\bigg(\frac{\beta_m+\theta}{\beta_m-\pi/N_r}\bigg)\Bigg]\end{aligned} \tag{E.11}$$

Applying the coordinates of the second point, i.e., $(0, y_2)$ to Equation E.11, the following expression is obtained:

$$y_2 = \alpha_m\Bigg[\ln\bigg(\frac{\beta_m}{\beta_m-\pi/N_r}\bigg)\Bigg] \tag{E.12}$$

From Equation E.12, the expression for the coefficient α_m is obtained as:

$$\alpha_m = y_2 \ln\left(\frac{\beta_m}{\beta_m-\pi/N_r}\right)^{-1} \tag{E.13}$$

Using the expression of α_m from Equation E.13 and substituting it in Equation E.11, the following expression is obtained:

$$\lambda_m(\theta) = y_2 \ln\left(\frac{\beta_m}{\beta_m-\pi/N_r}\right)^{-1} \ln\bigg(\frac{\beta_m+\theta}{\beta_m-\pi/N_r}\bigg) \tag{E.14}$$

Applying the coordinates of the third point, i.e., (x_1, y_1) in Equation E.14, the following expression is obtained:

$$y_1 = y_2 \ln\left(\frac{\beta_m}{\beta_m-\pi/N_r}\right)^{-1} \ln\bigg(\frac{\beta_m+x_1}{\beta_m-\pi/N_r}\bigg) \tag{E.15}$$

Using the earlier defined relation between y_1 and y_2 (i.e., $y_1 = y_2/2$) in Equation E.15, the following expression is obtained:

$$\frac{1}{2} = \ln\left(\frac{\beta_m}{\beta_m-\pi/N_r}\right)^{-1} \ln\bigg(\frac{\beta_m+x_1}{\beta_m-\pi/N_r}\bigg) \tag{E.16}$$

Rearranging Equation E.16 results in:

$$\frac{\sqrt{\beta_m}}{\sqrt{\beta_m-\pi/N_r}} = \frac{\beta_m+x_1}{\beta_m-\pi/N_r} \tag{E.17}$$

Again, rearranging Equation E.17, the following expression is obtained:

$$\beta_m^2 - \frac{\beta_m \pi}{N_r} = \beta_m^2 + 2\beta_m x_1 + x_1^2 \tag{E.18}$$

In Equation E.18, making β_m the subject of the formula, the following expression is obtained:

$$\beta_m = \frac{-x_1^2}{2x_1 + \pi/N_r} \tag{E.19}$$

Therefore, the coefficients (α_m, β_m, γ_m) of the motoring logarithmic function ($\lambda_m(\theta)$) are computed and defined by Equations E.10, E.13, and E.19, respectively. This concludes the method for computing the coefficients of the logarithmic curve fitting function, the summary of which is provided next:

- Compute the integration constant C_4:

$$C_4 = -\frac{2}{\kappa N_r \sqrt{L_a L_u}} \tan^{-1}\left\{\frac{\tan[(-\kappa\pi + \kappa N_r \phi)/2]}{\sqrt{L_a/L_u}}\right\}$$

- Compute the expression for the integral of $p_1(0)$, i.e., y_2:

$$y_2 = \frac{2}{\kappa N_r \sqrt{L_a L_u}} \tan^{-1}\left\{\frac{\tan[(\kappa N_r \phi)/2]}{\sqrt{L_a/L_u}}\right\} + C_4$$

- Compute the expression for x_1, such that $p_1(x_1) = y_1$ and $y_1 = y_2/2$:

$$x_1 = \frac{2}{\kappa N_r} \tan^{-1}\left\{\sqrt{\frac{L_a}{L_a}} \tan\left[\frac{\kappa N_r \sqrt{L_a L_u}\,(y_2/2 - C_4)}{2}\right]\right\} - \phi$$

- Using the point $(-\pi/N_r, 0)$, compute the coefficient γ_m:

$$\gamma_m = -\ln(\beta_m - \pi/N_r)$$

- Using the point $(0, y_2)$, compute the coefficient α_m:

$$\alpha_m = y_2 \cdot \ln\left(\frac{\beta_m}{\beta_m - \pi/N_r}\right)^{-1}$$

- Using the point (x_1, y_1) and $y_1 = y_2/2$, compute the coefficient β_m:

$$\beta_m = \frac{-x_1^2}{2x_1 + \pi/N_r}$$

APPENDIX F

GENERATING LOGARITHMIC FUNCTION COEFFICIENT ESTIMATION

This appendix presents a method of computing the expressions for the coefficients (α_g, β_g, γ_g) of the logarithmic curve fitting function $\lambda_g(\theta)$, which is used during generating. The logarithmic function is used to curve fit the integral of $p_1(\theta)$ (expressed by Equation 3.131), which is rewritten as:

$$\int p_1(\theta)\ d\theta = \lambda_g(\theta) \tag{F.1}$$

where, $\lambda_g(\theta) = \alpha_g\{\ln[1/(\beta_g - \theta)] + \gamma_g\}$. Since there are three unknowns to be solved for (i.e., α_g, β_g, γ_g), three points which lie on the function must be used. The first step involves obtaining the coordinates of the three points to be used. Since the expression for the original function (i.e., the integral of $p_1(\theta)$) that is being curve fit by $\lambda_g(\theta)$ is known, the coordinates are obtained based on the original function, which are then used to solve for the three unknowns of the logarithmic curve fitting function. To obtain the coordinates of the three points, consider the expression for the integral of $p_1(\theta)$ (from Equation 3.120), which is rewritten as:

$$\int p_1(\theta)\ d\theta = \frac{2}{\kappa N_r \sqrt{L_a L_u}} \tan^{-1}\left\{\frac{\tan[(\kappa N_r \theta + \kappa N_r \phi)/2]}{\sqrt{L_a/L_u}}\right\} + C_4 \tag{F.2}$$

However, the integration constant in Equation F.2, i.e., C_4, first needs to be computed for the generating scenario. This is done by considering the θ coordinate of the first point as: 0, as that represents where the rotor pole is aligned with the stator pole, indicating the beginning of generation. From Figure F.1, at $\theta = 0$, the value of the corresponding vertical axis coordinate (i.e., the value of the integral of $p_1(\theta)$) is zero, using the coordinates of the first point, i.e., $(0, 0)$, the value of the integration constant C_4 is computed by substituting the coordinate values in Equation F.2, which results in the following expression:

$$0 = \frac{2}{\kappa N_r \sqrt{L_a L_u}} \tan^{-1}\left[\frac{\tan(\kappa N_r \phi/2)}{\sqrt{L_a/L_u}}\right] + C_4 \tag{F.3}$$

From Equation F.3, the integration constant is expressed as:

$$C_4 = -\frac{2}{\kappa N_r \sqrt{L_a L_u}} \tan^{-1}\left[\frac{\tan(\kappa N_r \phi/2)}{\sqrt{L_a/L_u}}\right] \tag{F.4}$$

With the value of the integration constant (C_4) known, the θ coordinate of the second point, i.e., π/N_r is considered and its corresponding vertical axis coordinate, i.e., the value of the integral of $p_1(\pi/N_r)$, represented by y_2 (shown in Figure F.1),[1] is computed by substituting in $(\pi/N_r, y_2)$ in Equation F.2 and is expressed as:

$$y_2 = \frac{2}{\kappa N_r \sqrt{L_a L_u}} \tan^{-1}\left\{\frac{\tan[(\kappa\pi + \kappa N_r \phi)/2]}{\sqrt{L_a/L_u}}\right\} + C_4 \tag{F.5}$$

Finally, a third point with its θ coordinate lying in the range: $0 \leq \theta \leq \pi/N_r$, is considered (represented by ${x_1}^2$). The point is selected such that its corresponding vertical axis coordinate (i.e., the value of the integral of $p_1(\theta)$), represented as y_1 is equal to $y_2/2$ (the reason for this selection will become apparent later in the derivation). Therefore, the coordinates of the third point (x_1, y_1) are substituted in Equation F.2, resulting in the following expression:

$$y_1 = \frac{2}{\kappa N_r \sqrt{L_a L_u}} \tan^{-1}\left\{\frac{\tan[(\kappa N_r x_1 + \kappa N_r \phi)/2]}{\sqrt{L_a/L_u}}\right\} + C_4 \tag{F.6}$$

After rearranging Equation F.6, using the relation: $y_1 = y_2/2$, and making x_1 the subject of the formula, the following expression is obtained:

$$x_1 = \frac{2}{\kappa N_r} \tan^{-1}\left\{\sqrt{\frac{L_a}{L_a}} \tan\left[\frac{\kappa N_r \sqrt{L_a L_u}\ (y_2/2 - C_4)}{2}\right]\right\} - \phi \tag{F.7}$$

Now that all the coordinates of the three points are known, the coefficients of the logarithmic curve fitting function (α_g, β_g, γ_g) can be computed. This is because ideally, the logarithmic curve fitting function ($\lambda_g(\theta)$) must also pass through the same points that the original curve

[1]The vertical axis represents the integral of $p_1(\theta)$ and not the variable y; however, due to the common convention of assigning the variable y to the vertical axis, the same is done in this situation, i.e., y_2.

[2]The horizontal axis represents θ and not the variable x; however, due to the common convention of assigning the variable x to the horizontal axis, the same is done in this situation, i.e., x_1.

described by the integral of $p_1(\theta)$ passes through. To summarize, the three points considered are: $(0,0)$, $(\pi/N_r, y_2)$, and (x_1, y_1). The expressions for x_1 and y_2 are defined by Equation F.7 and Equation F.5, respectively and $y_1 = y_2/2$. The coordinates also use an integration constant C_4, which is defined by Equation F.4.

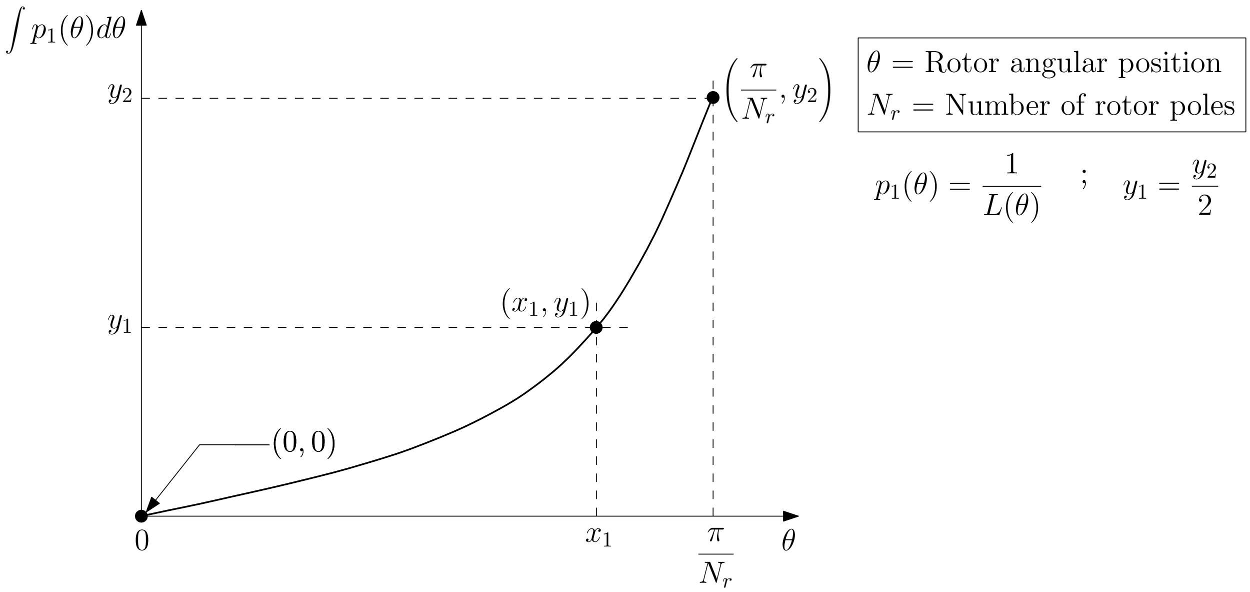

Figure F.1: Integral of $p_1(\theta)$ versus the rotor position (θ) during generation

The next step involves using the three points in the expression for the generating logarithmic curve fitting function $\lambda_g(\theta)$, which is defined by Equation 3.122 and is rewritten as:

$$\lambda_g(\theta) = \alpha_g \left[\ln\left(\frac{1}{\beta_g - \theta}\right) + \gamma_g \right] \tag{F.8}$$

Applying the coordinates of the first point, i.e., $(0,0)$ to Equation F.8, the following expression is obtained:

$$0 = \alpha_g \left[\ln\left(\frac{1}{\beta_g}\right) + \gamma_g \right] \tag{F.9}$$

From Equation F.9, the expression for the coefficient γ_g is obtained as:

$$\gamma_g = -\ln\left(\frac{1}{\beta_g}\right) \tag{F.10}$$

Using the expression of γ_g from Equation F.10 and substituting it in Equation F.8, the following expression is obtained:

$$\begin{aligned}\lambda_g(\theta) &= \alpha_g\left[\ln\left(\frac{1}{\beta_g-\theta}\right) - \ln\left(\frac{1}{\beta_g}\right)\right] \\ &= \alpha_g\left[\ln\left(\frac{\beta_g}{\beta_g-\theta}\right)\right] \qquad \text{(F.11)}\end{aligned}$$

Applying the coordinates of the second point, i.e., $(\pi/N_r, y_2)$ to Equation F.11, the following expression is obtained:

$$y_2 = \alpha_g\left[\ln\left(\frac{\beta_g}{\beta_g-\pi/N_r}\right)\right] \qquad \text{(F.12)}$$

From Equation F.12, the expression for the coefficient α_g is obtained as:

$$\alpha_g = y_2 \ln\left(\frac{\beta_g}{\beta_g-\pi/N_r}\right)^{-1} \qquad \text{(F.13)}$$

Using the expression of α_g from Equation F.13 and substituting it in Equation F.11, the following expression is obtained:

$$\lambda_g(\theta) = y_2 \ln\left(\frac{\beta_g}{\beta_g-\pi/N_r}\right)^{-1} \ln\left(\frac{\beta_g}{\beta_g-\theta}\right) \qquad \text{(F.14)}$$

Applying the coordinates of the third point, i.e., (x_1, y_1) in Equation F.14, the following expression is obtained:

$$y_1 = y_2 \ln\left(\frac{\beta_g}{\beta_g-\pi/N_r}\right)^{-1} \ln\left(\frac{\beta_g}{\beta_g-x_1}\right) \qquad \text{(F.15)}$$

Using the earlier defined relation between y_1 and y_2 (i.e., $y_1 = y_2/2$) in Equation F.15, the following expression is obtained:

$$\frac{1}{2} = \ln\left(\frac{\beta_g}{\beta_g-\pi/N_r}\right)^{-1} \ln\left(\frac{\beta_g}{\beta_g-x_1}\right) \qquad \text{(F.16)}$$

Rearranging Equation F.16 results in:

$$\frac{\sqrt{\beta_g}}{\sqrt{\beta_g-\pi/N_r}} = \frac{\beta_g}{\beta_g-x_1} \qquad \text{(F.17)}$$

Again, rearranging Equation F.17, the following expression is obtained:

$$\beta_g^2 - 2\beta_g x_1 + x_1^2 = \beta_g^2 - \frac{\beta_g \pi}{N_r} \tag{F.18}$$

In Equation F.18, making β_g the subject of the formula, the following expression is obtained:

$$\beta_g = \frac{x_1^2}{2x_1 - \pi/N_r} \tag{F.19}$$

Therefore, the coefficients (α_g, β_g, γ_g) of the motoring logarithmic function ($\lambda_g(\theta)$) are computed and defined by Equations F.10, F.13, and F.19, respectively. This concludes the method for computing the coefficients of the logarithmic curve fitting function, the summary of which is provided next:

- Compute the integration constant C_4:

$$C_4 = -\frac{2}{\kappa N_r \sqrt{L_a L_u}} \tan^{-1}\left[\frac{\tan(\kappa N_r \phi/2)}{\sqrt{L_a/L_u}}\right]$$

- Compute the expression for the integral of $p_1(0)$, i.e., y_2:

$$y_2 = \frac{2}{\kappa N_r \sqrt{L_a L_u}} \tan^{-1}\left\{\frac{\tan[(\kappa\pi + \kappa N_r \phi)/2]}{\sqrt{L_a/L_u}}\right\} + C_4$$

- Compute the expression for x_1, such that $p_1(x_1) = y_1$ and $y_1 = y_2/2$:

$$x_1 = \frac{2}{\kappa N_r} \tan^{-1}\left\{\sqrt{\frac{L_a}{L_a}} \tan\left[\frac{\kappa N_r \sqrt{L_a L_u}\ (y_2/2 - C_4)}{2}\right]\right\} - \phi$$

- Using the point $(0, 0)$, compute the coefficient γ_g:

$$\gamma_g = -\ln\left(\frac{1}{\beta_g}\right)$$

- Using the point $(\pi/N_r, y_2)$, compute the coefficient α_g:

$$\alpha_g = y_2 \cdot \ln\left(\frac{\beta_g}{\beta_g - \pi/N_r}\right)^{-1}$$

- Using the point (x_1, y_1) and $y_1 = y_2/2$, compute the coefficient β_m:

$$\beta_g = \frac{x_1^2}{2x_1 - \pi/N_r}$$

APPENDIX G

ESTIMATION OF THE MACHINE'S WINDING RESISTANCE

This appendix presents a method to accurately estimate the winding resistance (and other parasitic resistances) of the machine through a sample calculation. Before presenting the calculations, a single phase (along with the parasitic elements) of an asymmetric bridge converter is shown in Figure G.1, which is a modified version of Figure 2.30. The additional components shown in the figure are the source diode D_S, the source voltage V_S, the DC link capacitor C, the drive's circuit board resistance R_{pcb}, and the machine's winding resistance R_w. In Figure G.1, the voltage across the terminals of the machine phase is denoted by V_{srm}. The machine's phase is denoted by M, which represents its phase inductance and back EMF (the winding (R_w) and board (R_{pcb}) resistances are distributed as shown in Figure G.1).

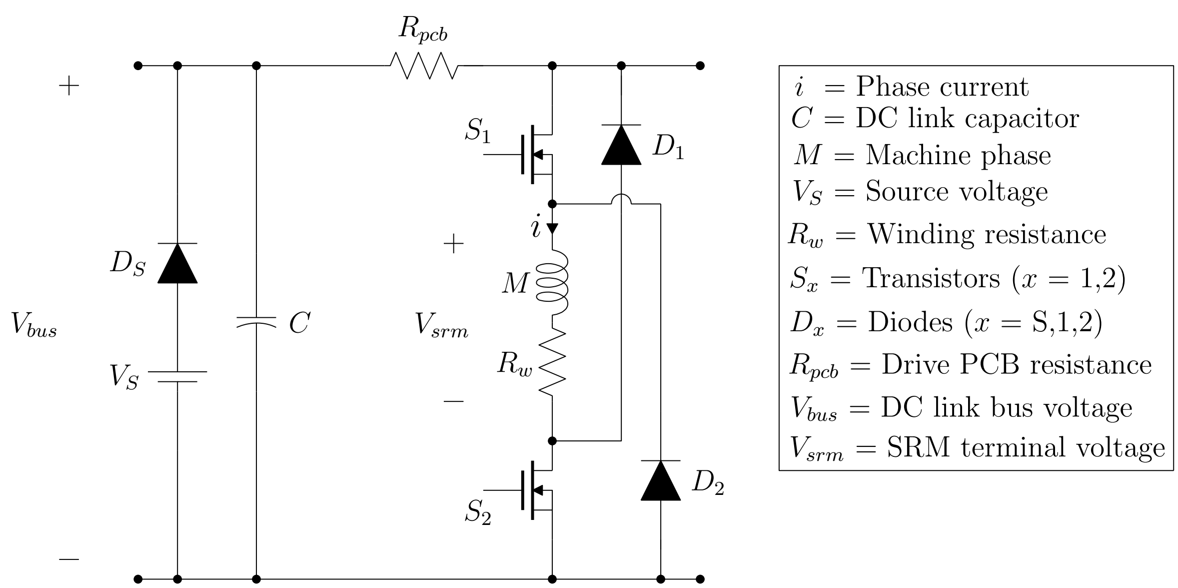

Figure G.1: Single phase asymmetric bridge converter along with parasitic elements

The first step in estimating the total resistance involves measuring the winding resistance (R_w) of the machine, which is performed by using an ohmmeter and placing it across the terminals of the machine when the asymmetric bridge converter is disconnected. The configuration of the setup while measuring the winding resistance is shown in Figure G.5. The winding resistance (R_w) value measured from the ohmmeter for the setup used is 2.5 Ω.

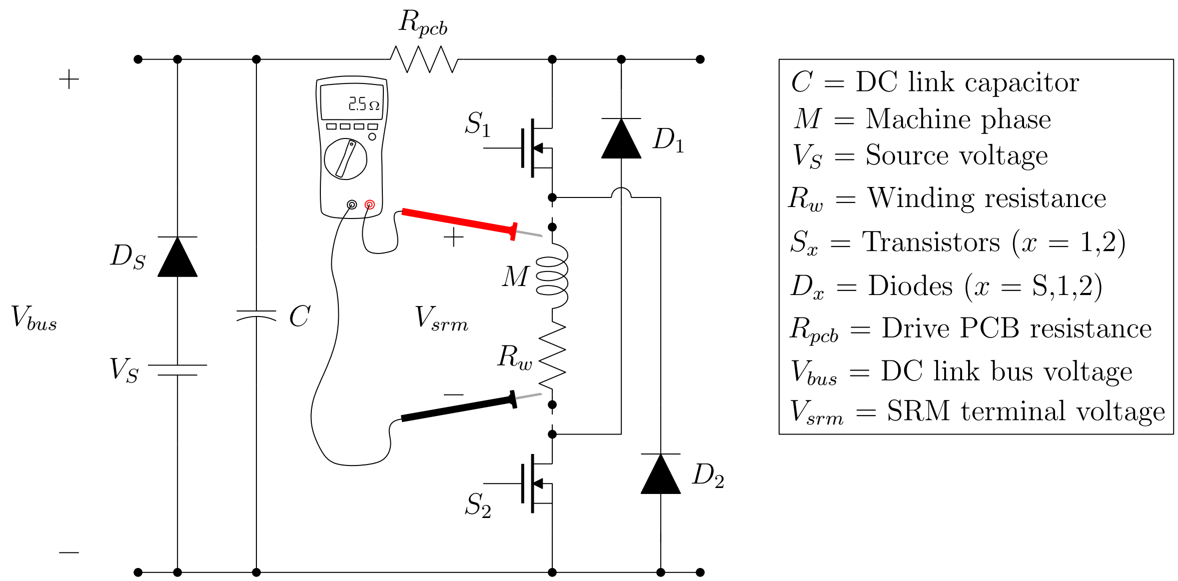

Figure G.2: Configuration of the setup while measuring the winding resistance (R_w) of the machine using an ohmmeter

The next step involves recording measurements during the magnetization phase, i.e., when the phase is switched on. However, before analyzing the recorded data, the expressions for the machine's terminal voltage (V_{srm}) during the magnetization phase are presented. The circuit during the magnetization phase is shown in Figure G.3 (along with the placement of the voltage and current probes), on which Kirchoff's voltage law (KVL) is applied along the highlighted red path in the clockwise direction beginning at the source voltage (V_S). The application of KVL around the loop results in the following expression:

$$-V_S + V_f + iR_{pcb} + iR_{DS(on)} + V_{srm} + iR_{DS(on)} = 0 \tag{G.1}$$

where, V_f is the forward voltage drop of the source diode D_S and $R_{DS(on)}$ is the on resistance of the MOSFETs S_1 and S_2. Rearranging Equation G.1, the following expression for the machine's terminal voltage (V_{srm}) is obtained:

$$V_{srm} = (V_S - V_f) - i(R_{pcb} + 2R_{DS(on)}) \tag{G.2}$$

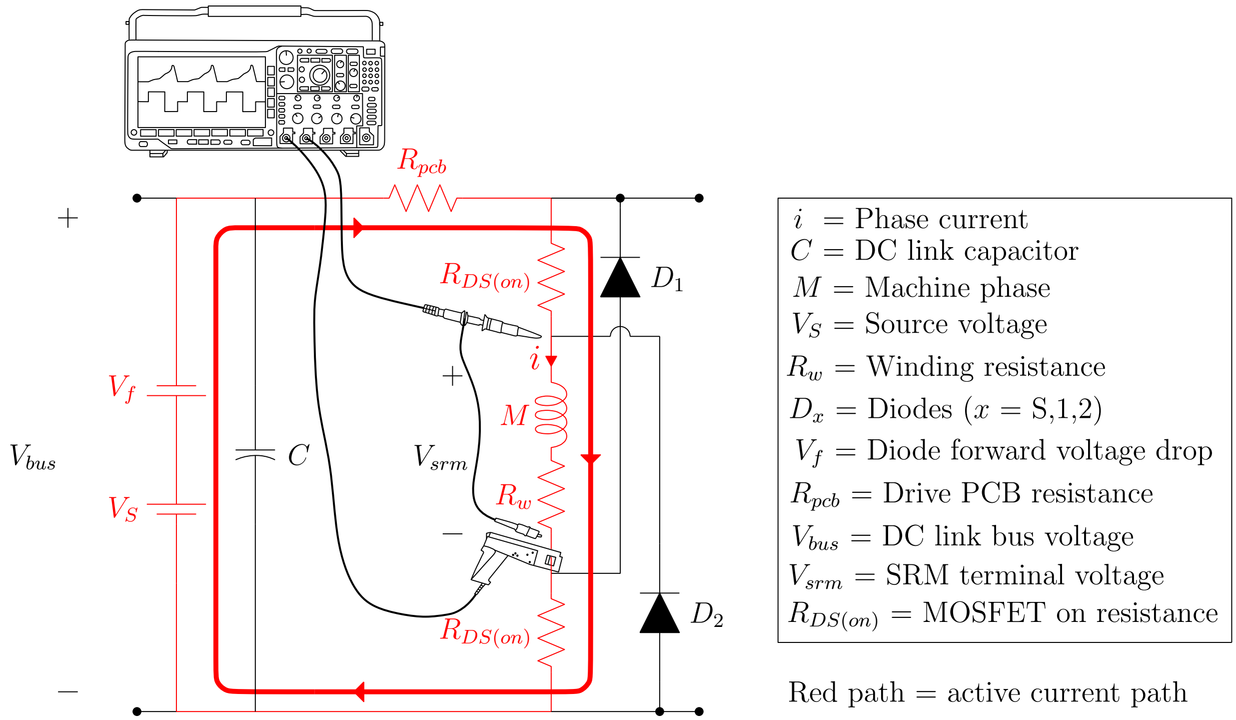

Figure G.3: Machine's terminal voltage and phase current measurements during the magnetization phase

Similarly, the circuit during the demagnetization phase is shown in Figure G.4 (along with the placement of the voltage and current probes), on which KVL is applied along the highlighted red path in the counterclockwise direction beginning at the bus voltage (V_{bus}). The application of KVL around the loop results in the following expression:

$$V_{bus} + V_f + V_{srm} + V_f + iR_{pcb} = 0 \tag{G.3}$$

Rearranging Equation G.3, the following expression for the machine's terminal voltage (V_{srm}) is obtained:

$$V_{srm} = -V_{bus} - iR_{pcb} - 2V_f \tag{G.4}$$

Now that the expressions for the machine's terminal voltage during the magnetization and demagnetization phases are obtained, numerical values are substituted in Equations G.2 and G.4 to solve for the value of R_{pcb}.

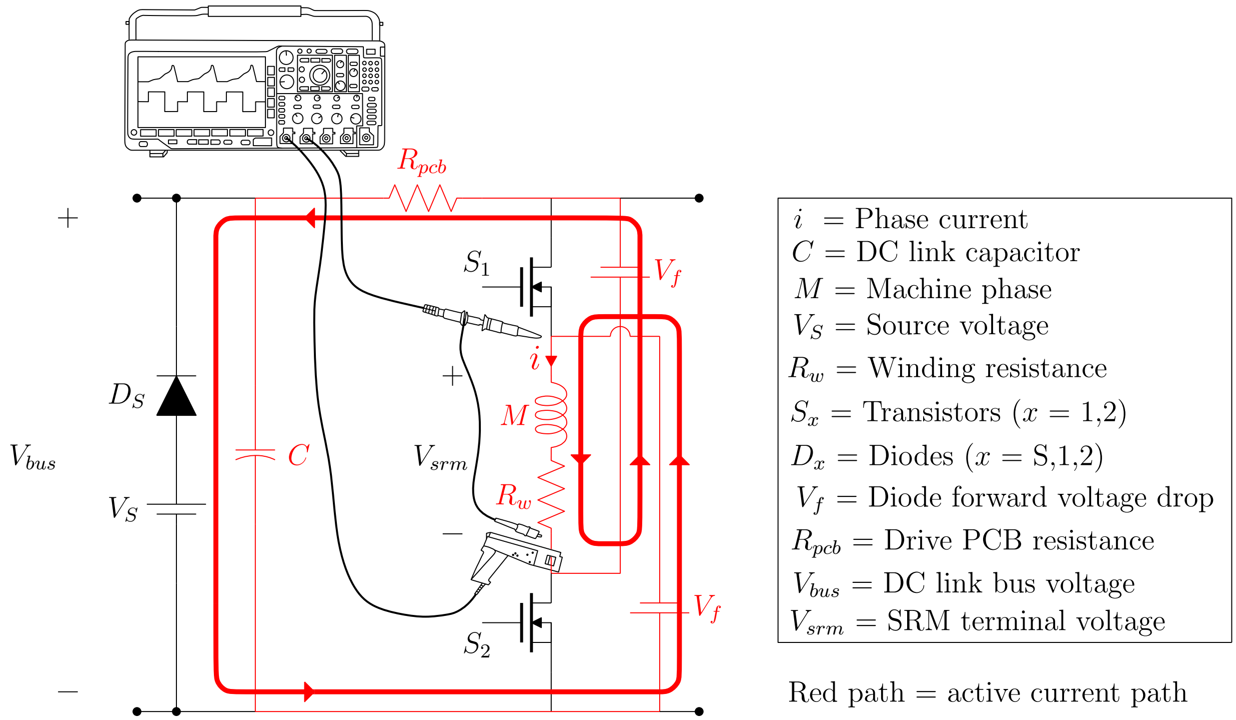

Figure G.4: Machine's terminal voltage and phase current measurements during the demagnetization phase

The machine's experimentally gathered terminal voltage and phase current waveforms at a particular operating point are captured and shown in Figure G.5 and their numerical values at different rotor positions are highlighted and are used in the sample calculation for the estimation of the total phase resistance ($R_{pcb}+R_w$). The applied source voltage is 11.2 V, the forward voltage drop of the diodes is 0.7 V, and the on resistance of the MOSFETs is 11 mΩ. From Figure G.5, at $\theta_{on} = -15°$, the phase current is 0 A. Substituting these values in Equation G.2, the machine's terminal voltage is given as:

$$\begin{aligned} V_{srm} &= (11.2 - 0.7) - 0\Big[R_{pcb} + (2 \times 11 \text{ m})\Big] \\ &= 10.5 \end{aligned} \tag{G.5}$$

At $\theta_{on} = -15°$, according to Figure G.5, the machine's measured terminal voltage is also 10.5 V. From Figure G.5, at $\theta_{on} = +15°$, the measured phase current is 1.1 A. Substituting these values of the phase current at $\theta_{on} = +15°$ in Equation G.2, the following expression for the machine's terminal voltage is obtained:

$$V_{srm} = (11.2 - 0.7) - 1.1\Big[R_{pcb} + (2 \times 11 \text{ m})\Big]$$

$$= 10.5 - 1.1R_{pcb} - 24.2 \text{ m} \tag{G.6}$$

Equating the value of the machine's terminal voltage from Equation G.6 to 9.7 V from Figure G.5, the value of R_{pcb} is calculated as 0.7 Ω.

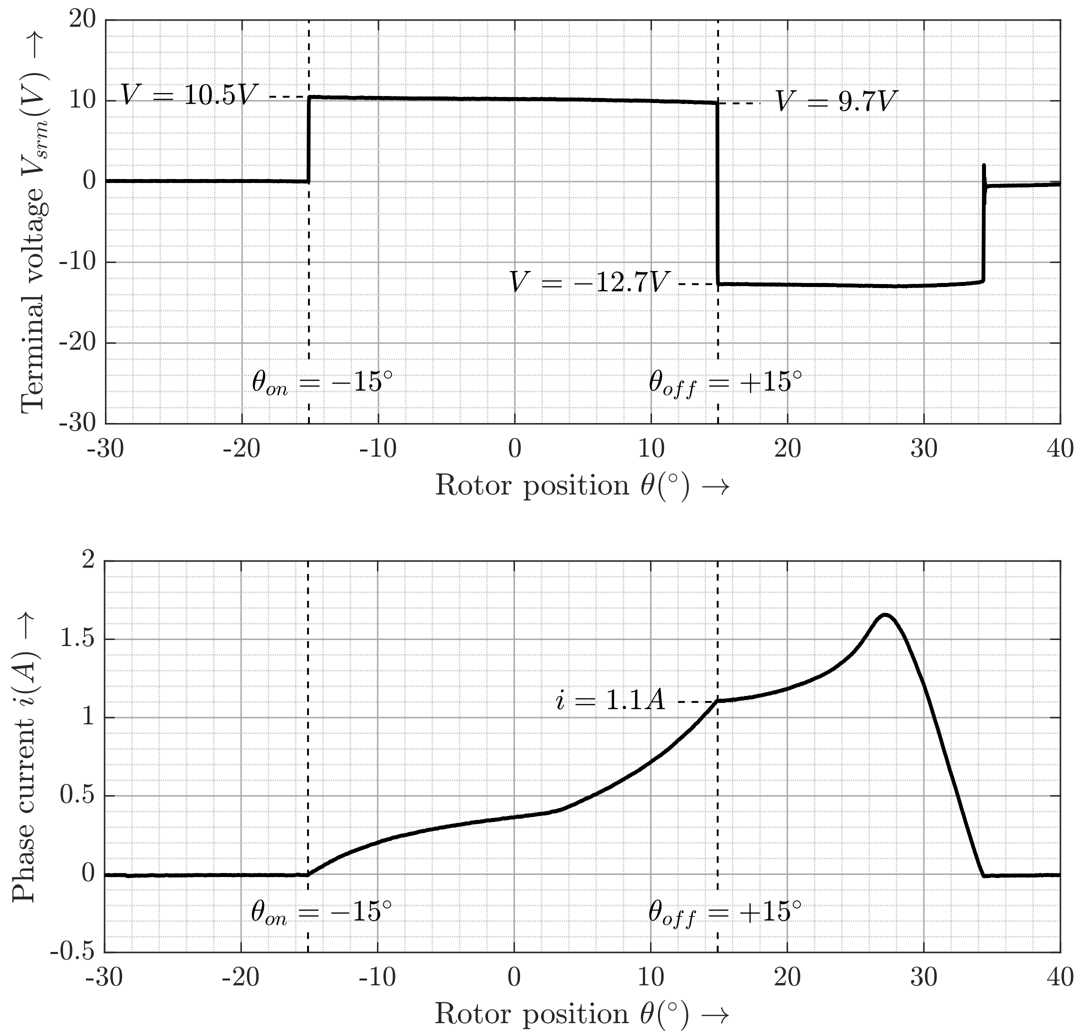

Figure G.5: Experimental waveforms of the machine's terminal voltage and phase current versus rotor position

As a sanity check, the machine's terminal voltage is calculated at $\theta_{on} = +15°$ when the phase is switched off. After substituting all the values in Equation G.4, the following value for the machine's terminal voltage is obtained:

$$\begin{aligned} V_{srm} &= -10.5 - (1.1 \times 0.7) - (2 \times 0.7) \\ &= -12.7 \end{aligned} \tag{G.7}$$

From Figure G.5, at $\theta_{on} = +15°$ when the phase is switched off, the machine's terminal voltage is -12.7 V, which is also the result of Equation G.7. This concludes the method to accurately estimate the phase resistance of a switched reluctance machine. For the machine considered, the phase resistance value is 3.2 Ω (i.e., the sum of the winding resistance: $R_w = 2.5$ Ω, the power converter's circuit board resistance: $R_{pcb} = 0.7$ Ω, and the MOSFETs on resistance: $2R_{DS(on)} = 22$ mΩ). It is worth noting that the MOSFETs on resistance only factors in during the magnetization phase and not during the demagnetization phase.

APPENDIX H

COMPARISON OF OUTPUT POWER IN NEGATIVE, ZERO, AND POSITIVE FEEDBACK SCENARIOS

This appendix presents a comparison of the output power generated from a switched reluctance generator when its phase currents enter a state of negative, zero, and positive feedback. Figure H.1 shows the experimental waveforms of the generating phase currents in negative, zero, and positive feedback. For the results shown in Figure H.1, phase advancing is employed with a turn-on angle specified by: $\theta_{on} = -15°$. The measured angular velocity (ω) of the rotor shaft is: 400 rpm, and the applied bus voltage used is: $V_{bus} = 12$ V. For the negative feedback generating phase current, the phase is switched off the earliest at: $\theta_{offa} = 7.8°$, and it eventually returns to zero at: $\theta_{enda} = 25.4°$. For the zero feedback generating phase current, the phase is switched off at: $\theta_{offb} = 12.5°$, and it eventually returns to zero at: $\theta_{endb} = 31.6°$. Lastly, for the positive feedback generating phase current, the phase

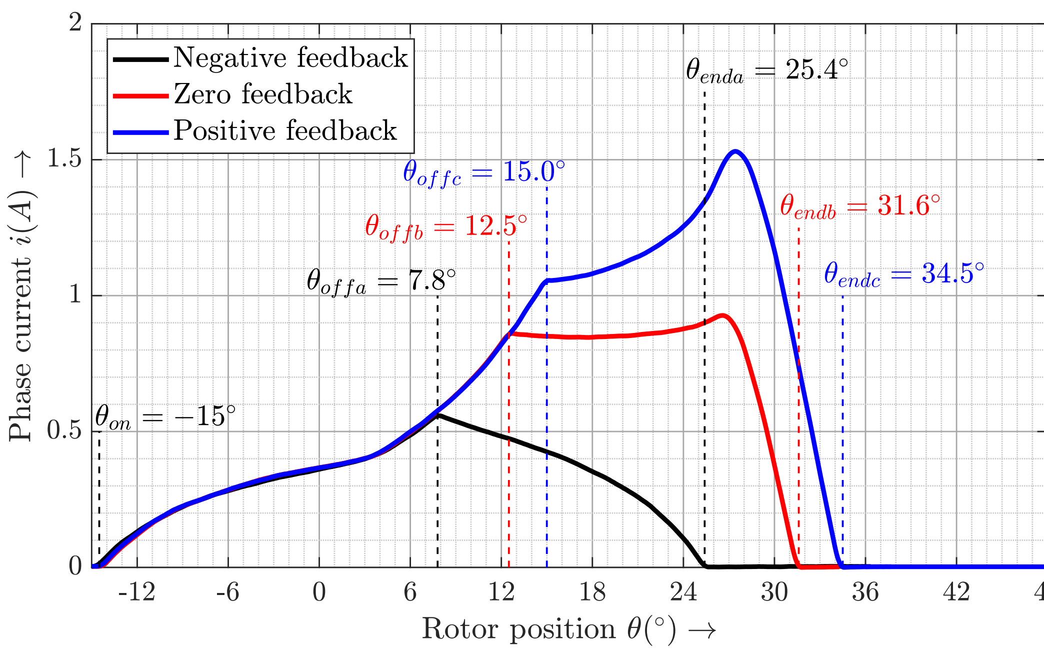

Figure H.1: Negative, zero, and positive feedback generating phase currents with respect to rotor position. $V_{bus} = 12$ V and $\omega = 400$ rpm is switched off the latest at: $\theta_{offc} = 15.0°$, and it eventually returns to zero at: $\theta_{endc} = 34.5°$. Next, the net charge is calculated for all three cases; however, in order to express the calculated net charge in terms of Coulombs, the horizontal axis of Figure H.1 must first be converted to time. To convert the horizontal axis to time, the θ axis of Figure H.1 is scaled by a factor of $1/\omega$, i.e., the expression used is given by:

$$t = \frac{\theta}{\omega} \tag{H.1}$$

Using a value of 400 rpm for angular velocity in Equation H.1 (the angular velocity must also be converted[1] from revolutions per minute to degrees per second), the scaling factor is calculated as:

$$\begin{aligned} t &= \theta \times \left(\frac{60}{400 \times 360} \right) \\ &= \frac{\theta}{2400} \end{aligned} \tag{H.2}$$

Using the scaling factor defined by Equation H.2, the horizontal axis of Figure H.1 is converted to a time axis and is shown in Figure H.2. The time axis of Figure H.2 has also been shifted in order to align the turn-on time t_{on} with zero. The operating points for the generating phase current waveforms shown in Figure H.2 are exactly the same as the ones for the generating phase current waveforms shown in Figure H.1. The difference between the two figures is the unit of the horizontal axis.

In terms of time (as shown in Figure H.2), for the negative feedback generating phase current, the phase is switched off the earliest at: $t_{offa} = 9.3$ ms, and it eventually returns to zero at: $t_{enda} = 16.6$ ms. For the zero feedback generating phase current, the phase is switched off at: $t_{offb} = 11.2$ ms, and it eventually returns to zero at: $t_{endb} = 19.2$ ms. Lastly, for the positive feedback generating phase current, the phase is switched off the latest at: $t_{offc} = 12.2$ ms, and it eventually returns to zero at: $t_{endc} = 20.3$ ms.

[1] 1 revolution per minute is equal to 360/60 degrees per second.

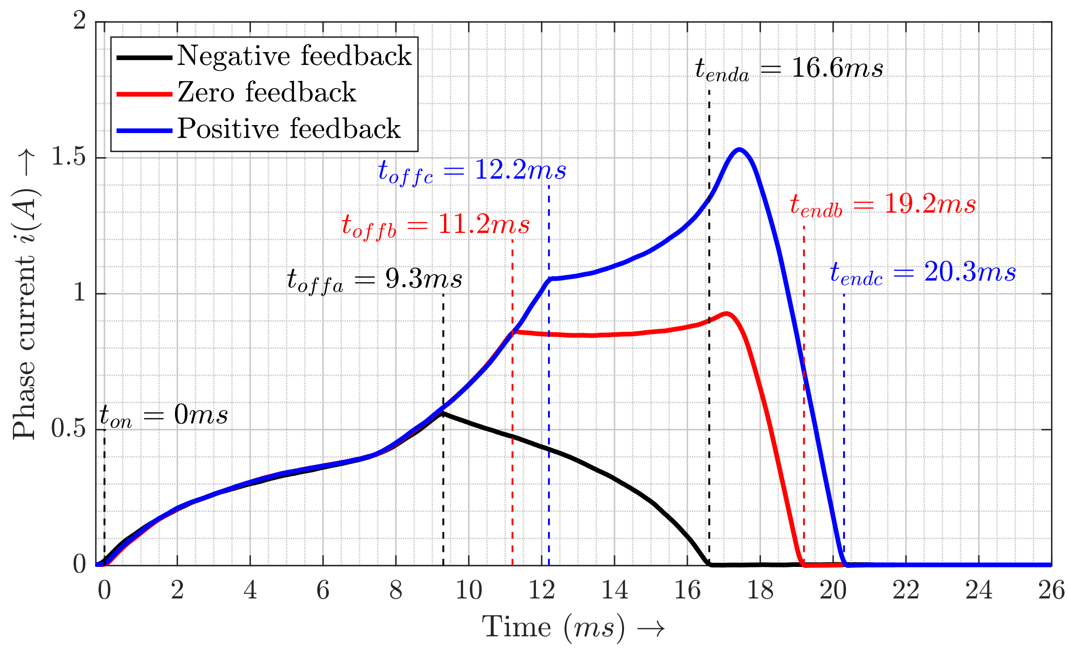

Figure H.2: Negative, zero, and positive feedback generating phase currents with respect to time. $V_{bus} = 12$ V and $\omega = 400$ rpm

The invested charge is defined by the area under the phase current from the instance the phase is switched on: t_{on}, to the instance it is switched off: t_{offx}, where $x = a, b, c$ represents the negative, zero, and positive feedback scenarios, respectively. The expression for invested charge Q_{inv} is given as:

$$Q_{inv} = \int_{t_{on}}^{t_{offx}} i \; dt \tag{H.3}$$

Similarly, the harvested charge is defined by the area under the phase current from the instance the phase is switched off: t_{offx}, to the instance the phase current returns to zero: t_{endx}, where $x = a, b, c$ represents the negative, zero, and positive feedback scenarios, respectively. The expression for harvested charge Q_{har} is given as:

$$Q_{har} = \int_{t_{offx}}^{t_{endx}} i \; dt \tag{H.4}$$

The net charge Q_{net} is defined as the difference between harvested and invested charge and is expressed as:

$$Q_{net} = Q_{har} - Q_{inv} \tag{H.5}$$

The output electrical energy of the system E_{out} is defined as the product of the net charge (Q_{net}) and bus voltage (V_{bus}) and is expressed as:

$$E_{out} = V_{bus} Q_{net} \tag{H.6}$$

Finally, the output electrical power P_{out} is calculated by considering the average of output electrical energy (E_{out}) over a generating cycle, which is expressed as:

$$P_{out} = \frac{E_{out}}{T_c} \tag{H.7}$$

where, T_c represents the time period of a generating cycle and is expressed as:

$$T_c = t_{endx} - t_{on} \tag{H.8}$$

The output electrical power (P_{out}) specified by Equation H.7 may also be represented as:

$$P_{out} = \frac{V_{bus}}{(t_{endx} - t_{on})} \left(\int_{t_{offx}}^{t_{endx}} i \, dt - \int_{t_{on}}^{t_{offx}} i \, dt \right) \tag{H.9}$$

Using the equations presented in this appendix, relevant parameters for the calculation of output power for the generating phase currents shown in Figure H.2 are listed in Table H.1. The net charge for the positive feedback scenario is the highest, which also results in the highest output power generated by the machine. From Table H.1, the output power generated from the positive feedback scenario is 45.6% higher than the zero feedback scenario.

Table H.1: Invested, harvested, and net charge along with output electrical energy and power for the current waveforms of Figure H.2

Feedback scenario	**Q_{inv} (mC)**	**Q_{har} (mC)**	**Q_{net} (mC)**	**E_{out} (mJ)**	**P_{out} (W)**
Negative	2.88	2.52	−0.36	−4.32	−0.26
Zero	4.26	6.13	1.87	22.44	1.16
Positive	5.50	8.37	2.87	34.44	1.69

The generating phase currents can also enter a state of negative, zero, and positive feedback based on different values of angular velocity. The experimental waveforms shown in Figure H.3, represent the generating phase currents in negative, zero, and, positive feedback. In each scenario the turn-on and turn-off angles are the same, specified by: $\theta_{on} = -15$degree (i.e., phase advancing is employed), and $\theta_{off} = 15$degree. However, the angular velocity (ω) of the rotor shaft is measured as: 130 rpm, 240 rpm, and 370 rpm for the negative, zero, and positive feedback scenarios, respectively. The applied bus voltage (V_{bus}) is 12 V.

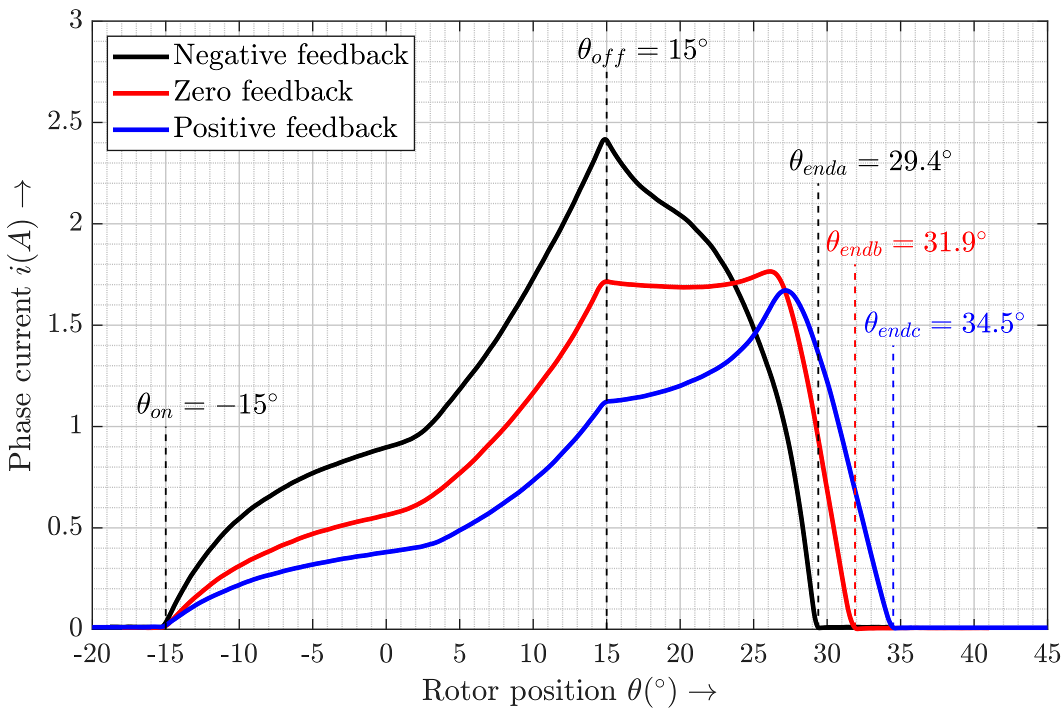

Figure H.3: Negative, zero, and positive feedback generating phase currents with respect to rotor position for $\omega = 130$ rpm, 240 rpm, and 370 rpm, respectively with $V_{bus} = 12$ V

A modified version of Equation H.9 to account for generating phase currents plotted with respect to rotor position rather than time (as shown in Figure H.3) is expressed as:

$$P_{out} = \frac{V_{bus}}{(\theta_{endx} - \theta_{on})} \left(\int_{\theta_{off}}^{\theta_{endx}} i \; dt - \int_{\theta_{on}}^{\theta_{off}} i \; dt \right) \tag{H.10}$$

Again, relevant parameters for the calculation of output power for the generating phase currents shown in Figure H.3 are listed in Table H.2. Though the harvested charge from the negative feedback scenario is the highest, it is also the scenario with the highest invested charge. On the other hand, the net charge for the positive feedback scenario is the highest, which also results in the highest output power generated by the machine. From Table H.2, the output power generated from the positive feedback scenario is 48.4% higher than the zero feedback scenario.

Table H.2: Invested, harvested, and net charge along with output electrical energy and power for the current waveforms of Figure H.3

Feedback scenario	**Q_{inv} (mC)**	**Q_{har} (mC)**	**Q_{net} (mC)**	**E_{out} (mJ)**	**P_{out} (W)**
Negative	39.60	30.68	−8.91	−106.92	−1.88
Zero	13.74	17.31	3.57	42.84	1.32
Positive	6.10	9.74	3.64	43.68	1.96

APPENDIX I

SINGLE PULSE PEAK PREDICTION CONTROL FLOWCHART

This appendix presents a flowchart (shown in Figure I.1) for a switched reluctance generator operating in single pulse mode, using the predictive control algorithm presented in Chapter 4.

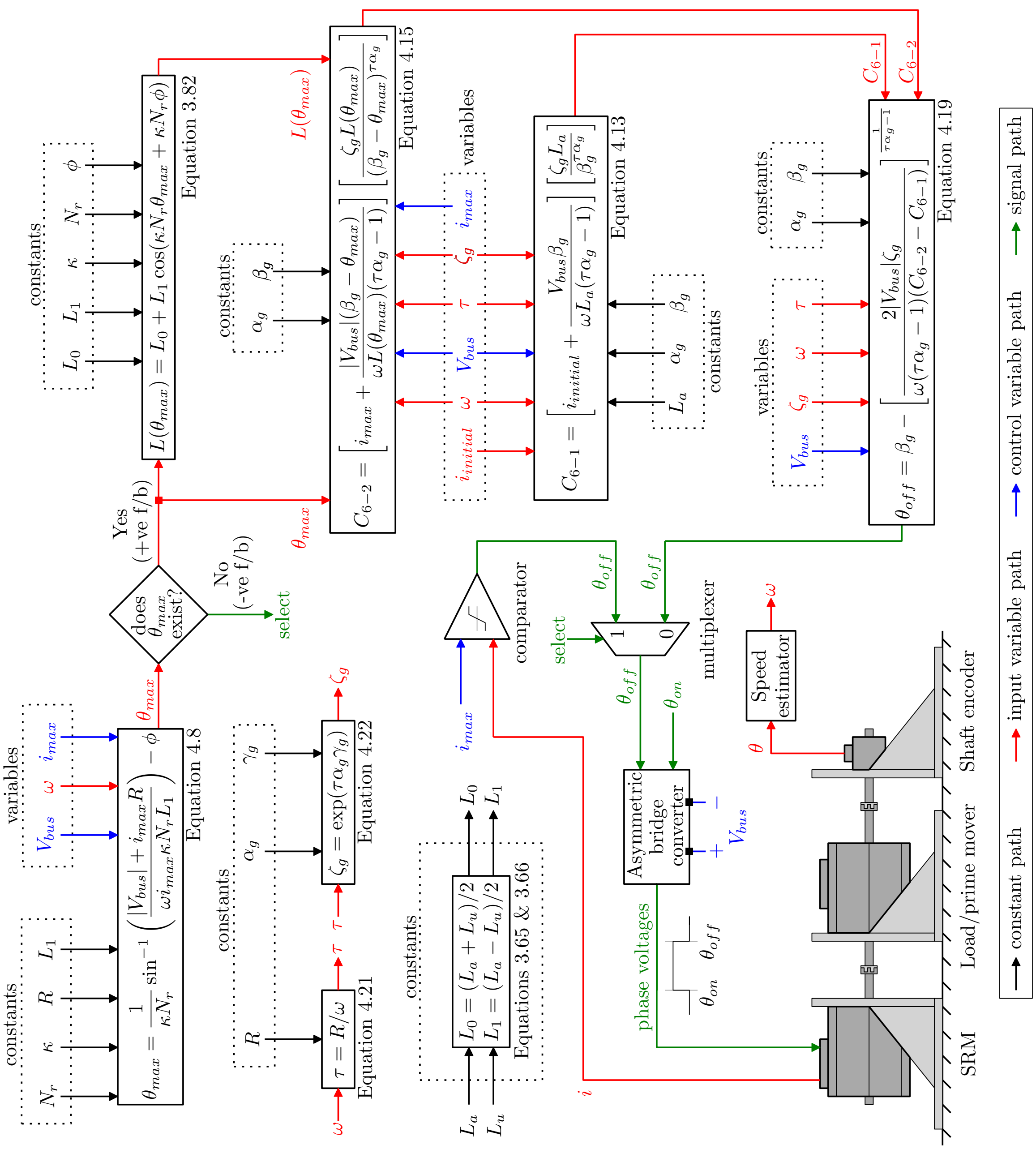

Figure I.1: Single pulse peak prediction control algorithm flowchart for SRGs

In Figure I.1, angular velocity (ω) is assigned as an input variable (i.e., a sensed variable or a measured sate, which is typically not a control variable) and its rate of change is determined by the application the machine is used in. For instance, in wind turbine applications, angular velocity is a slow changing variable compared to a commutation cycle. As a result, the controller need not update the turn-off angle (θ_{off}) every commutation cycle, thereby relaxing the constraints allowing for an increased computational time. On the other hand, the maximum allowable phase current (i_{max}) is assigned as a control variable in case the machine's output power needs to be modulated. The bus voltage (V_{bus}) is also assigned as control variable to accommodate for any changes in the DC bus or when the voltage levels are changed. The maximum allowable phase current (i_{max}) and bus voltage (V_{bus}) can be controlled as desired depending on the application the machine is used in. The remaining parameters shown in the figure represent constant values specific to the switched reluctance machine used and are calculated only in the beginning during the setting up and characterization of the hardware. In the flowchart provided in Figure I.1, the equation numbers are also provided for reference.

APPENDIX J

HARDWARE SETUP AND MACHINE TESTBED

This appendix presents images of the hardware used in order to record the experimental measurements. Figure J.1 shows the top layer, while Figure J.2 shows the bottom layer of a four phase asymmetric bridge converter's printed circuit board. The dimensions of the manufactured board are 12 inches long by 5 inches wide.

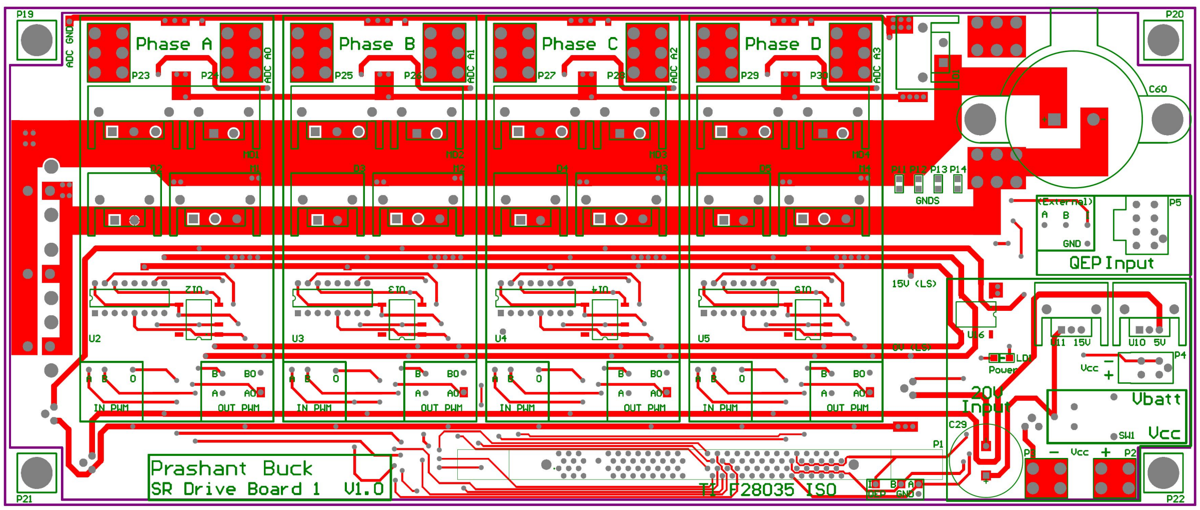

Figure J.1: Top layer of the asymmetric bridge converter's printed circuit board

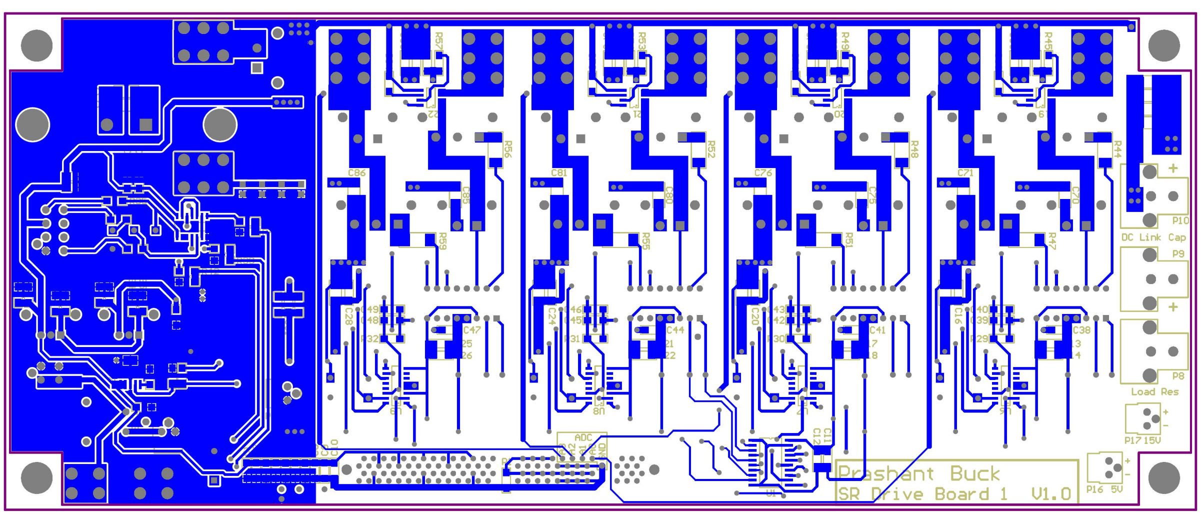

Figure J.2: Bottom layer of the asymmetric bridge converter's printed circuit board

Figure J.3 shows the top layer, while Figure J.4 shows the bottom layer of the printed circuit board housing the DC link load resistances and the DC link capacitors. Both the printed circuit boards are manufactured using 0.062 inch thick FR-4 composite material with a 1 ounce per square foot copper pour. Figures J.5 through J.8 show the manufactured and assembled asymmetric bridge converter printed circuit boards from various angles.

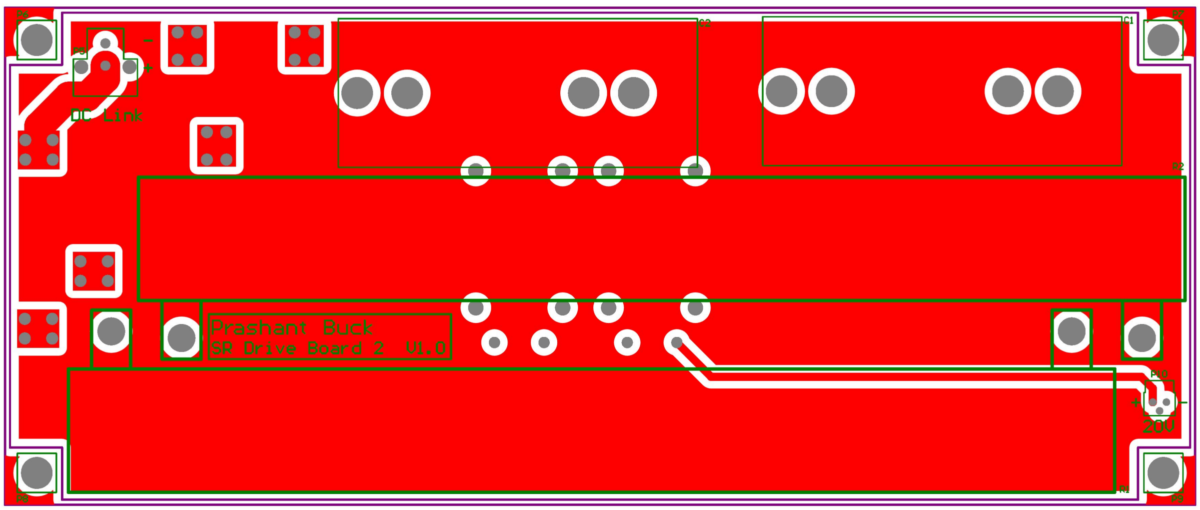

Figure J.3: Top layer of the printed circuit board for the DC link components

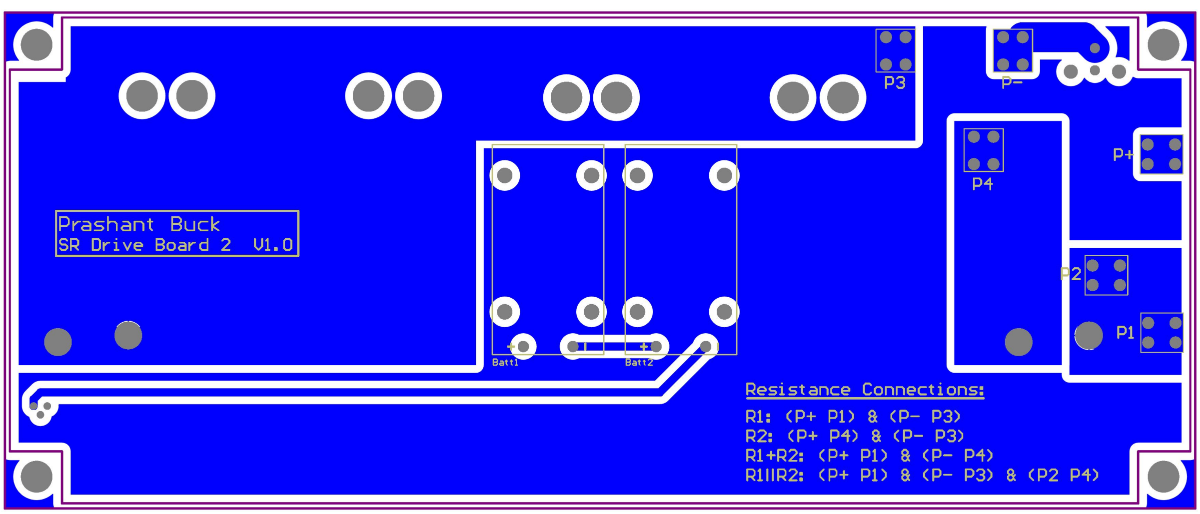

Figure J.4: Bottom layer of the printed circuit board for the DC link components

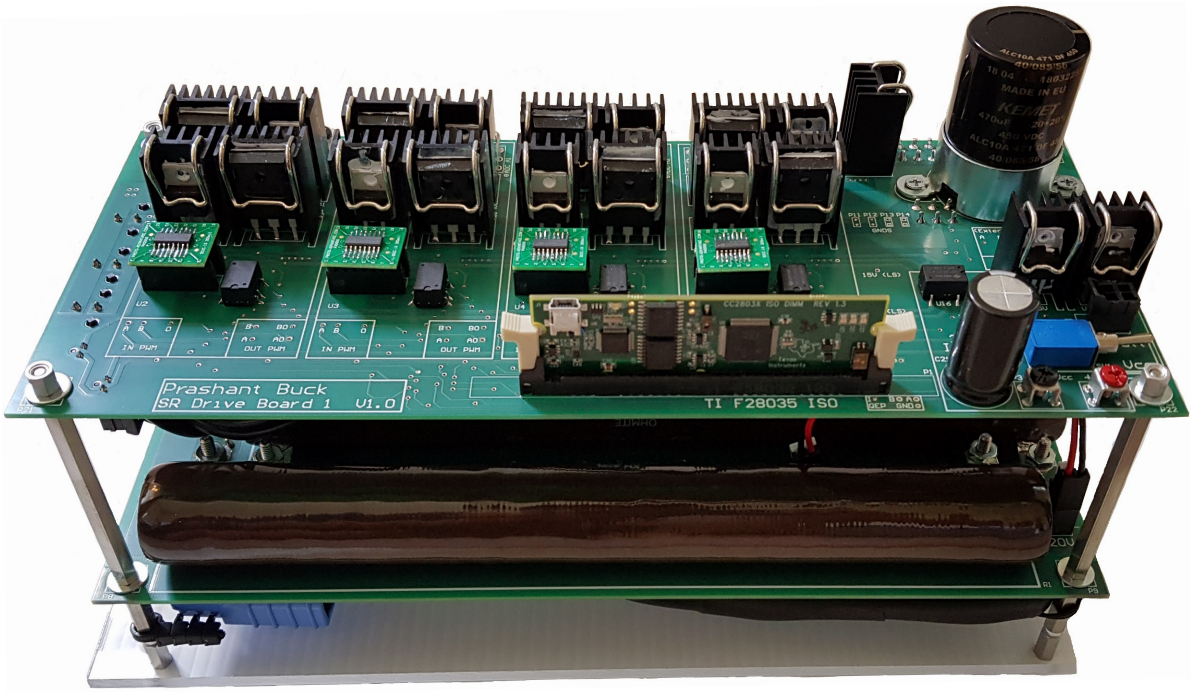

Figure J.5: Front view of the four phase asymmetric bridge converter

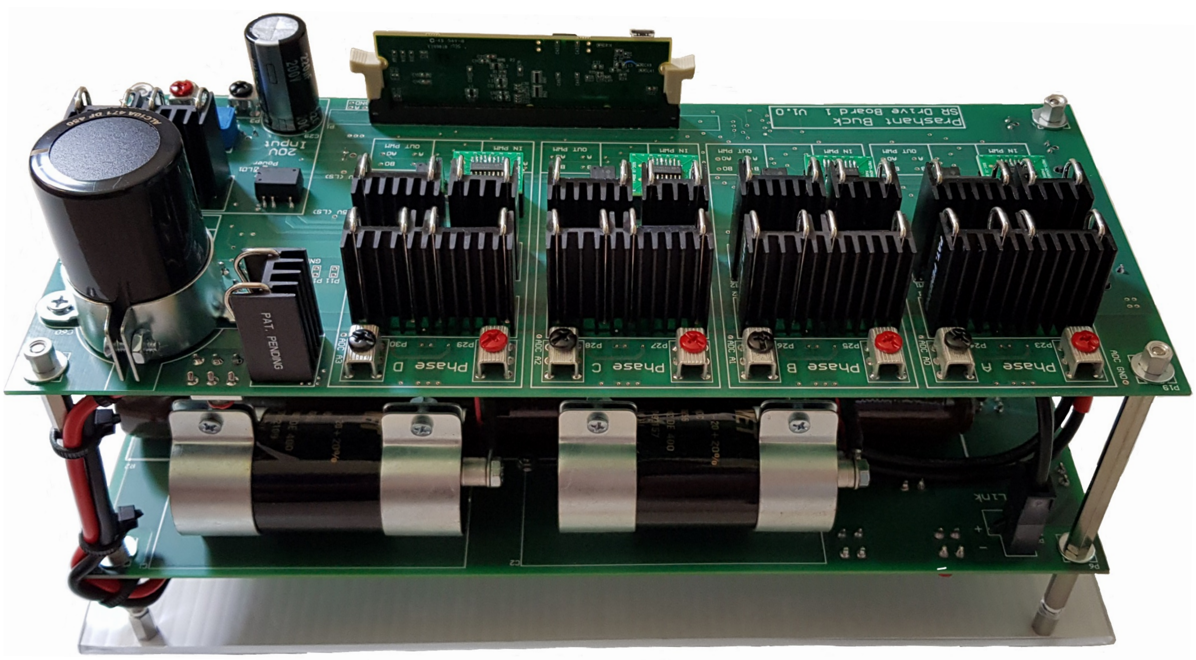

Figure J.6: Back view of the four phase asymmetric bridge converter

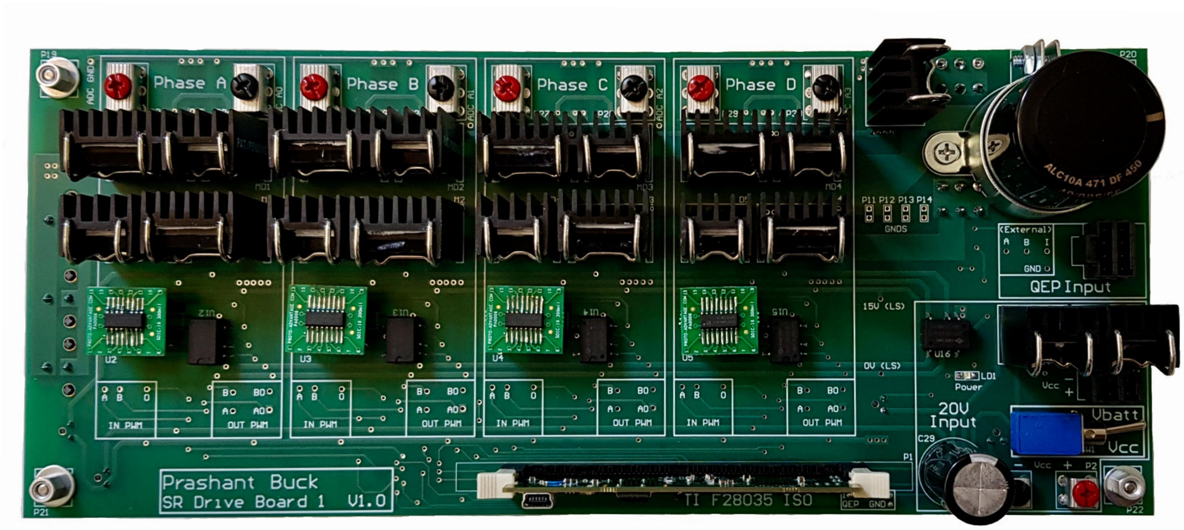

Figure J.7: Top view of the four phase asymmetric bridge converter

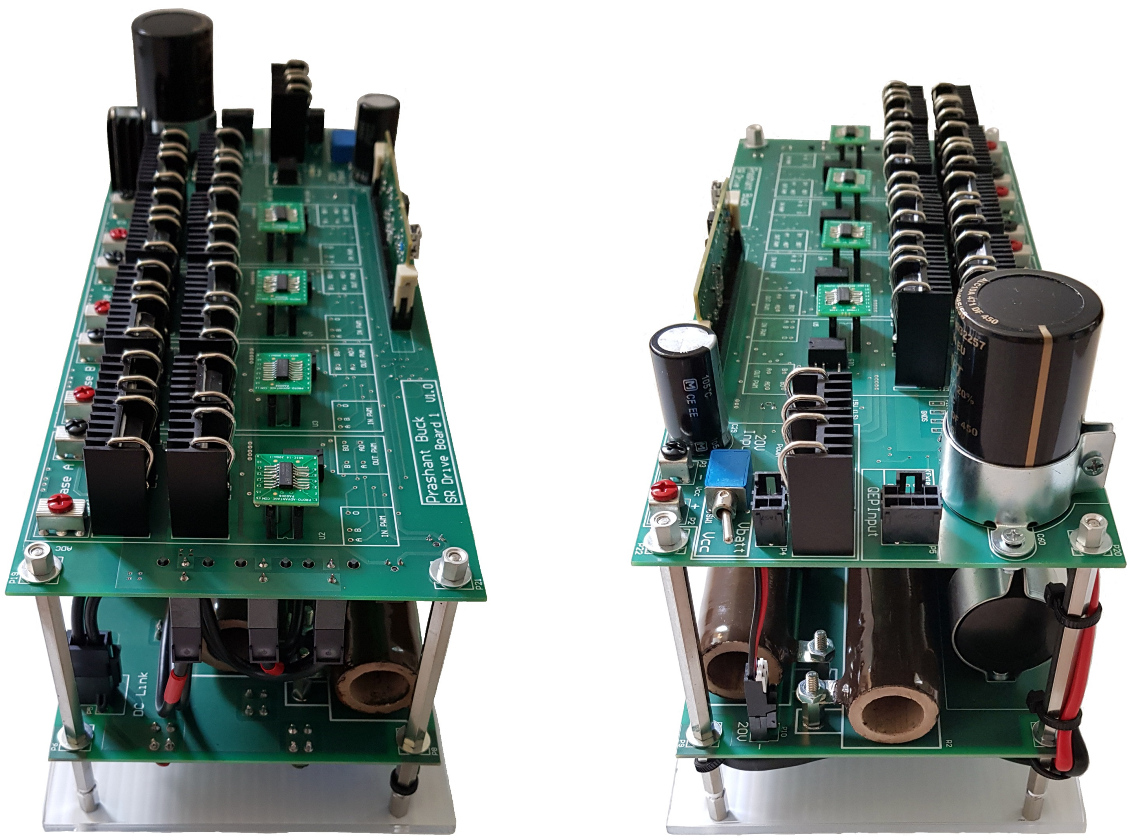

(a) (b)

Figure J.8: Four phase asymmetric bridge converter (a) left side view (b) right side view

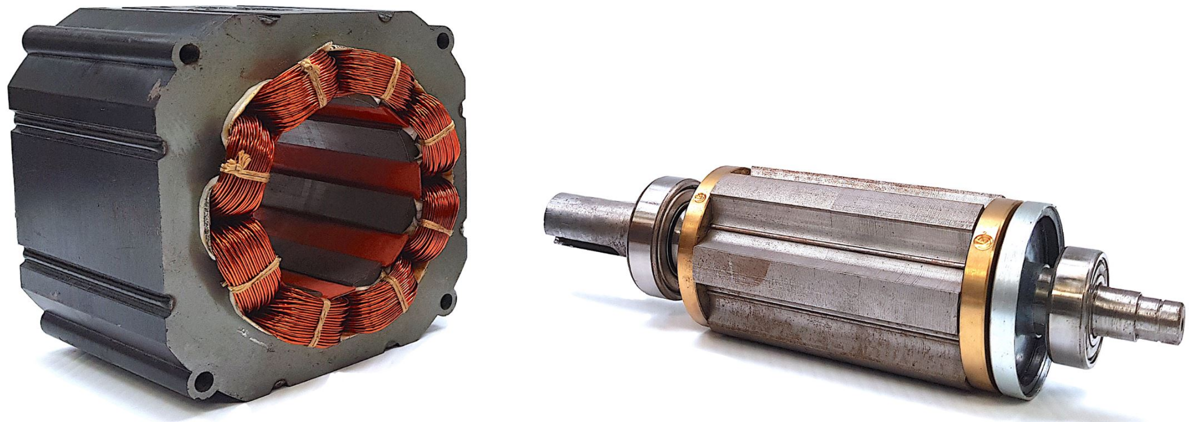

Figure J.9: Stator (left) and rotor (right) of the 8/6 switched reluctance machine used

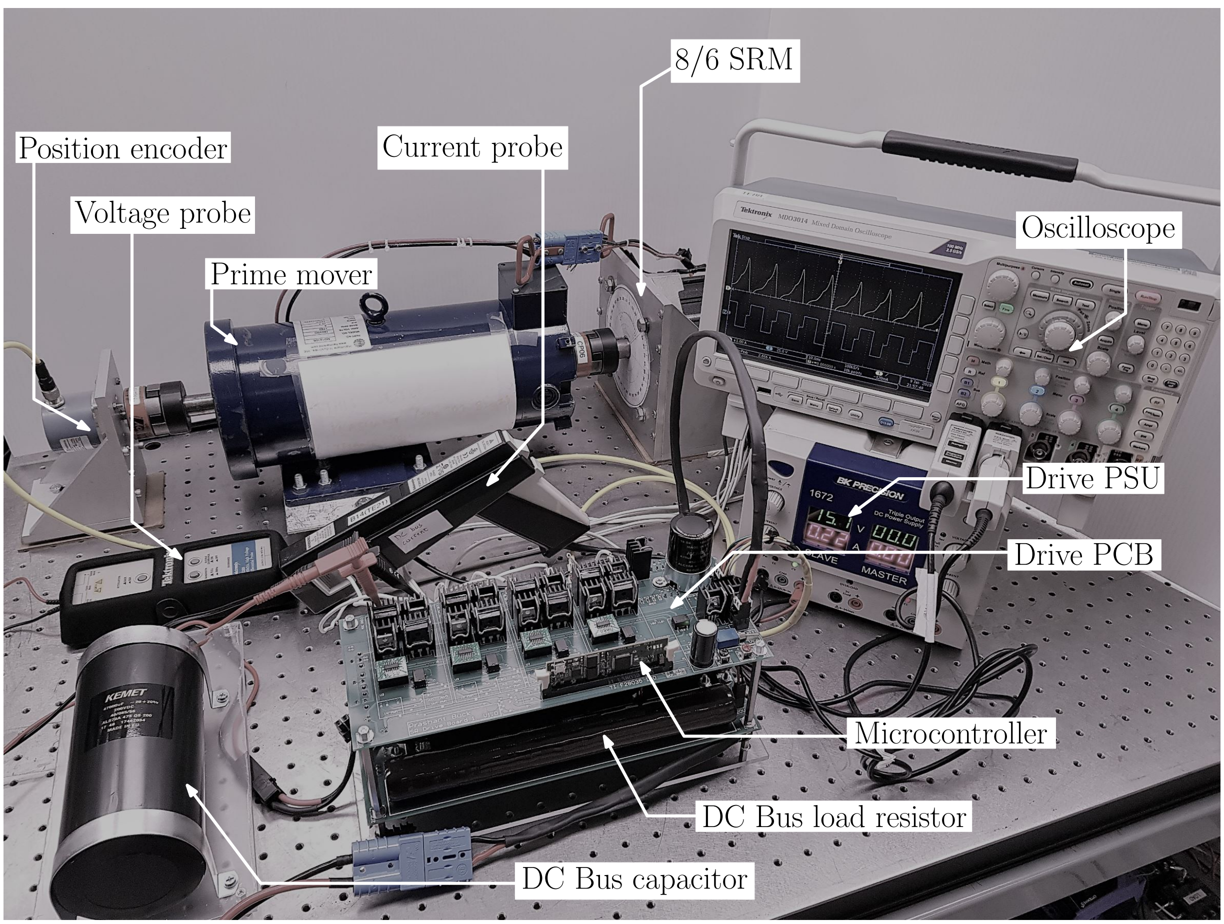

Figure J.10: Switched reluctance machine testbed

REFERENCES

[1] R. Krishnan, *Switched Reluctance Motor Drives: Modeling, Simulation, Analysis, Design, and Applications*, ser. Industrial Electronics. CRC Press, 2001.

[2] M. Abbasian, M. Moallem, and B. Fahimi, "Double-stator switched reluctance machines (dssrm): Fundamentals and magnetic force analysis," *IEEE Transactions on Energy Conversion*, vol. 25, no. 3, pp. 589–597, Sep. 2010.

[3] J. Jeong, J. Her, and C. Lee, "Novel permanent-magnet-assisted switched reluctance motor (ii): Concept, design, and analysis," in *2013 International Conference on Electrical Machines and Systems (ICEMS).* Busan, South Korea: Institute of Electrical and Electronics Engineers, Oct. 2013, pp. 609–614.

[4] H. Hwang, J. Her, and C. Lee, "Novel permanent-magnet-assisted switched reluctance motor (i): Concept, design, and analysis," in *2013 International Conference on Electrical Machines and Systems (ICEMS).* Busan, South Korea: Institute of Electrical and Electronics Engineers, Oct. 2013, pp. 602–608.

[5] Y. Liao, F. Liang, and T. A. Lipo, "A novel permanent magnet motor with doubly salient structure," *IEEE Transactions on Industry Applications*, vol. 31, no. 5, pp. 1069–1078, Sep. 1995.

[6] T. H. Kim, "A study on the design of an inset-permanent-magnet-type flux-reversal machine," *IEEE Transactions on Magnetics*, vol. 45, no. 6, pp. 2859–2862, Jun. 2009.

[7] T. J. E. Miller, Ed., *Electronic Control of Switched Reluctance Machines*, ser. Newnes Power Engineering Series. Elsevier Science, 2001.

[8] T. J. E. Miller, "Optimal design of switched reluctance motors," *IEEE Transactions on Industrial Electronics*, vol. 49, no. 1, pp. 15–27, Feb. 2002.

[9] Ansys Inc. ANSYS Maxwell. [Online]. Available: https://www.ansys.com/products/electronics/ansys-maxwell [Accessed May 20, 2019].

[10] M. T. DiRenzo, "Switched reluctance motor control - basic operation and example using the tms320f240," Texas Instruments, Tech. Rep. SPRA420A, Feb. 2000.

[11] D. A. Torrey, X. M. Niu, and E. J. Unkauf, "Analytical modelling of variable-reluctance machine magnetisation characteristics," *IEE Proceedings - Electric Power Applications*, vol. 142, no. 1, pp. 14–22, Jan. 1995.

[12] D. A. Torrey, "Switched reluctance generators and their control," *IEEE Transactions on Industrial Electronics*, vol. 49, no. 1, pp. 3–14, Feb. 2002.

[13] T. F. Stocker, D. Qin, G.-K. Plattner, M. Tignor, S. K. Allen, J. Boschung, A. Nauels, Y. Xia, V. Bex, and P. Midgley, Eds., *Climate Change 2013: The Physical Science Basis. Contribution of Working Group I to the Fifth Assessment Report of the Intergovernmental Panel on Climate Change.* Cambridge University Press, 2013.

[14] U.S. Energy Information Administration, "*International Energy Outlook 2018 Executive Summary*," Jul. 2018. [Online]. Available: https://www.eia.gov

[15] United Nations, "*United Nations Framework Convention on Climate Change*," 1992. [Online]. Available: https://unfccc.int/

[16] ——, "*The Paris Agreement*," 2015. [Online]. Available: https://unfccc.int/

[17] ——, "*Report of the Conference of the Parties on its twenty-first session, held in Paris from 30 November to 13 December 2015*," Oct. 2015. [Online]. Available: https://unfccc.int/

[18] National Development and Reform Commission, "*Enhanced Actions On Climate Change: China's Intended Nationally Determined Contributions*," Jun. 2015. [Online]. Available: https://www4.unfccc.int/sites/NDCStaging/Pages/All.aspx

[19] ——, "*China's Policies and Actions for Addressing Climate Change*," Oct. 2017. [Online]. Available: http://en.ndrc.gov.cn/

[20] National Bureau of Statistics of China. China statistical yearbook 2018. [Online]. Available: http://www.stats.gov.cn/tjsj/ndsj/2018/html/EN0915.jpg. [Accessed Apr. 22, 2019].

[21] Internatinoal Energy Agency. World energy outlook 2017: China. [Online]. Available: https://www.iea.org/weo/china/. [Accessed Apr. 22, 2019].

[22] Natural Resources Defense Council, "*The Road From Paris: China's Progress Toward Its Climate Pledge*," Nov. 2017. [Online]. Available: https://www.nrdc.org/

[23] F. Shen. (2018, Sep.) China steps up its push into clean energy. Bloomberg News. [Online]. Available: https://www.bloomberg.com/news/articles/2018-09-26/china-sets-out-new-clean-energy-goals-penalties-in-revised-plan. [Accessed Feb. 14, 2019].

[24] South China Morning Post. (2018, Sep.) China steps up green energy push with revised renewable target of 35 per cent by 2030. [Online]. Available: https://www.scmp.com/news/china/politics/article/2165831/china-steps-green-energy-push-revised-renewable-target-35-2030. [Accessed Feb. 13, 2019].

[25] Natural Resources Defense Council, "*The Road From Paris: India's Progress Toward Its Climate Pledge*," Nov. 2017. [Online]. Available: https://www.nrdc.org/

[26] Government of India Ministry of Power Central Electricity Authority, "*Draft National Electricity Plan*," Dec. 2016. [Online]. Available: http://www.cea.nic.in/

[27] Government of India Ministry of New and Renewable Energy. (2018) Annual report 2017-18. [Online]. Available: https://mnre.gov.in/file-manager/annual-report/2017-2018/EN/index.html. [Accessed Feb. 8, 2019].

[28] India Brand Equity Foundation, "*Renewable Energy*," Jan. 2019. [Online]. Available: https://www.ibef.org/

[29] International Energy Agency, "*Africa Energy Outlook*," Oct. 2014. [Online]. Available: https://www.iea.org/

[30] International Renewable Energy Agency, "*Africa 2030: Roadmap for a Renewable Energy Future*," Oct. 2015. [Online]. Available: https://www.irena.org/

[31] Global Wind Energy Council, "*Annual Market Update 2017: Global Wind Report*," Apr. 2018. [Online]. Available: https://gwec.net/

[32] Nederlandse Spoorwegen. Sustainable energy. [Online]. Available: https://www.ns.nl/en/about-ns/sustainability/energy/sustainable-energy.html. [Accessed Mar. 26, 2019].

[33] International Organization of Motor Vehicle Manufacturers. 2018 production statistics. [Online]. Available: http://www.oica.net/category/production-statistics/2018-statistics/. [Accessed Mar. 26, 2019].

[34] M. J. Coren. (2018, Aug.) Nine countries say they'll ban internal combustion engines. so far, it's just words. Quartz. [Online]. Available: https://qz.com/1341155/ [Accessed Jul. 14, 2019].

[35] Government of France. (2017, Jul.) Climate plan. [Online]. Available: https://www.gouvernement.fr/en/climate-plan [Accessed Jul. 14, 2019].

[36] R. Bhattacharjee. (2017, Nov.) Petrol, diesel cars will soon be history. The Economic Times. [Online]. Available: https://economictimes.indiatimes.com/industry/auto/cars-uvs/petrol-diesel-cars-will-soon-be-history/electric-cars-will-soon-rule-the-roads-globally/slideshow/61722377.cms [Accessed Jul. 14, 2019].

[37] Government Offices of Sweden, "*Statement of Government Policy 21 January 2019*," Jan. 2019. [Online]. Available: https://www.government.se/

[38] E. Alonso, A. M. Sherman, T. J. Wallington, M. P. Everson, F. R. Field, R. Roth, and R. E. Kirchain, "Evaluating rare earth element availability: A case with revolutionary demand from clean technologies," *Environmental Science & Technology*, vol. 46, no. 6, pp. 3406–3414, Feb. 2012.

[39] B. Zhou, Z. Li, and C. Chen, "Global potential of rare earth resources and rare earth demand from clean technologies," *Minerals*, vol. 7, no. 11, p. 203, Oct. 2017.

[40] G. P. Hatch, "Dynamics in the global market for rare earths," *Elements*, vol. 8, no. 5, pp. 341–346, Oct. 2012.

[41] S. Constantinides. (2016, Feb.) Permanent magnets in a changing world market. Magnetics Business & Technology. [Online]. Available: https://magneticsmag.com/permanent-magnets-in-a-changing-world-market/. [Accessed Mar. 4, 2019].

[42] S. Constantinides and J. D. Leon, "Permanent magnet materials and current challenges," Arnold Magnetic Technologies, Tech. Rep.

[43] U.S. Department of Energy, "*Critical Materials Strategy*," Dec. 2011. [Online]. Available: https://www.energy.gov/

[44] T. Elwert, D. Goldmann, F. Römer, M. Buchert, C. Merz, D. Schueler, and J. Sutter, "Current developments and challenges in the recycling of key components of (hybrid) electric vehicles," *Recycling*, vol. 1, pp. 25–60, Oct. 2015.

[45] K. Binnemans, P. T. Jones, B. Blanpain, T. V. Gerven, Y. Yang, A. Walton, and M. Buchert, "Recycling of rare earths: a critical review," *Journal of Cleaner Production*, vol. 51, pp. 1–22, Jul. 2013.

[46] W. P. Erickson, M. M. Wolfe, K. J. Bay, D. H. Johnson, and J. L. Gehring, "A comprehensive analysis of small-passerine fatalities from collision with turbines at wind energy facilities," *PLOS ONE*, vol. 9, no. 9, pp. 1–18, 2014.

[47] American Bird Conservancy. Wind energy. [Online]. Available: https://abcbirds.org/program/wind-energy-and-birds/. [Accessed Apr. 20, 2019].

[48] R. Cardenas, W. F. Ray, and G. M. Asher, "Switched reluctance generators for wind energy applications," in *Power Electronics Specialists Conference, 1995. PESC '95 Record., 26th Annual IEEE*, vol. 1. Atlanta, GA, USA: Institute of Electrical and Electronics Engineers, Jun. 1995, pp. 559–564.

[49] R. Cardenas, R. Pena, M. Perez, J. Clare, G. Asher, and P. Wheeler, "Control of a switched reluctance generator for variable-speed wind energy applications," *IEEE Transactions on Energy Conversion*, vol. 20, no. 4, pp. 781–791, Dec. 2005.

[50] D. A. Torrey, "Variable-reluctance generators in wind-energy systems," in *Power Electronics Specialists Conference, 1993. PESC '93 Record., 24th Annual IEEE*. Seattle, WA, USA: Institute of Electrical and Electronics Engineers, Jun. 1993, pp. 561–567.

[51] M. A. Mueller, "Design and performance of a 20 kw, 100 rpm, switched reluctance generator for a direct drive wind energy converter," in *IEEE International Conference on Electric Machines and Drives, 2005.* San Antonio, TX, USA: Institute of Electrical and Electronics Engineers, May 2005, pp. 56–63.

[52] B. Fahimi, A. Emadi, and R. B. Sepe, "A switched reluctance machine-based starter/alternator for more electric cars," *IEEE Transactions on Energy Conversion*, vol. 19, no. 1, pp. 116–124, Mar. 2004.

[53] B. Fahimi, "A switched reluctance machine based starter/generator for more electric cars," in *IEMDC 2001. IEEE International Electric Machines and Drives Conference (Cat. No.01EX485).* Cambridge, MA, USA: Institute of Electrical and Electronics Engineers, Jun. 2001, pp. 73–78.

[54] E. Mese, Y. Sozer, J. M. Kokernak, and D. A. Torrey, "Optimal excitation of a high speed switched reluctance generator," in *APEC 2000. Fifteenth Annual IEEE Applied Power Electronics Conference and Exposition (Cat. No.00CH37058)*, vol. 1. New Orleans, LA, USA: Institute of Electrical and Electronics Engineers, Feb. 2000, pp. 362–368.

[55] B. Fahimi, "On the suitability of switched reluctance drives for starter/generator application," in *Vehicular Technology Conference. IEEE 55th Vehicular Technology Conference. VTC Spring 2002 (Cat. No.02CH37367)*, vol. 4. Birmingham, AL, USA: Institute of Electrical and Electronics Engineers, May 2002, pp. 2070–2075.

[56] N. Schofield and S. Long, "Generator operation of a switched reluctance starter/generator at extended speeds," *IEEE Transactions on Vehicular Technology*, vol. 58, no. 1, pp. 48–56, Jan. 2009.

[57] M. Krishnamurthy, C. S. Edrington, A. Emadi, P. Asadi, M. Ehsani, and B. Fahimi, "Making the case for applications of switched reluctance motor technology in automotive products," *IEEE Transactions on Power Electronics*, vol. 21, no. 3, pp. 659–675, May 2006.

[58] A. Chiba, Y. Takano, M. Takeno, T. Imakawa, N. Hoshi, M. Takemoto, and S. Ogasawara, "Torque density and efficiency improvements of a switched reluctance motor without rare-earth material for hybrid vehicles," *IEEE Transactions on Industry Applications*, vol. 47, no. 3, pp. 1240–1246, May 2011.

[59] H.-C. Chang and C.-M. Liaw, "Development of a compact switched-reluctance motor drive for ev propulsion with voltage-boosting and pfc charging capabilities," *IEEE Transactions on Vehicular Technology*, vol. 58, no. 7, pp. 3198–3215, Sep. 2009.

[60] H. Gao, Y. Gao, and M. Ehsani, "Design issues of the switched reluctance motor drive for propulsion and regenerative braking in ev and hev," in *SAE Technical Paper*. SAE International, Aug. 2001.

[61] ——, “A neural network based srm drive control strategy for regenerative braking in ev and hev,” in *IEMDC 2001. IEEE International Electric Machines and Drives Conference (Cat. No.01EX485).* Cambridge, MA, USA: Institute of Electrical and Electronics Engineers, Jun. 2001, pp. 571–575.

[62] S. R. MacMinn and J. W. Sember, “Control of a switched-reluctance aircraft engine starter-generator over a very wide speed range,” in *Proceedings of the 24th Intersociety Energy Conversion Engineering Conference*, vol. 1. Washington, DC, USA: Institute of Electrical and Electronics Engineers, Aug. 1989, pp. 631–638.

[63] A. Radun, “Generating with the switched reluctance motor,” in *Applied Power Electronics Conference and Exposition, 1994. APEC ’94. Conference Proceedings 1994., Ninth Annual*, vol. 1. Orlando, FL, USA: Institute of Electrical and Electronics Engineers, Feb. 1994, pp. 41–47.

[64] D. E. Cameron and J. H. Lang, “The control of high-speed variable-reluctance generators in electric power systems,” *IEEE Transactions on Industry Applications*, vol. 29, no. 6, pp. 1106–1109, Nov. 1993.

[65] C. S. Edrington, B. Fahimi, and R. B. Sepe, “Sensorless super-high-speed switched reluctance generators,” in *IEEE 2002 28th Annual Conference of the Industrial Electronics Society. IECON 02*, vol. 2. Sevilla, Spain: Institute of Electrical and Electronics Engineers, Nov. 2002, pp. 1026–1031 vol.2.

[66] B.-S. Lee, H.-K. Bae, P. Vijayraghavan, and R. Krishnan, “Design of a linear switched reluctance machine,” *IEEE Transactions on Industry Applications*, vol. 36, no. 6, pp. 1571–1580, Nov. 2000.

[67] F. Daldaban and N. Ustkoyuncu, “A novel linear switched reluctance motor for railway transportation systems,” *Energy Conversion and Management*, vol. 51, no. 3, pp. 465–469, Nov. 2009.

[68] C. Hao and X. Guilin, “The parallel drive system of the double switched reluctance motors for locomotive traction application,” in *IECON’01: 27th Annual Conference of the IEEE Industrial Electronics Society (Cat. No.37243)*, vol. 2. Denver, CO, USA: Institute of Electrical and Electronics Engineers, Nov. 2001, pp. 1483–1487.

[69] I. McNeil, Ed., *An Encyclopedia of the History of Technology*, ser. Routledge Companion Encyclopedias. Taylor & Francis, 2002.

[70] S. A. Nasar, “D.C.-switched reluctance motor,” *Proceedings of the Institution of Electrical Engineers*, vol. 116, no. 6, pp. 1048–1049, Jun. 1969.

[71] Institute of Electrical and Electronics Engineers. (2019) IEEE edison medal recipients. [Online]. Available: https://www.ieee.org/about/awards/bios/edison-recipients.html#sect13. [Accessed Jan. 10, 2019].

[72] C. J. Hancock and J. R. Hendershot, "Electronically commutated reluctance motor," U.S. Patent 5 015 903, May 14, 1991.

[73] Nidec Corporation, "*Nidec Completes Acquisition of Emerson Electric Co.'s Motors, Drives and Electric Power Generation Businesses*," Feb. 2017. [Online]. Available: https://www.nidec.com/en-NA/

[74] G. Baoming, A. T. de Almeida, and F. J. T. E. Ferreira, "Design of transverse flux linear switched reluctance motor," *IEEE Transactions on Magnetics*, vol. 45, no. 1, pp. 113–119, Jan. 2009.

[75] J. G. Amoros and P. Andrada, "Sensitivity analysis of geometrical parameters on a double-sided linear switched reluctance motor," *IEEE Transactions on Industrial Electronics*, vol. 57, no. 1, pp. 311–319, Jan. 2010.

[76] J. F. Pan, Y. Zou, and G. Cao, "An asymmetric linear switched reluctance motor," *IEEE Transactions on Energy Conversion*, vol. 28, no. 2, pp. 444–451, Jun. 2013.

[77] J. Pan, N. C. Cheung, and J. Yang, "High-precision position control of a novel planar switched reluctance motor," *IEEE Transactions on Industrial Electronics*, vol. 52, no. 6, pp. 1644–1652, Dec. 2005.

[78] L. Kolomeitsev, D. Kraynov, S. Pakhomin, F. Rednov, E. Kallenbach, V. Kireev, T. Schneider, and J. Bocker, "Linear switched reluctance motor as a high efficiency propulsion system for railway vehicles," in *2008 International Symposium on Power Electronics, Electrical Drives, Automation and Motion*. Ischia, Italy: Institute of Electrical and Electronics Engineers, Jun. 2008, pp. 155–160.

[79] H. S. Lim and R. Krishnan, "Ropeless elevator with linear switched reluctance motor drive actuation systems," *IEEE Transactions on Industrial Electronics*, vol. 54, no. 4, pp. 2209–2218, Aug. 2007.

[80] A. Labak and N. C. Kar, "A novel five-phase pancake shaped switched reluctance motor for hybrid electric vehicles," in *2009 IEEE Vehicle Power and Propulsion Conference*. Dearborn, MI, USA: Institute of Electrical and Electronics Engineers, Sep. 2009, pp. 494–499.

[81] T. Lambert, M. Biglarbegian, and S. Mahmud, "A novel approach to the design of axial-flux switched-reluctance motors," *Machines*, vol. 3, pp. 27–54, Mar. 2015.

[82] C. Lin, W. Wang, and B. Fahimi, "Optimal design of double stator switched reluctance machine (dssrm)," in *2012 IEEE International Symposium on Industrial Electronics*. Hangzhou, China: Institute of Electrical and Electronics Engineers, May 2012, pp. 719–724.

[83] A. H. Isfahani and B. Fahimi, "Comparison of mechanical vibration between a double-stator switched reluctance machine and a conventional switched reluctance machine," *IEEE Transactions on Magnetics*, vol. 50, no. 2, pp. 293–296, Feb. 2014.

[84] M.-T. Khor, R. Sotudeh, and D. Lee, "Switched reluctance motor based on short flux path control method," in *39th International Universities Power Engineering Conference, 2004. UPEC 2004.*, vol. 2. Bristol, UK: Institute of Electrical and Electronics Engineers, Sep. 2004, pp. 559–562.

[85] C. Lee and R. Krishnan, "New designs of a two-phase e-core switched reluctance machine by optimizing the magnetic structure for a specific application: Concept, design, and analysis," *IEEE Transactions on Industry Applications*, vol. 45, no. 5, pp. 1804–1814, Sep. 2009.

[86] N. S. Lobo, "Doubly-salient permanent magnet flux-reversal-free-stator switched reluctance machines," Ph.D. dissertation, Virginia Polytechnic Inst. and State Univ. Blacksburg, Jan. 2011.

[87] R. P. Deodhar, S. Andersson, I. Boldea, and T. J. E. Miller, "The flux-reversal machine: a new brushless doubly-salient permanent-magnet machine," *IEEE Transactions on Industry Applications*, vol. 33, no. 4, pp. 925–934, Jul. 1997.

[88] T. H. Kim and J. Lee, "A study of the design for the flux reversal machine," *IEEE Transactions on Magnetics*, vol. 40, no. 4, pp. 2053–2055, Jul. 2004.

[89] B. Fahimi, G. Suresh, K. M. Rahman, and M. Ehsani, "Mitigation of acoustic noise and vibration in switched reluctance motor drive using neural network based current profiling," in *Conference Record of 1998 IEEE Industry Applications Conference. Thirty-Third IAS Annual Meeting (Cat. No.98CH36242)*, vol. 1. St. Louis, MO, USA: Institute of Electrical and Electronics Engineers, Oct. 1998, pp. 715–722.

[90] H.-Y. Yang, Y.-C. Lim, and H.-C. Kim, "Acoustic noise/vibration reduction of a single-phase srm using skewed stator and rotor," *IEEE Transactions on Industrial Electronics*, vol. 60, no. 10, pp. 4292–4300, Oct. 2013.

[91] Y. K. Choi, H. S. Yoon, and C. S. Koh, "Pole-shape optimization of a switched-reluctance motor for torque ripple reduction," *IEEE Transactions on Magnetics*, vol. 43, no. 4, pp. 1797–1800, Apr. 2007.

[92] H. Gao, F. R. Salmasi, and M. Ehsani, "Inductance model-based sensorless control of the switched reluctance motor drive at low speed," *IEEE Transactions on Power Electronics*, vol. 19, no. 6, pp. 1568–1573, Nov. 2004.

[93] G. Gallegos-Lopez, P. C. Kjaer, and T. J. E. Miller, "A new sensorless method for switched reluctance motor drives," *IEEE Transactions on Industry Applications*, vol. 34, no. 4, pp. 832–840, Jul. 1998.

[94] B. Fahimi, A. Emadi, and R. B. Sepe, "Four-quadrant position sensorless control in srm drives over the entire speed range," *IEEE Transactions on Power Electronics*, vol. 20, no. 1, pp. 154–163, Jan. 2005.

[95] H. H. Moghbelli, G. E. Adams, and R. G. Hoft, "Prediction of the instantaneous and steady state torque of the switched reluctance motor using the finite element method (fem)," in *Conference Record of the 1988 IEEE Industry Applications Society Annual Meeting*, vol. 1. Pittsburgh, PA, USA: Institute of Electrical and Electronics Engineers, Oct. 1988, pp. 59–70.

[96] T. Matsuo, J. Luo, E. P. Hoffman, and T. A. Lipo, "Self excited variable reluctance generator," in *Industry Applications Conference, 1997. Thirty-Second IAS Annual Meeting, IAS '97., Conference Record of the 1997 IEEE*, vol. 1. New Orleans, LA, USA: Institute of Electrical and Electronics Engineers, Oct. 1997, pp. 653–660.

[97] M. Barnes and C. Pollock, "Power electronic converters for switched reluctance drives," *IEEE Transactions on Power Electronics*, vol. 13, no. 6, pp. 1100–1111, Nov. 1998.

[98] K. Ha, C. Lee, J. Kim, R. Krishnan, and S.-G. Oh, "Design and development of low-cost and high-efficiency variable-speed drive system with switched reluctance motor," *IEEE Transactions on Industry Applications*, vol. 43, no. 3, pp. 703–713, May 2007.

[99] R. Krishnan and P. N. Materu, "Design of a single-switch-per-phase converter for switched reluctance motor drives," *IEEE Transactions on Industrial Electronics*, vol. 37, no. 6, pp. 469–476, Dec. 1990.

[100] S. Mir, I. Husain, and M. E. Elbuluk, "Energy-efficient c-dump converters for switched reluctance motors," *IEEE Transactions on Power Electronics*, vol. 12, no. 5, pp. 912–921, Sep. 1997.

[101] G. E. P. Box, "Science and statistics," *Journal of the American Statistical Association*, vol. 71, no. 356, pp. 791–799, Dec. 1976.

[102] L. Ljung, *System Identification: Theory for the User*, 2nd ed., ser. Prentice Hall information and system sciences series. Prentice Hall PTR, 1999.

[103] The MathWorks, Inc. System identification toolbox. [Online]. Available: https://www.mathworks.com/products/sysid.html [Accessed May 20, 2019].

[104] D. A. Torrey and J. H. Lang, "Modelling a nonlinear variable-reluctance motor drive," *IEE Proceedings B - Electric Power Applications*, vol. 137, no. 5, pp. 314–326, Sep. 1990.

[105] The MathWorks, Inc. Curve fitting toolbox. [Online]. Available: https://www.mathworks.com/products/curvefitting.html [Accessed May 23, 2019].

[106] T. J. E. Miller and M. McGilp, "Nonlinear theory of the switched reluctance motor for rapid computer-aided design," *IEE Proceedings B - Electric Power Applications*, vol. 137, no. 6, pp. 337–347, Nov. 1990.

[107] G. S. Buja and M. I. Valla, "Control characteristics of the srm drives. i. operation in the linear region," *IEEE Transactions on Industrial Electronics*, vol. 38, no. 5, pp. 313–321, Oct. 1991.

[108] ——, "Control characteristics of the srm drives. ii. operation in the linear region," *IEEE Transactions on Industrial Electronics*, vol. 41, no. 3, pp. 316–325, Jun. 1994.

[109] M. Stiebler and K. Liu, "An analytical model of switched reluctance machines," *IEEE Transactions on Energy Conversion*, vol. 14, no. 4, pp. 1100–1107, Dec. 1999.

[110] C. Roux and M. M. Morcos, "On the use of a simplified model for switched reluctance motors," *IEEE Transactions on Energy Conversion*, vol. 17, no. 3, pp. 400–405, Sep. 2002.

[111] T. J. E. Miller, M. Glinka, M. McGilp, C. Cossar, G. Gallegos-Lopez, D. Ionel, and M. Olaru, "Ultra-fast model of the switched reluctance motor," in *Conference Record of 1998 IEEE Industry Applications Conference. Thirty-Third IAS Annual Meeting (Cat. No.98CH36242)*, vol. 1. St. Louis, MO, USA: Institute of Electrical and Electronics Engineers, Oct. 1998, pp. 319–326.

[112] Z. Lin, D. S. Reay, B. W. Williams, and X. He, "Online modeling for switched reluctance motors using b-spline neural networks," *IEEE Transactions on Industrial Electronics*, vol. 54, no. 6, pp. 3317–3322, Dec. 2007.

[113] T. Lachman, T. R. Mohamad, and C. H. Fong, "Nonlinear modelling of switched reluctance motors using artificial intelligence techniques," *IEE Proceedings - Electric Power Applications*, vol. 151, no. 1, pp. 53–60, Jan. 2004.

[114] B. Fahimi, G. Suresh, J. Mahdavi, and M. Ehsami, "A new approach to model switched reluctance motor drive application to dynamic performance prediction, control and design," in *PESC 98 Record. 29th Annual IEEE Power Electronics Specialists Conference (Cat. No.98CH36196)*, vol. 2. Fukuoka, Japan: Institute of Electrical and Electronics Engineers, May 1998, pp. 2097–2102.

[115] D. A. Andrade and R. Krishnan, "Characterization of switched reluctance machines using fourier series approach," in *Conference Record of the 2001 IEEE Industry Applications Conference. 36th IAS Annual Meeting (Cat. No.01CH37248)*, vol. 1. Chicago, IL, USA: Institute of Electrical and Electronics Engineers, Sep. 2001, pp. 48–54.

[116] G. Pólya. [Online]. Available: https://www.goodreads.com/quotes/995300-in-order-to-solve-this-differential-equation-you-look-at [Accessed Jun. 3, 2019].

[117] S. H. Strogatz, *Nonlinear Dynamics and Chaos: With Applications to Physics, Biology, Chemistry, and Engineering*, 2nd ed. Westview Press, 2015.

[118] D. G. Zill and M. Cullen, *Advanced Engineering Mathematics*, ser. Prindle, Weber & Schmidt series in mathematics. PWS-KENT Publishing Company, 1992.

[119] M. Kiani, "Model predictive control of stator currents in switched reluctance generators," in *2014 IEEE 23rd International Symposium on Industrial Electronics (ISIE)*. Istanbul, Turkey: Institute of Electrical and Electronics Engineers, Jun. 2014, pp. 842–846.

[120] V. Nasirian, S. Kaboli, and A. Davoudi, "Output power maximization and optimal symmetric freewheeling excitation for switched reluctance generators," *IEEE Transactions on Industry Applications*, vol. 49, no. 3, pp. 1031–1042, May 2013.

[121] S. Dixon and B. Fahimi, "Enhancement of output electric power in switched reluctance generators," in *IEEE International Electric Machines and Drives Conference, 2003. IEMDC'03.*, vol. 2. Madison, WI, USA: Institute of Electrical and Electronics Engineers, Jun. 2003, pp. 849–856.

[122] S. Dixon, "Enhancement of output electric power in switched reluctance generators through a freewheeling switching strategy," Master's thesis, Dept. Elect. Eng., Univ. of Missouri Rolla, Rolla, 2003.

[123] Texas Instruments, Inc. Piccolo TMS320F28035 Isolated controlCARD. [Online]. Available: http://www.ti.com/tool/TMDSCNCD28035ISO [Accessed Jun. 4, 2019].

[124] The MathWorks, Inc. (2018, Sep.) MATLAB R2018b. [Online]. Available: https://www.mathworks.com/products/matlab/whatsnew.html. [Accessed Jan. 4, 2019].

BIOGRAPHICAL SKETCH

Prashant Carl Buck, son of Dr. Dipti Buck and Mr. Amarjit Buck, was born in 1989 at the foothills of the Himalayas in Dehradun, India. He spent his early childhood years in Dehradun, where he completed his initial schooling. He attended middle and senior school at The Cathedral & John Connon School in Mumbai, India. He received his Bachelor of Technology (B.Tech) degree in Electronics and Communications Engineering in 2011 from SRM Institute of Science & Technology, Tamil Nadu, India. He received his Master of Science (MS) degree in Electrical Engineering, specializing in Circuits and Systems in 2013 from The University of Texas at Dallas, United States of America. He then began the pursuit of his doctoral degree wherein his research focused on modeling techniques for switched reluctance machines, especially on the phase current reconstruction and peak prediction for switched reluctance generators operated in positive feedback single pulse mode. Prashant worked as a Teaching and Research Assistant at the Electrical and Computer Engineering Department of The University of Texas at Dallas during his doctoral studies. He was nominated for the President's Teaching Excellence Award for Teaching Assistants in 2017 and was recognized for instructional excellence as a Teaching Assistant by the Erik Jonsson School of Engineering and Computer Science in 2018. During his time as a doctoral student, he was also awarded the Louis Beecherl, Jr. Graduate Fellowship in 2014 and 2016.

CURRICULUM VITAE

Prashant Carl Buck

prashantbuck@gmail.com

EDUCATION

University of Texas at Dallas	*2019*
Doctor of Philosophy (PhD) in Electrical Engineering	GPA: 3.909/4
Department of Electrical Engineering	
University of Texas at Dallas	*2013*
Masters of Science (MS) in Electrical Engineering	GPA: 3.900/4
Department of Electrical Engineering	
SRM University	*2011*
Bachelor of Technology (B.Tech)	GPA: 9.26/10
Electronics and Communication Engineering	

TECHNICAL STRENGTHS

IC Design & Testing CAD Tools:	HSpice, VHDL, Cadence (350nm, 130nm, 90nm), Waveview, Cosmoscope, Synopsys, Tetramax
Simulation Software:	Ansys Maxwell, Simulink, PLECS, LabVIEW, LTspice, TINA-TI, FilterPro
Hardware:	Altium, Code Composer Studio, Embedded-C TI C2000 Microcontrollers: F28035, F28335
Programming Languages:	C, C++, MATLAB Scripting
FPGA Tools:	Xilinx, Modelsim, Verilog

COURSE WORK - University of Texas at Dallas

Testing and Testable Design, Analog Integrated Circuit Design, Digital Signal Processing, VLSI Design, RF & Microwave Systems Engineering, Advanced Digital Logic, Design Automation of VLSI Systems, Special Topics in Power Electronics, Power Management Circuits, Control Modeling and Simulation in Power Electronics, Semiconductor Processing Technology

TEACHING ASSISTANT - University of Texas at Dallas

EE/CE 3120 Digital Circuits Laboratory, EE/CE 3320 Digital Circuits, ENGR 2300 Linear Algebra, EECT/CE 6325 VLSI Design, EEPE 6354 Power Electronics, CE 6303 Testing and Testable Design

AWARDS/SCHOLARSHIPS

· Erik Jonsson ECS Instructional Excellence, Teaching Assistant Award	*2018*
· Nominated for President's Excellence in Teaching Award	*2017*
· Louis Beecherl, Jr. $4,000 Graduate Fellowship	*2016*
· Louis Beecherl, Jr. $4,000 Graduate Fellowship	*2014*
· Jonsson School $1,000 Graduate Study Scholarship	*2013*

PROFESSIONAL ASSOCIATIONS/MEMBERSHIPS

· Institute of Electrical and Electronics Engineers (IEEE)
· Integrated Design, Engineering, and Algorithmics (IDEA) Laboratory research group
· Renewable Energy and Vehicular Technology (REVT) Laboratory